

## ABSTRACT

Title of Dissertation:      **WAVE CHAOS IN MICROWAVE COUPLED  
ENCLOSURES, RESERVOIR COMPUTING,  
AND PHOTONIC TOPOLOGICAL INSULATOR  
GRAPHS: THEORY AND EXPERIMENT**

Shukai Ma  
Doctor of Philosophy, 2022

Dissertation Directed by:   **Professor Steven M. Anlage  
Department of Physics**

Complex scattering exists in many diverse physical and real-life scenarios. Examples include reactions of atomic nuclei, transport through quantum dots, and the propagation of electromagnetic (EM) waves in over-moded resonant systems. These systems are *Wave Chaotic*, meaning that minute perturbations will lead to a drastic change in the wave properties of the system. The underlying chaotic property in the short wavelength limit makes deterministic modeling of wave properties vulnerable to small perturbations. Because of this, statistical methods play a central role in wave chaotic system studies. The Random Coupling Model (RCM) has been successfully applied to predict the statistics of *single* chaotic EM enclosures. We here expand RCM to systems consisting of *multiple* volumes that are coupled together, and do so with highly reduced computational complexity. Going beyond knowledge-based modeling, we employ machine-learning techniques to identify hidden information embedded in the scattering properties of wave chaotic systems.

Reservoir computing (RC) is a genre of neural networks employed in machine learning studies. Its training is radically simplified (compared to a full back-propagation process in neural networks) because the input and reservoir layers remain unchanged during the process. Recent work shows that RC can reasonably predict the future evolution of spatio-temporal chaotic systems. We aim to reverse the thinking: to emulate a software RC using the spatio-temporal chaotic wave fields in physical EM enclosures. A proof-of-principle hardware RC is demonstrated experimentally, and tested through a series of complex tasks carried out at ns-time scales.

The concept of photonic topological insulator (PTI) is translated from the study of topological insulators (TIs) in condensed matter physics. For a TI material, the charge will only flow in topologically-protected states on the boundary surrounding the material, rather than in the bulk. We experimentally demonstrated a novel composite PTI system with quantum Hall (QH) and quantum spin Hall (QSH) topological phases. The TI effect also introduces a synthetic spin- $\frac{1}{2}$  degree-of-freedom to the guided waves. The Fermionic two-state property, absent in the bosonic photon world, is now accessible using the PTI system. Using this PTI system, I realize a chaotic graph system that falls in the Gaussian Symplectic Ensemble (GSE) universality class, which in principle only exists in the Fermionic world. We use simulations to show that GSE statistics will emerge in an appropriately designed PTI graph obeying anti-unitary symmetry.

WAVE CHAOS IN MICROWAVE COUPLED  
ENCLOSURES, RESERVOIR COMPUTING,  
AND PHOTONIC TOPOLOGICAL INSULATOR  
GRAPHS: THEORY AND EXPERIMENT

by

Shukai Ma

Dissertation submitted to the Faculty of the Graduate School of the  
University of Maryland, College Park in partial fulfillment  
of the requirements for the degree of  
Doctor of Philosophy  
2022

Advisory Committee:

Professor Steven M. Anlage, Chair/Advisor

Professor Yanne K. Chembo, Dean's Representative

Professor Thomas M. Antonsen

Professor Edward Ott

Professor Rajarshi Roy

© Copyright by  
Shukai Ma  
2022

## Acknowledgments

This thesis would not have been possible without the inspiration and support of many remarkable individuals — my thanks and appreciation to all of them for being part of this journey and making this thesis possible. I owe my deepest gratitude to my principal supervisor Professor Steven M. Anlage. Without his enthusiasm, encouragement, support, and endless optimism, this thesis would hardly have been completed. He had faith in my skills, allowed me to explore seemingly parallel subjects, and helped me grow as an early-career professional.

Besides my advisor, I express my warmest gratitude to my associate supervisor, Prof. Thomas M. Antonsen, and Prof. Ed Ott. Their guidance into the domain of theoretical modeling, statistical analysis, and machine learning has been a valuable input for this thesis. I want to thank Prof. Yanne K. Chembo and Prof. Rajarshi Roy for agreeing to be the committee member. I also want to express my gratitude to my collaborators, Prof. Gregor Tanner, Prof. Gabriele Gradoni, and Prof. Sendy Phang at the University of Nottingham, Prof. Zhen Peng at UIUC, Prof. Gennady Shvets and Dr. Yang Yu at Cornell, and Dr. Zachary Drikas and Dr. Bisrat Addissie at Naval Research Laboratory. Their unwavering help and immense knowledge have significantly influenced many of the concepts presented in this thesis. Their work has significantly influenced many of the concepts presented in this thesis.

It is a pleasure to thank my friends at the basement/sub-basement: Bo Xiao, Seokjin Bae, Bakhrom Oripov, Min Zhou, Jingnan Cai, and Lei Chen, for the beautiful times we shared, especially the Tuesday group lunches. I am also thankful for the help from Tamin Tai, Ben Frazier, Arthur Carlton-Jones, and Jared Erb. In addition, I would like to thank all my friends in College Park who gave me the necessary distractions from my research and made my stay in Maryland memorable. I would also like to thank Quantum Material Center for hosting my experiments and taking care of all the administrative matters. It is impossible to remember all, and I apologize to those I have inadvertently left out.

Finally, my deep and sincere gratitude to my family for their continuous and unparalleled love, help, and support. I am grateful to my partner, Dr. Qixin Yang, for always being there for me. If I have ever faltered, she has always stood by to pick me up. Saying ‘Thank you’ is hardly enough. I am forever indebted to my parents, Mr. Qi Ma and Mrs. Xiangyun Shen, for giving me the opportunities and experiences that have made me who I am. They selflessly encouraged me to explore new directions in life and seek my own destiny. This journey would not have been possible if not for them, and I dedicate this milestone to them.

## Table of Contents

Acknowledgements	ii
Table of Contents	iv
List of Tables	vii
List of Figures	viii
List of Abbreviations	xviii
Chapter 1: Introduction	1
1.1 Introduction to the Phenomenon of Chaos . . . . .	1
1.2 Introduction to Random Matrix Theory . . . . .	4
1.3 Introduction to the Random Coupling Model . . . . .	7
1.4 Outline of the Thesis . . . . .	10
Chapter 2: Random Coupling Model for Multi-Enclosure Wave Chaotic Systems	12
2.1 Overview of the Multi-enclosure RCM . . . . .	13
2.2 Multi-enclosure RCM Formalism . . . . .	17
2.3 Scaled-structure Experimental Setup . . . . .	18
2.4 Experimental and RCM Results . . . . .	20
Chapter 3: Hybrid Power Balance-RCM Method for Multi-enclosure Wave Chaotic Systems	26
3.1 Power Balance Method . . . . .	27
3.2 Hybrid Method Overview . . . . .	28
3.3 Hybrid Method Details Part I: RCM Treatment . . . . .	30
3.4 Hybrid Method Details Part II: Detailed Single Cavity Treatments . . . . .	32
3.5 Hybrid Method Details Part III: Finalizing the Hybrid Model . . . . .	34
3.6 Experimental Results and Discussion . . . . .	35
3.7 Hybrid Model Limitations . . . . .	39
Chapter 4: Application of Machine Learning to Wave Chaotic Systems	42
4.1 Machine Learning Applications, Overview . . . . .	43
4.2 Multi-enclosure Experimental Setup . . . . .	43
4.3 ML Model I: Neural Network . . . . .	48
4.4 Task I: Multi-cavity System Classification Task . . . . .	50

4.5	Task II: Chaotic Cavity S-parameter Series Prediction . . . . .	54
4.6	Discussion and Summary . . . . .	55
Chapter 5:	Late-Time Time-Domain Random Coupling Model . . . . .	58
5.1	Overview . . . . .	58
5.2	Details of TD-RCM Formulation . . . . .	59
5.2.1	TD-RCM Equation of Motion . . . . .	60
5.2.2	System Port Treatments . . . . .	62
5.2.3	Generating of System Eigenmodes with RMT . . . . .	64
5.3	Gigabox Short-pulse Experiment . . . . .	65
5.4	Statistical Analysis and Discussion . . . . .	67
5.5	Discussion and Summary . . . . .	70
Chapter 6:	Wave-Based Reservoir Computing . . . . .	73
6.1	Introduction . . . . .	73
6.2	Software Origin of RC . . . . .	75
6.3	Hardware Realization of RC . . . . .	77
6.4	Chaotic Wave-based RC . . . . .	78
6.4.1	Operating Principles . . . . .	78
6.4.2	Reservoir Expansion Techniques . . . . .	80
6.4.3	Experimental Set-up . . . . .	82
6.4.4	Benchmark Test Results . . . . .	83
6.4.5	Discussions and Summary . . . . .	87
Chapter 7:	Chaotic 1D Graphs with Photonic Crystal Waveguides . . . . .	92
7.1	Introduction of PC Defect Waveguide . . . . .	93
7.2	Photonic Crystal Graph . . . . .	96
7.3	Eigenmode Spacing Statistical Analysis . . . . .	101
7.4	Eigenfunction Analysis . . . . .	103
Chapter 8:	Quantum Hall - Quantum Spin Hall Composite Photonic Topological Insulator . . . . .	110
8.1	Introduction to PTI Technology . . . . .	111
8.2	Design of QH-QSH BMW Structure . . . . .	113
8.3	Composite QH-QSH Systems . . . . .	115
8.4	Topological Y-junction . . . . .	117
8.5	Topological 4-port Circulator . . . . .	121
Chapter 9:	Chaotic Gaussian Symplectic Ensemble Structures with Photonic Topological Insulator Graphs . . . . .	124
9.1	Overview . . . . .	124
9.2	Design of QVH-QSH Graphs . . . . .	127
9.3	Symplectic Group Analysis for BMW Systems . . . . .	130
9.4	Numerical Results . . . . .	134
9.5	Room-temperature Experimental Results . . . . .	136

9.6	Low-temperature Experimental Results . . . . .	143
9.7	Discussion . . . . .	147
Chapter 10: Conclusions		148
Appendix A: Multi-cavity RCM Modeling		151
A.1	Single Cavity Treatment . . . . .	151
A.2	Total Admittance of an N-Cavity Chain . . . . .	153
A.3	Input and Trans-Impedances . . . . .	154
Appendix B: Multi-cavity RCM Experimental Details		156
B.1	Aperture and port radiation admittance studies . . . . .	156
B.2	Convergence of the RCM formalism with inclusion of aperture modes . . . . .	157
B.3	Additional cavity cascade experimental studies . . . . .	159
Appendix C: Multi-channel analysis for the cavity cascade system		160
Appendix D: Applying the Hybrid Model to Generic Cavity Systems		167
Appendix E: Simplified PWB-RCM Hybrid Method		169
Appendix F: Wave-based Reservoir Computing Details		173
F.1	Simulation setup . . . . .	173
F.2	Observer tasks for dynamical systems . . . . .	173
F.3	Benchmark tests . . . . .	175
F.4	RC operation speed analysis . . . . .	176
Appendix G: Heterogeneous BMW Structure Details		178
G.1	Experimental Methods . . . . .	178
G.2	Ferrite Material . . . . .	179
G.3	Kink mode Back-scattering Studies . . . . .	180
G.4	Coupled waveguide issue . . . . .	183
G.5	QH-QSH structure with no external magnetic field . . . . .	185
G.6	Topological Y-junction . . . . .	187
Appendix H: Extended Symplectic Group Analysis of BMW Hamiltonian		188
Bibliography		190

## List of Tables

- 7.1 The summarized consecutive mode spacing ratios of the photonic crystal graph (PC-Graph) system, the graph system with random ratio order, and the theoretical predictions for the GOE, GUE and GSE systems [1]. . . . 103

## List of Figures

1.1	<p>Figures (a) and (b) show the trajectories of two billiard balls inside a non-chaotic square billiard, and a chaotic sinai billiard (square billiard with a center circular block), respectively. Figure (c) shows the quarter bowtie billiard (open plate view). Figure (d) shows the eigenfunction profile of one system eigenmode at 12.57 GHz. Figures (a) and (b) are from the internet. Figure (d) is based on Ref. [2]. . . . .</p>	5
2.1	<p>Schematic of the cavity cascade experimental set-up. <math>N</math> identical cavities are connected in a linear chain with aperture connections. Single-mode ports are installed at the first and last cavities in the chain. The scattering properties are measured with a VNA and frequency extenders. Independently controlled mode stirrers are located in each cavity. <math>a</math> and <math>b</math> refer to the two sides of a cavity in the cascade. More details on the experimental setup can be found in Section 2.3. . . . .</p>	14
2.2	<p>(a) The scaled 3 cavity cascade case (where the second one is hidden behind the vertical copper supporting plate) connected to single-mode WR10 waveguides. The inset shows how the second cavity is arranged and the location of the two circular apertures. (b) Picture of the full scale cavity cascade set-up with one wall of cavity 2 removed. The cavities are connected through circular apertures. Individual perturbers and RF absorber cones are employed inside the enclosures (not shown). . . . .</p>	18
2.3	<p>Comparison of distributions of the imaginary part of trans-impedance (<math>Im(Z_t)</math>) between the experimental curves and the theoretical predictions for 2 and 3 cavity cascade system. The red curves are for two-cavities and blue are for three-cavities. Figure (a) and (b) are from scaled measurements with rectangular and circular shaped apertures, respectively. Figure (c) is from the full-scale system. The inset shows schematically the shape of the aperture that is applied in the experiment. . . . .</p>	20
2.4	<p>The PDFs of induced voltage on a 50 Ohm load attached to the last cavity (cav) of the full scale cavity cascade systems (3.95-5.85GHz) and its scaled counterparts (75-110GHz), assuming 1W input on the single-mode port of the first cavity. The curves corresponding to the 1, 2 and 3 cavity system are color-coded in blue, yellow and green, respectively. The full scale system experimental (theoretical) data are shown at dashed (solid) lines, and the scaled experiment data are shown as dotted lines. . . . .</p>	25

3.1	Schematic illustration of the hybrid model applied to a 3-cavity cascade. In the hybrid model, we use the PWB method to characterize the power flow from the first cavity to the next to last cavity. The fluctuations in the final cavity are described using the RCM method using the mean power flow values obtained from PWB as an input. . . . .	27
3.2	The PDFs of load induced voltage $ U_L $ of 2- and 3-cavity experiments (solid) and hybrid model calculations (dashed). The single cavity loss parameter is varied from 9.7, 7.5, 5.7 and 1.7 from (a-d), respectively. The inset in (b) shows the 2- and 3-cavity experiment averaged induced voltage values $\langle  U_L  \rangle$ with respect to different loss parameters $\alpha$ . Multi-mode ( $\sim 100$ modes) circular apertures are employed between the cavities.	36
3.3	The 3-cavity case load induced voltage $ U_L $ values computed with the PWB-only model. The single cavity loss parameter is varied from 9.7, 7.5, 5.7 and 1.7 from (a-d), respectively. Multi-mode ( $\sim 100$ modes) circular apertures are employed between the cavities. . . . .	38
3.4	Comparison of induced load voltage statistics for the hybrid model (dotted), RCM predictions (dashed) and experimental results (solid) for the case of 2 and 3 cavity cascades with single-cavity loss parameter $\alpha = 9.7$ , and circular multi-mode apertures between the cavities. The frequency range is from 3.95 to 5.85 GHz. . . . .	40
4.1	Schematic of the experimental set-up. We measure the S-parameter of a 3-cavity cascade system with a VNA. The cavities are connected through circular apertures. Rotatable mode stirrers are employed in each cavity to generate different system configurations. The scale of the operating wavelength $\lambda_{op}$ is shown as the bar. . . . .	44
4.2	Multi-cavity diagonal impedances $Z_{11}$ from 2-port measurements on either 1-cavity (blue), 2-cavity (red) or 3-cavity (green) cascade. The inset in (c) is the schematic diagram of the Z-parameter measurement of 1-, 2- and 3-cavity cascade structures. (a) and (d): the real and imaginary parts of $Z_{11}$ from 3.95-5.85GHz for a single realization of the system, whose detailed views are shown in (b) and (e), and the corresponding statistical analysis over a large ensemble of $Re(Z_{11})$ and $Im(Z_{11})$ are plotted in (c) and (f). The single cavity loss parameter is $\alpha = 9.7$ . . . . .	46
4.3	Generalized (recurrent) neural network architecture with two hidden layers. The NN consists of the one input layer, hidden layers and one output layer. The RNN is built upon the NN structure with the addition of “memory effects” at each hidden layer (shown as the dashed arrows). . . . .	47
4.4	The NN classification algorithm performance for 1-, 2-, and 3-cavity $Re(Z_{11})$ data. (a-c): The cost function $f_{cost}$ (blue, left logarithmic axis) and test accuracy (red, right linear axis) results are evaluated to 500 iterations of the algorithm. The dimension of the input vector is 2000, 5000 and 16001 in (a), (b) and (c), respectively. (d): The test accuracy results with and without additional Gaussian noise. The dimension of the input vector is 5000. The signal to noise ratio values are -5, 5, 15 dB and the original data.	52

4.5	The $ S_{21} $ prediction of a wave chaotic electromagnetic system future states using measured $ S_{11} $ . The measured $ S_{21} $ data (colored solid lines) and algorithm predictions (colored dashed lines) from 5 frequency points are compared for cavity realizations 900 to 1000. The black lines show the absolute magnitude of the difference between the measured data and the algorithm prediction. . . . .	56
5.1	Diagrams of the TD-RCM port load modeling. <b>a.</b> The linear load at port $j$ is represented with an impedance $Z_j$ . <b>b.</b> The schematic of a diode-loaded port. <b>c.</b> The schematic of a multi-mode aperture. Note that the subscript “in” corresponds to waves following the arrow, going into the cavity. . . . .	62
5.2	The TD-RCM simulated RX port voltage signal from 0 to 1000ns. Five realizations with distinct cavity eigenmode spectra and coupling are shown. The injected waveform is a 5GHz center frequency and 5ns long sine pulse. . . . .	65
5.3	Schematic of the short pulse time-domain experiment setup. The injected waveform (left inset) is generated through IQ modulation using the arbitrary waveform generator (AWG) and the programmable signal generator (PSG). The short pulse is broadcast into the enclosure through the transmitting (TX) port (star). The data ensemble is created by rotating a motorized mode-stirrer inside the enclosure. The receiver (RX) port (star) induced voltage signal (right inset) is measured by the oscilloscope. A lab computer is used for instrument control and data transmission/collection. . . . .	66
5.4	We plot the measured gigabox RX port voltage signals in (a), and the corresponding TD-RCM simulation in (b). In each figure, the port signals from 20 realizations are overlaid to show the diversity of system response. . . . .	67
5.5	The statistics of the maximum RX port voltage studied at different frequencies merged in the gigabox. The input pulse is a single-frequency 20ns sine pulse. The center frequency $f_c$ changes from 5GHz to 10GHz. Note that the input pulse has a finite rise/fall time ( $1 \sim 2ns$ ). Data histograms (blue) are compared to the predictions of the TD-RCM model (red). . . . .	68
5.6	Mean values of the receiver port maximum voltage PDFs shown in Fig. 5.5 as a function of the center frequency of the 20ns pulse in the Gigabox. The error bar is one standard deviation. . . . .	69
5.7	The root-mean-square ensemble averaged RX port signal comparison. The injected pulse is a 5GHz single frequency sine wave with a duration sweeping from 5 to 30ns. Experimental and TD-RCM simulation results are shown in <b>a</b> and <b>b</b> , respectively. The insets are the blow-up of the early-time (before 100ns) curves. . . . .	71

6.1	<b>Wave chaotic systems for reservoir computing.</b> <b>a</b> , Schematic of the experimental setup. The input information is transferred from a lab computer to the AWG and broadcast into the reservoir. The amplified waveform is injected into the chaotic enclosure through an electric dipole antenna. Several diode-loaded antennas are used to probe the EM field, whose voltage signals are measured by the oscilloscope and further transferred to the lab computer for training. <b>b</b> , Measured port signals (solid) under random input stream (dashed). <b>c</b> , Schematics of the diode-loaded port. <b>d</b> , The dynamics of diode-port voltages (red) under single frequency input at 4 GHz (black). <b>e</b> , The FT of the diode-port signal shown in <b>d</b> . . . . .	78
6.2	<b>Reservoir Expansion Techniques (RETs).</b> <b>a</b> and <b>b</b> show the schematics of the boundary condition perturbation method and the frequency-stirring method, respectively. The first method may be realized by the translation of a metallic perturber shown as the cylindrical rod. Under the same input waveform $u_0$ , uniquely different evolutions of the EM fields inside the enclosure area are created by means of translating the perturber to new locations. In <b>b</b> , the frequency stirring technique utilizes small changes of center frequency of a given input waveform to create new wave field configurations. In the experiment, the input wavelet is stretched/shrunk (shown as $u_1 \sim u_3$ ) in order to shift the center frequency. <b>c</b> , Schematics of the RET concept. The combined reservoir consists of the observable nodes from various single realizations of reservoirs. . . . .	81
6.3	<b>Benchmark tests and the RC performance map on system parameters.</b> <b>a</b> and <b>c</b> , Rössler observer task testing set performance (blue) from a combined RC of 630 nodes. The true states are shown as red dashed lines in <b>a</b> , <b>c</b> and <b>e</b> . <b>b</b> , The deviation of normalized mean square error for the Rössler observer task: contour as a function of the input duration $T_{osc}$ and the system decay time $T_{decay}$ . The dashed boundary outlines the optimal parameter island (error deviation $< 20\%$ ) from where the combined 630-node RC is built. <b>e</b> , NARMA10 task testing set performance at the optimal system parameters from a 90-node RC, shown as the cross in <b>f</b> . <b>f</b> , The deviation of normalized mean square error for the NARMA10 task. . . . .	84
6.4	<b>Experimental demonstration of the task-versatility.</b> <b>a</b> illustrates that a single wave chaotic RC is able to execute different tasks with a simple switch of output couplers, and thus serves as an ideal platform an edge device. The RC performances (blue) for the function simulator, Hénon-map observer, and the nonlinear channel equalizer tasks are shown in <b>b-d</b> , respectively. The targets are shown as red dashed lines in <b>b-d</b> . In <b>e-g</b> , we show the simulated (dashed) and experimental (solid) RC performance as a function of the dimension of the reservoir. . . . .	88

7.1	<p><b>a.</b> The open-plate view of the photonic crystal lattice with an L-shaped defect waveguide region. <b>b.</b> The side view of the PC unit cell. A dielectric rod is sandwiched between two PEC (perfect electric conductor) surfaces. The quantities <math>h_0</math> and <math>d_0</math> are the height and diameter of the rod. <b>c.</b> The photonic band structure from a supercell defect waveguide simulation. The waveguide modes appear in the bulk bandgap region (delineated by the blue dashed lines). <b>d.</b> The E-field profile of one of the waveguide mode solutions (the red circle in <b>c</b>). The black dashed line marks the center of the waveguide. . . . .</p>	95
7.2	<p><b>a.</b> The simulated S-parameters of the PC-graph right-angle junction (solid), as well as the S-parameter from a 3.5mm uniform coaxial cable 2-port right-angle connector (dashed), which serves as a reference. Inset: the schematics of the PC right-angle junction and the 2-port coaxial cable junction. <b>b.</b> The simulated S-parameters of the PC-graph T-junction (solid) and the S-parameters from a coaxial cable 3-port ‘tee’ connector (dashed). Inset: the schematics of the PC T-junction and the 3-port coaxial cable junction. All PC-junction S-parameters are frequency averaged with a 500MHz window to remove the effect of spurious reflections. . . . .</p>	98
7.3	<p><b>a.</b> Schematic diagram of the PC waveguide graph system. The graph bonds are shown as the clear gray channels and the rectangular lattice is shown as a lattice of dielectric rods (black circles). <b>b.</b> The simulated <math> E_z </math> profile of the graph system eigenmode at 2.8GHz. <b>c</b> shows the statistics of the normalized mode spacing from graph simulation (histogram). The theoretical predictions for the GOE, GUE and GSE systems are shown in red, yellow and purple curves. <b>d</b> shows the spectral rigidity <math>\Delta(L)</math> of the normalized spectrum from graph simulation (blue circles). The theoretical predictions for the GOE and GUE systems are shown in red and yellow curves. <b>e</b> shows the statistics of the consecutive mode spacing ratio <math>r</math> (histogram) and the theoretical predictions for the GOE, GUE and GSE systems. . . . .</p>	100
7.4	<p><b>a.</b> Probability amplitude distribution of photonic crystal defect waveguide graph eigenmodes values (<math>v</math>) obtained from the grid-wise method (symbols connected by blue line). The theoretical prediction for systems with GOE statistics are in red. <b>b.</b> shows the statistics of the normalized bond amplitude value <math> a </math> (symbols connected by blue line) and the Gaussian distribution (red dashed). . . . .</p>	105
7.5	<p><b>a.</b> The inverse participation ratio (IPR) of graph eigenmodes obtained from the bond-value method, computed based on the method IIa. The simulated <math> E_z </math> profile of the red (black) circled mode in <b>a</b> is shown in <b>c</b> (<b>d</b>). <b>b.</b> The inverse participation ratio (IPR) of graph eigenmodes computed based on the method IIb. The simulated <math> E_z </math> profile of the red (black) circled mode in <b>b</b> is shown in <b>e</b> (<b>f</b>). . . . .</p>	106

8.1	(a) Quantum Hall (QH) unit cell model with $h_0 = 36.8mm$ , $h_1 = 1.45mm$ , $d_0 = 12.7mm$ and $d_1 = 8.8mm$ . A QH rod consists of two ferrite disks (blue) straddling a middle metallic rod, sandwiched by two metallic plates. (b) Photonic band structure for a QH bulk region. The horizontal-axis is the $k_x$ vector mapping an excursion in the 1st Brillouin zone and the vertical-axis is the eigenmode frequency. Under $H_z = 1350Oe$ the QH bulk bandgap (shaded area from 5.9 to 6.3 GHz) matches the quantum spin Hall bandgap [3]. The inset offers an oblique view of a typical open-plate BMW hexagonal lattice with lattice constant $a_0 = 36.8mm$ . . . . .	113
8.2	$ S_{21} $ transmission results through a bulk QH structure in the $\Gamma - K(K')$ direction for both magnetized and un-magnetized ferrites. With $H_z$ on (magnetized ferrites, red curve), we observe a decrease in transmission S-parameter at 5.9-6.3 GHz, which is caused by the absence of bulk modes inside the bandgap region. Inset: schematic of the experiment. . . . .	116
8.3	(a) and (b) are the measured edgemode transmission along the QH-QSH interface with opposite H-field directions applied to the QH region. The black-dot(red-line) curves represent the right(left)-going waves. The insets show the locations of port A and B along with the direction of the applied H-field. The white arrows mark the expected edgemode propagating directions. We find that the edgemode propagation direction is reversed when the biasing magnetic field direction is inverted. . . . .	118
8.4	(a): The Y-junction design consist of three different topological domains: two QSH domains (green and blue) and a QH region (red), creating three interfaces: ab, bd and bc. The $\psi^{\uparrow/\downarrow}$ represents an edgemode with spin up/down. Purple/yellow arrows: propagation directions of $\psi^{\uparrow/\downarrow}$ modes. Plot (b-d) are the transmission measurements of the Y-junction with $-H_z$ in the QH region. The edgemode will follow the $2 \rightarrow 1$ and the $1 \rightarrow 3$ paths strictly without backscattering. Port 3 becomes a forbidden source as shown in (b). . . . .	119
8.5	Experimental results of edge waves propagating in a topologically protected 4-port circulator. The QH (QSH with $\Delta_{SOC} > 0$ and $\Delta_{SOC} < 0$ ) domains are color-coded as red (green and blue) for all insets. The applied H-field direction is inverted between plots (a-b) and (c-d), creating a clockwise and counter-clockwise circulation around the center QH island, respectively.	121

9.1	<p><b>a.</b> The schematic of the unit cell structure that define the QVH and QSH regions. The quantities <math>l_v, g_v, h_v</math> are the prism side length, the air gap distance, and the prism height of one QVH rod. The quantities <math>d_s, h_s</math> are the diameter and height of the QSH cylinder rod. <b>b.</b> The photonic band structure of the QSH-QVH interface waveguide. Inset shows a schematic of the supercell simulation model. The red-dashed line marks the interface between the QSH (left) and the QVH (right) region. <b>c.</b> The side-view of the QSH-QVH structure (same structure as the <b>b</b> inset). The top and bottom metallic plates are separated by <math>h_0</math>. All QSH rods are attached to one of the metallic plates, and the QVH rods are mounted on both plates, leaving an air gap. . . . .</p>	126
9.2	<p>The open-plate view of the PTI-graph structure. Shown are the top and bottom metallic plates and the rods/prisms attached to each one of them. The top plate has the top part of the QVH rods. On the bottom plate, we have installed the QSH rods as well as the bottom part of the QVH rods. Several supporting rods are installed which will spread out the weight of the top-plate evenly, and provide a fixed and uniform separation between the plates, <math>h_0</math>. . . . .</p>	129
9.3	<p>The simulated eigenmode results of a PTI-graph realization. It is clearly shown that the two-fold degeneracy is present at the bulk bandgap frequencies. At the edge of the bandgap (<math>\sim 23.5GHz</math>), we observe a hybridization of the edgemode and bulk modes. Inset shows the graph structure used in this numerical study, consisting of a QSH region show by blue circles and a QVH region shown by grey triangles. The second inset shows an enlarged region of the QVH-QSH boundary. . . . .</p>	135
9.4	<p><b>a</b> The histogram approximation probability distribution of the PTI graph nearest-neighbor mode-spacing <math>s</math>. The prediction of the GOE, GUE, and GSE groups are plotted as solid lines for reference. <b>b.</b> The integrated probability function of <math>s</math> along with the theory predictions of the three groups. . . . .</p>	136
9.5	<p>Top view of the graph bottom plate, showing all QSH rods, and showing the bottom half of the QVH rods. The white dashed lines are drawn to outline the interface between the QVH and QSH domains, which represents the graph that hosts the topologically-protected modes. The ports locations are marked by the black stars, along with their numbering. . . . .</p>	137
9.6	<p><b>a.</b> The measured reflection S-parameters as a function of frequency in the bulk bandgap at Ports 3 and 4 of the composite QSH-QVH shown in Fig. 9.5 at room temperature. The measured complex Wigner time delay curves near 24.20 and 24.46 GHz, shown in <b>b</b> and <b>c</b>, respectively. The fitting results are shown in solid red curves. . . . .</p>	140
9.7	<p><b>a</b> and <b>b</b> show the real and imaginary parts of the <math>\tau_W</math> as a function of frequency computed using different values of <math>\eta</math>, respectively. The <math>Re(\tau_W)</math> and <math>Im(\tau_W)</math> show two divergences as <math>\eta</math> is varied (marked out by the blue arrows) and match the values of <math>\Gamma_1</math> and <math>\Gamma_2</math>. . . . .</p>	141

9.8	<b>a</b> and <b>b</b> show the front and top views of the PTI-graph structure mounted below the mixing chamber plate, respectively. <b>c</b> . The thermal connection (copper connectors and heat straps) and cable connection on the PTI-graph structure. The inset shows the heat-strap fixations on the mixing chamber plate. . . . .	142
9.9	<b>a</b> and <b>b</b> show the real and imaginary part of the measured PTI-graph $\tau_W$ versus temperature and frequency, respectively. <b>c</b> and <b>d</b> are the top view of <b>a</b> and <b>b</b> . To guide the eye, white dashed lines are added to mark the temperatures at which $Re(\tau_W)$ changes sign and $Im(\tau_W)$ diverges. . . .	144
9.10	<b>a</b> shows the 4 cable connections at the top of the fridge. These cables connect to the VNA in room temperature, and go to the PTI-graphs in low temperature environment. <b>b</b> and <b>c</b> show the measured S-parameter and the real part of $\tau_W$ , respectively. Different colors represent data measured at 130 different temperatures (from 80K to 4K). . . . .	146
10.1	Summary of the projects. There are three themes in the thesis: wave chaos, microwave topological photonics, and machine learning. The corresponding chapter indices for the projects are also shown in this diagram. Wave chaos takes the center stage. The topological photonics and the machine learning projects also intersects with the wave chaos themes. . . . .	149
A.1	Schematic diagram of the $i^{th}$ cavity in a cascade with port $a$ on the left and port $b$ on the right. Here $U$ and $I$ refer to the voltage and current at each port (a vector quantity in general). . . . .	152
B.1	The model set-up for aperture admittance matrix calculations in the CST simulations. A PEC plate is carved with the dimension of the aperture, and attached to a vacuum box. The port is assigned at the 2D surface of the aperture. The wave enters the aperture (blue arrow) and flows into the vacuum space before absorbed by the surrounding radiation boundaries (orange arrows). . . . .	157
B.2	Statistics of the imaginary part of the trans-impedance for a scaled 3-cavity cascade with circular aperture connections, illustrating the convergence of the theoretical model with increasing mode number included in the aperture admittance matrix. The circular aperture allows 100 propagating modes. The model PDFs curves are nearly unchanged when the non-propagating modes are included. . . . .	158
B.3	(a) and (b): Statistics of the imaginary part of the trans-impedance of 2- and 3-cavity cascades when the loss of the system changes. (c): Comparison of the $Re(Z_t)$ statistics experimental and model results for the scaled 2 cavity set-up, with circular aperture connection. In (a), (b) and (c), the single cavity loss parameter $\alpha$ is measured to be $\alpha = 5.7, 7.5$ and $9.1$ , respectively. . . . .	159

C.1	Schematic of a cavity cascade array with many-channel connecting apertures between all cavities except that between cavity $i$ and cavity $i + 1$ . Note the definition of input and output powers at each cavity aperture. . . . .	160
E.1	The PDFs of load induced voltage $ U_L $ of 2- and 3-cavity experiments (solid), hybrid model (dashed), and the simplified hybrid model (dash-dotted). The single cavity loss parameter is varied from 9.7, 7.5, 5.7 and 1.7 from (a-d), respectively. . . . .	170
G.1	An open-plate view of the experimental set-up of the 4-port BMW circulator structure. Each region is color coded to match the insets in Fig. 5. . . . .	179
G.2	The photonic band structure of a $15 + 15$ period QH-QSH Supercell structure from COMSOL simulations. The insets are the supercell structures near the QH-QSH interface. The dashed lines represent the location of the QH-QSH interface. Under applied magnetic field in opposite directions ( $-H_z/ + H_z$ in (a)/(b)), the supported kink mode will have opposite synthetic spin (up/down-spin shown as $\psi^{\uparrow/\downarrow}$ ) and group velocity. Dirac points are at $k_x a_0 = \pm 2\pi/3$ . Boxed tags: the Chern numbers of the bulk modes below the bandgap for QSH and QH domains. . . . .	181
G.3	An open-plate view of the QH-QSH interface 2-port isolator experimental set-up. Note that the biasing magnets on the QH region are not shown. . . . .	182
G.4	Plots of kink mode transmission measurement in (a) propagating and (b) non-propagating directions along a QH-QSH interface. In both plots, the S-parameters represent the transmission between two ports: $S_2$ is measured at a port further from the source (port A) than $S_1$ . The plots show that the amplitude of the kink mode along the propagating direction does not attenuate significantly, while the amplitude of kink mode in the backward direction is always low. . . . .	182
G.5	The 3-QSH supercell PBS near the Dirac point. The positive/negative group velocity parts (blue/red) are mixture of the up/down-spin mode localized at the top interface and down/up-spin mode at the bottom interface. Near the secondary bandgap at about 6.06-6.09 GHz, there is a four-mode mixing. . . . .	184
G.6	Supercell simulations results of the kink mode at the Dirac point. Color: $ \mathbf{E} $ of the eigenmodes near 6.1 GHz. The 5 and 7 periods of unit cell separation cases cause E-field spreading in the entire middle QSH region, while the 9-period separation case makes the kink modes better localized at the interfaces. . . . .	185
G.7	Zero magnetic field transmission measurement between port A and B. Two ports are in the same locations as in the measurement shown in Fig. 3, located on the QH-QSH interface. We find that the transmission profile between two ports are very similar, indicating the time-reversal symmetry in not broken in the un-magnetized ferrite case. . . . .	186

G.8 The open-plate view of the topological Y-junction. The magnets for QH region and the upper QSH rods are not shown in this view. The three topological regions are color-coded as in Fig. 4(a). The dashed lines mark the interface between different topological phases. The stars are the locations of the ports. . . . . 187

## List of Abbreviations

AWG	Arbitrary waveform generator
BMW	Bi-anisotropic meta-waveguide
CPA	Coherent perfect absorption
COMSOL	COMSOL Multiphysics
CST	Computer simulation technology
DL	Deep learning
EM	Electromagnetic
EMC	Electromagnetic compatibility
GHz	Gigahertz
GOE	Gaussian orthogonal ensemble
GUE	Gaussian unitary ensemble
GSE	Gaussian symplectic ensemble
HFSS	High-frequency structure simulator
LSTM	Long-short term memory
ML	Machine learning
MXC	Mixing chamber plate
NC	Neuromorphic computing
NN	Neural network
PC	Photonic crystal
PDF	Probability density function
PEC	Perfect electrical conductor
PTI	Photonic topological insulator
PSG	Programmable signal generator
PWB	Power balance method

QH	Quantum Hall
QVH	Quantum valley-Hall
QSH	Quantum spin-Hall
RC	Reservoir computing
RCM	Random coupling model
RET	Reservoir expansion technique
RMT	Random matrix theory
RNN	Recurrent neural network
RIS	Re-configurable intelligent surface
RX	Receiver
SO	Short Orbit
TD	Time domain
TI	Topological insulator
TX	Transmitter
VNA	Vector network analyzer

## Chapter 1: Introduction

### 1.1 Introduction to the Phenomenon of Chaos

“Chaos” is a common concept in life. A good hint for “chaoticity” is to examine the complex behavior of the system and see if it is sensitive to the initial conditions [4]. One may consider two states of the system with very similar initial conditions. In a chaotic system, these two states can evolve quickly into starkly different states under time evolution. Such a characteristic of chaotic systems makes the precise analysis of any long-term behaviors challenging, for example, the weather prediction for an extended period of time. A great example of the phenomenon of chaos is the famous butterfly effect proposed by Lorenz in 1972 [5]. The butterfly effect presents a poetic picture of the sensitivity of the outcome to minute changes, expressed as the exact formation time of a tornado in Texas and a butterfly flapping its wings in the Amazonian forest. Such an effect is very different from the linear system where the superposition principle will hold. However, linear systems are usually the idealized simplifications of many real-life phenomena. Many real-life systems can be considered nonlinear, meaning that the outcome of two closely-spaced initial conditions is not proportional to the initial condition difference. Examples include the swinging of a double pendulum, the trajectory of billiard balls in a chaotic billiard, and the mechanism underlying self-oscillating circuits.

Suppose we go back to the butterfly effect as an introduction to chaotic phenomena. In that case, one may argue that the above example is more attributed to the lack of precise modeling of the weather system, and/or the unforeseeable events that may perturb the weather condition, rather than the “chaotic” nature of the system. Even though weather forecasting is challenging to model, we mean to say that even with the precise knowledge of a particular system, for example, knowing all equations of a dynamical system, the initial condition would need to be precisely known to produce a future state prediction of good accuracy. Here we use the double pendulum system to illustrate the idea better. The governing equations can be written out explicitly, and the computation of the pendulum motion can be quickly conducted on a personal computer with reasonably small numerical error. However, the system is still chaotic as a slight initial condition difference in the pendulum angle will lead to very different future evolution. This is a good example of a deterministic system with chaotic dynamics. One may produce a good approximation of the system’s future evolution within a specific error tolerance range. However, this prediction is only sound in the near-term future.

Besides the qualitative description of chaos, here we introduce a more mathematical way of characterizing the chaoticity of a system. For a dynamical system, a Lyapunov exponent can be calculated for each degree of freedom of the system. The Lyapunov exponent is defined as the separation rate, with respect to time, between two close trajectories. A chaotic system must have at least one positive Lyapunov exponent. For example, the Rossler and Lorenz system will each have 3 Lyapunov exponents corresponding to the

$x, y, z$  variables [6, 7]. The chaotic Rossler system is governed by

$$\begin{aligned} dx/dt &= -y - z, \\ dy/dt &= x + ay, \\ dz/dt &= b + z(x - c), \end{aligned} \tag{1.1}$$

where typical parameter values are  $a = 0.5, b = 2.1, c = 3.5$ . The Lorenz attractor is a set of equations that models fluid motion. The chaotic Lorenz system is expressed as

$$\begin{aligned} dx/dt &= -ax + ay, \\ dy/dt &= bx - y - xz, \\ dz/dt &= cz + xy, \end{aligned} \tag{1.2}$$

where typical parameter values are  $a = 10, b = 28, c = 8/3$ . The Lyapunov exponent of the dynamical variable  $z$  for the two above systems will be positive. Depending on the choice of system parameters, the system can either fall into the chaotic regime or not. The specific value of the Lyapunov exponent is linked to the divergence rate of system states. One may evaluate the Lyapunov exponent values of a particular system through numerical calculation, and the process of ensemble averaging over different initial conditions is usually applied. Note that we will re-encounter these equations in Chapter 6 in the context of reservoir computing with wave chaotic systems.

To sum up the section, chaotic phenomena are commonly found in real-life scenarios and also scientific studies. The detailed, deterministic study of chaotic systems are usually computationally intensive. Moreover, the computed results are tightly linked to the initial

conditions. Any uncertainty in the initial conditions will eventually invalidate the computed deterministic solutions. I will introduce a better way to characterize chaotic systems, which is to look at the statistical descriptions of the quantity of interest. In the next two sections, I will introduce the Random Matrix Theory (RMT) and the Random Coupling Model (RCM). Random Matrix Theory is a well-studied method of characterizing the spectral properties of wave chaotic systems. Here at Maryland, our Wave Chaos group has invented the Random Coupling Model for wave chaotic systems. It will be clear later that RMT is an important part in the RCM.

## 1.2 Introduction to Random Matrix Theory

The Random Matrix Theory (RMT) is proposed by Wigner and later developed by Dyson and Mehta [8, 9, 10]. RMT is originally developed to study the energy level spacing statistics in nuclear physics. The study of spectral properties investigates the correlation between system energy levels, such as the level spacing between nearest-neighbor levels and the total number of levels within a given frequency range. Differing from the level-repulsion phenomenon in chaotic systems (i.e., Sinai billiard in Fig. 1.1 (b)), the nearest-neighbor level spacing of systems with integrable dynamics (e.g., square billiard in Fig. 1.1 (a), and circular billiard) shows Poissonian statistical behavior. Note that one usually studies these statistical properties of a large number of quantum systems rather than a particular realization. Besides studying the eigenvalue spacing statistics, there is also studies for the eigenfunction profiles for chaotic system states. The eigenfunction study is related to the distribution of the probability density of system eigenstates.

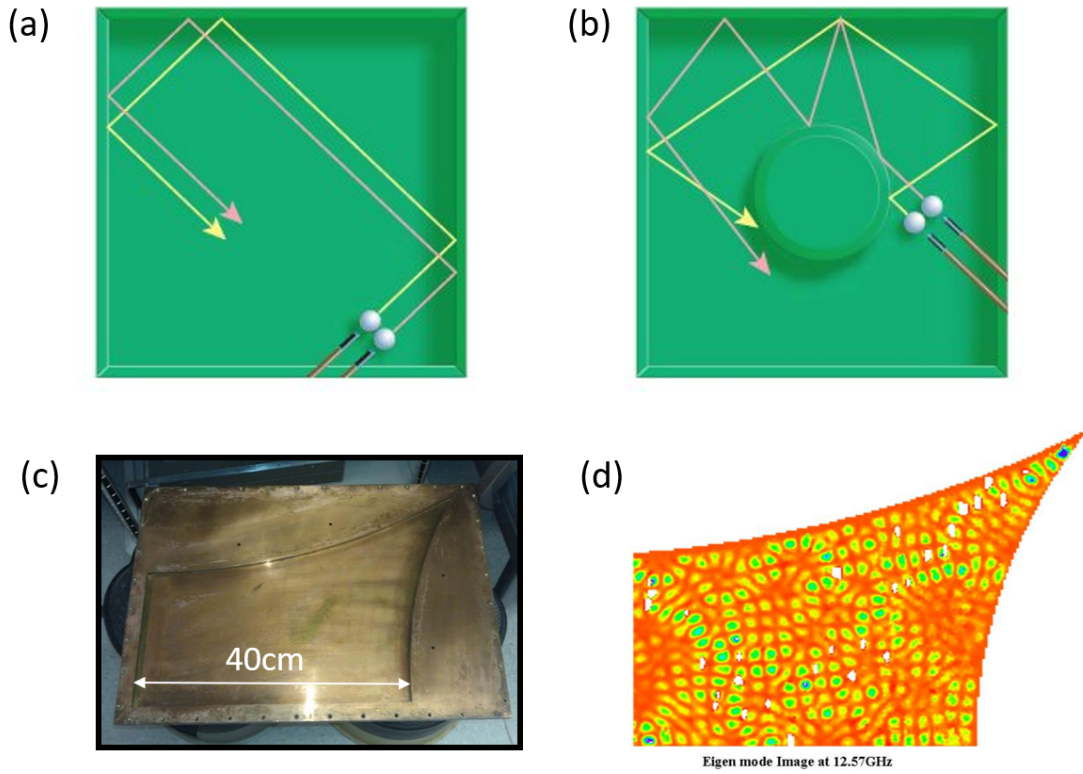


Figure 1.1: Figures (a) and (b) show the trajectories of two billiard balls inside a non-chaotic square billiard, and a chaotic Sinai billiard (square billiard with a center circular block), respectively. Figure (c) shows the quarter bowtie billiard (open plate view). Figure (d) shows the eigenfunction profile of one system eigenmode at 12.57 GHz. Figures (a) and (b) are from the internet. Figure (d) is based on Ref. [2].

Depending on the system's symmetry, the spectral properties of a certain chaotic system can be categorized into one of 3 groups. The first two groups are the Gaussian Orthogonal Ensemble (GOE) and Gaussian Unitary Ensemble (GUE) of random matrices for a system with and without time-reversal symmetry, respectively. The third group is the so-called Gaussian Symplectic Ensemble (GSE) of random matrices for a system with half-integer spins and time-reversal symmetry. It is often the case that the spectral statistical properties of systems from the same group show a universal behavior. It was later conjectured by Bohigas-Giannoni-Schmit (BGS conjecture) that the spectral statistical properties of systems that show chaos in the classical limit are well described by the statistics of random matrices [11]. Based on the BGS conjecture, RMT has found a wider range of application in many other chaotic physical systems (atoms, quantum dots, quantum wires, microwave enclosures, and others) [12, 13].

The field of microwave wave chaos aims to study the EM field propagation in electrically large, chaotic shaped enclosures/resonators. In the regime where the microwave wavelength is much smaller than the dimension of the system, the propagation of waves can be thought of as particles traveling in straight trajectories and having specular reflection at the system boundaries. Because the systems have a chaotic shape, the future propagation of the ray trajectories are extremely sensitive to the boundary condition details. Fig. 1.1 illustrates the behavior of wave chaotic enclosures. Fig. 1.1 (a) shows the ray orbits inside a non-chaotic square billiard. After several bounces, the two billiard balls still keep the same displacements as the initial value. However, in a chaotic billiard shown in Fig. 1.1 (b), the displacement between the two billiard balls will increase exponentially with time. Thus chaotic billiard systems are sometimes said to be ray-chaotic. Many numerical

and experimental studies have shown that the properties of chaotic microwave billiards and graphs agreed nicely with the RMT predictions [14, 15]. In microwave experiments, the chaotic dynamics of the system can be nicely manifested in measurable quantum quantities (i.e., scattering parameters). Because of this, many experimental studies of quantum chaos are conducted in microwave wave chaotic systems. In our lab, we studied different types of microwave wave chaotic systems, ranging from 1D graphs, 2D billiard, and 3D enclosures. Fig. 1.1 (c) shows the bowtie-billiard used in our lab. Because of its chaotic shape, the eigenfunction for a system eigenmode at 12.57GHz shows highly complicated patterns (Fig. 1.1 (d)).

### 1.3 Introduction to the Random Coupling Model

It is of interest to study the scattering properties of complex ray-chaotic systems in the semi-classical limit [16]. Examples include reactions of atomic nuclei [12], quantum dot transport [13], and the flow of electromagnetic (EM) waves through electrically-large resonant systems (defined as those for which  $\lambda \ll V^{1/3}$ , where  $\lambda$  is the wavelength of light and  $V$  is the system volume) [17, 18, 19, 20, 21]. These settings are typically found to be ray-chaotic and highly over-moded (i.e., many resonant modes at and below the frequency of interest), posing challenges to both numerical and experimental analysis means. A ray-chaotic enclosure has the property that two rays launched with slightly different initial conditions will separate exponentially with time as they continue bouncing from boundary walls and obstructions inside the structure [4, 22]. On the other hand, a minute change of the structure boundary condition can drastically affect the pre-established field

profile inside the system [23, 24, 25]. Though deterministic approaches are available [26], the chaotic properties make the numerical solutions vulnerable to small changes and uncertainties of interior structure details.

As introduced above, the statistical and/or approximate approaches in these wave systems can be more beneficial than deterministic methods (e.g., detailed numerical computations for a specific configuration). The Random Coupling Model (RCM) determines the statistical properties of the impedance ( $Z$ ) and scattering ( $S$ ) parameters for complex enclosures [3, 8, 27, 28, 29, 30, 31]. In contrast to the other methods mentioned above, the RCM generates both deterministic and statistical predictions, treats interference, and utilizes a minimum of information, namely, the system coupling details, and the enclosure loss parameter [32, 33, 34, 35, 36]. The scattering parameters describe the steady-state electrical transmission and reflection properties of a system. For an  $N$ -port system, the  $N$ -by- $N$   $S$ -matrix connects the incoming and outgoing voltage waves by  $[V_o] = [S][V_i]$ . Here the  $N$ -by-1 vector  $[V_{o,i}]$  represents the outgoing/incoming complex voltage waves at all  $N$  ports. The impedance parameters connects the total voltages and currents at the terminals of the port transmission lines in an electrical system by  $[V] = [Z][I]$ . The  $Z$ -parameters and  $S$ -parameters can be computed by knowing the other one. Both parameters are of great importance in terms of characterizing the reflection and transmission properties of an electrical system. The  $S$ -matrix can be written as  $|S| = \begin{bmatrix} 0 & 1 \\ 1 & 0 \end{bmatrix}$  for a 2-port reflectionless and lossless transmission line. The  $S$ -matrix and  $Z$ -matrix are linked by the bi-linear transformation  $\underline{S} = \underline{Z}_0^{1/2}(\underline{Z} + \underline{Z}_0)^{-1}(\underline{Z} - \underline{Z}_0)\underline{Z}_0^{-1/2}$ , where  $\underline{Z}_0$  is a diagonal matrix whose elements are the transmission line characteristic impedance (usually 50 Ohm).

The RCM cavity impedance matrix of an individual cavity is created via a normalized impedance matrix  $\underline{\xi}_{\underline{RCM}}$  derived from a random matrix ensemble [27, 28, 37, 38]. The distribution function of the complex fluctuating  $\underline{\xi}_{\underline{RCM}}$  is governed by a single parameter, called the loss parameter  $\alpha$ . In terms of the normalized impedance matrix, the fluctuating cavity impedance matrix is written as

$$\underline{Z}_{cav} = iIm[\underline{Z}_{avg}] + Re[\underline{Z}_{avg}]^{1/2} \cdot \underline{\xi}_{\underline{RCM}} \cdot Re[\underline{Z}_{avg}]^{1/2},$$

where the quantity  $\underline{Z}_{avg}$  is the ensemble averaged system impedance (discussed more in the next two chapters). Here,  $\underline{\xi}_{\underline{RCM}}$  is defined as

$$\underline{\xi}_{\underline{RCM}} = -\frac{i}{\pi} \sum_n^N \frac{\underline{w}_n \underline{w}_n^T}{(k_0^2 - k_n^2) / \Delta k_n^2 + i\alpha},$$

where the sum over  $n$  represents a sum over the modes inside the closed cavity ( $n = 1, 2, \dots, N$ ). The vector  $\underline{w}_n$ , whose number of elements equals the number of ports, consists of independent, zero mean, unit variance random Gaussian variables, which represent the coupling between each port and the  $n^{th}$  cavity mode. This random choice of mode-port coupling originates from the so-called Berry hypothesis, where the cavity modes can be modeled as a superposition of plane waves with random direction and random phase [39]. The quantities  $k_0$  and  $k_n$  are wave-numbers corresponding to the operating frequency  $\omega_0 = k_0 c$  and the resonant frequencies of the cavity modes,  $\omega_n = k_n c$ . Rather than use the accurate resonant frequencies of the cavity, a representative set of frequencies is generated from a set of eigenvalues of a random matrix selected from the

relevant Random Matrix Theory ensemble [18, 37, 40, 41]. These RMT eigenvalues are appropriately normalized to give the correct spectral density via the parameter  $\Delta k_n^2$ , the density of states near the operating wave-number. The loss parameter  $\alpha = k^2/(Q \Delta k_n^2)$  where  $k$  is the wave vector of interest and  $Q$  is the quality factor [31]. The loss parameter varies from 0 (no loss) to  $\infty$  (high loss). The RCM loss parameter is also related to the finesse parameter  $F$  that is widely used in the optical cavities. We have  $\alpha = F^{-1} = \frac{k}{2Q\Delta k}$  where the  $\Delta k^2 = 2k\Delta k$  approximation is used [42].

## 1.4 Outline of the Thesis

The next chapter will introduce our effort to extend the Random Coupling Model (RCM) from a single chaotic enclosure to more complex systems with multiple coupled chaotic sub-systems. Although the full RCM description of multiple enclosure systems coupled with electrically-large apertures is successful, it is computationally intensive when the coupling channel (aperture size) grows. In chapter 3, I further discuss a hybrid multi-enclosure method formulated with both RCM and the power balance model. This new method is much simpler and faster than the full RCM treatment. To better utilize the large ensemble of measured data collected for the multi-enclosure projects, we have applied machine learning techniques to distinguish subtle details in the experiment that are not visible to the eye (chapter 4). I further study the time-domain modeling of wave chaotic systems in chapter 5. In chapter 6, I employed the rich dynamics of the chaotic EM waves to execute several different machine learning tasks. Unlike the 3D cavity wave chaos studies in chapters 2 to 5, in chapter 7, I studied the properties of quantum graphs

based on defect photonic crystal waveguides. The theme of chapter 8 is not centered around wave chaos. Here we discuss our experimental realization of a composite photonic topological insulator (PTI) system with QH and QSH domains. Chapter 9 turns back to the chaos-related study, where I utilize the spin-1/2 property of PTI system modes to realize GSE statistics using PTI graphs. I will summarize the thesis and discuss future directions in chapter 10.

## Chapter 2: Random Coupling Model for Multi-Enclosure Wave Chaotic Systems

This work was a collaborative effort with the Naval Research Laboratory group and is published as Ref. [16]. In the previous chapter, we introduced the study of single wave chaotic systems using the Random Coupling Model. We think that concatenating two or more such systems is also of great interest, but not as extensively studied. Such coupled cavity systems can be realized in a wide range of physical platforms from inter-connected photonic crystal cavities [43], to Cooper pair boxes in superconducting resonators [44], to microwave (MW) billiards [45], and the complex acoustic and electromagnetic environment in ships and aircraft containing multiple connected compartments [46]. It has proven possible to perform experiments for such inter-connected systems and to measure transmission as a function of coupling. Examples include measurements of conductance of quantum dots systems with coupled electron billiards [47, 48, 49], resistance of disordered nanowires modeled by a cascade of quantum dots [50, 51, 52, 53], and simulating resonance strength of coupled quantum mechanical systems with superconducting MW billiards [54], etc. Likewise, the EM wave properties of inter-connected electrically large enclosures, like the power flow and the impedance or scattering parameters, are also widely studied in engineering [55, 56] and realistic situations ranging from computer enclosures to rooms

or buildings [46, 57, 58, 59]. It was recently demonstrated that two single enclosures with a specific scaling relationship concerning size, frequency, and the RCM loss parameter  $\alpha$  share the same normalized impedance statistics [60]. In this work, the authors study a scaled cavity (75-110 GHz, cavity longest dimension = 6.375 cm) and its  $\times 20$  full scale version (3.7-5.5 GHz, cavity longest dimension = 127.5 cm). The degrees of lossyness for the two systems are matched by increasing the scaled cavity Q-factor in a low-temperature environment. The loss parameter  $\alpha$  describes the degree of lossyness of the system. With  $\alpha$  known, one is able to generate the statistical ensemble of system impedance by generating new system modes and mode-port coupling coefficients using RCM. In the experiment, an ensemble of system impedance can be created by rotating a mode-stirrer inside the cavity. The impedance statistics of the full scale and scaled cavities were found to be the same, and in agreement with RCM predicted statistics for the same  $\alpha$ . This work paves the way for experimentally testing the wave properties of large, coupled complex systems in a typical lab environment by studying their scaled-down-in-size counterparts [61, 62].

## 2.1 Overview of the Multi-enclosure RCM

The statistics of the scattering of waves inside single ray-chaotic enclosures have been successfully described by the Random Coupling Model (RCM). We expand the RCM to systems consisting of multiple complex ray-chaotic enclosures with various coupling scenarios. The statistical properties of the model-generated quantities are tested against measured data of electrically large multi-cavity systems of various designs. The

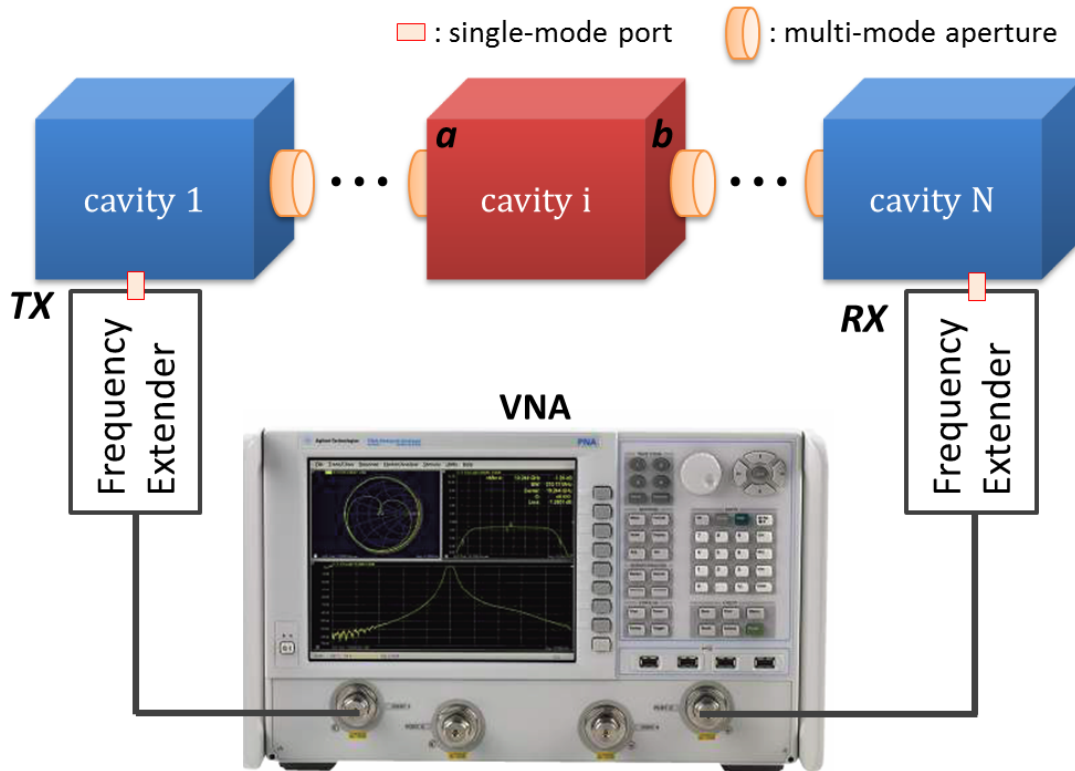


Figure 2.1: Schematic of the cavity cascade experimental set-up.  $N$  identical cavities are connected in a linear chain with aperture connections. Single-mode ports are installed at the first and last cavities in the chain. The scattering properties are measured with a VNA and frequency extenders. Independently controlled mode stirrers are located in each cavity.  $a$  and  $b$  refer to the two sides of a cavity in the cascade. More details on the experimental setup can be found in Section 2.3.

statistics of model-generated trans-impedance and induced voltages on a load impedance agree well with the experimental results. The RCM coupled chaotic enclosure model is general and can be applied to other physical systems including coupled quantum dots, disordered nanowires, and short-wavelength electromagnetic and acoustic propagation through rooms in buildings, aircraft and ships.

Here, we apply an RCM-based model which can be used to make statistical predictions of impedance values in inter-connected systems of chaotic cavities. The multi-enclosure RCM method builds on an earlier work for single-mode connection between cavities [33]. As shown schematically in Fig. 2.1, our approach first adopts RCM to describe each individual chaotic enclosure [31, 60]. The system-specific details are identified in orange in Fig. 2.1. These consist of the single-mode waveguide ports and the multi-mode apertures between cavities, and are described by the radiation impedance  $Z_{port}$ , and the radiation admittance matrix  $\underline{Y_{aper}}$ , respectively. With known geometry, these frequency dependent complex coupling quantities can be determined through either full-wave numerical simulations or direct radiation measurements. For an N-mode aperture we utilize the aperture admittance matrix  $\underline{Y_{aper}}$  (an  $N \times N$  matrix) to describe its deterministic properties as a function of frequency. We use  $Z_{port}$  to represent the deterministic properties of the single-mode ports in a manner identical to previous treatments of the port radiation impedance [30, 37, 60, 63].

An important consideration is the number of aperture modes (both propagating and evanescent) to include in  $\underline{Y_{aper}}$ . The single cavity radiation admittance matrix can be

written as a block-diagonal complex and frequency-dependent matrix

$$\underline{\underline{Y_{rad}}} = \begin{bmatrix} \underline{\underline{Y_{rad,a}}} & 0 \\ 0 & \underline{\underline{Y_{rad,b}}} \end{bmatrix} \quad (2.1)$$

As shown in Fig. 2.1, the  $\underline{\underline{Y_{rad}}}$  subscripts “a” and “b” refer to the connection on the left and right sides of the cavity in the linear chain. The choice of  $\underline{\underline{Y_{rad}}}$  solely depends on the specific cavity connection (i.e., a port or aperture that allows  $N_a$  modes in “a” and  $N_b$  modes in “b”). The off-diagonal zeros reflect the assumption that the apertures and ports are sufficiently separated such that no direct connection exists between them. This assumption can be lifted if direct illumination exists between apertures and ports [42]. The RCM single cavity admittance matrix  $\underline{\underline{Y_{cav}}}$  is then constructed as shown in Eqn. 2.2 from  $\underline{\underline{Y_{rad}}}$  and the  $(N_a + N_b) \times (N_a + N_b)$  dimensionless universal fluctuation matrix  $\underline{\underline{\xi_{RCM}}}$  whose statistics are determined solely by the loss parameter  $\alpha$  of the cavity,

$$\underline{\underline{Y_{cav}}} = i \cdot \text{Im} \left( \underline{\underline{Y_{rad}}} \right) + \text{Re} \left( \underline{\underline{Y_{rad}}} \right)^{0.5} \cdot \underline{\underline{\xi_{RCM}}} \cdot \text{Re} \left( \underline{\underline{Y_{rad}}} \right)^{0.5} \quad (2.2)$$

The matrix  $\underline{\underline{\xi_{RCM}}}$  can be calculated using a Monte-Carlo technique [27, 28, 58, 60]. The single cavity admittance matrix  $\underline{\underline{Y_{cav}}}$  reflects the chaotic universal fluctuations from  $\underline{\underline{\xi_{RCM}}}$  [31], “dressed” by the system-specific properties of the ports and apertures described by  $\underline{\underline{Y_{rad}}}$ .

## 2.2 Multi-enclosure RCM Formalism

For a description of the statistical properties of the entire cavity cascade, cavities can be connected together by enforcing continuity of voltages and currents at the cavity coupling planes.

$$\begin{cases} \begin{bmatrix} \underline{I}_a \\ \underline{I}_b \end{bmatrix} = \underline{Y}_{cav}^{(i)} \cdot \begin{bmatrix} \underline{U}_a \\ \underline{U}_b \end{bmatrix} \\ -\underline{I}_b = \underline{Y}_L^{(i+1)} \cdot \underline{U}_b \end{cases} \quad (2.3)$$

In Eqn. 2.3, the superscript  $i$  refers to the index of the cavity running from 1 to  $N$  as shown in Fig. 2.1.  $\underline{Y}_L^{(i+1)}$  is the overall load admittance including the  $(i+1)^{st}$  cavity and everything beyond it. By solving Eqn. 2.3 in matrix form, we have:

$$\underline{U}_b = - \left( \underline{Y}_{bb}^{(i)} + \underline{Y}_L^{(i+1)} \right)^{-1} \underline{Y}_{ba}^{(i)} \underline{U}_a \quad (2.4)$$

$$\underline{Y}_L^{(i)} = \underline{Y}_{aa}^{(i)} - \underline{Y}_{ab}^{(i)} \left( \underline{Y}_{bb}^{(i)} + \underline{Y}_L^{(i+1)} \right)^{-1} \underline{Y}_{ba}^{(i)} \quad (2.5)$$

Eqn. 2.4 connects the voltages on two sides of a cascade unit, and Eqn. 2.5 gives the  $\underline{Y}_L$  recursion relationship which calculates the load admittance  $\underline{Y}_L^{(i)}$  of the  $i^{th}$  cavity given the knowledge of  $\underline{Y}_L^{(i+1)}$ . With this recipe, the complete RCM cavity cascade model is created as follows. Starting by computing the load admittance  $\underline{Y}_L^{(i)}$  presented by the load impedance at the  $N^{th}$  cavity ( $Y_L^{(N)}$ ) and working back to the first cavity using Eqn. 2.5. Combined with the single cavity admittance matrices and the input voltage at the first cavity, we use Eqn. 2.4 to calculate the voltages at each cavity connection, and finally at the output port of the  $N^{th}$  cavity. (Detailed information of the  $\underline{Y}_{ab}$  matrices can be found

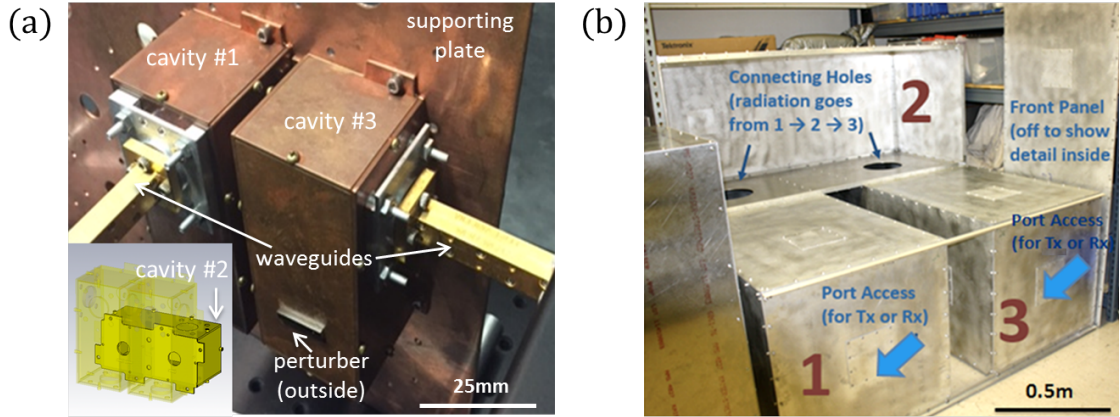


Figure 2.2: (a) The scaled 3 cavity cascade case (where the second one is hidden behind the vertical copper supporting plate) connected to single-mode WR10 waveguides. The inset shows how the second cavity is arranged and the location of the two circular apertures. (b) Picture of the full scale cavity cascade set-up with one wall of cavity 2 removed. The cavities are connected through circular apertures. Individual perturbers and RF absorber cones are employed inside the enclosures (not shown).

in Appendix A.) One can then make predictions for the statistics of  $Z_{in}$  and  $Z_t$  of the entire system (see Eqns. A.8, A.9 in Appendix A) based on the minimal information of cavity loss and system coupling.

### 2.3 Scaled-structure Experimental Setup

The details of the cascade cavity experimental set-up are shown in Fig. 2.2. The scaled and full scale 3-cavity cascade structures are shown in Fig. 2.2 (a) and (b), respectively. The scaled experiments are conducted at the University of Maryland, and the full scale version at the Naval Research Laboratory. My predecessor Bo Xiao acquired the equipment and set up many parts of the scaled structure facility. I took over in June of 2017. In our experiments, we use the Vector Network Analyzer (VNA) to conduct S-parameter measurements. The S-parameter (S-matrix) is introduced in the previous chapter. The VNA can produce faithful measurement of the full S-matrix for an electrical

system. Here we will briefly describe the experimental method. Before the measurement, we will first calibrate the VNA so that the calibration plane is right at the end of the VNA cable. A good quality calibration will essentially render the VNA as a matched load throughout the entire bandwidth. During the measurement, the VNA will first inject a signal into the system from one of its ports, and measure the reflection/transmission signals at the other ports. In our cascade cavity setup, energy will be injected into the first cavity through the waveguide port, then transmitted into the rest of the cavities through the apertures, and finally leak out through both the transmitting port and the receiving ports. The full S-matrix is measured by computing the ratio between the measured reflected/transmitted signals to the injected signal. The resulting S-parameters are complex functions of frequency. In all our experiments, we measure the S-matrix with the VNA and then store the data on a workstation. Other quantities (Z-matrix, induced voltages values at the ports, etc.) can be computed from the S-matrix. For our setup, the characteristic length of a single cavity is about 9 cm. We conduct measurements from 75 to 110 GHz with the help of frequency extenders made by Virginia Diodes (Tx/Rx WR10 module). At room temperature and mmWave frequencies, the single cavity Q-factor is in the range of 5000 to 6000 (which results in RCM loss parameter values  $\alpha \in (7.5, 9.5)$ ). Note that we connected the frequency extenders to the VNA to boost the bandwidth from 26GHz to mmWave frequencies. More details of the experimental setup are included in Appendix B.

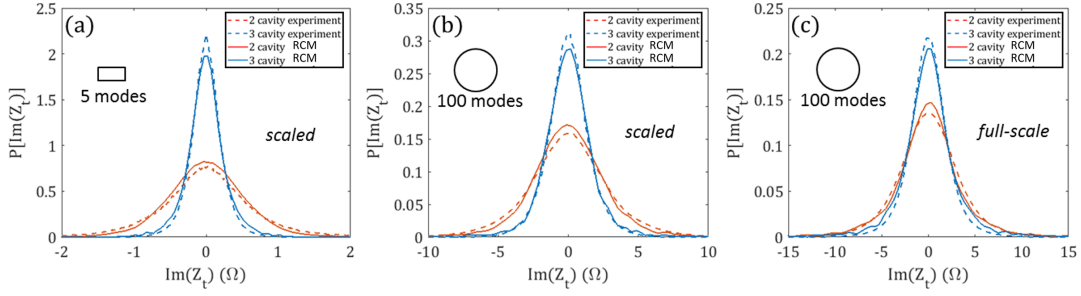


Figure 2.3: Comparison of distributions of the imaginary part of trans-impedance ( $Im(Z_t)$ ) between the experimental curves and the theoretical predictions for 2 and 3 cavity cascade system. The red curves are for two-cavities and blue are for three-cavities. Figure (a) and (b) are from scaled measurements with rectangular and circular shaped apertures, respectively. Figure (c) is from the full-scale system. The inset shows schematically the shape of the aperture that is applied in the experiment.

## 2.4 Experimental and RCM Results

To kick-off the build-up of multi-cavity RCM, the loss parameter of each single cavity is required. The loss parameters, obtained from single cavity measurements, are  $\alpha = 9.1$  for the scaled cavity and  $\alpha = 9.7$  for the full scale cavity with 6 absorber cones present in the cavity [16]. With the single cavity losses made equal and the physical dimensions carefully scaled, nominally identical electromagnetic conditions are achieved between the two set-ups [60]. We have put the scaled cavity system into the dilution refrigerator to decrease the loss of the system. Since all the cavities inside the linear array are electrically identical (nominally), the same cavity loss parameter  $\alpha$  will be assigned to each cavity in the cascade. The port and the aperture radiation admittances are obtained by direct measurements and numerical simulations in Computer Simulation Technology (CST), respectively (see Appendix B. (a)). Combining this information, we generate an ensemble of 2 and 3-cavity cascade system impedances, and compare its statistics with

those of the measured data. Note that the multi-enclosure RCM model is a numerical method rather than an analytical method. We conduct Monte-Carlo simulations of random matrices so that a statistical ensemble of data can be generated by the RCM program. In Fig. 2.3, we compare the statistics of  $Im(Z_t)$  for cavity cascade systems with various cavity numbers, coupling strengths and physical dimensions. Fig. 2.3 (a) show PDF's of  $Im(Z_t)$  for 2 and 3 cavity systems when the cavities are connected by rectangular shaped apertures having 5 propagating modes ( $10^{-4}$  coupling strength). The statistics of the 2 and 3 cavity cascade theory generated  $Im(Z_t)$  (solid lines) match well with the measured data (dashed lines). A minor mismatch between the 2-cavity  $Im(Z_t)$  statistical comparison is observed. Compared to the measurements, the theory generated  $Im(Z_t)$  PDFs have higher peak values near zero, which indicates that the theory predictions tend to have smaller magnitude values. The inter-cavity coupling strength is increased to  $10^{-2}$  by employing the circular shaped aperture, and as shown in Fig. 2.3 (b), this increases the magnitude of fluctuations of the trans-impedance for both the 2 and 3 cavity systems. Results for the full-scale measurements with circular aperture connections are shown in Fig. 2.3 (c). Good agreement between model and measurements are obtained in all cases. Additional cavity cascade experimental results are shown in Appendix B (c).

Aside from validating the prediction performance of the RCM cavity cascade model, another key aspect of our experiment is to study the miniature cavity technique for the multi-cavity systems. As introduced in section I, the full scale cavity is built with linear dimensions 20 times larger compared with its scaled counterpart. With the operating frequency properly scaled and loss parameter made equal by adjusting the wall conductivity, the statistical wave properties of the two set-ups are expected to be identical [60]. The

direct comparison of system trans-impedance statistics can be examined by comparing the  $Im(Z_t)$  PDFs shown in Fig. 2.3 (b) and (c). The peak values and spreads of the scaled and full scale 2 and 3 cavity  $Im(Z_t)$  PDFs are in similar ranges. For the scaled 2 and 3 cavity  $Im(Z_t)$  PDFs, the peak values are 0.17 and 0.28 and the FWHMs are 5.1 and  $3\Omega$ , respectively. For the full scale 2 and 3 cavity  $Im(Z_t)$  PDFs, the peak values are 0.15 and 0.21 and the FWHMs are 5.8 and  $4\Omega$ , respectively. We believe that this imperfect agreement between scaled and full scale  $Im(Z_t)$  PDFs is caused by a difference in the aperture thickness. The circular aperture thickness is about  $1\lambda_{op}$  in the scaled cavities, but only  $0.04\lambda_{op}$  in the full scale set-up ( $\lambda_{op}$  represents the characteristic operating wavelength). Note that the finite thickness of the apertures are included in the full-wave  $\underline{Y_{rad}}$  simulations, resulting in good agreement between model and measurements. By scaling the thickness of the full scale aperture to  $\sim 1\lambda_{op}$ , we calculate the frequency dependent  $\underline{Y_{rad}}$  with CST. The corresponding full scale  $\underline{Y_{rad}}$  is identical to that of the scaled aperture. If one conducts full scale multi-cavity RCM calculations using this ‘thick aperture’  $\underline{Y_{rad}}$ , the obtained impedance statistics match well with the scaled cases (solid lines in Fig. 2.3 (b)).

We are also able to calculate the statistics of the magnitude of the induced voltage delivered to a  $50\Omega$  load impedance attached to the last cavity in the 1D chain due to a given input to the port on the first cavity. On the experimental side, the load induced voltage  $V_L$  is calculated from the measured impedance based on the analysis presented in Refs. [58, 62]. More specifically, the induced voltage signal at the load can be expressed as  $|V_L| = \left| \sqrt{\frac{2P_{in}|Z_p|^2|Z_{11}|^2}{Re(Z_{11})}} \right|$ , where  $Z_p = \frac{Z_{12}Z_L/Z_{eq}}{Z_{22}+Z_L}$  and  $Z_{eq} = Z_{11} - \frac{Z_{12}^2}{Z_{22}+Z_L}$ . The quantities  $P_{in}$  is the source power,  $Z_L$  is the load impedance, and  $Z_{11}, Z_{12}, Z_{22}$  are

the measured system impedance matrix elements. On the RCM theory side, the model-generated induced voltage is calculated using Eqns. A.8 and A.9 in appendix A. The input powers used in the experimental and model-generated  $V_L$  are set to be  $1W$ , and the statistical analysis of  $V_L$  are conducted throughout the entire frequency range. Thus, with the input power known, one is able to compute the fluctuating induced voltage signal at the RX port through the fluctuating quantities  $Z_{in}$  and  $Z_t$  (Eqns. A.8 and A.9). Despite the differences in aperture thickness, good agreement between these two set-ups is found for the induced voltage statistics shown in Fig. 2.4. The experimental results of the load induced voltage PDFs for scaled and full scale cavity systems are represented by dotted and dashed lines, respectively. The results show that such a scaling technique can be very conveniently extended from single to multi-cavity systems, allowing investigation of systems with a large number of cavities and more sophisticated connection topology. The experimental results in Fig. 2.4 are also in good agreement with the model predictions (solid lines).

The proposed theoretical formulation is not expected to work at the extreme high-loss limits ( $\alpha \rightarrow \infty$ ) due to the failure of the random plane wave hypothesis, which is a prerequisite of the RCM. This breakdown can be expected when the estimated 3dB width of a mode becomes comparable to the operating frequency ( $Q \sim 1$ ). However, the model is valid for moderately large loss ( $\alpha \gg 1$ ), and the impedance statistics simplify to Gaussian distributions in this limit [27, 28]. The RCM theoretical formulation can be applied to lower loss systems ( $\alpha \leq 1$ ), but the stronger impedance fluctuations of very low-loss systems poses great challenges for the acquisition of good statistical ensemble data by either numerical or experimental methods [64, 65]. The formulation

will also require modifications of the cavity total admittance matrix when the inter-cavity coupling strength is increased substantially. Non-zero off-diagonal components of the  $\underline{Y}_{rad}$  matrix (Eqn. 2.1) must be determined when direct coupling between the input and output channels of the cavity is prominent. Failure to include these off-diagonal terms may contribute to the lack of detailed agreement between the model-generated and experimental results in Fig. 2.3.

To sum-up, we have established the multi-enclosure RCM model to treat interconnected single chaotic systems. The proposed model is able to cover different coupling details between each sub-enclosure. We have conducted experimental tests and found good agreement between the measured data and RCM simulation. Limitations of the RCM formalism is also discussed.

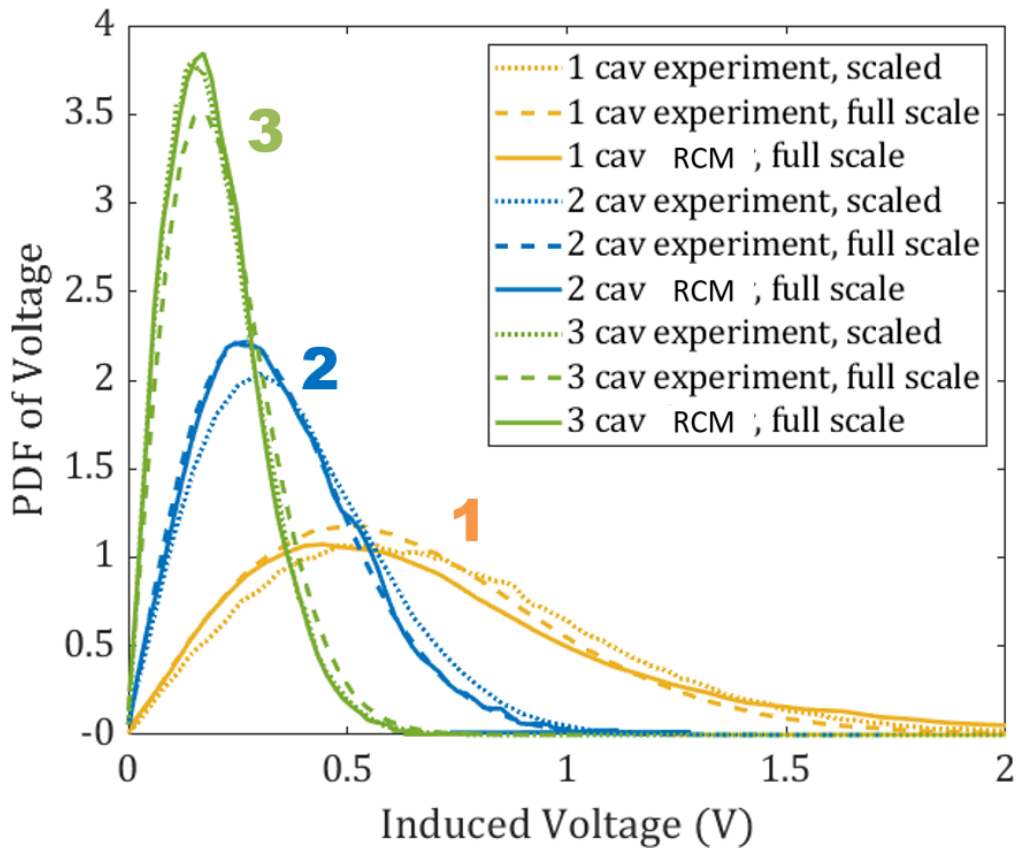


Figure 2.4: The PDFs of induced voltage on a 50 Ohm load attached to the last cavity (cav) of the full scale cavity cascade systems (3.95-5.85GHz) and its scaled counterparts (75-110GHz), assuming 1W input on the single-mode port of the first cavity. The curves corresponding to the 1, 2 and 3 cavity system are color-coded in blue, yellow and green, respectively. The full scale system experimental (theoretical) data are shown at dashed (solid) lines, and the scaled experiment data are shown as dotted lines.

## Chapter 3: Hybrid Power Balance-RCM Method for Multi-enclosure Wave Chaotic Systems

This work was a collaborative effort with the University of Nottingham group and the Naval Research Laboratory group, and is published as Ref. [66]. The Random Coupling Model (RCM) has been successfully applied to predicting the statistics of currents and voltages at ports in complex electromagnetic (EM) enclosures operating in the short wavelength limit [27, 28, 37, 58]. Recent studies have extended the RCM to systems of multi-mode aperture-coupled enclosures. However, as the size (as measured in wavelengths) of a coupling aperture grows, the coupling matrix used in the RCM increases as well, and the computation becomes more complex and time consuming. A simple Power Balance Model (PWB) can provide fast predictions for the *averaged* power density of waves inside electrically-large systems for a wide range of cavity and coupling scenarios. However, the important interference induced fluctuations of the wave field retained in the RCM are absent in PWB. Here we aim to combine the best aspects of each model to create a hybrid treatment and study the EM fields in coupled enclosure systems [66]. The proposed hybrid approach provides both mean and fluctuation information of the EM fields without the full computational complexity of coupled-cavity RCM. We compare the hybrid model predictions with experiments on linear cascades of over-moded cavities.

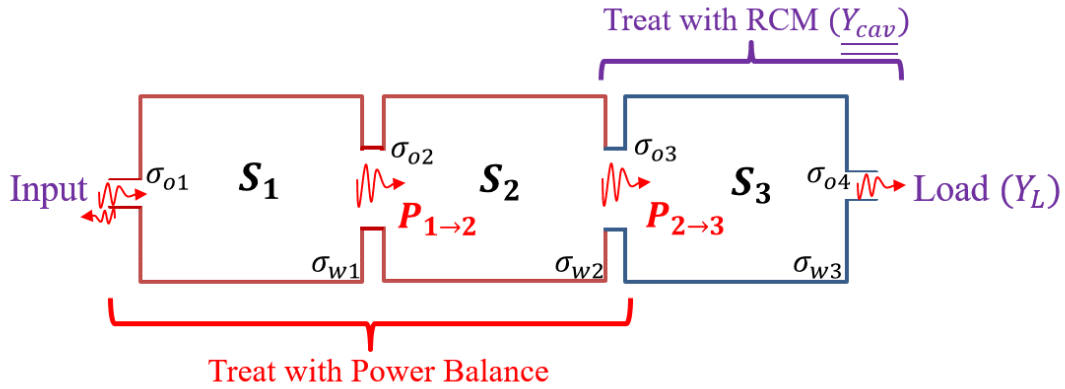


Figure 3.1: Schematic illustration of the hybrid model applied to a 3-cavity cascade. In the hybrid model, we use the PWB method to characterize the power flow from the first cavity to the next to last cavity. The fluctuations in the final cavity are described using the RCM method using the mean power flow values obtained from PWB as an input.

We find good agreement over a set of different loss parameters and for different coupling strengths between cavities. The range of validity and applicability of the hybrid method are tested and discussed.

### 3.1 Power Balance Method

The PWB method can be used to determine mean values of EM power flow and energy in systems of coupled cavities [56, 57, 67, 68]. For a multi-enclosure problem, the PWB method assumes uniform energy density in each enclosure, and solves for the mean power density  $S_i$  ( $i$  is the cavity index) by balancing the powers entering and leaving each cavity. These power transfer rates are characterized in terms of area cross-sections ( $\sigma$ ), such that the power transferred is  $\sigma S_i$ . Various loss channels, such as aperture/port leakage, cavity wall absorption and lossy objects inside the enclosure are characterised through the corresponding cross sections  $\sigma_o$ ,  $\sigma_w$  and  $\sigma_{obj}$ , respectively

[57]. Constant power is injected into the coupled systems through sources in some or all of the enclosures. The PWB method solves for a steady state solution when the time-independent inputs and losses are made equal for each individual cavity in the system. This requires reaching the so-called power balanced condition. The PWB method does not contain phase information of the EM fields and thus does not describe fluctuations due to interference. This can lead to an inaccurate prediction of enclosure power flow in the case of small apertures.

### 3.2 Hybrid Method Overview

As stated in previous sections, RCM is able to produce accurate prediction of multi-enclosure systems. The computational complexity of the RCM grows, however, with the addition of large apertures connecting together multiple enclosures. In the RCM an aperture is treated as a set of  $M$  correlated ports, the number of which scales with the area of the aperture as measured in wavelengths squared. For example, a circular shaped aperture whose diameter corresponds to four operating wavelengths allows  $\sim 100$  propagating modes, leading to  $M \sim 100$  ports in the RCM modelling of the interconnected cavities. A cavity with  $M$  ports is described by an  $(M \times M)$  matrix [16, 28, 37, 42]. When large apertures are present, connecting multiple cavities, the RCM model can become cumbersome. First there is the need to calculate the matrix elements for each aperture that describe the passage of waves through an aperture radiating into free space. Second these matrices must be combined with random matrices that give the statistical fluctuations. Third, the RCM is a Monte-Carlo method in which the matrices simulating

the cavities are constructed for each realization, and many realizations may be required to get accurate statistical results. Finally, the matrices must be connected together which involves inverting the sub-matrices representing the sub-volumes inside a complex system for each realization [16]. There is thus a need to develop a simple statistical method that applies in cases where the apertures are larger than a wavelength, but small enough so that the two enclosures connected by the aperture can be considered as two separate volumes.

Here, we introduce a hybrid approach that combines the PWB and RCM to generate statistical predictions of the EM field for multi-cavity systems without the computational complexity of a full RCM treatment. The hybrid approach is valid in cases where the coupling between adjacent cavities is carried by many channels due to, for example, large apertures as described above. Using the hybrid method, we apply the PWB method for computing the average EM field intensities in each cavity and use RCM to predict the fluctuations in the cavity of interest only. The modeling of multiple channels between adjacent cavities is thus reduced to computing a scalar coupling coefficient in the PWB model, often given through simple expressions involving the area of the aperture.

A coupled RCM model still needs to be applied where the number of connecting channels between enclosures is small. Such small apertures act as “bottlenecks” for the wave dynamics and a full RCM treatment is necessary to characterize the fluctuations correctly, see Appendix C and D. One may further reduce the computational cost of the hybrid model using a simplified treatment as proposed in Appendix E. This simplified version of the hybrid model does not require additional knowledge of the frequency-dependent aperture admittance, which is usually obtained through full-wave simulations.

### 3.3 Hybrid Method Details Part I: RCM Treatment

Random Coupling Model provides an alternative method to describe the statistics of the EM fields in a wide variety of complex systems. In contrast with PWB, the RCM deals with both the mean and fluctuations of the cavity fields.

For coupled-cavity systems, the RCM multi-cavity treatment begins with the modeling of the fluctuating impedance matrix of each individual cavity [16]. These matrices relate the voltages and currents at the ports of a cavity. When cavities are connected the voltages at the connecting ports are made equal and the connecting currents sum to zero. The input port on the first cavity is excited with the known signal. This leads to a linear system of equations that can be solved for all the voltages and currents. This system is resolved for each realization of the cavity impedance matrices.

As introduced earlier, the RCM normalized impedance matrix can be written as

$$\underline{\underline{Z}}_{cav} = iIm[\underline{\underline{Z}}_{avg}] + Re[\underline{\underline{Z}}_{avg}]^{1/2} \cdot \underline{\underline{\xi}}_{RCM} \cdot Re[\underline{\underline{Z}}_{avg}]^{1/2}.$$

System-specific information  $Z_{avg}$  can be calculated by assuming the walls of the cavity have been moved far from each port, and each port responds as if there were only outgoing waves from the port. In the case of apertures as ports, the transverse electric and magnetic fields in the aperture opening are expanded in a set of basis modes with amplitudes that are treated as port voltages in the case of electric field, and port currents in the case of magnetic field. The linear relation between these amplitudes is calculated for the case of radiation into free space, and this becomes the average aperture admittance/impedance

matrix. Each mode in the aperture field representation is treated as a separate port in the cavity matrix. Thus, the dimensions of the matrix grows rapidly with the addition of a large aperture [42].

In the cavity cascade system, the above mentioned apertures (with  $M$  propagating modes) are adopted as the connecting channel between neighbouring cavities. With  $M$  connecting channels between cavities, the dimension of the above defined cavity impedance matrix becomes  $M \times M$ . The matrix multiplications and inversions in the calculation of RCM multi-cavity formulations [16] thus have complexity which grows as  $O(M^{2.4})$  using common algorithms [69]. Thus for large  $M$ , the computational cost of the RCM scales roughly as  $N \times M^{2.4}$ , where  $N$  represents the number of cavities in the system.

Here we propose a hybrid method for multi-cavity problems that combines both PWB and RCM as shown schematically in Fig. 3.1. In an  $N$ -cavity cascade system with multiple channel connections between adjacent cavities, we utilize the PWB to characterize the mean flow of EM waves from the input port of the first cavity to the input aperture of the last ( $N^{th}$ ) cavity. The RCM method is now applied to the last cavity and the connected load at the single-mode output port of that cavity. Thus the hybrid method combines the strengths of both methods: the fluctuations of the EM field will be captured with RCM, and the computational cost is greatly reduced using the PWB method.

In the following, we discuss the hybrid model formulation in detail based on the 3-cavity system example shown in Fig. 3.1. We will first introduce the PWB treatment to the first two cavities in the chain, followed by the modeling of the last cavity using RCM. We will then discuss how to connect the PWB and RCM models at the aperture

plane between the last two cavities. With the model formulation introduced, we will look into the validity of the hybrid model in section. A step-by-step protocol to apply the PWB-RCM fusion to generic cavity systems is detailed in Appendix D.

### 3.4 Hybrid Method Details Part II: Detailed Single Cavity Treatments

PWB characterizes the flow of high-frequency EM waves inside a complex interconnected system based on the physical dimensions of the cavities, the cavity quality factors  $Q$ , and the coupling cross sections  $\sigma_o$  as well as the incident power  $P_{in}$  driving the system [57, 67]. PWB then calculates the power densities of each individual cavity in steady state. For the 3-cavity cascade system in Fig. 3.1, the PWB equations are

$$\begin{bmatrix} \sigma_{w1} + \sigma_{o1} + \sigma_{o2} & -\sigma_{o2} & 0 \\ -\sigma_{o2} & \sigma_{w2} + \sigma_{o2} + \sigma_{o3} & -\sigma_{o3} \\ 0 & -\sigma_{o3} & \sigma_{w3} + \sigma_{o3} + \sigma_{o4} \end{bmatrix} \begin{bmatrix} S_1 \\ S_2 \\ S_3 \end{bmatrix} = \begin{bmatrix} P_{in} \\ 0 \\ 0 \end{bmatrix} \quad (3.1)$$

where the  $\sigma_{w_i}$ 's refer to the wall loss cross section and  $S_i$  is the power density of the  $i^{th}$  cavity,  $\sigma_{o1}$  and  $\sigma_{o4}$  are the cross section of the input and output ports, while  $\sigma_{o2}$  and  $\sigma_{o3}$  represent the aperture cross sections, see Fig. 3.1. The cross sections can be expressed explicitly from known physical dimensions and cavity wall properties [57].  $P_{in}$  is the (assumed steady) incident power flow into the first cavity. In this example, we assume that only the first cavity receives EM power from external sources. The balance between the input and loss is achieved by solving Eq. (3.1) for the steady state power densities  $S_i$ . For example, the power balance condition of the first enclosure is expressed as  $(\sigma_{w1} +$

$\sigma_{o1} + \sigma_{o2}) \cdot S_1 = P_{in} + \sigma_{o2} \cdot S_2$ . The LHS of this equation represent the loss channels of the cavity, including the cavity wall loss and the leakage through the input port and the aperture. The RHS describes the power fed into the cavity, consisting of the external incident power and the power flow from the second cavity. The net power that flows into the last cavity in the cascade is expressed as  $P_{2 \rightarrow 3} = \sigma_{o3}(S_2 - S_3)$ .

The last cavity is characterized by the RCM method. With the knowledge of the cavity loss parameter  $\alpha$  and the port coupling details, the full cavity admittance matrix of the last cavity can be expressed as [42]

$$\underline{\underline{Y}}_{cav} = i \cdot Im(\underline{\underline{Y}}_{rad}) + Re(\underline{\underline{Y}}_{rad})^{0.5} \cdot \underline{\underline{\xi}} \cdot Re(\underline{\underline{Y}}_{rad})^{0.5}.$$

The quantity  $\underline{\underline{Y}}_{rad}$  is a frequency-dependent block-diagonal matrix whose components are the radiation admittance matrices of all the ports and apertures of that cavity. We assume no direct couplings between apertures because the direct line-of-sight effect is small in the experimental set-up. Consider a cavity with two  $M$ -mode aperture connections, the dimension of the corresponding matrix  $\underline{\underline{Y}}_{rad}$  is  $2M \times 2M$ . The matrix elements are complex functions of frequency in general and can be calculated using numerical simulation tools. We use here the software package *CST Studio* to calculate the aperture radiation admittance. The RCM normalized impedance  $\underline{\underline{\xi}}$  is a detail-independent fluctuating “kernel” of the total cavity admittance  $\underline{\underline{Y}}_{cav}$ . The loss parameter  $\alpha$  describes the degree of lossyness of the system. With known  $\alpha$ , an ensemble of the normalized admittance  $\underline{\underline{\xi}}$  can be generated through random matrix Monte Carlo approaches [58]. Combining the fluctuating  $\underline{\underline{\xi}}$  and  $\underline{\underline{Y}}_{rad}$ , an ensemble of “dressed” single cavity admittance matrices for the

final cavity can be generated. It is later shown in Appendix E that a substantial reduction of the hybrid model computational cost is made possible using an aperture-admittance-free treatment, at the price of reduced accuracy for longer cascade chains.

### 3.5 Hybrid Method Details Part III: Finalizing the Hybrid Model

We next connect the PWB and RCM treatments at the interface between the second and the third cavity. As discussed in the previous section, the power flow into the third cavity,  $P_{2 \rightarrow 3}$ , is calculated from the 3-cavity PWB calculation. Identical system set-ups are utilized in the PWB and RCM treatments, including the operating frequency range, the dimensions of the cavities, ports and apertures, and the loss of the cavity (achieved by a simple analytical relationship between the RCM  $\alpha$  parameter and  $\sigma_w$ ). To transfer the scalar power values  $P_{2 \rightarrow 3}$  generated by PWB into an aperture voltage vector required for RCM, we assign random voltages  $\underline{U}_{o3}$  drawn from a zero mean, unit variance Gaussian distribution for the  $M$ -mode aperture and calculate the random aperture power using

$$P_{o3} = \frac{1}{2} \text{Re}(\underline{U}_{o3}^* \cdot \underline{Y}_{rad} \cdot \underline{U}_{o3}).$$

These randomly assigned aperture voltages  $\underline{U}_{o3}$  are then normalized by the ratio  $P_{2 \rightarrow 3}/P_{o3}$  to match with the value calculated from PWB. Combined with the RCM generated cavity admittance matrix  $\underline{Y}_{cav}$ , an ensemble of induced voltage values  $U_L$  at the load on the last cavity is computed utilizing Eq. (A.9) in Ref. [16]. The power delivered to the load is obtained using

$$P_L = \frac{1}{2} \text{Re}(U_L^* \cdot Y_L \cdot U_L),$$

where  $Y_L$  is the load admittance, taken to be  $1/(50\Omega)$  here.

With the formulation of the hybrid model now explained, here we discuss the improvement in computational time and memory usage by replacing the full RCM multi-cavity method with the hybrid model. For an  $N$ -cavity system connected through  $M$ -mode apertures, the hybrid model requires only a fraction of  $1/[(N - 1)M^2]$  of the memory consumption as compared to the full RCM method, enabled by the reduced cavity impedance matrix storage for the first  $N - 1$  cavities. Moreover, the computation time is also reduced by eliminating the RCM modeling of the prior cavities. For example, the computation/CPU time for the two-cavity cascade system with circular aperture connections reduces from about 120s to 40s with application of the hybrid method (tests run on a typical workstation). In addition, the computation time of the full RCM method scales with the total number of cavities in the system  $N$ , while the hybrid method is insensitive to the further addition of cavities. Aside from the difference in the CPU time, there is a finite loading time to move the data (e.g. random matrices to model single cavities) from the hard drive to RAM. Compared to the full RCM method, the hybrid model reduces the number of cavities that need RCM modeling from  $N$  to 1, and thus decreases the data loading time. The advantage of the method becomes more prominent for larger lengths of the cavity chain  $N$  and larger apertures (having  $M$  modes).

### 3.6 Experimental Results and Discussion

We now conduct the PWB-RCM hybrid analysis for the multi-cavity experiment and compare with measurements. The experiment setup is shown in Fig. 2.1, and photos

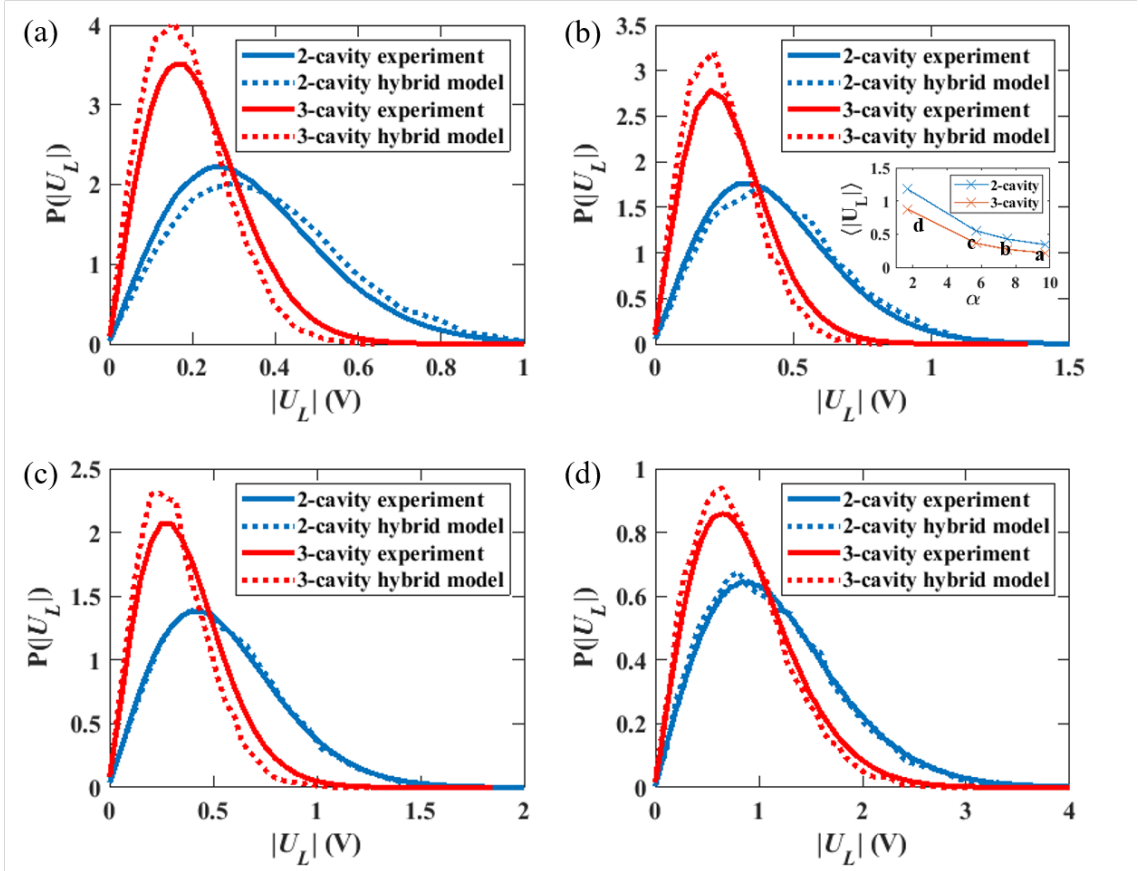


Figure 3.2: The PDFs of load induced voltage  $|U_L|$  of 2- and 3-cavity experiments (solid) and hybrid model calculations (dashed). The single cavity loss parameter is varied from 9.7, 7.5, 5.7 and 1.7 from (a-d), respectively. The inset in (b) shows the 2- and 3-cavity experiment averaged induced voltage values  $\langle |U_L| \rangle$  with respect to different loss parameters  $\alpha$ . Multi-mode ( $\sim 100$  modes) circular apertures are employed between the cavities.

of the actual measurement setup can be found in Fig. 2.2. We consider 2- and 3-cavity cascades with large (on the scale of the wavelength) apertures between the cavities and single-mode connections to the load in the last cavity. The induced voltages at the load  $|U_L|$  are calculated from data using the methods reported in Refs. [58, 62], and these experimental results are shown as solid lines in Fig. 3.2. An ensemble of induced load voltages for the multi-cavity system is created by moving the mode stirrers in all cavities between each measurement. The losses in the single cavities is altered by inserting equal amounts of RF absorbers in each cavity. In addition, the hybrid PWB-RCM method is used to calculate  $|U_L|$  and the resulting distributions are shown as dotted lines in Fig. 3.2. Good agreement between the measured and model generated results are observed over a range of different total cavity numbers and single cavity loss values. Under varying cavity loss conditions, the probability density function (PDF) of the induced load voltage  $|U_L|$  of the 3-cavity system has a lower mean value and smaller fluctuations compared to the 2-cavity system results. Going from two to three cavities will decrease the energy density in the last cavity and thus the power delivered to the load. This difference between the 2- and 3-cavity  $|U_L|$  becomes smaller when the single cavity loss decrease as can be seen following Fig. 3.2 (a) to Fig. 3.2 (d), see also the inset in Fig. 3.2 (b).

For comparison purposes, we computed the induced load voltage  $U_L$  value of the 3-cavity system using just PWB for the entire 3-cavity system (Fig. 3.3). The computation covers the entire operating bandwidth (3.75 to 5.50 GHz). The ensemble averaged values of  $U_L$  obtained from the PWB-RCM hybrid model computations (Fig. 3.2) are 0.19, 0.24, 0.32, 0.82 V for cases (a-d), respectively. With window averaging, the corresponding averaged  $U_L$  values from the PWB-only method are 0.17, 0.22, 0.30, 0.85 V. Thus, we

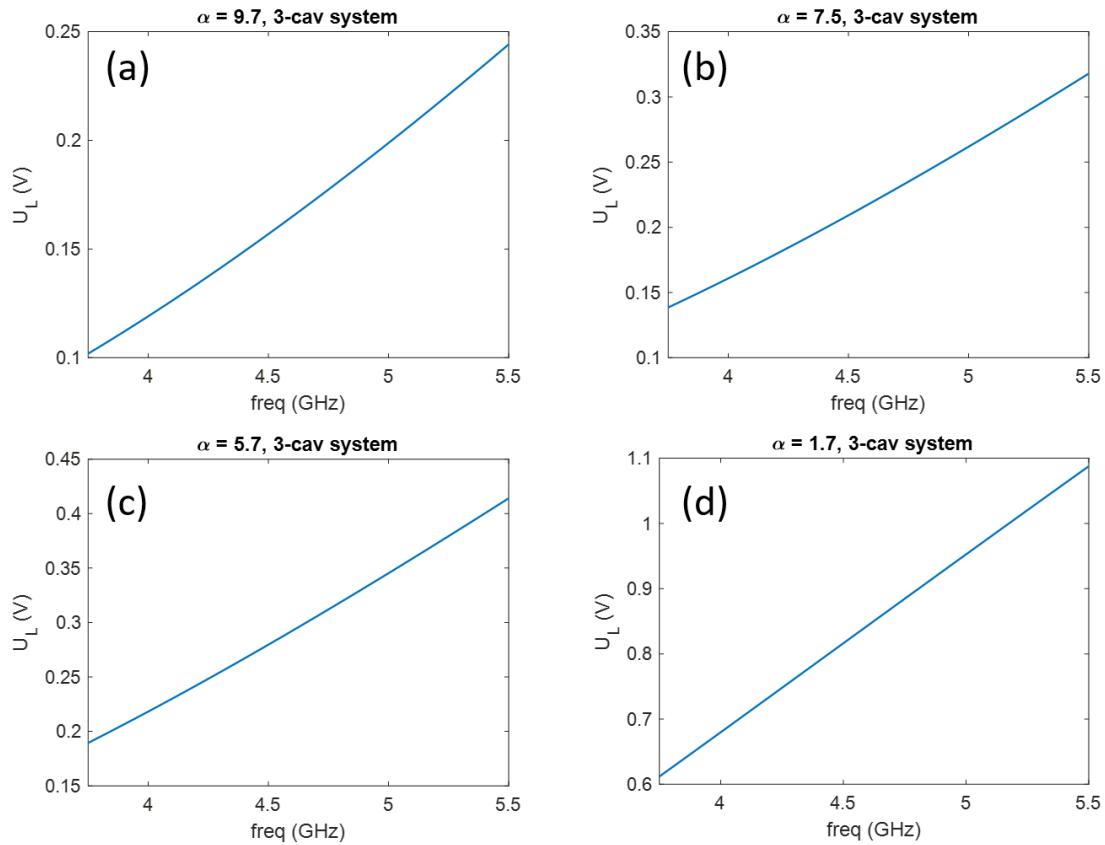


Figure 3.3: The 3-cavity case load induced voltage  $|U_L|$  values computed with the PWB-only model. The single cavity loss parameter is varied from 9.7, 7.5, 5.7 and 1.7 from (a-d), respectively. Multi-mode ( $\sim 100$  modes) circular apertures are employed between the cavities.

find relatively good agreement between the mean induced voltage from the hybrid model and the PWB-only model result.

The induced load voltage PDFs of the multi-cavity system can be generated solely with the RCM formulation [16]. A comparison between the  $|U_L|$  PDFs generated with full RCM method, the hybrid method, and the experiments are shown in Fig. 3.4. Both theoretical approaches are able to generate statistical ensembles which agree well with the experimental results. We find that the RCM results (dashed lines) slightly outperform the hybrid method (dotted lines) for the two-cavity case. However, the computation time and storage cost of the full RCM method is  $N$  times larger than the hybrid method, where  $N$  refers to the total number of connected cavities in the cascade.

### 3.7 Hybrid Model Limitations

The hybrid model is based on the assumption that the fluctuations in a given cavity are independent of the fluctuations in adjacent cavities and thus of the fluctuations in the power flowing between cavities (as a function of frequency, for example). We assess the validity of these assumptions by analysing a multi-channel cascaded cavity system in Appendix C. We study in particular the effect of the total number of effective cavity-cavity coupling channels  $M_n$  between the  $n$ th and  $(n + 1)$ st cavity on the fluctuation levels of the load-induced power  $P_L$  connected to the final cavity. Since  $P_L \propto |U_L|^2$ , the conclusions drawn from the power flow studies can also be applied to voltage-related results as presented below in Section IV. Defining the load power fluctuation levels as the ratio  $\kappa = \langle P_L \rangle^2 / \langle P_L^2 \rangle$ , where  $\langle \dots \rangle$  represents averaging over an ensemble, we treat  $\kappa$  as

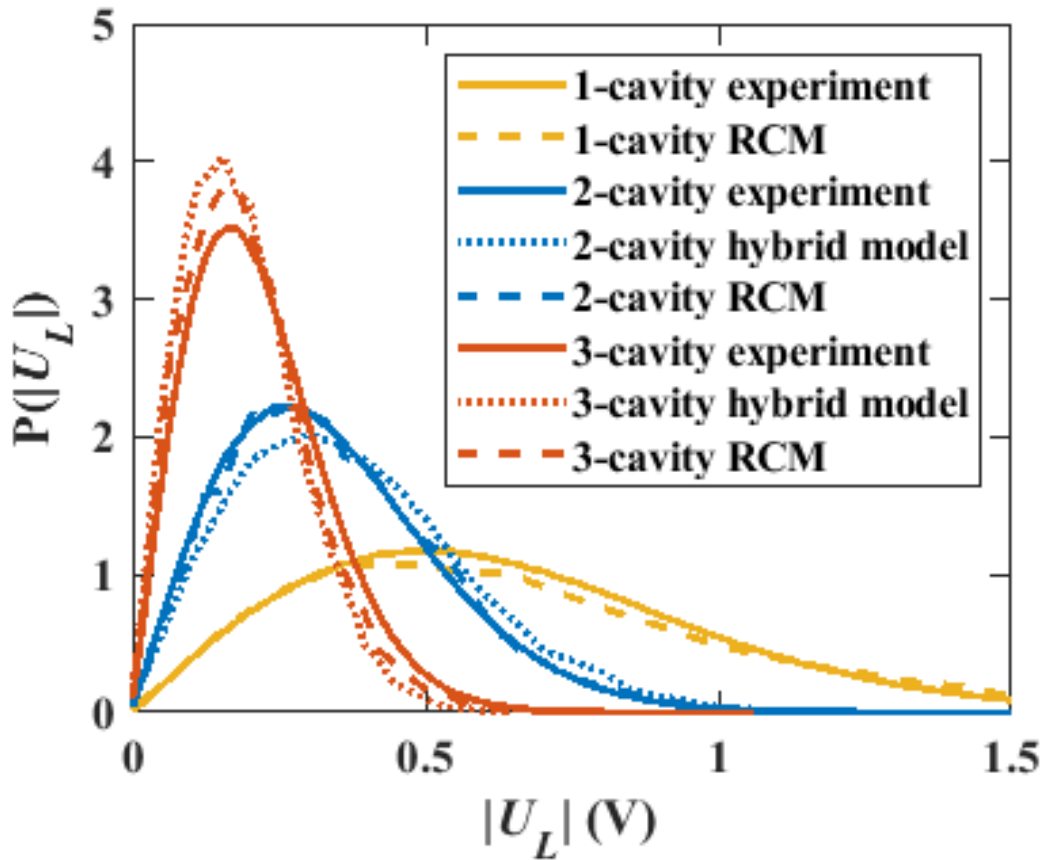


Figure 3.4: Comparison of induced load voltage statistics for the hybrid model (dotted), RCM predictions (dashed) and experimental results (solid) for the case of 2 and 3 cavity cascades with single-cavity loss parameter  $\alpha = 9.7$ , and circular multi-mode apertures between the cavities. The frequency range is from 3.95 to 5.85 GHz.

a measure characterising the level of fluctuations of the power. Here,  $\kappa \sim 1$  and  $\kappa \gg 1$  refer to low and high fluctuations of the power values, respectively. In Appendix C, it is shown that

$$\kappa \propto \prod_{n=1}^N (1 + M_n^{-1}), \quad (3.2)$$

where the product is over all the cavities in the cascade. If cavities  $n = 1$  to  $n = N - 1$  have strong multi-channel connections due to, for example, large apertures with  $M_n \gg 1$  propagating modes at the operating frequency, then  $M_n^{-1} \rightarrow 0$  and the contributions to (3.2) not including the coupling to the load, that is,  $\prod_{n=1}^{N-1} (1 + M_n^{-1}) \rightarrow 1$ ; this holds for the experiments described in Section IV with  $M_n \approx 100$  at the frequencies considered. The quantity  $M_n$  is small when a single-mode waveguide connects the last cavity ( $N$ ) to the load. At the last cavity ( $N$ ) there is a single mode output port,  $M_n = 1$  and the  $1 + M_n^{-1} = 2$  which induces higher fluctuations at the load compared to the case where all apertures are large. Similar small  $M_n$  situations appear when a ‘‘bottleneck’’ is introduced between cavities. It is therefore sensible to adopt RCM for just the last cavity to capture the power fluctuations at the load, while it is sufficient to include the influence of the intervening cavities with PWB only giving the required information about the mean power flow.

## Chapter 4: Application of Machine Learning to Wave Chaotic Systems

This work was a collaborative effort with the Naval Research Laboratory group and is published as Ref. [70]. The wave properties of complex scattering systems that are large compared to the wavelength, and show chaos in the classical limit, are extremely sensitive to system details. A solution to the wave equation for a specific configuration can change substantially under small perturbations. Due to this extreme sensitivity, it is difficult to discern basic information about a complex system simply from scattering data as a function of energy or frequency, at least by eye. In this work, we employ supervised machine learning algorithms to reveal and classify hidden information about the complex scattering system presented in the data [70]. As an example we are able to distinguish the total number of connected cavities in a linear chain of weakly coupled lossy enclosures from measured reflection data. A predictive machine learning algorithm for the future states of a perturbed complex scattering system is also trained with a recurrent neural network. Given a finite training data series, the reflection/transmission properties can be forecast by the proposed algorithm.

## 4.1 Machine Learning Applications, Overview

Machine learning (ML) techniques have enjoyed intense research interest in recent years [71, 72]. A ML algorithm treats any given task as a mathematical problem and does not utilize knowledge of the specific physics underlying the data. Benefiting from this ‘model-free’ nature, the ML algorithms find broad application in various sub-fields of physics, such as the identification of phase transitions in condensed matter studies [73, 74], the classification of multi-qubit states of trapped-ion experiments [75], the auto-tuning of gate voltages in quantum dots system [76, 77], and the future state predictions of spatio-temporal chaotic systems [78, 79, 80]. Although successfully applied in various studies, one crucial drawback of the ML techniques is the trade-off between a successfully trained program and the amount of data required during its training phase. However, the problem of training data acquisition does not pose a great challenge to the analysis of wave chaotic systems. In order to compare experimental data to theoretical predictions based on the statistical methods mentioned in the previous paragraph, a large statistical ensemble of measured data is required. This feature of wave chaotic system analysis is suitable for building a successfully trained machine learning algorithm.

## 4.2 Multi-enclosure Experimental Setup

We study the transmission and reflection of electro-magnetic (EM) waves in wave chaotic enclosures. Short-wavelength EM waves from 3.95-5.85 GHz are injected into cavities of dimension  $0.762 \times 0.762 \times 1.778m^3$  through WR178 single-mode waveguides.

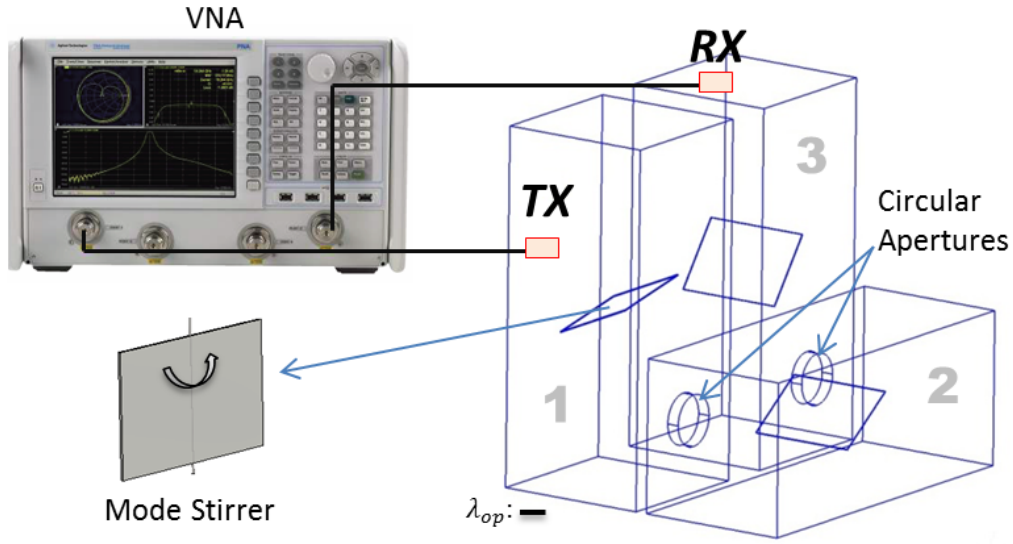


Figure 4.1: Schematic of the experimental set-up. We measure the S-parameter of a 3-cavity cascade system with a VNA. The cavities are connected through circular apertures. Rotatable mode stirrers are employed in each cavity to generate different system configurations. The scale of the operating wavelength  $\lambda_{op}$  is shown as the bar.

The cavities are electrically large ( $\sim 10^4$  modes at the operating frequency range) in order to simulate real-life examples of wave chaotic settings such as rooms in buildings and cabins in a ship. A series of individual cavities can be connected into a linear cascade chain through apertures as shown in Fig. 4.1. The total number of connected cavities is varied from 1 to 3. Independent mode stirrers are employed inside each cavity to create a large ensemble of statistically distinct realizations of the system [38, 81, 82, 83]. Single-mode ports are mounted on the first and last cavity in the cascade, shown as T(R)X in Fig. 4.1. The  $2 \times 2$  Scattering(S)-parameters of the entire cavity cascade system are measured with a Vector Network Analyzer (VNA), and the  $2 \times 2$  impedance(Z)-parameters are calculated. The S and Z parameters are connected through the bilinear transformation,  $\underline{\underline{S}} = \underline{\underline{Z}}_0^{0.5}(\underline{\underline{Z}} + \underline{\underline{Z}}_0)(\underline{\underline{Z}} - \underline{\underline{Z}}_0)^{-1}\underline{\underline{Z}}_0^{-0.5}$ , where  $\underline{\underline{Z}}_0$  is a diagonal matrix whose elements are

the characteristic impedance of the waveguide channels leading to the ports. All mode stirrers are rotated simultaneously to ensure a low correlation between each transmission measurement, and the S-parameter measurements are carried out when the mode stirrers are stationary. A total number of 200 distinct realizations of the cavity cascade are created. The degree of loss in each cavity is altered by placing RF absorber cones in each cavity. The single cavity “lossyness” is described by the RCM loss parameter  $\alpha$  which is defined as the ratio of the 3-dB bandwidth of a resonance mode to the mean spacing between the modes [31, 60], and is basically the number of overlapping modes at a given frequency. The loss parameter can have values ranging from 0 (no loss) to infinity (extremely lossy). With  $\alpha$  known, one is able to generate the statistical ensemble of system impedance using RCM.

The real and imaginary parts of diagonal impedance  $Z_{11}$  measurements for a single realization is shown in Fig. 4.2. The curves correspond to systems with a different number of connected cavities, varying from 1 to 3. The cavities are nominally identical, in that all cavities share the same physical dimension and a uniform single cavity loss parameter value:  $\alpha = 9.7$ . It has been demonstrated both theoretically and experimentally that the statistical properties of the diagonal impedance  $Z_{11}$  of a high-loss ( $\alpha \gg 1$ ) cavity cascade system remain virtually unchanged regardless of the total number of connected cavities in the chain [33]. The real and imaginary parts of measured  $Z_{11}$  values of multi-cavity systems are shown in Fig. 4.2 (a) and (d). Direct observation of the frequency dependent  $Z_{11}$  results cannot provide useful information to classify the number of connected cavities, since the curves are essentially on top of each other and effectively indistinguishable vs. frequency. The detailed  $Re(Z_{11})$  and  $Im(Z_{11})$  from 5.605-5.62GHz are shown in Fig.

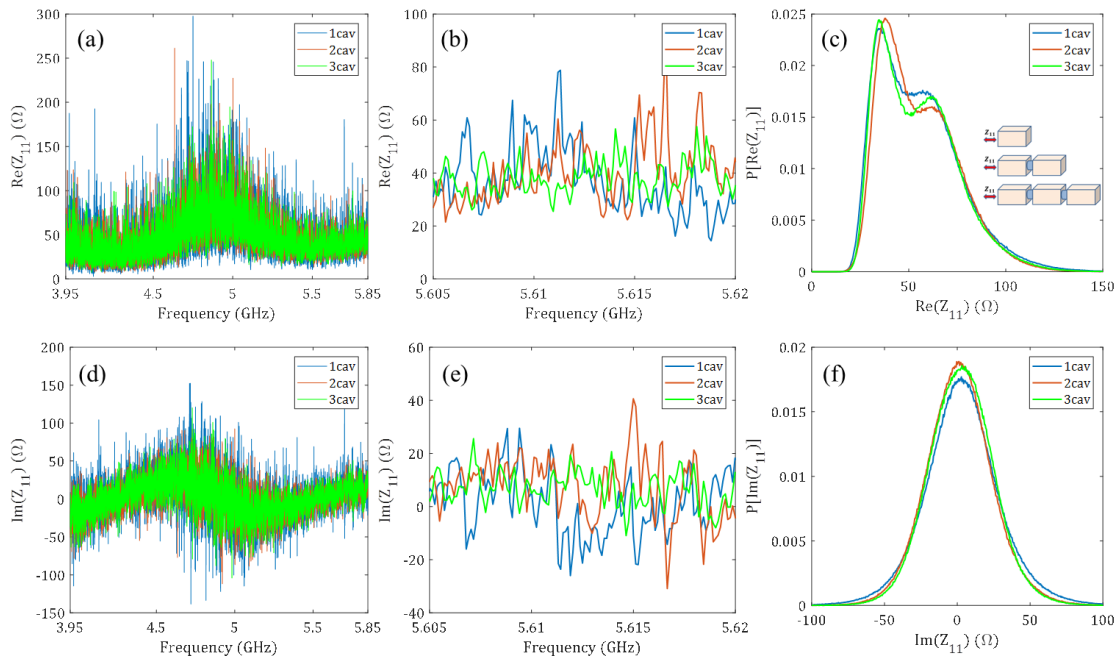


Figure 4.2: Multi-cavity diagonal impedances  $Z_{11}$  from 2-port measurements on either 1-cavity (blue), 2-cavity (red) or 3-cavity (green) cascade. The inset in (c) is the schematic diagram of the Z-parameter measurement of 1-, 2- and 3-cavity cascade structures. (a) and (d): the real and imaginary parts of  $Z_{11}$  from 3.95-5.85GHz for a single realization of the system, whose detailed views are shown in (b) and (e), and the corresponding statistical analysis over a large ensemble of  $Re(Z_{11})$  and  $Im(Z_{11})$  are plotted in (c) and (f). The single cavity loss parameter is  $\alpha = 9.7$ .

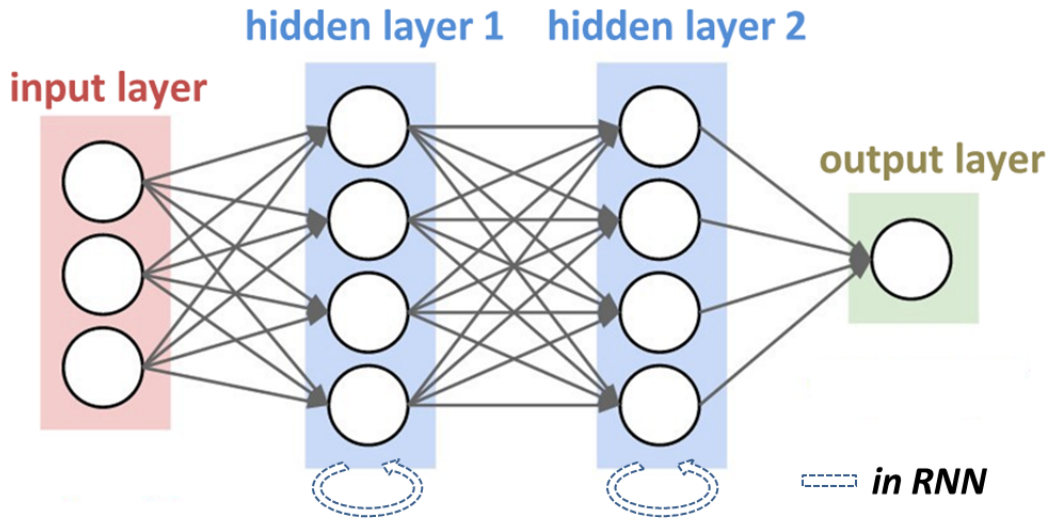


Figure 4.3: Generalized (recurrent) neural network architecture with two hidden layers. The NN consists of the one input layer, hidden layers and one output layer. The RNN is built upon the NN structure with the addition of “memory effects” at each hidden layer (shown as the dashed arrows).

4.2 (b) and (e). Even with the detailed view, it is still hard to differentiate the  $Z_{11}$  curves from either the mode density, the level of fluctuation, or the averaged  $Z_{11}$  value levels. Statistical analysis of the  $Re(Z_{11})$  and  $Im(Z_{11})$  measurements are shown in 4.2 (c) and (f). The  $Z_{11}$  PDFs of 1-, 2- and 3-cavity cascade are very similar to each other and difficult to systematically distinguish. The Fourier transforms of the multi-cavity  $Z_{11}$  data show similar time-domain responses. We first wish to see if an ML algorithm can be trained to correctly distinguish the number of cavities in the cascade simply from raw data such as that shown in Fig. 4.2. The second objective is to see if an ML algorithm can predict the evolution of the S- (or Z-) parameters as the cavity cascade is systematically perturbed.

### 4.3 ML Model I: Neural Network

The neural network (NN) and its modifications, inspired by the electric signal propagation mechanism of brain neuron cells, are widely applied in various fields, such as speech identification, pattern recognition and picture captioning [84]. A neural network is one of the supervised learning algorithms whose goal is to utilize the given training set information and establish a generic method to assign labels to the testing sets. As a typical example of classifying cat and dog pictures, a supervised learning algorithm refines its classification rule using thousands of images of correctly labeled cat and dog images. More specifically, the algorithm identifies the label of a given picture through the images pixel values. A typical structure of a NN is shown in Fig. 4.3. We will next briefly introduce the operating principle of the NN with the example of an  $m$ -class picture classification task ( $m = 2$  for the cat and dog classification example).

In each iteration, the information of one picture from the training set is prepared into a column vector and used as the input of the NN algorithm. For example, a picture of  $L \times L$  pixels is reshaped into a  $(L^2, 1)$  vector  $x$  by simply concatenating the  $L \times 1$  lines  $L$  times. The input vector is further modified as  $\tilde{x} = \frac{x - \langle x \rangle}{\sigma_x}$  in order to improve the performance of the algorithm, where  $\langle x \rangle$  and  $\sigma_x$  are the mean and standard derivation of  $x$ . After the input preparation, the  $i^{th}$  input  $\tilde{x}^{(i)}$  is passed on to the first (represented in the subscripts) hidden layer  $h_1^{(i)}$  (with  $n_1$  units) through  $h_1^{(i)} = \sigma(W_1^{(i)} \cdot \tilde{x}^{(i)} + b_1^{(i)})$ , where  $W_1^{(i)}$  and  $b_1^{(i)}$  are a  $(n_1, L^2)$  coupling matrix and a  $(n_1, 1)$  bias vector, respectively. The non-linear function  $\sigma(\cdot)$  adds to the complexity of the NN and further expands the network's functionality. The first hidden layer vector  $h_1^{(i)}$  is transferred to the second hidden layer through  $h_2^{(i)} =$

$\sigma(W_2^{(i)} \cdot h_1^{(i)} + b_2^{(i)})$ , where  $W_2^{(i)}$  and  $b_2^{(i)}$  are the coupling matrix and the bias of the second hidden layer, and the same nonlinear function  $\sigma(\cdot)$  is used. The algorithm labels the input picture using  $y_{NN}^{(i)} = f[\sigma(W_{n+1}^{(i)} \cdot h_n^{(i)} + b_{n+1}^{(i)})]$ . Similarly,  $W_{n+1}^{(i)}$  and  $b_{n+1}^{(i)}$  are the coupling matrix and bias at the output coupling layer, and  $f$  is a normalization function which transforms the value of  $\sigma(W_{n+1}^{(i)} \cdot h_n^{(i)} + b_{n+1}^{(i)})$  into a ‘one-hot’ label vector. The ‘one-hot’ label is a one-column vector with  $m$  elements representing the  $m$  possible output classes. For a given training data input, the normalization function  $f$  sets only one vector element of  $y_{NN}^{(i)}$  to 1, which represents the label of the class for that particular data set, and the other elements to zero. In the meantime, a cost function  $f_{cost} = \|y_{NN}^{(i)} - y^{(i)}\|$  is calculated to describe the distance between the algorithm label  $y_{NN}^{(i)}$  and the known label  $y^{(i)}$  for that given input  $x^{(i)}$ . The goal of the training process is to minimize the value of  $f_{cost}$  through the so-called back propagation process, where the algorithm refines the values of all coupling matrices  $W$  and biases  $b$ , utilizing the derivative values  $\frac{df_{cost}}{dW}$  and  $\frac{df_{cost}}{db}$ . The back propagation process is repeated for all pictures in the training set. The values of all network parameters are fixed after the training. In the testing phase, unseen pictures are fed into the trained network with their machine predicted labels calculated, while the back propagation process is not used. If the predicted labels agree well with the correct labels, the classification NN algorithm is successfully trained.

The recurrent neural network (RNN) structure is based on the neural network with the addition of a memory effect. As shown in Fig. 4.3, extra loops are employed in every hidden layer. The RNN hidden layer  $h^{(i)}$  has an additional influence from its previous state  $h^{(i-1)}$  through the  $h \rightarrow h$  coupling matrix  $W_{h \rightarrow h}^{(i)}$ . This feature grants a RNN the ability to store information from previous iterations, and the potential to predict future

states. Differing from the NN algorithm, which is insensitive to the specific order of the input information, a RNN algorithm requires that the inputs are fed into the algorithm following a strict time-ordering or systematic evolution.

#### 4.4 Task I: Multi-cavity System Classification Task

We utilize the neural network algorithm to classify different wave chaotic systems based on raw scattering data. The goal is to train the machine to classify the total number of cavities in the linear cascade chain by using the raw impedance ( $Z$ ) matrix measurements. As discussed in section I, the diagonal element  $Z_{11}$  of 1-, 2- and 3-cavity systems is very difficult to distinguish by eye, and also shares nearly identical statistical properties as shown in Fig. 4.2. In the 1-, 2- and 3-cavity cascade measurements, we rotate the mode stirrer to 200 unique and distinct angles in order to generate a large ensemble of measured data. The impedance measurement sweep is from 3.95-5.85 GHz with 16001 frequency points. One-hot vectors of size  $(3, 1)$  are created as the correct labels for all configurations. 80% of the total measurements ( $3 \times 200 = 600$  realizations from 1-, 2- and 3-cavity cascade cases) are used to train the algorithm, and 20% of the data is reserved as a testing data set. The NN employs 4 hidden layers which have 25, 26, 33 and 18 units, respectively. The specific choice of the total number of layers and units per layer can be varied. We use the Tensorflow package in the back propagation process. The training and testing results are shown in Fig. 4.4. To speed up the algorithm, we select subsets of size 2000 (Fig. 4.4 (a)) and 5000 (Fig. 4.4 (b)) uniformly chosen frequency points out of the total 16001  $Re(Z_{11})$  measurements as input vectors (the  $Im(Z_{11})$  input

algorithm also works just as well but the results are not shown). In both cases, the cost function decreases sharply and the testing set accuracy reaches above 95% within 500 cost-function minimization iterations. We observe that training the algorithm with 5000 data points in the input vectors (Fig. 4.4 (b)) reaches a higher testing accuracy (98.3%) as compared to the fewer data point case (95%). The testing accuracy reaches to 100% (Fig. 4.4 (c)) when all measured data points are fed into the NN algorithm. One can understand the improvement of test performance from the fact that more information are delivered to the algorithm with the increase of input vector size. The algorithm successfully identifies the total number of connected cavities in the cascade utilizing only the knowledge of the system diagonal impedance as a function of frequency. The result indicates that the algorithm is able to detect and utilize “hidden orders” embedded in the measured data, completing a task that is hard to achieve with either visual inspection or by more sophisticated analysis and statistical means [74].

We further explore the limitations and robustness of the developed multi-cavity classification algorithm. We first test the algorithm’s ability to identify unseen measured data. An algorithm is trained to successfully classify the  $Re(Z_{11})$  measured data from the 1- and 3-cavity cascade systems. The NN output has three classes: the 1- and 3-cavity systems whose data are seen by the algorithm in the training phase, and an untrained 2-cavity system class. In the testing phase, we mix in the  $Re(Z_{11})$  data from 2-cavity cascade measurements. We find that the algorithm classifies the 2-cavity data into the all three categories with equal probabilities. This result indicates that the classification algorithm applies strictly to the data drawn from the training ensemble. We next test the algorithm’s tolerance level to noise. The algorithm is successfully trained to classify the

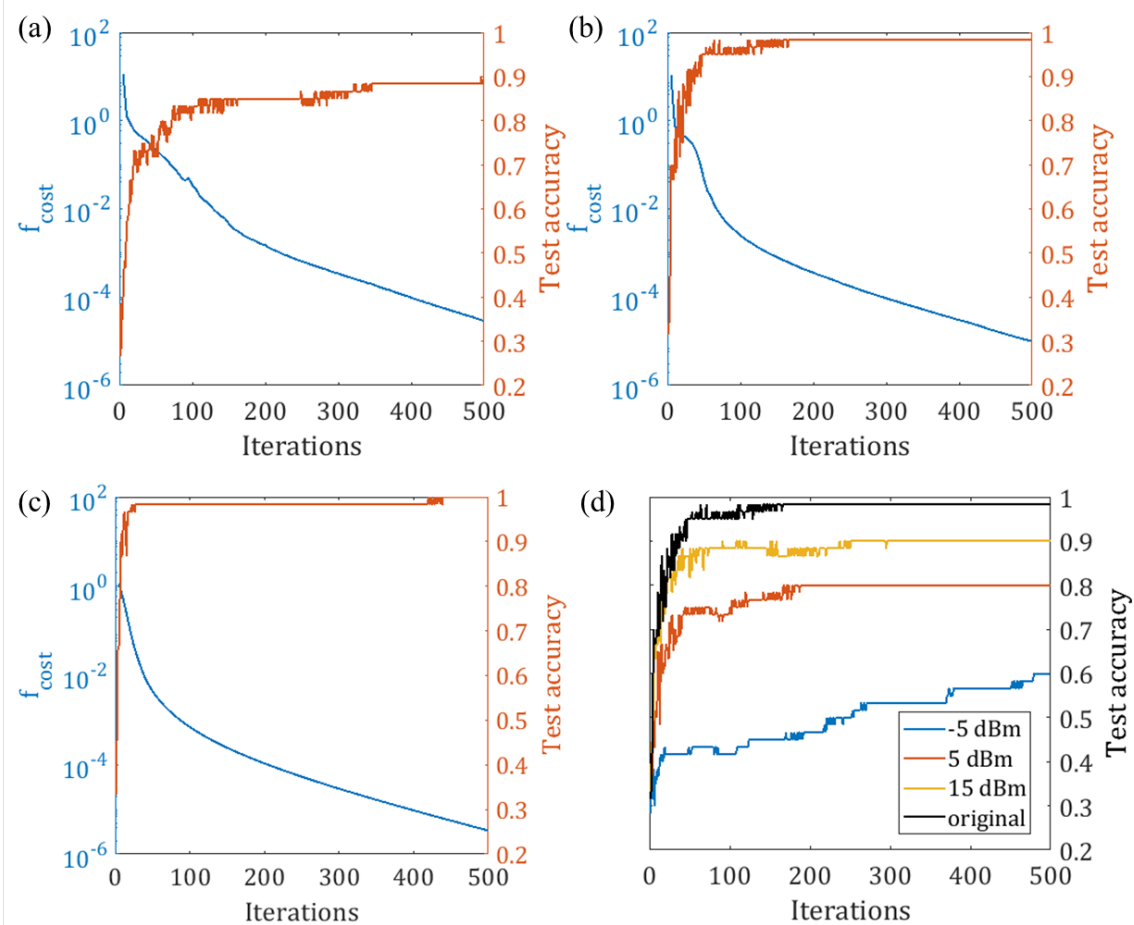


Figure 4.4: The NN classification algorithm performance for 1-, 2-, and 3-cavity  $Re(Z_{11})$  data. (a-c): The cost function  $f_{cost}$  (blue, left logarithmic axis) and test accuracy (red, right linear axis) results are evaluated to 500 iterations of the algorithm. The dimension of the input vector is 2000, 5000 and 16001 in (a), (b) and (c), respectively. (d): The test accuracy results with and without additional Gaussian noise. The dimension of the input vector is 5000. The signal to noise ratio values are -5, 5, 15 dB and the original data.

$Re(Z_{11})$  data from 1-, 2-, and 3-cavity cascade measurements with minimal experimental noise. In the testing phase, Gaussian noise are added to the  $Re(Z_{11})$  measurements to achieve signal to noise ratios (SNR) of -5, 5 and 15 dB. The power level of the noise  $P_n$  is calculated from  $SNR = 10 \log_{10}(P_s/P_n)$  based on the signal power level  $P_s$ . As shown in Fig. 4.4 (d), the final test accuracy changed from 0.9 to 0.66 (saturating after the 1000 iterations) with the decrease of SNR from +15 to -5 dB. The result shows that the classification algorithm retains its ability to distinguish the cavity number when the noise level is not too high.

The use of the frequency and realization-averaged  $Z_{11}$  values was investigated as a possible alternative to the machine learning algorithm. The 1-, 2- and 3-cavity cascade  $\langle Re(Z_{11}) \rangle$  are nearly identical (varying by 0.7% of the average value). The ML algorithm fully retains the classification performance for the multi-cavity  $Re(Z_{11})$  data even after it has been normalized by the average values. This demonstrates that the algorithm utilizes details that are not easily summarized when making a high resolution distinction between the three scattering scenarios based on statistics. With statistical methods, repetitive independent measurements of the multi-cavity system can produce stable mean values of  $\langle Re(Z_{11}) \rangle$  to further distinguish the different cases. To obtain a good estimation of  $\langle Re(Z_{11}) \rangle$  and decrease the uncertainty, this approach involves a large number of measurements of each different system in the data-gathering phase. In the prediction phase, given an unknown system, a large amount of additional data is required to acquire a good measurement of  $\langle Re(Z_{11}) \rangle$  to perform classification. By contrast, a trained ML algorithm can distinguish an unknown system with only one round of measurement. Compared to the statistical method, the ML algorithm requires considerably less data

to produce a confident classification of the system.

## 4.5 Task II: Chaotic Cavity S-parameter Series Prediction

Inspired by the recent progress of predicting the future evolution of classically chaotic systems with machine learning techniques [78, 79, 80], we utilize the RNN algorithm to predict the evolution of a wave chaotic system under systematic perturbation. We record the  $2 \times 2$  S-parameter matrix of a single wave chaotic enclosure under a sequential and systematic perturbation from a rotating mode stirrer. The dimension of the single cavity is  $0.038 \times 0.038 \times 0.089m^3$ . EM waves from 75-110GHz are fed into the cavity ( $\sim 10^4$  modes at the operating frequency range) through single-mode WR10 waveguides from Virginia Diodes VNA Extenders and the S-parameters are measured by a VNA. The mode stirrer is rotated to 1000 unique angles with uniform step angle size. A full rotation of the mode stirrer takes  $\sim 120$  steps. There exists some correlations between the measurements. The task is to use a portion of the measured  $S_{11}$  and  $S_{21}$  data to train the RNN algorithm, and then generate predictions of  $S_{21}$  by supplying additional measured  $S_{11}$  data obtained later in the sequence. It is difficult to predict the future state of a wave chaotic system based solely on its history information, since minute changes of the system's boundary condition can drastically affect the EM wave properties [58].

The RNN algorithm is implemented with the layer recurrent neural network function from the Matlab Deep Learning Toolbox. Similar to the neural network training, we first prepare the input vectors  $\tilde{x} = \frac{x - \langle x \rangle}{\sigma_x}$  to improve the performance of the algorithm. In contrast with the input labeling process in the NN, one must prepare the input and

output vectors in the correct evolutionary order. We next define the desired network parameters, such as the sizes of the hidden layer units and the method of back-propagation optimization. In the chaotic cavity S-parameter prediction task, the input vectors are assembled from measured  $|S_{11}|$  at 50 frequency points with 175MHz spacing from 75-110 GHz. The output vectors are from measured  $|S_{21}|$  at 5 frequency points with 2.5GHz spacing ( $\sim 1000$  modes exist in this frequency interval). It is not shown here, but the algorithm also works for the real/imaginary parts of the S-parameters as input and output. The adopted RNN structure has 38 units in 1 hidden layer. The testing results from all frequency points are shown in Fig. 4.5. The first 900 realization of the measured data are used as the training set, and the testing begins with the 901<sup>st</sup> realization. Only measured reflection information ( $|S_{11}|$ ) is fed to the algorithm, serving as the observer of the system [78, 80], and we record the machine predicted transmission information ( $|S_{21}|$ ). As shown in Fig. 4.5, we observe good agreement between the algorithm-generated and measured transmission  $|S_{21}|$  at least for the first 40 or so realizations for all 5 frequency points. The prediction degrades beyond this point.

## 4.6 Discussion and Summary

The ML techniques are shown to successfully classify different wave chaotic systems and to give predictions of future system states. Benefiting from its model-free property, ML can be versatile for various tasks. However, the training process of ML methods requires large amounts of measured or simulated data, and the tuning of algorithm hyper-parameters, including the number of layers, the number of units per layer, etc. These

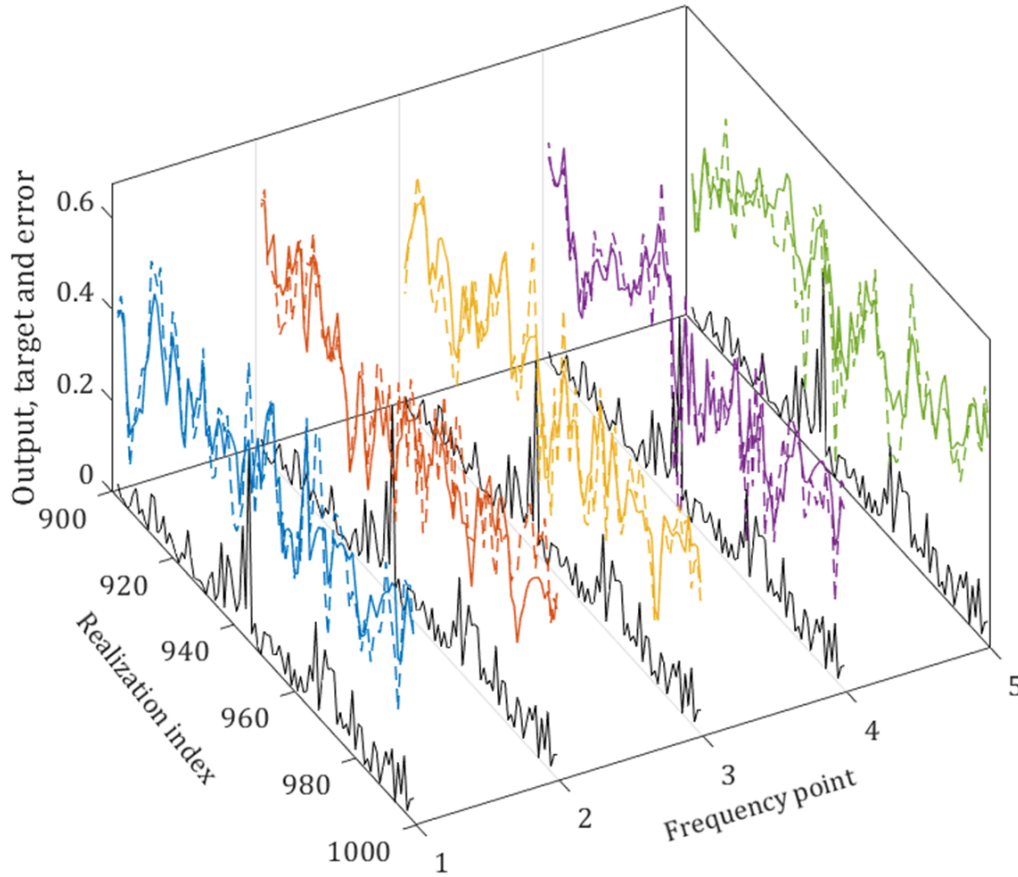


Figure 4.5: The  $|S_{21}|$  prediction of a wave chaotic electromagnetic system future states using measured  $|S_{11}|$ . The measured  $|S_{21}|$  data (colored solid lines) and algorithm predictions (colored dashed lines) from 5 frequency points are compared for cavity realizations 900 to 1000. The black lines show the absolute magnitude of the difference between the measured data and the algorithm prediction.

choices must be guided by experience with the algorithms rather than knowledge of the physical problem. The NN based wave chaotic classification task can be further developed into a cavity loss parameter ( $\alpha$ ) detector, or an algorithm to distinguish different types of perturbation of a wave chaotic system, for example. The application of RNN and other techniques, such as the long short-term memory methods, the nonlinear autoregressive neural network and reservoir computing, may give predictions for the future evolution of the S-matrix when the boundary condition of the enclosure is subject to systematic perturbation. The algorithm could be utilized to predict the future S-matrix of an evolving system, thus allowing identification of coherent perfect absorption conditions of a wave chaotic system, for example.

## Chapter 5: Late-Time Time-Domain Random Coupling Model

### 5.1 Overview

The complex scattering of electromagnetic (EM) fields can be found in various scenarios. In the short-wavelength limit, the wave dynamics of chaotic systems are extremely sensitive to the geometrical details, which poses challenges for the modeling of wave evolution. Benefiting from powerful numerical tools, accurate time-domain modeling of the wave propagation can be simulated when the exact geometrical details of a scattering system are known. However, the results obtained from deterministic methods will not hold when perturbations are applied to the system, for example, a simple change of system boundary condition. Under these circumstances, statistical studies are advantageous for studying chaotic wave systems.

As we have introduced in the previous chapters, for frequency-domain quantities, the Random Coupling Model (RCM) has found great success in characterizing the statistical properties of various quantities, for example, the complete system scattering matrix and the impedance matrix. The RCM method is based on the Random Plane Wave hypothesis, which models the chaotic wave field as a superposition of many plane waves with random phases, amplitudes, and directions. The coupling coefficients between the system ports and the system modes are modeled as Gaussian random variables with unit variance.

Here, we aim to further expand the utilization of RCM from the frequency domain to the time domain. By analogy with the frequency domain RCM, we construct the time domain RCM (TD-RCM) by computing a set of system modes, each modeled by a damped, driven, harmonic oscillator equation, using the finite-difference method. The lossyness of the enclosure is modeled by the damping factor in each mode evolution equation. System-specific quantities, such as the radiation resistance of the antennas, are also included in the TD-RCM method. This chapter will first introduce the fundamental equations of the TD-RCM method and then introduce the gigabox short-pulse experiments used to verify the theory, followed by a comparison between experimental and TD-RCM simulated results, and then finally I summarize our discussion. We would also note that, as will be clear later, we are working towards a newer version of the TD-RCM method, which includes the enclosure's deterministic early-time (short orbit) behavior. Thus the version of modeling discussed here should be taken as the late-time version of TD-RCM.

## 5.2 Details of TD-RCM Formulation

In this section, we will discuss the detailed formulation of the TD-RCM program. The TD-RCM program models an enclosure with a volume  $V$  and supporting  $N$  eigenmodes in the operating frequency bandwidth. The enclosure can have  $M$  ports, where each of the ports can serve as a transmitting port or a receiving port. The type of load connected at each of the ports can be different, and the degree of lossyness for each of the modes can also be specified. The radiation resistance of the ports  $R_{rad}$  can be assigned with a frequency dependence.

### 5.2.1 TD-RCM Equation of Motion

The time-domain Random Coupling Model (TD-RCM) computes the temporal evolution of the cavity modes and port signals. The cavity modes ( $U_n, n = 1, 2, \dots, N$ ) are represented by the voltages  $U_n$ , where  $n$  is the mode index. The signal at port  $j$  is represented by the port voltage  $V_j$  and port current  $I_j (j = 1, \dots, M)$ .

The cavity modes are described by the damped harmonic oscillator equation

$$\frac{d^2}{dt^2}U_n + v_n \frac{d}{dt}U_n + \omega_n^2 U_n = \omega_n \sum_{j=1}^M c_{nj} K_{nj} \frac{d}{dt}I_j, \quad (5.1)$$

where the port subscript  $j$  runs through all  $M$  system ports. The port voltages ( $V_j, j = 1, 2, \dots, M$ ) are modeled by a linear summation over all cavity modes,

$$V_j = \sum_{n=1}^N c_{jn} K'_{jn} U_n - V_{jc}. \quad (5.2)$$

As such, the ports act to couple all the modes to each others.

In Eqn. 5.1, the damping term  $v_n = \frac{\Delta\omega_n^2}{|\omega|} \alpha$  is derived from frequency domain RCM. The loss parameter is defined as  $\alpha = k^2 / (Q \Delta k^2)$ . The loss parameter  $\alpha$  describes the degree of lossyness of the system. With  $\alpha$  known, one is able to generate the statistical ensemble of system impedance using RCM. The quantities  $k, Q, \Delta k^2$  are the operating wavenumber, enclosure quality factor, and the mean-mode-spacing, respectively;  $\omega_n$  and  $\Delta\omega_n^2$  are the eigenmode frequency and mean-mode-spacing near  $\omega_n$ ;  $c_{jn}$  is the coupling coefficient for mode  $n$  and port  $j$  (assumed to be Gaussian random variables); and  $K_{nj} =$

$-\left(\frac{\mu}{\epsilon}\right)^{\frac{1}{4}}\left[\frac{2R_{rad,j}(\omega_n)\Delta\omega_n}{\pi\omega_n}\right]^{\frac{1}{2}}$ , where  $\mu$  and  $\epsilon$  are the (assumed uniform) permeability and permittivity of the enclosure volume material, and  $R_{rad,j}(\omega_n)$  is the frequency domain radiation resistance of port  $j$  at frequency  $\omega_n$ . In Eqn. 5.2, the random coupling coefficient  $c_{jn}$  and mode voltages  $U_n$  are the same quantities as in Eqn. 5.1;  $K'_{jn}$  is defined as  $K'_{jn} = -\left(\frac{\epsilon}{\mu}\right)^{\frac{1}{4}}\left[\frac{2R_{rad,j}(\omega_n)\Delta\omega_n}{\pi\omega_n}\right]^{\frac{1}{2}} = \sqrt{\frac{\epsilon}{\mu}}K_{nj}$ ;  $V_{jc}$  represents the electrostatic mode contribution of port  $j$ , defined as  $C_p\frac{d}{dt}V_{jc} = -I_j$ ; the term  $C_p$  is the port radiation reactance at low frequency ( $< 100\text{MHz}$ ). We note that the order of subscript for the quantities  $K_{nj}$  and  $K'_{jn}$  is flipped. The reason for this setting is just putting the subscript that runs over the summation in the second spot.

For an enclosure with  $N$  modes and  $M$  ports, we will have  $N$  sets of Eqns. 5.1 and  $M$  sets of Eqns. 5.2. The unknown quantities that will be solved are the  $N$   $U_n$ s and  $M$   $V_j$ s as a function of time. Usually we will set the initial condition as  $U_n(t=0) = V_j(t=0) = 0$ , representing a quiet cavity. When the input pulses are turned on, the port voltage values at the transmitting ports will have nonzero values as well as nonzero time derivatives. As shown in the RHS of Eqn. 5.1, the change of port signals will drive cavity modes to oscillate. The oscillating cavity modes will further contribute to the nonzero signals at all ports (the RHS of Eqn. 5.2). With all equations and parameters given, it seems that one is able to solve for all system mode voltages and port voltages using finite-difference time-domain evolution methods. However, we still need to have an explicit relationship between the port voltage and current signals, and this is related to the load attached at each port.

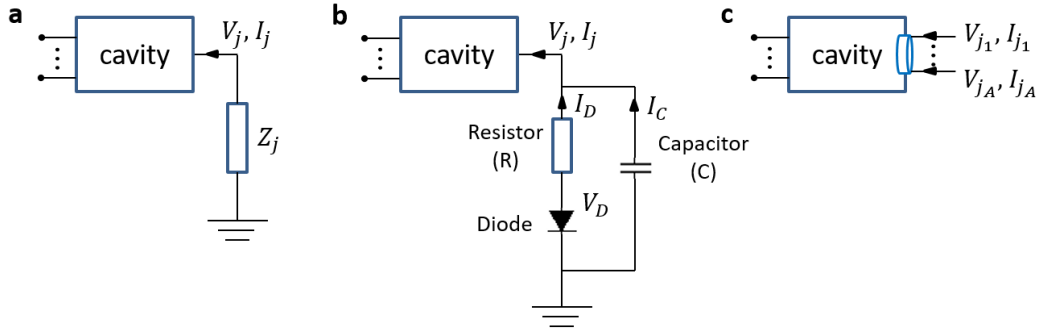


Figure 5.1: Diagrams of the TD-RCM port load modeling. **a.** The linear load at port  $j$  is represented with an impedance  $Z_j$ . **b.** The schematic of a diode-loaded port. **c.** The schematic of a multi-mode aperture. Note that the subscript “in” corresponds to waves following the arrow, going into the cavity.

### 5.2.2 System Port Treatments

In this subsection, we will discuss the treatment of two generic types of loads (Fig. 5.1): a linear impedance load and a nonlinear diode load. We first show the treatment of ports with a linear load. The voltage and current at the port  $j$  can be expressed by

$$\begin{aligned} V_j &= V_{in} + V_{out}, \\ I_j &= (V_{in} - V_{out})/Z_j, \end{aligned} \tag{5.3}$$

where  $V_{in}$  ( $V_{out}$ ) represents the incident (reflected) voltage wave coming into (out of) the port from the cavity. The direction of wave is shown as arrows in Fig. 5.1. So that “in” corresponds to waves going into the cavity. The value of the load impedance  $Z_j$  is usually  $50\Omega$ , which is represented by the load connected between the cavity and the ground in Fig. 5.1 (a). Note that the TD-RCM allows the cavity to have multiple ports, shown schematically with the lines connected to the left side of the cavity. For an input port, we have  $I_j = \frac{V_{in}-V_{out}}{Z_j} = \frac{2V_{in}-V_j}{Z_j}$  where the  $V_{in}$  is the waveform injected into the cavity. For

an output port, we have  $I_j = -V_j/Z_j$  since  $V_{in} = 0$ .

We may further combine the I-V relation of both input and output ports by the following vector expression

$$\underline{I} = \underline{Y}\underline{V} + \underline{D}. \quad (5.4)$$

Vector quantities are used here for simplicity:  $\underline{I}$  and  $\underline{V}$  are two M-by-1 column vectors for all port currents and voltages, whose elements are just  $I_j$  and  $V_j$ . Here  $\underline{Y}$  is a diagonal M-by-M matrix where  $Y_{jj} = 1/Z_j$ , and  $\underline{D}$  is a time-dependent vector with  $D_j = 2V_{in}/Z_j$ . Now we have obtained enough equations to solve for the port voltages. Note that the values of port load impedance and the injected voltage signal values are known quantities, and the above equation is only for one time step.

We next study the case with nonlinear output ports as illustrated in Fig. 5.1 (b). As a true time-domain model, one of TD-RCM's strengths is the ability to treat ports loaded with nonlinear elements. As shown in Fig. 5.1 (b), the diode-loaded port is modeled with a series resistance ( $R$ ) and a shunt capacitance ( $C$ ). The diode-port is modeled by the following equations:

$$\begin{aligned} V_j &= V_D + R I_D, & I_j &= -(I_C + I_D) \\ I_C &= C \frac{d}{dt} V_j, & I_D &= I_0 [e^{\frac{eV_D}{kT}} - 1]. \end{aligned} \quad (5.5)$$

The subscripts  $D$  and  $C$  represent the diode and capacitor. For convenience, we set  $I_D = 0$  for negative voltages. Eqn. 5.5 can be simplified to

$$C \frac{d}{dt} V_j + \frac{V_j}{R} + I_j = -\frac{V_D}{R}, \quad (5.6)$$

$$V_D = \frac{kT}{e} \ln\left(1 + \frac{V_j - V_D}{R I_0}\right). \quad (5.7)$$

We will apply a finite difference expression for Eqn. 5.6. Port voltage and currents are expressed by  $V_j(t) = [V_j(t+1) + V_j(t)]/2$ ,  $I_j(t) = [I_j(t+1) + I_j(t)]/2$ , and  $V_j'(t) = [V_j(t+1) - V_j(t)]/h$ , where  $h$  represents the time increment. The voltage across the diode  $V_D$  is computed by solving the transcendental equation 5.7. The Eqn. 5.6 can be rewritten in a similar form as Eqn. 5.4. The matrix  $\underline{Y}$  is still a diagonal M-by-M matrix where  $Y_{jj} = 1/R + 2C/h$ , and the vector  $\underline{D}$  is expressed by  $D_j = (\frac{2C}{h} - \frac{1}{R})V_j - I_j - \frac{2}{R}V_D$ .

### 5.2.3 Generating of System Eigenmodes with RMT

Note that one will need to provide a list of eigenmodes of the closed system to run TD-RCM. It is possible to obtain all system eigenmodes with good accuracy using numerical simulation tools. However, such a process would be time-consuming for an electrically large system and not possible if the system's geometrical details are not accessible. Here we utilize the property of a chaotic system to simulate a list of system modes by only knowing the macroscopic system information (i.e., volume, area) and the operating frequency. The list of system eigenmode  $\omega_n$  is generated using Random Matrix Theory (RMT). We start by computing the eigenvalues  $\lambda_{rmt}$  of large random matrices. The matrix size equals to the total number of system modes that we want to model, and the matrix elements are drawn from a Gaussian distribution controlled by the symmetry group of the system. The system eigenmode  $k_n = \omega_n/c$  is computed from the relation  $\lambda_{rmt} = \frac{k_c^2 - k_n^2}{\Delta k^2}$ , where  $k_c$  is the center frequency of the band that we want to model and  $\Delta k^2$  is the mean mode spacing. To sum-up, one first uses the total number of modes

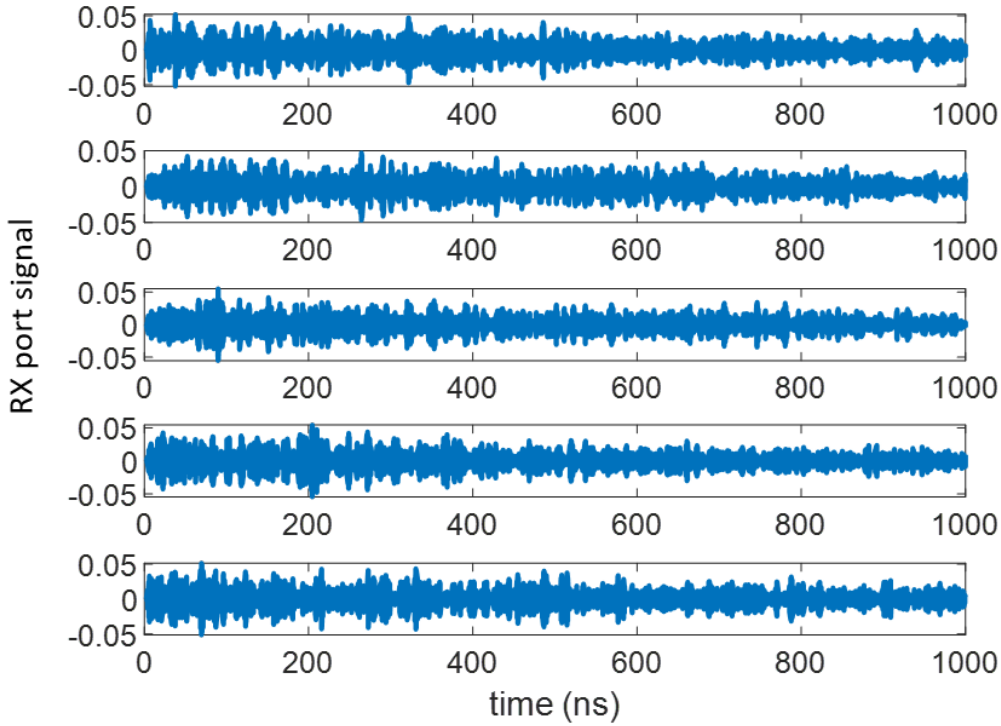


Figure 5.2: The TD-RCM simulated RX port voltage signal from 0 to 1000ns. Five realizations with distinct cavity eigenmode spectra and coupling are shown. The injected waveform is a 5GHz center frequency and 5ns long sine pulse.

( $N$ ) to generate  $N$  random matrix eigenvalues, and then uses the center frequency and mean-mode-spacing to generate  $N$  system modes. Here we show several examples of the TD-RCM simulated RX (receiver) port signals in Fig. 5.2. A diverse RX port response can be clearly seen.

### 5.3 Gigabox Short-pulse Experiment

To test the applicability of the TD-RCM method, we conducted short pulse injection experiments in a 3D enclosure (shown in Fig. 5.3). The gigabox is a metallic enclosure with a volume of  $\sim 1m^3$ . A mode-stirrer, consisting of two thin metallic panels, is

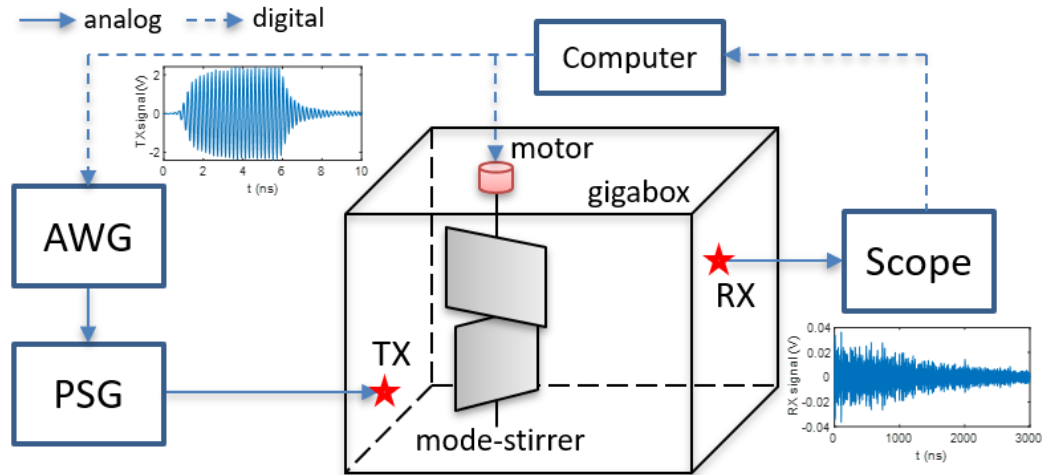


Figure 5.3: Schematic of the short pulse time-domain experiment setup. The injected waveform (left inset) is generated through IQ modulation using the arbitrary waveform generator (AWG) and the programmable signal generator (PSG). The short pulse is broadcast into the enclosure through the transmitting (TX) port (star). The data ensemble is created by rotating a motorized mode-stirrer inside the enclosure. The receiver (RX) port (star) induced voltage signal (right inset) is measured by the oscilloscope. A lab computer is used for instrument control and data transmission/collection.

located inside the gigabox to randomize the ray trajectories. One may rotate the angle of the mode-stirrer through many values to obtain an ensemble of data. To expedite the measurement process, we installed a motor outside the gigabox to control the rotation of the mode stirrer. We will conduct a 2-port time-domain experiment. One of the locations serves as the input port, where a single center frequency modulated by a short pulse envelope is injected into the gigabox. The injected signal will bounce around and excite many gigabox eigenmodes within the pulse bandwidth. A non-zero induced voltage signal will be measured at the receiver (RX) port. Typical input and output waveforms are shown as insets in Fig. 5.3. Here we set the input wave as a single frequency sine wave with 20 ns duration and a center frequency  $f_c$ . In the experiment we use a series of different  $f_c$  values ranging from 5 to 10 GHz. We rotate the mode-stirrer 200 times for each choice of

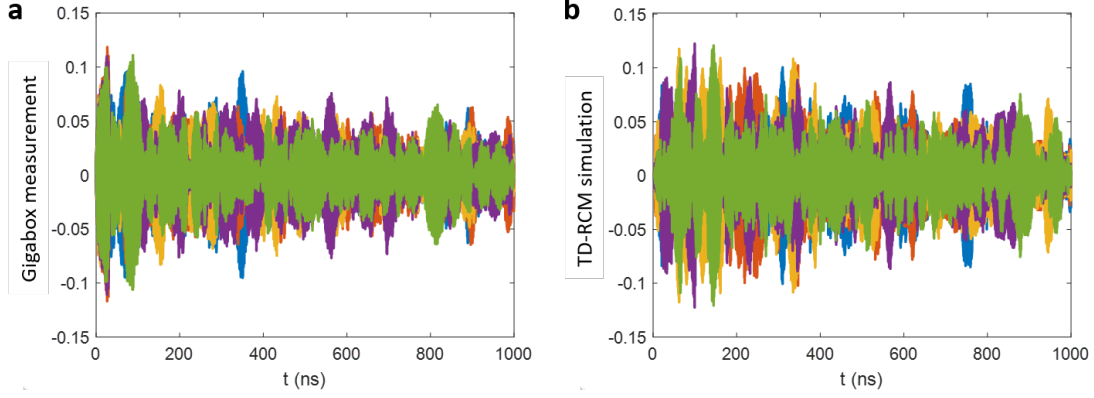


Figure 5.4: We plot the measured gigabox RX port voltage signals in (a), and the corresponding TD-RCM simulation in (b). In each figure, the port signals from 20 realizations are overlaid to show the diversity of system response.

center frequency to create an ensemble of measurement systems and resulting transmitted waveforms  $V_j(t), n = 1, 2, \dots, 200$ .

## 5.4 Statistical Analysis and Discussion

To test the performance of the proposed TD-RCM method, we have conducted short-pulse injection experiments in the gigabox, and measured the induced voltage waveform at a second part. Using realistic information for the experimental setup, namely the gigabox mode-spacing at the input pulse center frequency  $f_c$ , the loss parameter  $\alpha_{rcm}$ , and the measured I/O antenna radiation resistance, we can simulate our pulse injection measurement with TD-RCM code at least as far as the statistical properties are concerned. We show the simulated RX port signal and the data gathered from gigabox experiment in Fig. 5.4 (b) and (a), respectively. Both data sets show a diverse response in terms of the RX port pattern.

We studied the statistics of the maximum receiver (RX) port voltage in the time

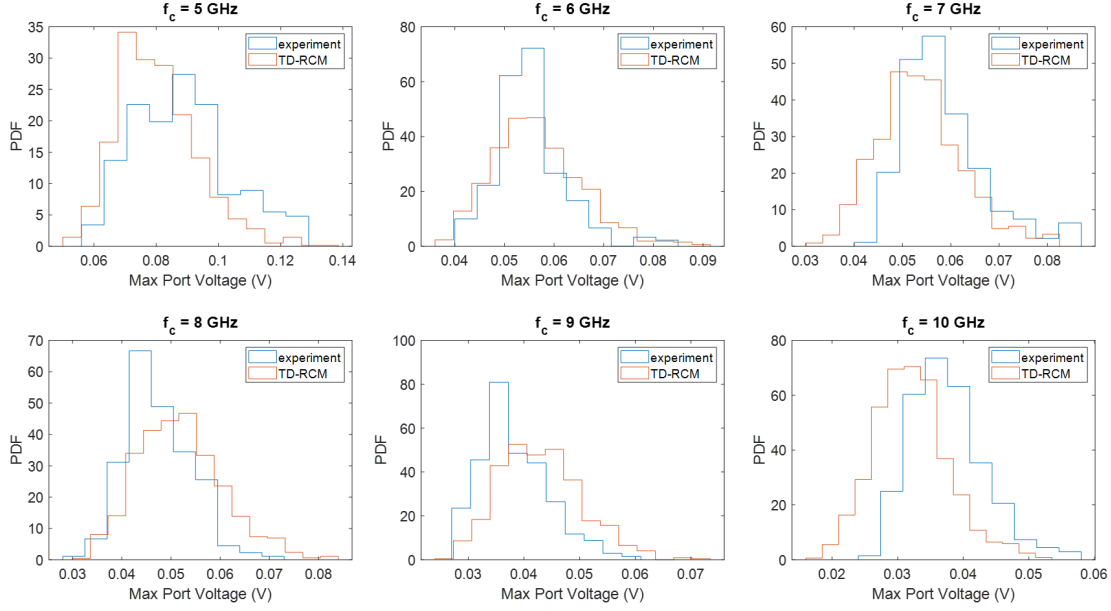


Figure 5.5: The statistics of the maximum RX port voltage studied at different frequencies merged in the gigabox. The input pulse is a single-frequency 20ns sine pulse. The center frequency  $f_c$  changes from 5GHz to 10GHz. Note that the input pulse has a finite rise/fall time ( $1 \sim 2ns$ ). Data histograms (blue) are compared to the predictions of the TD-RCM model (red).

domain. This quantity is defined as the maximum induced voltage signal at the port after the input pulse is injected. The ensemble size of the TD-RCM is usually set as 1000 realizations, created by drawing a new list of system eigenmodes and the coupling strength between the ports and the eigenmodes. As summarized in Figs. 5.5 and 5.6, we have found relatively good agreement between the TD-RCM model prediction and experimental data. Note that in Figs. 5.5, we find that the value of the RX port signal decreases as the center frequency increases. This can be explained by the loss parameter of the gigabox increases from  $\alpha \sim 3$  (5GHz) to  $\alpha \sim 12$  (10GHz).

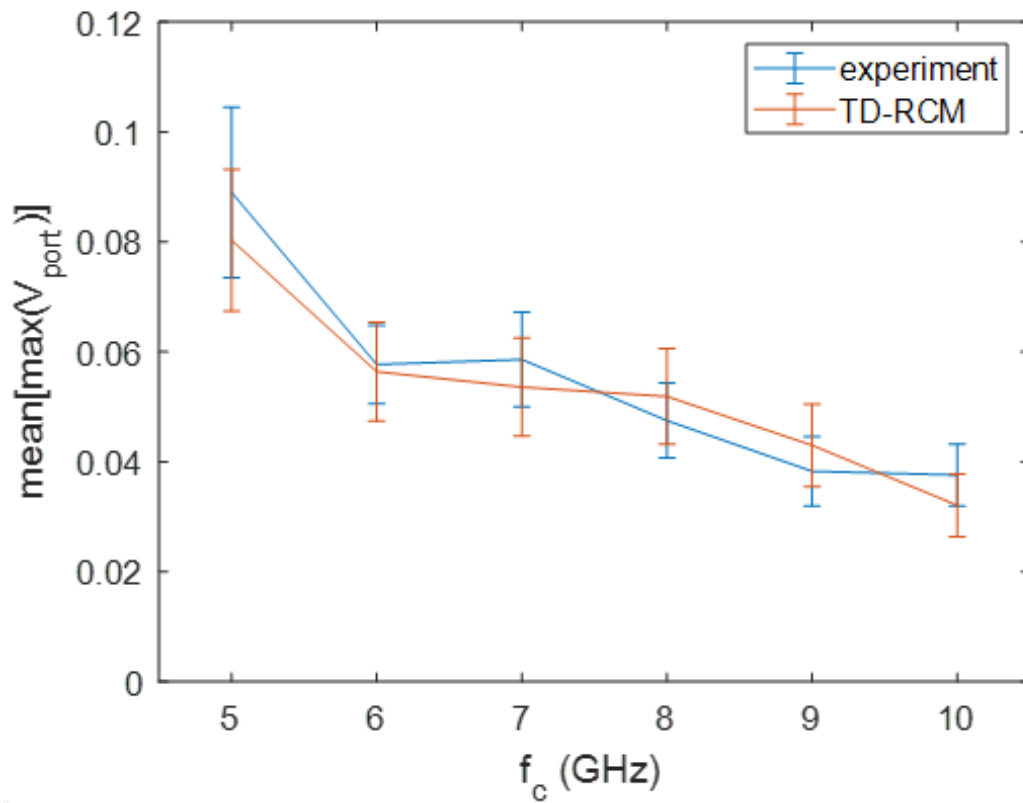


Figure 5.6: Mean values of the receiver port maximum voltage PDFs shown in Fig. 5.5 as a function of the center frequency of the 20ns pulse in the Gigabox. The error bar is one standard deviation.

## 5.5 Discussion and Summary

We studied the statistics of the maximum receiver (RX) port voltage in the time domain. A relatively good agreement between the experimental data and the TD-RCM simulation is observed. We have included the effect of SO by directly adding SO signal to the TD-RCM simulated RX port voltages. To expand the applicability of TD-RCM model, we have also worked out the formula for including nonlinear port loads. Note that we have not tested these functionalities experimentally.

As mentioned earlier in the chapter introduction section, one of the limitations of TD-RCM is an incomplete characterization of the early-time wave dynamics. In practice, the proper setup of the reverberant field environment inside the chaotic enclosure usually takes several  $T_{rt}$ , where  $T_{rt}$  represents the characteristic cavity time scale of the ray completing one round-trip inside the enclosure. Before the setup of the reverberant fields, the RX port-induced voltage signal will be mainly influenced by the short-orbit responses. As shown in Fig. 5.7 (a), the experimental ensemble-averaged RX port signal shows a sharp rise up at early time, and then starts to show an exponential decay trend at late-time. The reason for the early-time RX signal rise-up comes from a highly repetitive and stable prompt-response at the port location in many realizations of the cavity ensemble. One can also find that the duration and amplitude of the rise-up increase is in proportion to the injected pulse duration. However, as shown in Fig. 5.7 (b), our current TD-RCM simulated port response does not have a similar short-time rise-up as seen in the experimental case. Instead, one observes a smooth rise up for the ensemble-averaged port signals.

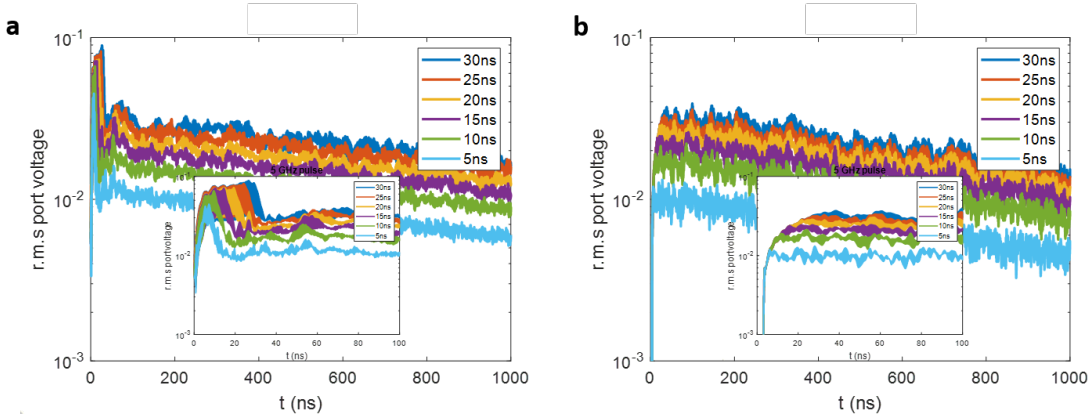


Figure 5.7: The root-mean-square ensemble averaged RX port signal comparison. The injected pulse is a 5GHz single frequency sine wave with a duration sweeping from 5 to 30ns. Experimental and TD-RCM simulation results are shown in **a** and **b**, respectively. The insets are the blow-up of the early-time (before 100ns) curves.

There are several difficulties for including realistic early time response into TD-RCM. Firstly, the TD-RCM has no spatial information. Early time responses are due to short-orbits, and this requires knowing the interior geometry of the closed enclosure. This in turn requires computing many short-orbit trajectories between the input and output ports and determining how much of them survive the ensemble averaging process, and considering the effect of the phase difference between the transmitted pulses travelling along different trajectories [30]. This is similar to the Rician or Rayleigh fading scenario in the wireless communication multi-path problems.

Another practical limitation is the trade-off between computing speed versus the system mode-density. The TD-RCM models the  $N$  system eigenmodes. We can estimate the required number of eigenmodes  $N = BW/\Delta f(f_c)$ , where  $BW$  is the bandwidth of the injected pulse, and  $\Delta f(f_c)$  represents the system mean-mode-spacing at the pulse center frequency  $f_c$ . Here is an estimate of the scale of  $N$  in our gigabox short-pulse experiment: there are  $\sim 23.5k$  modes in the frequency range from 4.5  $\sim$  5.5GHz, and

there are  $\sim 93.8k$  modes in the frequency range from  $9.5 \sim 10.5\text{GHz}$ . Hence, the computation speed of the gigabox short pulse experiments is limited by the total number of modes. One may increase the pulse duration to decrease the  $BW$ . However, this trick might be useful for proof-of-principle studies, and a method of systematically reducing the total mode number is desired.

To sum up, the TD-RCM model computes the temporal evolution of the cavity modes and port signals. A list of cavity modes is randomly generated using RMT by knowing the realistic system mode-spacing. Each of the cavity modes is characterized by a driven damped harmonic oscillator equation, where its equation parameters are computed using the system loss parameter  $\alpha_{rcm}$  and port radiation resistance  $R_{rad}$ . The port signal is computed by summing up all cavity mode signals. A TD-RCM user will need to input the basic enclosure information (mode-density and  $\alpha_{rcm}$ ), port information ( $R_{rad}$  and voltage-current relationship for all nonlinear port loads), and the injected waveform. The TD-RCM model will compute the temporal evolution of system modes and port voltages. An ensemble can be created by changing the list of eigenmodes and the mode-port random coupling coefficients. One can then study many statistical properties of the time-dependent port voltages and eigenmode dynamics. As shown with the maximum RX port voltage distribution study, the TD-RCM predictions show relatively good agreement with the experimental results. Furthermore, we will be working towards improved versions of TD-RCM to overcome the current model limitations. Topics to be addressed include time-domain aspects of short orbits, as well as the inclusion of large multi-mode apertures.

## Chapter 6: Wave-Based Reservoir Computing

### 6.1 Introduction

This work was a collaborative effort with the Maryland Wave Chaos group and the preprint can be found in Ref. [85]. From recognizing images to becoming a Go world champion, machine learning (ML) has changed our lives in myriad ways. These brain-inspired techniques are able to imitate other processes without explicitly knowing their underlying governing rules or equations of motion, and thus excel in starkly different applications [84]. ML techniques and scientific exploration have become increasingly intertwined [79, 86]. However, the computing speed and power efficiency of ML algorithms largely depend on their computing substrates, which are usually computers based on von Neumann architecture. Such machines only execute serial instructions and their speed is limited by the ‘von Neumann bottleneck’, which is induced by the serial transfer of data between the memory and the processor [87, 88]. Secondly, CPU clock speed stagnation has appeared as the Moore’s Law scaling continues to falter, and the Dennard Scaling has broken down due to heat dissipation induced failures [89]. Thirdly, large amounts of data are produced non-stop in both research and everyday activities that are hard to store, both for physical and financial reasons. On the other hand, the ceaseless development of ML has introduced massively parallel schemes which are clearly unfit for von Neumann

machines, whereas matching hardware to algorithms could lead to both fast and low-power data analysis. Thus, researchers are prompted to explore alternative computing paradigms, namely neuromorphic computing (NC), whose physical structures better fit with the ML algorithms.

With a biologically-inspired physical structure, the NC approach aims to overcome the challenges of current computers and to further realize the full potential of brain-like ML algorithms [88, 90]. The construction of NC machines are deeply customized to enable the parallel and low-cost execution of various ML schemes, ranging from the spiking neural networks [91, 92], recurrent neural networks (RNN) [93], convolutional neural networks [94] and reservoir computing (RC) systems [95, 96, 97, 98, 99]. The application of NC can realize ‘all-in-one’ machines with fast data collection, storage and analysis, and thus are suitable in various fields such as high-throughput experiments [100], IoT and edge computing applications [101]. Compared to the electronic NC approaches, photonics realizations promise an enhancement in computational speed and power efficiency by utilizing speed-of-light information transmission and the intrinsic parallelism of light [88, 102, 103, 104]. But current photonic approaches are still in their infancy due to the challenges of creating and measuring high-dimensional physical networks [93, 105]. For instance, the component number in a RNN device must grow as  $N^2$  where  $N$  is the network size, just to maintain the parallel implementation of matrices. Recently, the time-multiplexing concept has been implemented in delay systems for creating high-dimensional RC-inspired hardware [106, 107]. However, this enhancement of network scale directly results in a decrease of processing speed, as the virtual time-delayed computing nodes must operate in a serial fashion [101, 108].

Here, we present an elegant solution to the ‘speed vs. scale’ dilemma with RC inspired computing realized through a generic wave chaotic system. By exploiting the chaotic dynamics of EM fields, our approach, in principle, could emulate arbitrarily high-dimensional reservoir networks using only one physical structure. Promised by the parallelism of light, the proposed architecture evolves autonomously and with high speed. The computing power and versatility of the wave chaotic RC is demonstrated by performing five different benchmark tests with only one device. We have also introduced reservoir extension techniques (RETs) that allow the further enhancement of network scale utilizing only modest measurement capabilities. More detailed content of the RC setups are included in Appendix F.

## 6.2 Software Origin of RC

Reservoir computing is a general type of ML whose structure can be specified as follows. Sequential (e.g., time-dependent) input variables, at time  $n$  denoted by the  $N_u$ -dimensional vector column  $u_n$  ( $n = 1, 2, 3, \dots$ ), drive the evolution of a reservoir state column vector  $\hat{r}_n$ ,

$$\hat{r}_{n+1} = f(\hat{r}_n, u_n). \quad (6.1)$$

In Eq. 6.1, it is assumed that  $f$  satisfies the ‘echo-state’ property: for an initial condition  $\hat{r} = \hat{r}_1$  and a given sequence  $u_1, u_2, \dots, u_n, \dots$ , as  $n$  becomes large  $\hat{r}_n$  becomes independent of the initial condition  $\hat{r}_1$ . The RC system output, denoted  $s_n$  is taken to depend linearly

on a vector column  $r_n$  (of dimension  $N_r$ ) derived from the reservoir state  $\hat{r}_n$ ,

$$s_n = W \cdot r_n, \quad r_n = g(\hat{r}_n) \quad (6.2)$$

where  $W$  is a rectangular matrix. To promote effectiveness of the RC functionality,  $N_r$  is typically taken to be much greater than  $N_u$ . The elements of the matrix  $W$  are viewed as adjustable parameters whose values are chosen through a ‘training’ procedure, whereby, based on training data consisting of many examples  $(u_n, \hat{s}_n)$  of inputs  $u_n$  and the corresponding desired resulting outputs  $\hat{s}_n$ ,  $W$  is determined by minimizing the deviations overtime of  $s$  (the actual RC output) from  $\hat{s}$ . Heuristically, the basic idea of reservoir computing is that, if the dimension  $N_r$  is large, and the  $N_r$  individual elements of the time-dependent vector  $r$  evolve in diverse ways, then the best fit of  $s = Wr$  to  $\hat{s}$  will indeed be a very good approximation to the time varying vector  $\hat{s}$ . The basic ML assumption is that, following training, the outputs will continue to give a good approximation to the outputs that would be desired for the post-training inputs. Operationally, this is promoted by the application use of training regularization (typically, for RC, ridge regression) meant to prevent over-fitting [78, 79]. In general, either the function  $f$ , or the function  $g$ , or both should be nonlinear to allow the RC to perform a wide variety of nonlinear tasks [109]. We note that, by virtue of the relation (Eq. 6.2), the training of an RC reduced to a simple linear regression [78, 79]. Thus the training of an RC can be very fast [110].

### 6.3 Hardware Realization of RC

As introduced above, the RC architecture is a type of RNN which consists of a large number of nonlinear nodes connected through recurrent links. Compared with other deep learning approaches, the key insight behind RC is its radically simplified training process: only the output layer is optimised, by means of common regression methods [78, 79]. In the meantime, RC demonstrates the same level of performance as compared with other deep learning approaches [110]. The unique characteristics of RC make it an ideal blueprint for neuromorphic computing applications [101, 108]. The training of a hardware RC is completed in one shot by only optimising an out-coupling matrix, while the entire physical structure remains un-disturbed and intact. In contrast, the training of many inverse-designed [102, 103] or neural-network photonic devices [93, 111] relies on the iterative tuning of all physical components, which requires extra time and energy consumption. Moreover, the re-programming of the above devices is either impossible [102, 103, 111] or involves a complete re-training process [93], while RC devices require merely a simple switch of the output coupling matrix. RC-inspired hardware enjoys a high training efficiency and task flexibility among different NC genres, and thus attracts a great deal of research interest [101]. Earlier hardware RCs were built from distributed physical computing nodes with high processing speed, but their network scales are limited in practice [112]. Major efforts in the field were then directed to delay-based RCs which circumvent such limitations with virtual temporal nodes. However, this approach is palliative as its processing speed decreases with an increased network scale.

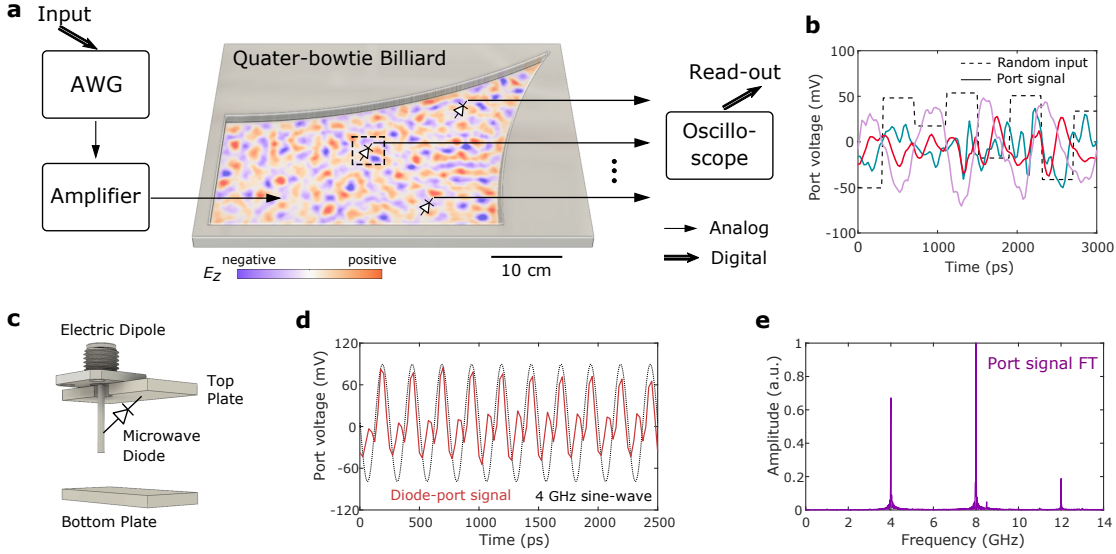


Figure 6.1: **Wave chaotic systems for reservoir computing.** **a**, Schematic of the experimental setup. The input information is transferred from a lab computer to the AWG and broadcast into the reservoir. The amplified waveform is injected into the chaotic enclosure through an electric dipole antenna. Several diode-loaded antennas are used to probe the EM field, whose voltage signals are measured by the oscilloscope and further transferred to the lab computer for training. **b**, Measured port signals (solid) under random input stream (dashed). **c**, Schematics of the diode-loaded port. **d**, The dynamics of diode-port voltages (red) under single frequency input at 4 GHz (black). **e**, The FT of the diode-port signal shown in **d**.

## 6.4 Chaotic Wave-based RC

### 6.4.1 Operating Principles

The proposed wave chaotic RC solves the ‘speed vs. scale’ dilemma by exploiting the parallelism of light and the richness of chaotic dynamics. Complex systems exist in multiple physical and real-life scenarios. Examples include atomic nuclei, quantum dots, and electromagnetic (EM) waves in electrically-large resonant systems. These systems are chaotic in the short-wavelength limit where minute perturbations will lead to a drastic change to the wave field configuration. Wave chaotic systems in the semi-

classical limit are successfully described with the Random Plane Wave hypothesis, where the system wave properties can be simulated with a superposition of plane waves with random amplitudes, phases and directions [37, 113]. Recently, researchers have exploited the rich dynamics of chaotic systems to create novel phenomenon including wavefront manipulations [114, 115, 116, 117] and ultra-fast random number generation [118]. Since the software RCs are essentially constructed with complex networks, here we aim to utilize such similarity and realize a new platform for RC-inspired hardware with nonlinear wave chaotic systems.

Fig. 6.1a shows in detail the photonic signal processing and the reservoir dynamics of the proposed RC. The digital input signals are transformed into analog waveforms by the AWG (arbitrary waveform generator) for both the training and testing sets. Later, the input pulse is amplified and injected into the chaotic quarter-bowtie billiard. The input stream will excite hundreds of system eigenmodes, where each mode displays a distinct eigenfunction pattern due to the chaotic nature of the enclosure in the short wavelength limit. The EM field emerges as the real-time superposition of all system modes, sampled at discrete locations in the wave chaotic system (as shown in Fig. 6.1b). Nonlinear dynamics are introduced by the microwave diodes connected at the output antennas (Fig. 6.1c). The nonlinearity is demonstrated by the port signal distortion (Fig. 6.1d) and higher harmonics responses (Fig. 6.1e). Thus, the complexity of the wave chaotic reservoir is ensured by the ray-chaotic property and the nonlinear elements.

Here the induced voltage signals at the diode-loaded ports serve as the observable reservoir nodes, and these are further transferred to a lab computer for off-line training (Fig. 6.1a). In contrast to the existing hardware RCs which consist of physical or

virtual discrete-nodes, the dimension of the wave chaotic RC is arbitrarily high as its reservoir layer is embodied by the continuum wave field inside the chaotic enclosure. Therefore, the wave chaotic RC has brought the conventional RC structure to its optimal stage: an arbitrarily high dimensional reservoir layer is made possible with a complex scattering continuum. Constructing such a continuum reservoir is hardly practical in software, but directly feasible in a photonic platform due to the true parallelism of light. And high-speed evolution of the wave chaotic RC is always promised regardless of the reservoir dimension. We note that similar continuum RC constructions have been studied numerically and realized with a water-bucket or in the spatial light modulator systems [119, 120, 121, 122]. However, the water-RC is nowhere suitable for application and the evolution of the latter system requires significant assistance from von Neumann computers.

## 6.4.2 Reservoir Expansion Techniques

Challenges arise because the total number of measurement channels in the physical RC is limited in practice. To overcome this limitation, we introduce novel Reservoir Expansion Techniques (RETs) with the boundary condition perturbation method (Fig. 6.2a) and the frequency stirring method (Fig. 6.2b). Both methods aim to create a large ‘combined’ RC through the hybridization of many smaller ‘unit’ reservoirs. Fig. 6.2a and b show snapshots of the electric field  $E_z$  landscape from time-domain simulations. Small variations of system boundary condition, as well as the stimulating wavelengths, are implemented by translating a metallic cylindrical perturber, and stretching or shrinking the duration of the input pulse, respectively. Based on the intrinsic chaoticity, the application

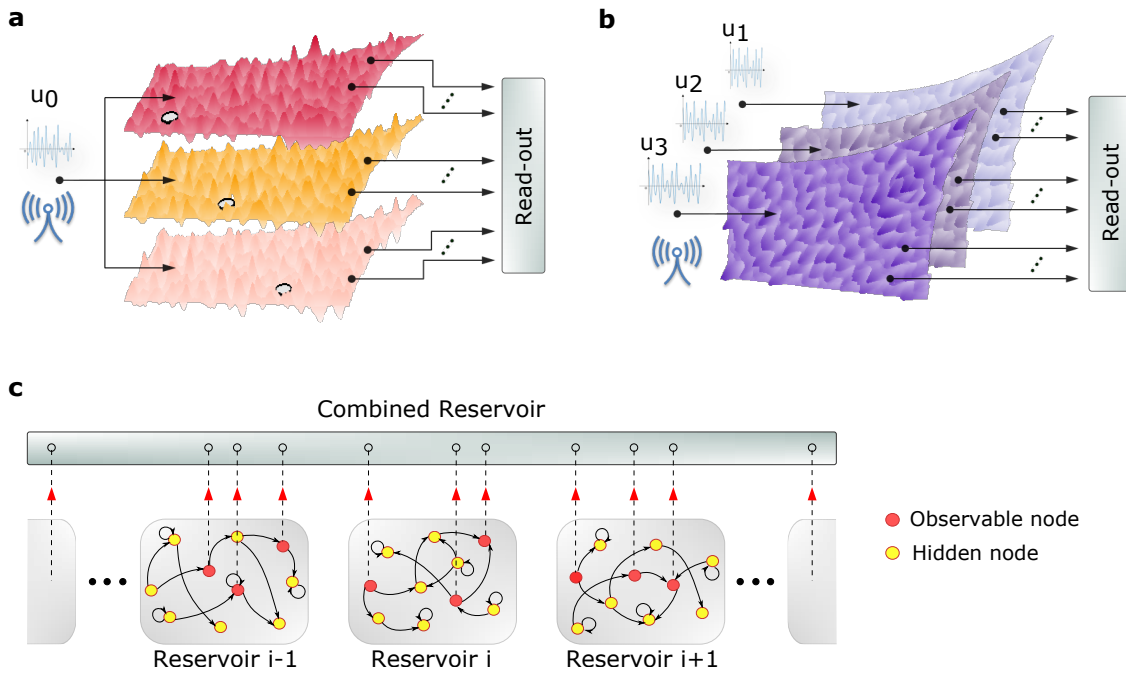


Figure 6.2: **Reservoir Expansion Techniques (RETs)**. **a** and **b** show the schematics of the boundary condition perturbation method and the frequency-stirring method, respectively. The first method may be realized by the translation of a metallic perturber shown as the cylindrical rod. Under the same input waveform  $u_0$ , uniquely different evolutions of the EM fields inside the enclosure area are created by means of translating the perturber to new locations. In **b**, the frequency stirring technique utilizes small changes of center frequency of a given input waveform to create new wave field configurations. In the experiment, the input wavelet is stretched/shrunk ( $u_1 \sim u_3$ ) in order to shift the center frequency. **c**, Schematics of the RET concept. The combined reservoir consists of the observable nodes from various single realizations of reservoirs.

of RETs results in a drastically different wave response, which is illustrated by the  $E_z$  patterns (Fig. 6.2). New unit reservoirs each having distinct temporal dynamics are thus created. Although a unit reservoir dimension might be limited in practice, its complex dynamics are ensured by the high-dimensional continuum EM reservoir ‘substrate’. As illustrated in Fig. 6.2c, each unit continuum reservoir can be seen as a large reservoir layer with many hidden nodes, and the port signals are just the observable nodes which are sampled at discrete locations. Based on RETs, we have realized high-dimensional combined RCs and demonstrated various tasks using a single chaotic enclosure with only three measurement channels.

### 6.4.3 Experimental Set-up

The shape of the billiard is similar to a quarter of a bow-tie with an area of  $A = 0.115m^2$  [37, 123]. The characteristic length of the billiard is of  $A^{0.5} \sim 35cm$  and thus is electrically large compared to the operating wavelength ( $\sim 5cm$ ). With a height of  $d = 0.79cm$ , the billiard is considered to be quasi-2D because the electric field is polarized in the z-direction for  $f < c/(2d) = 18.9GHz$ . The inputs are converted from a digital time series to analog waveforms and then broadcasted by a high speed AWG (Tektronix 70000A) with a sampling rate of 50 Gs/s. For a typical RC input waveform (i.e., the Rossler observer task), we set the center frequency at  $f_c \sim 4GHz$  so that the corresponding oscillation period is  $\sim 0.25$  ns. The BW of this Rossler observer task input waveform is about 100 MHz where  $\sim 3$  resonator eigenmodes exist. We set the system loss parameter at a range of  $\alpha \sim 50$ , meaning that about 50 modes can be excited within

one mode's 3dB BW. Thus we estimate that there are at most 150 modes excited in the Rossler observer task. The input waveform is amplified by the RF-Lambda 2-18GHz amplifier (RFLUPA0218G5). The output ports consist of SMA dipole antennas with high switching speed diodes (Infineon BAS7004) connected between the center pin and the billiard top plate (Fig. 6.1c) [123]. The voltage signals are measured with an oscilloscope (Agilent DSO91304A) with a sampling rate of 40Gs/s. Ensembles of new uncorrelated reservoirs are created by translating a metallic perturber (a 1.5cm radius, 0.75cm high circular cylinder) and/or changing the signal carrier frequency from the AWG [27, 124]. For an input waveform centered at  $f_0 = 4GHz$ , we translate the perturber by 1cm ( $\sim 0.2\lambda_0$ ) or shift the  $f_0$  by  $\Delta f = 100MHz$  ( $\sim 3$  resonator eigenmodes) to create a new reservoir. The scaling of  $f_0$  is equivalent to the stretching and shrinking of the enclosure volume. Microwave absorbers are employed inside the billiard to alter the fading memory of the system. For tasks running at  $\sim GHz$  rates, the system decay time is in the  $\sim ns$  range which is common in most real-life settings [25].

#### 6.4.4 Benchmark Test Results

Fig. 6.3 illustrates the computing ability and the effect of varying system parameters of the wave chaotic RC. The observer task for the 3-component Rössler chaotic attractor (Fig. 6.3a-d) and the NARMA10 task (Fig. 6.3c and d) are executed with the wave chaotic RC. See detailed information in Appendix F. For the observer task, the RC is expected to produce continuous predictions for all of the variables of a complex dynamical system (in our case, the Rössler y and z component) based only on input from a subset of the

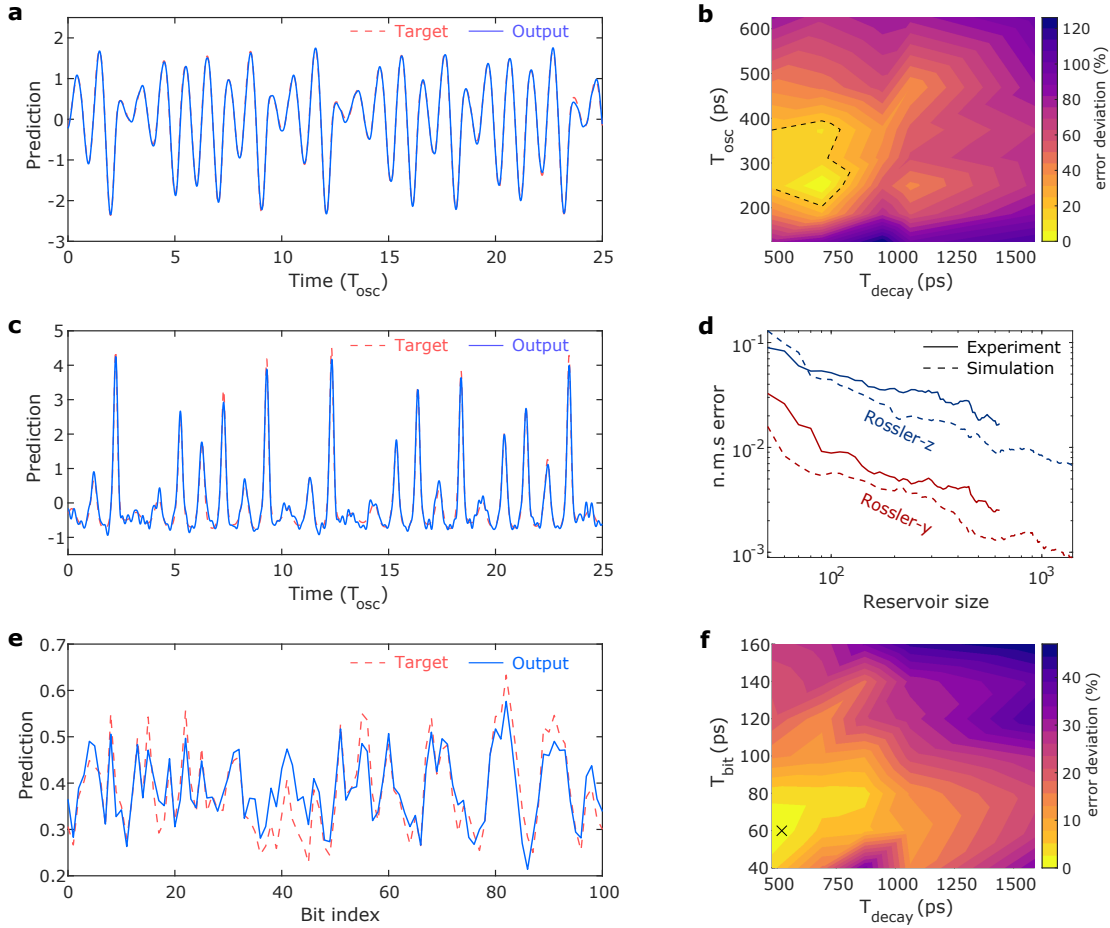


Figure 6.3: **Benchmark tests and the RC performance map on system parameters.** **a** and **c**, Rössler observer task testing set performance (blue) from a combined RC of 630 nodes. The true states are shown as red dashed lines in **a**, **c** and **e**. **b**, The deviation of normalized mean square error for the Rössler observer task: contour as a function of the input duration  $T_{osc}$  and the system decay time  $T_{decay}$ . The dashed boundary outlines the optimal parameter island (error deviation  $< 20\%$ ) from where the combined 630-node RC is built. **e**, NARMA10 task testing set performance at the optimal system parameters from a 90-node RC, shown as the cross in **f**. **f**, The deviation of normalized mean square error for the NARMA10 task.

system (Rössler  $x$  component). Like other ML methods, this prediction task is carried out without knowledge of the equations of motion of the Rössler system, but using only a finite amount of data of all three components for training. The performance of the RC prediction  $s^* = (x, y, z)$  is evaluated with the normalized mean square defined as  $\text{NMSE} = \sum_n [s^*(n) - s(n)]^2 / \sum_n s(n)^2$ , where  $s$  is the target and  $n$  is the index of the testing set data. With RET, a high-dimensional reservoir of 630 nodes is created and this RC achieved an  $\text{NMSE} = (0.002, 0.017)$  for predictions of the Rössler  $y$  and  $z$  components, respectively. We visualize the high accuracy of the RC prediction by directly comparing the testing set output to the target, shown as the blue and red curves in Fig. 6.3a and c, respectively. As shown in Fig. 6.3a, the predicted Rössler  $y$  component is practically overlapped with the target. The predicted Rössler  $z$  component covers the target curve faithfully, where deviations only appear systematically at low-amplitude points due to noise. For the NARMA10 task, the input stream is a random series drawn from the interval  $[0, 0.5]$ , and the goal is to infer a computed series based on the random input bits run through a specific nonlinear, 10-state memory equation (Appendix F). The successful execution of the NARMA10 poses a demanding requirement of both long-short term memories in the ML system. With optimal system parameters (cross in Fig. 6.3f), a wave chaotic RC with 90 nodes has achieved a record-setting performance of  $\text{NMSE} = 0.034$  which is  $\sim 5$  times lower than reported hardware RCs [87]. Thus the complex memory capacity of the wave chaotic RC is fully demonstrated.

Despite the phenomenal empirical successes of ML in many applications, its system parameters and underlying mathematical mechanisms remain poorly understood. In contrast, the governing parameters of the wave chaotic RC present a clear real-world physical

meaning: the input oscillation period  $T_{osc}$  (or bit duration  $T_{bit}$ ) controls the RC input speed, and the exponential decay time  $T_{decay}$  of the reservoir dynamics determines the fading-memory of the reservoir. The overall RC performance is thus a function of both time-scales. As shown in Fig. 6.3b, the optimal reservoirs lie near the domain where  $T_{decay} \sim 2.5T_{osc}$ , which indicates a fading-memory of  $\sim 2.5$  recent periods is preferred for the Rössler observer task. For the NARMA10 tests, the optimized performance island arises when  $T_{decay} \sim 9T_{bit}$  (Fig. 6.3f). This empirical observation agrees nicely with the setup of the NARMA10 task where each output bit is determined by its 10 previous inputs. For the Rössler observer task, a high-quality combined RC of 630 nodes is built from the unit reservoir on the optimized island (the dashed area in Fig. 6.3b). As shown in Fig. 6.3d, the RC performance has enjoyed a substantial boost with the application of RET, and will show further improvement through building a higher dimensional combined RC, as demonstrated by the numerical tests.

Compared with the flexibility of electronic systems, neuromorphic photonics have not yet developed into general-purpose applications [104]. Among different approaches, the RC-inspired system enjoys a high task-flexibility benefited from its efficient training procedure. Here we demonstrate the versatility of the wave chaotic RC by executing benchmark tests with distinctly different goals utilizing just one physical device, namely the nonlinear function simulator task, the Hénon-map observer task, and the nonlinear channel equalizer (NCE) task. As shown in Fig. 6.4a, the wave chaotic RC, serving as an edge device, may switch between different tasks with a simple change of the output coupling matrix. The wave chaotic RC is also able to incorporate with a wide range of input speed. In the experiment, we have employed a  $T_{osc} \sim 200ps$  for the function

simulator task and  $T_{bit} \sim 80ps$  for the Hénon-map observer task and NCE tasks. All three tasks are successfully executed with high accuracy, shown by the overlapping RC output and the target curves in Fig. 6.4b-d.

Besides experimental tests, we have also conducted numerical simulations of the physical RC with the same shape billiard, identical degree of system loss, and realistic model of the diodes (Appendix F). As shown in Figs. 6.3d and 6.4e-g, all of our experimental cases are faithfully simulated with EM simulation numerical tools. The accurate simulation capability of wave chaotic RC greatly benefits future RC optimization and follow-up studies.

### 6.4.5 Discussions and Summary

As discussed earlier, the scale and the operation speed are the major measures of the capability for both software and hardware ML. In practice, finding the ideal balance between the two factors has been the center of the field of hardware RC, but current realizations tend to focus only on one factor. Benefiting from the underlying ray chaos of our wave system, we are able to construct an arbitrarily high-dimensional reservoir with just one physical device. In the meantime, high-throughput computation is promised by the autonomous evolution of the EM wave reservoir at the speed of light. Utilizing only modest measurement resources (3 measuring channels), we introduce RETs and create a large combined RC with over 600 nodes (Fig. 6.3d). The application of RETs would introduce extra system operation time. However, the operation time can be linearly scaled down by using higher frequency inputs, as well as enlarging the number of measurement

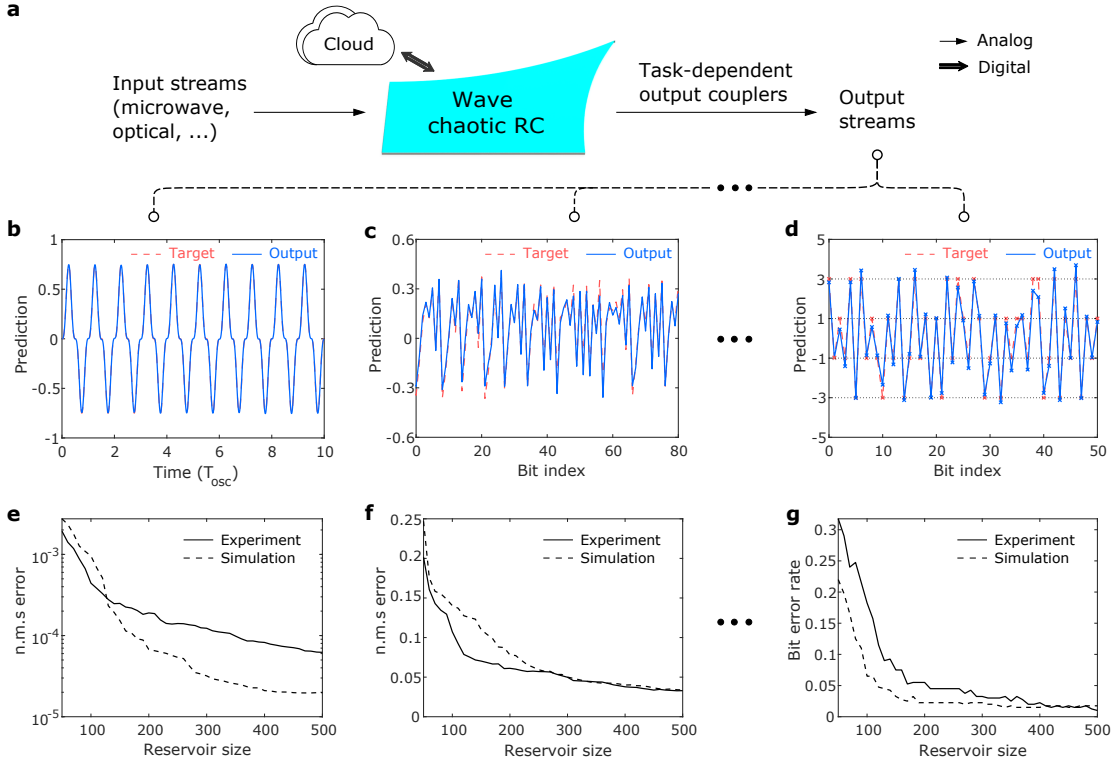


Figure 6.4: **Experimental demonstration of the task-versatility.** **a** illustrates that a single wave chaotic RC is able to execute different tasks with a simple switch of output couplers, and thus serves as an ideal platform an edge device. The RC performances (blue) for the function simulator, Hénon-map observer, and the nonlinear channel equalizer tasks are shown in **b-d**, respectively. The targets are shown as red dashed lines in **b-d**. In **e-g**, we show the simulated (dashed) and experimental (solid) RC performance as a function of the dimension of the reservoir.

channels (see Appendix F). Under current experimental conditions, the combined wave chaotic RC of 500 nodes performs on the order of  $10^{14}$  OPS (operations per second) which is close to the state-of-art supercomputers ( $10^{15}$  to  $10^{17}$  OPS) [122]. The concept of RC can be realized in photonic crystal cavity systems and operate at optical frequencies [98, 120]. With an all-optical realization, the RC operation speed will enjoy a further enhancement by changing the carrier frequency from from  $\sim 1$  GHz to  $\sim 10^3$  THz. Both RETs can be executed in an all-electronic manner: the boundary condition perturbation may be implemented with reconfigurable metasurfaces [116], and one can shift the input waveform center frequency  $f_c$  with AWG Sequencing which allows the fast switching between different input waveforms.

Since our method applies for any reverberant environment for EM waves, the wave chaotic RC may be realized in a broad range of wavelengths, spanning from WiFi waves in real-life indoor environments [25] to on-chip nanophotonic chaotic cavities [114]. By scaling up to the THz range, the wave chaotic RC will reach a much faster processing speed with a highly compact device (Sup. Mat.). With state-of-art high speed cameras [118], the number of observable nodes will also increase substantially by probing the entire EM reservoir. Our RC paradigm can also be applied to other Random Plane Wave systems such as multi-mode fibers.

Compared to existing hardware RCs, our chaotic RC shows a better robustness against structural defects. The Random Plane Wave hypothesis further ensures that the RC performance remains stable despite the specific location of the ports. The wave chaotic RC also has an edge due to its high energy efficiency because the system is entirely passive and the establishment of the reservoir layer is created by the EM radiation. All

of these characters are of great importance for practical utilities, such as edge computing applications. Fig. 6.4 shows that a single wave chaotic RC can process different types of tasks with a simple swap of output coupling matrix. As shown in Fig. 6.4a, the wave chaotic RC, serving as an edge device, will carry out the in-situ data analysis and transfer only the useful information back to the cloud. Because the device operates fully with light, a wave chaotic RC combining with online output couplers allows high-throughput analysis of raw inputs directly taken from various sensors. As an example, we have demonstrated a 99.95% accuracy on the NCE task (Fig. 6.4d,g), which is a paradigm for telecommunication applications. A stand-alone wave chaotic RC is also well-suited for IoT applications, such as the on-site image classification and RF radar analysis for Smart Cars. Its high-throughput computation is especially advantageous for applications which demands fast and robust data analysis, for example the autonomous cars.

We note that the optimal ridge parameter region ( $T_{osc} \in [200, 500]ps$ ) in the Fig. 6.3b contour does not extend to the lower and higher ends of  $T_{osc}$ . The values of  $T_{osc}$  cannot be arbitrarily low considering the fundamental (lowest) frequency of the EM enclosure ( $\sim 700$  MHz). The higher end of  $T_{osc}$  is constrained by the practical limitation of our equipment sampling rate. One is able to increase the mode density by letting the RC operate at a higher speed. For example, the same bowtie billiard will host around 100 modes inside a 100 MHz bandwidth at 10 GHz. Utilizing an AWG with a higher sampling rate, we should be able to increase the speed of the RC. The wave chaotic RC also faces common practical limitations in nonlinear effects since the microwave diode requires a sufficiently high field amplitude to display nonlinear properties [88, 123]. The existence of noise, arising from the background noise or the limited analog-to-digital conversion

resolution, would also dampen the RC performance [78, 95]. We also note that the analogue photonic systems are hard to compute with electronic devices in terms of high-precision computation, but AI applications usually function nicely with low-precision operation [104]. The efficacy of the output coupler may degrade as the RC scattering properties lose fidelity over time. However, one can re-calibrate for the performance drift with a simple update of the output coupling matrix because the training of the RC is fast.

We have experimentally demonstrated a new physical platform for neuromorphic computation utilizing the chaotic dynamics of waves, and found good agreement between experiments and simulations. The computational power of the wave chaotic RC is clearly presented by the successful execution of numerous benchmark tests, and the RC performance is controlled by clearly defined and controllable physical properties. We present elegant solutions to create a high-dimensional reservoir with minimal hardware requirements, a substantial challenge for the field of NC. With all its unique qualities, we believe that the wave chaotic RC will secure its place in future applications.

## Chapter 7: Chaotic 1D Graphs with Photonic Crystal Waveguides

This work was a collaborative effort with the Maryland Wave Chaos group and the preprint can be found in Ref. [125]. The statistical properties of wave chaotic systems of varying dimensionalities and realizations have been studied extensively. These systems are commonly characterized by the statistics of the short-range and long-range eigenmode-spacing, and the one-point and two-point eigenfunction correlations. Here, we propose photonic crystal (PC) defect waveguide graphs as a new physical setting for chaotic graph studies. Photonic crystal graphs have two novel features, namely an unusual dispersion relation for the propagating modes, and complex scattering properties of the junctions and bends. Compared to traditional microwave cable graph systems, the PC-graph bond lengths and node scattering properties are more easily modified. Moreover, the electromagnetic fields in the entire graph, including both bonds and nodes, can be more easily measured and analyzed in both experiments and numerical simulations. Here we present numerically determined statistical properties of an ensemble of such PC-graphs including both eigenfunction amplitude and eigenmode-spacing studies. Our proposed system is compatible with silicon nanophotonic technology and opens chaotic graph studies to a new community of researchers.

## 7.1 Introduction of PC Defect Waveguide

Wave-chaotic phenomena have been studied in various systems, ranging from 1D graphs [117, 126, 127, 128, 129], 2D billiards [14, 37, 130, 131, 132, 133, 134] to 3D enclosures [16, 58, 60, 66, 70, 116]. The statistical properties of many system quantities, such as the closed system eigenvalues and the open system scattering/impedance matrices, exhibit universal characteristics, which only depend on general symmetries (e.g., time-reversal, symplectic) and the degree of system loss. Random Matrix Theory (RMT) has enjoyed great success in describing the energy level spacing statistics of large nuclei [10, 135]. The statistics of complex systems that show time-reversal invariance (TRI) are described by the Gaussian orthogonal ensemble (GOE) of random matrices, the statistics of systems showing broken time-reversal invariance are described by the Gaussian unitary ensemble (GUE), and the statistics of systems with TRI and antiunitary symmetry show Gaussian symplectic ensemble (GSE) statistics [16, 18, 37]. It was later conjectured by Bohigas, Giannoni, and Schmit that any system with chaotic dynamics in the classical limit will also have wave properties whose statistics are governed by RMT associated with one of these three ensembles [11]. In practice, identifying RMT statistical properties in experimental data is difficult due to the presence of non-universal features that obscure the universal fluctuations. The Random Coupling Model (RCM) has found great success in characterizing the statistical properties of a variety of experimental systems by removing the non-universal effects induced by port coupling and short-orbit effects [16, 27, 29, 30, 34, 37, 58, 60, 66, 123, 136].

Chaotic microwave graphs support complex scattering phenomena despite their

relatively simple structure [117, 126, 127, 128, 129]. A microwave graph structure can be realized with coaxial cables as graph bonds connected at Tee-junctions. The graph architecture allows for various useful circuit components (such as phase shifters and attenuators) to be incorporated into the structure [117, 128, 129]. Recent studies show that non-universal statistical features exist in chaotic graph systems, and these are hypothesized to be caused by the non-zero reflection at the graph vertices. These reflections create trapped modes that pollute the spectral statistics of the graph [129, 137, 138, 139]. However, the experimental investigation of such phenomena is complicated by the fact that information about the waves is accessible only at the nodes in cable graph systems, which are the common choice for conducting graph experiments.

Here, we introduce an alternative type of chaotic graph built with photonic crystal (PC) systems. Photonic crystals find extensive use in semiconductor-based nanophotonic technology, where they act as low-loss waveguides for visible and infrared light [140]. The PC graph bonds are realized with defect waveguides and the nodes are formed by the waveguide junctions. As TRI is preserved and spin-1/2 behavior is absent, chaotic PC-graph systems are expected to fall into the GOE universality class of RMT. With numerical simulation tools, we conduct a series of statistical tests of the chaotic photonic crystal graph system including both eigenvalue and eigenfunction studies of closed graphs. The advantages of using PC structures for quantum chaos studies are as follows. Compared to other experimental graph systems (i.e., coaxial cables), one may probe the fields propagating in PC waveguide graphs bonds easily. In addition, the bond lengths of PC-graphs can also be altered by means of lithographic fabrication [140]. Secondly, the scattering properties of PC-graph nodes can be engineered by changing the rod properties and geometry.

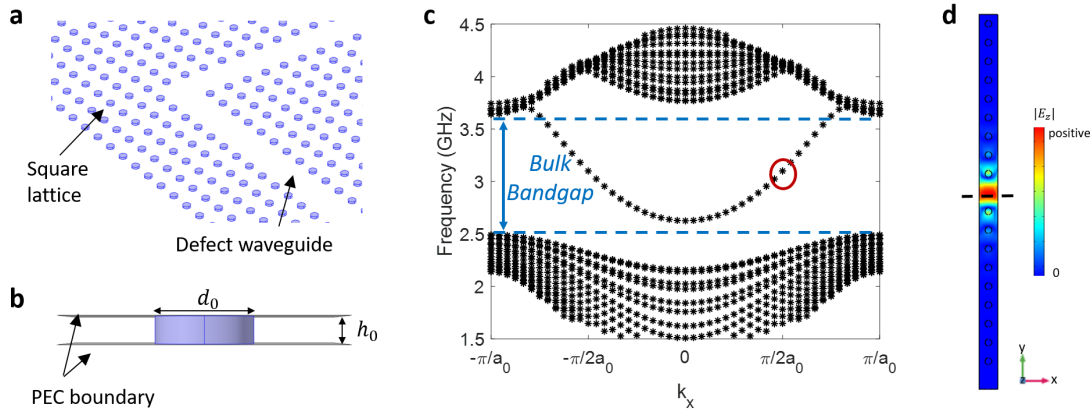


Figure 7.1: **a.** The open-plate view of the photonic crystal lattice with an L-shaped defect waveguide region. **b.** The side view of the PC unit cell. A dielectric rod is sandwiched between two PEC (perfect electric conductor) surfaces. The quantities  $h_0$  and  $d_0$  are the height and diameter of the rod. **c.** The photonic band structure from a supercell defect waveguide simulation. The waveguide modes appear in the bulk bandgap region (delineated by the blue dashed lines). **d.** The E-field profile of one of the waveguide mode solutions (the red circle in **c**). The black dashed line marks the center of the waveguide.

Moreover, PC waveguides and cavities are technologies that are widely used in the field of integrated nanophotonics. To our knowledge, PC graphs have not been previously utilized for quantum graph studies.

The paper is organized as follows. In Section II, we introduce the design details of the proposed PC graph structure as well as its numerical implementation methods. We present the chaotic closed-graph mode-spacing study in section III, and focus on the discussion of closed-graph eigenfunction studies in section IV. Different methods of conducting eigenfunction statistical studies are also discussed. We summarize the paper and discuss the future applications of the proposed PC graphs in section V.

## 7.2 Photonic Crystal Graph

A photonic crystal system consists of a regular lattice of artificial atoms (or scatterers) whose spacing is comparable to the operating wavelength [141, 142]. The material properties and the geometrical details of the atoms are carefully designed in order to achieve a specific functionality. A PC system is usually constructed as a 2D planar structure, which makes it especially good for lithographic fabrication and photonics applications. Importantly, a 2D PC can show a complete bulk bandgap in its electromagnetic excitation spectrum [141, 142]. In PC-based devices, waveguides and cavities can be constructed for example by making air defects (removing a certain number of the atoms) in the original lattice. This creates guided propagating modes in the bulk bandgap, which ensures that the modes are confined to the defect region. A variety of defect waveguides can be realized by changing the atom properties [141]. Recent photonic topological insulator (PTI) studies present an alternative form of PC waveguide using the interface between two different topological domains [3, 143, 144, 145, 146]. Such PTI-based waveguides can also be utilized as the bonds for realizing graphs. The interesting properties of the topologically protected modes may further enhance the quantum graph studies. Here, we will utilize the defect waveguide modes to build chaotic graph structures. Note that these PC defect waveguide graphs are distinctly different from photonic crystal slabs and billiards [134, 147, 148], and from coupled resonant dielectric cylinders [128, 149] studied previously.

The construction of the chaotic PC graph starts by building a square lattice with identical dielectric rods (the blue lattice in Fig. 7.1(a)). The lattice constant is  $a_0 =$

36.8mm. The dielectric rod lattice is located between two metallic surfaces and installed in a vacuum background. The defect waveguide is created by simply removing one row or column of the dielectric rods. The detailed shape of the dielectric rod is shown in Fig. 7.1(b). The diameter of the dielectric rod is  $d_0 = 13.2mm$  and the height is  $h_0 = 0.1a_0 = 3.68mm$ . Because the PC lattice is thin in the vertical direction ( $z$ -direction), the waveguide modes considered here are transverse magnetic (TM) polarized ( $E_z \neq 0$ ,  $E_{x,y} = 0$ ,  $H_z = 0$  and  $H_{x,y} \neq 0$ ). The relative permittivity and permeability of the dielectric rods are  $\epsilon_r = 11.56$  and  $\mu_r = 1$ . We realize the proposed PC structure numerically with COMSOL Multiphysics Software. The presence of the waveguide mode is clearly demonstrated by the supercell photonic band structure (PBS) simulation (Fig. 7.1(c)). The supercell simulation model consists of a single column of PC lattice with Floquet periodic boundaries on the two long sides. That is, fields on opposite long sides differ by a phase factor  $\theta = k_x a_0$ . The two short-end surfaces are assigned totally absorbing boundary conditions. We remove the center rod to create the defect waveguide region. The PBS simulation is conducted by computing the system eigenmodes while varying the wavenumber  $k_x$  in the range  $[-\pi/a_0, \pi/a_0]$ . As shown in Fig. 7.1(c), the defect waveguide modes have emerged inside of the bulk bandgap region from 2.5 ~ 3.6GHz. Here we see the first unique feature of PC graphs – the PC waveguide modes present a more complicated dispersion relationship between  $\omega$  and  $k_x$  (e.g., modes near 2.6GHz in Fig. 7.1(c)) as compared with coaxial cable ( $\omega = ck_x$ ). In Fig. 7.1(d), the  $|E_z|$  profile of the entire simulation domain shows clearly that the mode solution is indeed a guided wave because its amplitude is highly localized in the defect region.

Besides graph bonds, it is also important to characterize the scattering properties

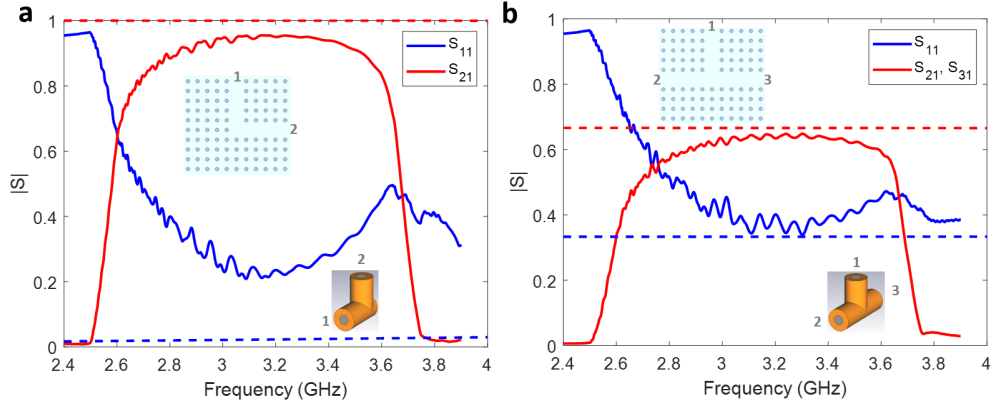


Figure 7.2: **a.** The simulated S-parameters of the PC-graph right-angle junction (solid), as well as the S-parameter from a  $3.5\text{mm}$  uniform coaxial cable 2-port right-angle connector (dashed), which serves as a reference. Inset: the schematics of the PC right-angle junction and the 2-port coaxial cable junction. **b.** The simulated S-parameters of the PC-graph T-junction (solid) and the S-parameters from a coaxial cable 3-port ‘tee’ connector (dashed). Inset: the schematics of the PC T-junction and the 3-port coaxial cable junction. All PC-junction S-parameters are frequency averaged with a 500MHz window to remove the effect of spurious reflections.

of graph nodes [150]. The PC graph structure is realized by connecting multiple straight defect waveguides with both right-angle and T-shaped junctions. We have characterized the scattering matrix of both types of the junctions with COMSOL and CST Microwave STUDIO. For the right-angle junctions, non-zero transmission is found only in the bulk bandgap region. As shown in Fig. 7.2(a), The transmission values ( $S_{21}$ ) vary systematically near but below 1 as a function of frequency, which qualifies the right-angle bends as vertices with a non-trivial scattering matrix in a graph. The PC-graph T-junction presents a complex scattering profile over the entire bandgap region. As shown in Fig. 7.2(b), the magnitude of the reflection (transmission) coefficient deviates systematically from  $1/3$  ( $2/3$ ) as a function of frequency. The scattering properties of coaxial cable right-angle bends and tee-junctions are shown as red and blue dashed lines in Fig. 7.2, and they show virtually no variation over the bandgap. These nontrivial junction scattering parameters

are a second unique feature of PC graphs, and can be expected to influence the properties of the graph eigenmodes. We note that alternative methods of making waveguide bends, or connecting waveguides, can be applied, for example by removing or adding dielectric rods at the right-angle turn, in order to tune the transmission property of the waveguide joints [151]. The engineering of the node reflection and transmission properties is beyond the scope of this paper.

We simulate the closed PC graphs with the COMSOL eigenvalue solver. The graph topology is that of a flattened tetrahedral graph having 14 straight segments and 13 junctions (including both 3-way junctions and right-angle junctions). The four exterior faces of the parallel-plate PC structure (see Fig. 7.3(a)) are assigned totally absorbing boundary conditions. The total length of the simulated graph is on the scale of  $\sim 9m$ , which hosts about 80 eigenmodes (within the bulk PC bandgap) in a typical realization. We note that one is able to decrease the mode-spacing by enlarging the size of the PC graph, and we choose the current system scale due to limited computational power. One can create a statistical ensemble of chaotic PC graphs by changing the length of the bonds for a given graph topology.

The E-field profile for a particular eigenmode solution of a graph (shown in Fig. 7.3(a)) is shown in Fig. 7.3(b). It is clear that the graph mode is localized to the defect waveguide region and displays a longitudinal sinusoidal standing wave pattern. The mode amplitude on a single bond is uniform but varies between different bonds (shown by the color differences), where bonds are defined as straight waveguide regions between 3-way junctions and right-angle bends.

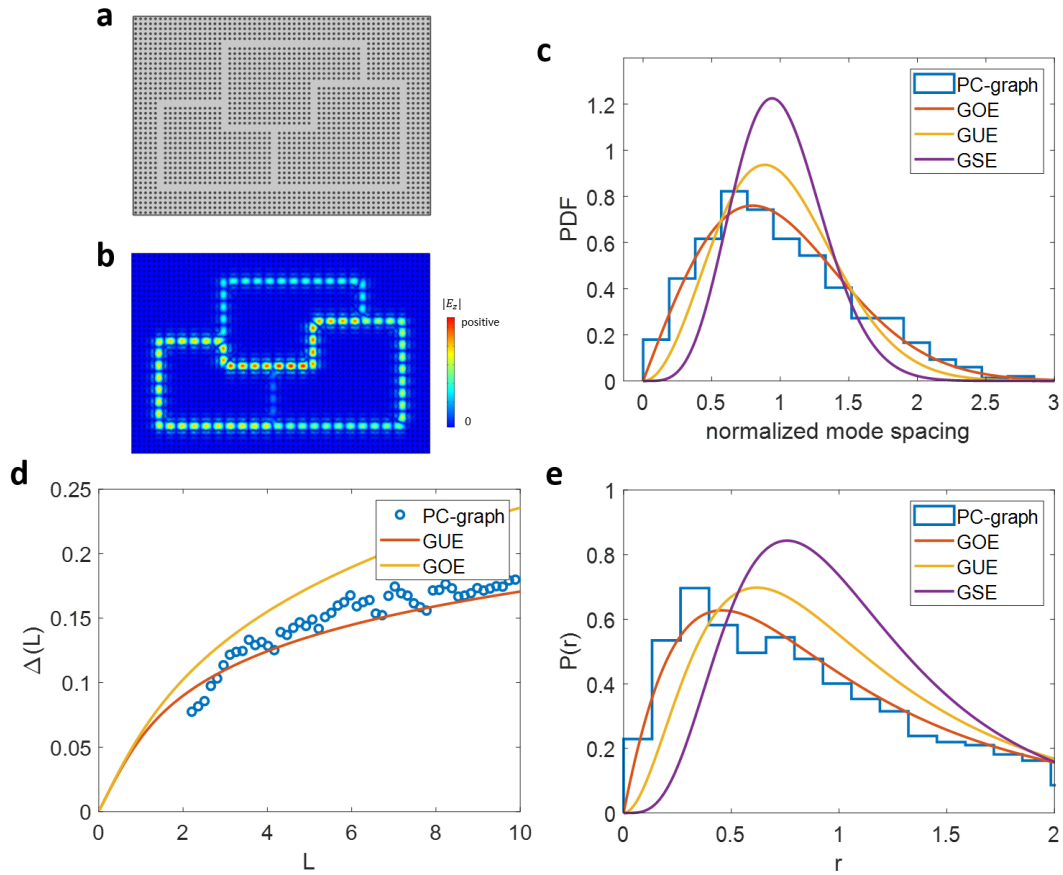


Figure 7.3: **a.** Schematic diagram of the PC waveguide graph system. The graph bonds are shown as the clear gray channels and the rectangular lattice is shown as a lattice of dielectric rods (black circles). **b.** The simulated  $|E_z|$  profile of the graph system eigenmode at 2.8GHz. **c** shows the statistics of the normalized mode spacing from graph simulation (histogram). The theoretical predictions for the GOE, GUE and GSE systems are shown in red, yellow and purple curves. **d** shows the spectral rigidity  $\Delta(L)$  of the normalized spectrum from graph simulation (blue circles). The theoretical predictions for the GOE and GUE systems are shown in red and yellow curves. **e** shows the statistics of the consecutive mode spacing ratio  $r$  (histogram) and the theoretical predictions for the GOE, GUE and GSE systems.

### 7.3 Eigenmode Spacing Statistical Analysis

We start by conducting the nearest neighbor mode spacing analysis of the proposed PC graphs. An ensemble of 10 different graph realizations are studied numerically and we obtained  $\sim 800$  eigenfrequency values from the ensemble. The graph topology ranges from 13  $\sim$  16 straight segments and 11  $\sim$  14 junctions. We note that this ensemble of graphs is conducted with the eigenvalue simulation in COMSOL. The simulation results are used for mode-spacing studies here, as well as the eigenfunction statistics in Sec. IV. The graph topology is kept fixed in the eigenfunction studies discussed below. Because the topology and the total length  $L_{tot}$  of each graph realization is different, we normalized the system eigenmodes solutions using the following method. We considered 10 different graphs. For each graph we calculated eigenfrequencies in the range 2.8 GHz to 3.6 GHz and placed the eigenfrequencies in ascending order. The eigenfrequencies were then converted to eigen-wavenumbers ( $k_i$ ,  $i$  is the mode index) using the dispersion relation for the PC-waveguide PBS shown in Fig. 7.1(c). This results in a tabulation of consecutive wave-numbers. We then fit the mode-number index to the wave-number using a quadratic fitting function  $n(k) = c_1 k^2 + c_2 k + c_3$ , where  $c_{1,2,3}$  are fitting parameters and  $n(k)$  is the total number of modes below  $k$  [41]. For a typical graph we found  $c_1 = 0.0054$ ,  $c_2 = 2.21$  and  $c_3 = -55.28$ . The small value of  $c_1$  indicates the  $n(k)$  is nearly linear in  $k$  as expected for chaotic graphs. We then evaluate the fitting functions at the calculated  $k$ -values for each graph, creating a list of normalized eigenvalues  $e_i = n_{fit}(k_i)$ . The nearest neighbor spacings are finally computed as  $s_i = e_{i+1} - e_i$ .

The distribution of the normalized mode spacing values of the entire ensemble is

shown as the histogram in Fig. 7.3(c). We have also included the approximate theoretical predictions of the mode-spacing statistics for the GOE, GUE, and GSE in the figure. The three theoretical predictions are based on RMT [39, 152, 153], which is widely studied as a seminal method of understanding the universal statistical properties of wave-chaotic systems [11, 154]. As shown in Fig. 7.3(c), the distribution of the normalized mode-spacing matches reasonably well with the theoretical prediction for the GOE universality class. Good agreement between the graph nearest neighbor mode-spacing statistics and the RMT theoretical prediction is also reported in various works on graphs, although long-range statistical quantities tend to show non-universal behavior due to the trapped-mode issue mentioned above [129, 137, 138, 139].

To test the long-range statistical properties of the eigenmodes, we compute the spectral rigidity of the graph spectrum  $\Delta(L)$ , where  $L$  is the length of a segment in the normalized spectrum. Detailed discussion of the  $\Delta(L)$  computation and theoretical predictions can be found in Refs. [135, 137, 138, 139]. Previous studies find that the long-range statistics of quantum graphs usually shows some degree of agreement with the GOE prediction in the range of roughly  $L \in [2, 5]$  [126, 137, 138]. The quantity  $\Delta(e, L)$  is the least square deviation of  $n(e)$  from its best line fit inside the range  $[e, e + L]$ . Using the spectrum from one graph realization, one can compute the  $\Delta(L)$  by averaging over the  $\Delta(e, L)$  computed with non-overlapping segments of spectrum. Finally an ensemble averaging process is conducted with the  $\Delta(L)$  data computed from all 10 graph realizations. As shown in Fig. 7.3(d), the PC-graph spectrum actually shows a better agreement with the GUE theory curve. Because the operating bandwidth of the proposed PC-graph system is relatively narrow (Fig. 7.1 (c)), we believe the long-range statistics are corrupted

	PC-Graph	Random Order	GOE	GUE	GSE
$\langle r \rangle$	1.89	1.57	1.75	1.37	1.18
$\langle \tilde{r} \rangle$	0.51	0.56	0.54	0.60	0.68

Table 7.1: The summarized consecutive mode spacing ratios of the photonic crystal graph (PC-Graph) system, the graph system with random ratio order, and the theoretical predictions for the GOE, GUE and GSE systems [1].

by finite-size effects, unless the graph size is increased substantially.

In addition to the mode-spacing distribution test, we note that the method of consecutive mode spacing ratios  $r_i = \frac{s_i}{s_{i-1}}$  and  $\tilde{r}_i = \min\left(r_i, \frac{1}{r_i}\right)$  can also be adopted [1]. This type of statistical study does not require unfolding the spectrum. For the PC graphs, the averaged values of  $\langle r \rangle = 1.89$  and  $\langle \tilde{r} \rangle = 0.51$ , are closer to the GOE theoretical predictions than the GUE and GSE predictions (Table. 7.1). We note that the high value of  $\langle r \rangle$  in the PC-graph is related to the correlation between consecutive level-spacings. To eliminate the correlation, we have randomized the order of original consecutive level spacings and then computed the level spacing ratio values. The averaged values of the 1000 random draws for the ratio are included in the Random Order column in Table. 7.1. We further present the distribution of mode-spacing ratios  $r$  of the PC graphs and corresponding theoretical predictions of the GOE, GUE and GSE systems in Fig. 7.3(e). The statistics of  $r$  match reasonably well with the GOE prediction.

## 7.4 Eigenfunction Analysis

We next study the statistics of the closed PC graph eigenfunctions. The eigenfunction statistics have been studied experimentally in 2D chaotic systems by probing the electromagnetic (EM) standing wave field inside a microwave cavity [2, 14, 155, 156, 157, 158]. In those

studies, the experimental probability amplitude distribution and two-point correlation function agree well with the random plane wave conjecture. Here, the wave properties of the entire closed PC graph (nodes and bonds) can be faithfully simulated. We employ the same eigenvalue simulation model used in the mode-spacing studies above. For a graph system, the telegrapher's equation is formally equivalent to the 1D Schrödinger equation, where the wavefunction  $\psi$  is represented by the wave voltage. For thin parallel plate waveguides, the wave voltage difference between the top and bottom metallic plates is represented by the  $E_z$  value at the middle cutting plane (at the height of  $z = h_0/2$ ). Because the PC graph bonds have a finite width, the bond eigenfunction will be evaluated along a 1D line at the center of the waveguide (shown as the black dashed line in Fig. 7.1(d)). We next examine two PC graph eigenfunction characterization methods.

*Method I: grid-wise representation.* For each eigenmode of each graph realization, we will use the entire set of the graph bond  $|E_z|^2$  vs. longitudinal position along the center-line of the waveguide data points to represent the eigenfunction. The name 'grid-wise' comes from the granular nature of this method, where the total number of eigenfunction data points is inversely proportional to the computational grid size. We study the wavefunction statistics of the PC graph by computing the distribution of the normalized probability density  $v$ , which is defined as the square of the eigenfunction values  $v_j = |\psi(r_j)|^2 = \frac{|E_z(r_j)|^2 \cdot L_{tot}}{\sum_j |E_z(r_j)|^2 \cdot \Delta L_j}$ , where  $L_{tot}$  is the total length of the graph,  $r_j$  and  $\Delta L_j$  are the location and the grid size of the  $j'$ th grid point,  $|E_z(r_j)|$  is the z-directed electric field magnitude at the  $j'$ th grid point, and the summation in the denominator runs over every graph grid point. In our simulation, the grid size  $\Delta L_j \sim 0.05\lambda_{op}$  where  $\lambda_{op} = 10cm$  is the operating wavelength at  $3GHz$ . The distribution of the probability density values is computed using

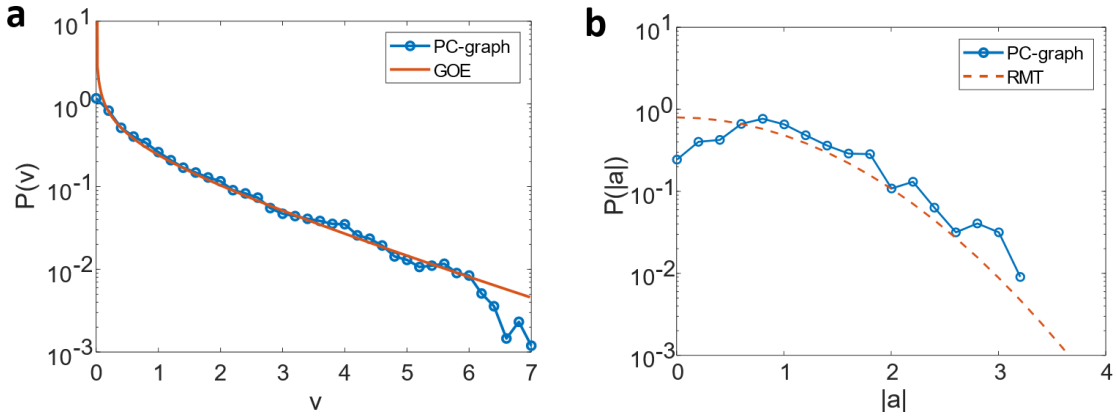


Figure 7.4: **a.** Probability amplitude distribution of photonic crystal defect waveguide graph eigenmodes values ( $v$ ) obtained from the grid-wise method (symbols connected by blue line). The theoretical prediction for systems with GOE statistics are in red. **b.** shows the statistics of the normalized bond amplitude value  $|a|$  (symbols connected by blue line) and the Gaussian distribution (red dashed).

the data from all simulated eigenmode solutions (48 to be specific) for a single realization of the graph, and the results are shown in Fig. 7.4(a), and discussed below.

*Method II: bond-value representation.* For each graph realization, the eigenfunction of a mode is represented by a set of ‘bond-values’  $E_z(b_m)$  which is defined as the amplitude of the standing-wave wavefunction on the graph bond  $b_m$ . The quantity  $m$  is the index of the bond and runs from 1 to 14. The standing wave on the bond is made up of two counter propagation waves  $\psi(x) = a_m e^{ikx} + a_m^* e^{-ikx}$ , where  $a_m$  is the wavefunction amplitude at bond  $b_m$  and  $x$  is the distance from a vertex along the bond. We first conduct a sine-fit of the raw  $E_z(x)$  values on each bond, which yields the amplitude, and the value of  $|a_m|$  is obtained as 1/2 of the amplitude value. The normalization process follows the same method as in Ref. [159] which ensures that  $\sum_m L(b_m)|a_m|^2 = L_{tot}$  where  $L(b_m)$  is the length of bond  $b_m$ . Here the distribution of the probability density values is computed over  $14 \times 78$  data points, where 14 is the number of the bonds and 78 is the number

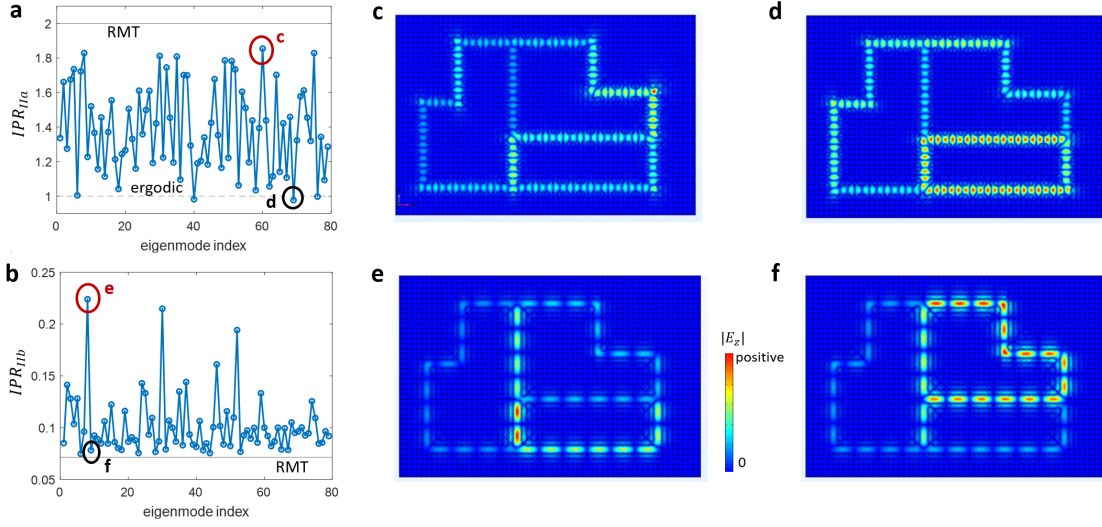


Figure 7.5: **a.** The inverse participation ratio (IPR) of graph eigenmodes obtained from the bond-value method, computed based on the method IIa. The simulated  $|E_z|$  profile of the red (black) circled mode in **a** is shown in **c** (**d**). **b.** The inverse participation ratio (IPR) of graph eigenmodes computed based on the method IIb. The simulated  $|E_z|$  profile of the red (black) circled mode in **b** is shown in **e** (**f**).

of eigenmode solutions from one realization of the graph, and the results for  $P(|a|)$  are shown in Fig. 7.4(b).

We first discuss the eigenfunction statistics obtained using the grid-wise method in Fig. 7.4(a). The theoretical prediction of the GOE systems, given by  $P(x) = \frac{1}{\sqrt{2\pi x}} e^{-x/2}$ , is shown as a solid red line. We find that the simulated PC graph result matches reasonably well with the GOE prediction. We notice that a mismatch between the graph data and the GOE prediction exists at the small and large probability density values. One possibility is that this method tends to over-count the appearance of medium-sized eigenfunction values (similar to the systematic errors experienced in Ref. [14]). It may also indicate that the data simply does not match the GOE prediction. In addition to the discrete eigenfunction imaging method, we note that the eigenfunction statistics may also be tested through resonance width distributions in transmission measurements (Porter-Thomas statistics)

[131, 160].

The random plane wave hypothesis underlying RMT eigenfunction treatments [39, 113] predicts that the complex coefficients  $a_m$  should have Gaussian random fluctuations [159, 161]. Here we use *Method II* to study the distribution of the normalized bond-values  $|a|$ , in Fig. 7.4(b), and find some degree of agreement with the random plane-wave prediction. However, a clear deviation from Gaussian statistics is seen for low amplitudes, similar to the deviation observed with *Method I*. Together, these results suggest that the wavefunction statistics of this simple graph are not fully consistent with the random plane wave hypothesis.

We next present the inverse participation ratio (IPR) computation based on the bond-value method (*Method II*) in Fig. 7.5. IPR is a measure of the degree of localization for a wave function [159, 161], and can be used to quantify the degree of deviation of wavefunction statistics from the random plane wave hypothesis. Based on its IPR value, the eigenfunction behavior varies between two limits, namely the maximum ergodic limit where the wave function occupies each graph bond with equal chance, and the maximum localization limit where the eigenmode is confined to only one bond. RMT predicts an IPR value by assuming Gaussian random fluctuation of the eigenfunctions. Two different IPR definitions are tested here. Method IIa follows the definition in Ref. [159], where the IPR value for each graph mode is evaluated using the formula  $IPR_{IIa} = \langle |a_m|^4 \rangle$ . As shown in Fig. 7.5(a), the IPR values of the photonic crystal graph modes vary erratically but lie between the maximum ergodic limit ( $IPR_{IIa} = 1$ ) and the RMT prediction limit ( $IPR_{IIa} = 2$ ) [159]. In the maximum localization limit the  $IPR_{IIa} = B$ , where  $B = 14$  is the number of graph bonds, and the results are far from this limit. Method IIb follows

the definition in Ref. [161] where  $IPR_{IIb} = \sum_m |\tilde{a}_m|^4 / [\sum_m |\tilde{a}_m|^2]^2$ . The quantity  $\tilde{a}_m$  is the un-normalized bond wavefunction amplitude. Here, the graph IPR values also vary erratically from mode to mode (Fig. 7.5(b)), but lie well below the maximum localization limit ( $IPR_{IIb} = 1$ ) and closer to the RMT prediction limit ( $IPR_{IIb} = 1/B = 0.07$ ) [161].

The conclusions we draw from the above two methods are not exactly the same. For Method IIa, two exemplary eigenfunction profiles are shown in Figs. 7.5(c) and d, which correspond to the RMT and ergodic limits, respectively. One may directly spot the different nature of these two modes based on their eigenfunction patterns, which is a unique advantage of the photonic crystal graph system. For Method IIb, we present the eigenfunction profile of two neighboring graph modes in Figs. 7.5(e) and (f). The eigenmode in Fig. 7.5(e) has a larger value of  $IPR_{IIb}$  and shows a strongly localized distribution. That in Fig. 7.5(f) has a small value of  $IPR_{IIb}$  and is more evenly distributed over the bonds. The average value of IPR over all the modes are more meaningful in this case, and we have  $\langle IPR_{IIa} \rangle = 1.39$  and  $\langle IPR_{IIb} \rangle = 0.10$  which are closer to the ergodic and RMT limits, respectively, than to the localization limit. Previous work [126, 159] on IPR on quantum graphs shows the surprising results that larger graphs, with the number of vertices  $> 10$ , tend to show strong deviations from RMT predictions, while smaller graphs show better agreement.

Taking into account the eigenfunction and IPR statistics, it would appear that PC graphs are close to the random plane wave condition for tetrahedral graphs, but clear systematic differences from RMT predictions remain. The complex vertex scattering properties of right-angle bends and T-junctions, along with the unusual  $\omega(k)$  dispersion

relation of PC defect waveguide modes, suggest that PC defect graphs may be very effective for future wave chaotic studies.

To conclude, we have designed and simulated an alternative chaotic graph system with photonic crystal defect waveguides that show an unusual dispersion relation. We show that a series of statistical studies can be carried out on closed graphs, including nearest-neighbor spacing statistics and eigenfunction statistics studies. Because both the graph bonds and nodes can be probed directly in a convenient 2D geometry, one may better analyze the non-universal features of chaotic graphs using a PC system. Because both the defect region size and rods can be changed locally, one is able to change the graph bond length easily by adding/removing rods, as well as change the graph node scattering properties by engineering the rod property near the graph nodes. We note that the PC 3-way and right-angle junctions have complicated scattering properties, and it should be possible to adjust the degree of wave localization by engineering the scattering properties of the PC waveguide junctions. These properties of the PC waveguides may facilitate further studies of localization phenomena in graphs, for example the emergence or suppression of trapped modes.

## Chapter 8: Quantum Hall - Quantum Spin Hall Composite Photonic Topological Insulator

This work was a collaborative effort with the Cornell group, and has been published as Ref. [144]. I have also written a review article on microwave PTI (photonic topological insulator) realizations, published as Ref. [145], but not included in this thesis. Photonic topological systems, the electromagnetic analog of the topological materials in condensed matter physics, create many opportunities to design optical devices with novel properties. We present an experimental realization of the BMW (Bi-anisotropic Meta-Waveguide) photonic system replicating both QH (quantum Hall) and QSH (quantum spin Hall) topological insulating phases. With careful design, a composite QH-QSH photonic topological material is created and experimentally shown to support reflection-free edgemodes, a heterogeneous topological structure that is unprecedented in condensed matter physics. The effective spin degree of freedom of such topologically protected modes determines their unique pathways through these systems, free from backscattering and able to travel around sharp corners. As an example of their novel properties, we experimentally demonstrate reflectionless photonic devices including a 2-port isolator, a unique 3-port topological device, and a full 4-port circulator based on composite QH and QSH structures.

## 8.1 Introduction to PTI Technology

During the past few years the realization of topological properties in photonic systems has paved the way for many novel applications and the creation of new states of light [162, 163, 164, 165, 166, 167, 168]. Translating concepts from condensed matter physics into the optical domain has come from mapping electronic Hamiltonians, such as the Kane-Mele Hamiltonian, into photonic platforms [165, 169, 170, 171, 172]. The photonic topological insulators (PTIs) possess similar topological properties to their electronic counterparts and allow light traveling through sharp corners without reflection [172]. The observation of topologically protected surface waves (TPSWs) at microwave frequencies has been reported with biased magneto-optical photonic crystals with broken time-reversal invariance [173, 174, 175, 176, 177, 178, 179]. Due to the difficulty of achieving strong magnetic effects at optical frequencies, a class of time-reversal invariant PTIs has been proposed: these include coupled resonators [180, 181, 182, 183, 184] and bi-anisotropic meta-waveguide (BMW) PTIs [143, 185, 186, 187, 188, 189, 190]. Recent studies revealed new designs of time-reversal-invariant PTIs based on emulating the quantum valley Hall (QVH) degree of freedom (DOF) in photonic systems [190, 191, 192, 193, 194, 195]. Elegant Floquet topological photonic designs are also reported [196, 197, 198, 199]. In this manuscript, we focus on the experimental realization of quantum spin Hall (QSH) and quantum Hall (QH) PTIs in the context of the BMW structure. We believe that this is the first-ever realization of a time-reversal invariance breaking heterogeneous topological system based on two different microscopic Hamiltonians, in either the photonic or electronic domains.

The BMW approach to PTIs is unique in that it allows for integration of different photonic topological paradigms based on the same unperturbed structure. Here we present the first demonstration of a non-reciprocal BMW structure and integrate it with a reciprocal PTI domain to create a completely new class of PTI materials. In such composite BMW structures, a spin-momentum-locked TPSW can be spatially guided and filtered into desired channels at the junction points between different topological domains with high efficiency and free from backscattering [200]. We begin with the simulation and experimental studies of the QH-PTIs followed by integration of QH-QSH PTIs. We are the first to observe TPSWs at the interface of the QH-QSH composite system which effectively serves as a 2-port PTI isolator. We then introduce experimental demonstrations of more complex PTI structures, namely a unique topological Y-junction and a full 4-port circulator. Our realized circulator structure has unique advantages over conventional photonic designs where the guided modes are not topologically protected. The topologically trivial resonator-based circulators generally suffer from narrow bandwidth and are susceptible to backscattering due to impedance mismatches [201]. An alternative QH-PTI based circulator faces challenges with respect to device size (tens of wavelengths) and the lack of a spin DOF [202]. On the contrary, the topological protection and spin DOF ensure the propagation of guided waves in heterogeneous BMW-PTI systems is backscatter-free, with higher directivity [200]. The utilization of topologically protected waves allows for a broad spectral operating range, compact design, integration with other PTI paradigms and potential for high-power operation.

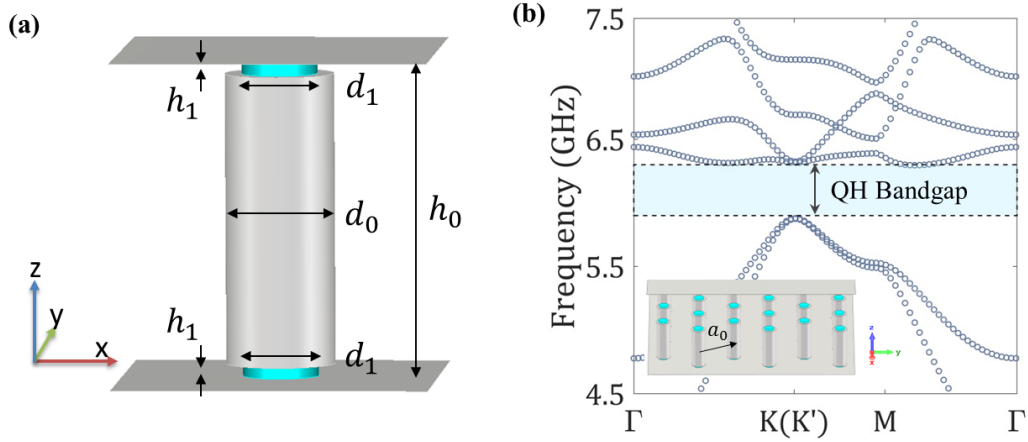


Figure 8.1: (a) Quantum Hall (QH) unit cell model with  $h_0 = 36.8\text{mm}$ ,  $h_1 = 1.45\text{mm}$ ,  $d_0 = 12.7\text{mm}$  and  $d_1 = 8.8\text{mm}$ . A QH rod consists of two ferrite disks (blue) straddling a middle metallic rod, sandwiched by two metallic plates. (b) Photonic band structure for a QH bulk region. The horizontal-axis is the  $k_x$  vector mapping an excursion in the 1st Brillouin zone and the vertical-axis is the eigenmode frequency. Under  $H_z = 1350\text{Oe}$  the QH bulk bandgap (shaded area from 5.9 to 6.3 GHz) matches the quantum spin Hall bandgap [3]. The inset offers an oblique view of a typical open-plate BMW hexagonal lattice with lattice constant  $a_0 = 36.8\text{mm}$ .

## 8.2 Design of QH-QSH BMW Structure

The BMW PTIs are based on an unperturbed structure of metallic rods arranged in a hexagonal lattice sandwiched between two metal plates [3, 200, 203, 204, 205, 206]. The structure dimensions are carefully designed to ensure the TE and TM modes are degenerate at the Dirac points with the same group velocity in the photonic band structure (PBS). The two orbital DOF are emulated with left/right-hand circular polarizations and the two synthetic spin DOF by the in-phase and out-of-phase linear combinations of the TE and TM modes at the Dirac point [200]. This mode crossing at the Dirac point can be destroyed by a broad range of spatial perturbations [187, 206] thus creating a band gap, analogous to a bulk electronic insulator. In the present case, we create a QSH-

PTI by adding an air gap between the rods and one plate, resulting in a bi-anisotropic response and an effective spin-orbit coupling (SOC) [3]. Ref. [200] Eqn. 6 shows the Hamiltonian for the BMW system near the Dirac point, which has a same form as the Kane-Mele Hamiltonian. More discussions on the BMW Hamiltonian can be found in Eqn. 9.5. Alternatively one can create a QH-PTI by placing magneto-optical materials in the gap. For QSH and QH domains, the spin-Chern numbers  $2C_{s,v}^{SOC} = \pm 1 \times \text{sgn}(\Delta_{SOC})$  and a global Chern number  $2C_{s,v}^T = \text{sgn}(\Delta_T)$ , where  $s = \uparrow, \downarrow$  is the spin state label and  $v = K, K'$ , are defined to quantify the topological properties of the upper and lower bands [200]. The spin-orbit coupling  $\Delta_{SOC}$  and time-reversal invariance breaking  $\Delta_T$  perturbations are defined as the overlap integrals of unperturbed modes' field components within the perturbed volume in the QSH and QH regions, respectively. An interface separating two PTIs with different Chern numbers will support edge states that are spectrally localized in the bulk bandgap [162, 185, 206]. Both QSH and QVH types of BMW have been experimentally realized [3, 190, 193], leaving the experimental demonstration of the QH-BMW structure un-reported. Recent theoretical studies [200] pave the way for realizing QH-PTIs in a BMW base by sandwiching biased gyromagnetic materials on top and bottom of the metallic rod (Fig. 8.1(a)). In contrast with [200] which characterized the ferrites using a dielectric permittivity  $\epsilon_r = 1$  and a simplified permeability tensor, here the QH region is re-designed in order to incorporate realistic ferrite properties. Figure. 8.1 (a) and (b) show the bulk QH unit-cell model and its PBS, respectively. This band diagram is obtained with first-principles electromagnetic simulation using COMSOL Multiphysics. The ferrites are characterized by  $\epsilon_r = 14$  and the Polder permeability tensor [207] (see Appendix G). As shown in Fig. 8.1(b), under

an external bias magnetic field of  $H_z = 1350Oe$ , a bandgap opens throughout the first Brillouin Zone, and matches closely with that of our existing QSH bulk structure [3, 206]. The degeneracy of TE and TM modes in the vicinity of the Dirac point is well-preserved as shown in Fig. 8.1 (b).

### 8.3 Composite QH-QSH Systems

We conduct transmission measurements through the proposed QH bulk structure. The gyromagnetic disks are made of commercial Yttrium Garnet ferrites which are magnetized along the  $z$  axis using Nd-Fe-B permanent magnets located outside the structure on the top and bottom plates. The QH region contains a  $14 \times 5$  ferrite-loaded lattice. Experimental results are presented as transmission S-parameters in Fig. 8.2. The inset of Fig. 8.2 shows the measurement method: the two ports of the Vector Network Analyzer (VNA) are connected to antennas at the center of a QH bulk structure and its perimeter. By switching on the H-field to magnetize the ferrites, we observed an averaged 20 dB decrease of transmission from port 1 to port 2 from 5.95 to 6.2 GHz which is slightly narrower compared to the photonic bandgap predicted in Fig. 8.1(b).

We next construct a heterogeneous PTI structure with two topological phases: QH and QSH PTIs. This composite PTI structure has an interface that will support topologically protected edgemodes in the operating bandwidth (the shaded area in Fig. 8.1(b)) inside the original bandgap frequencies for both QSH and QH bulk structures. The key requirement is to maintain the spin degeneracy of the modes in the composite structure, which allows edgemodes propagating without reflection [200].

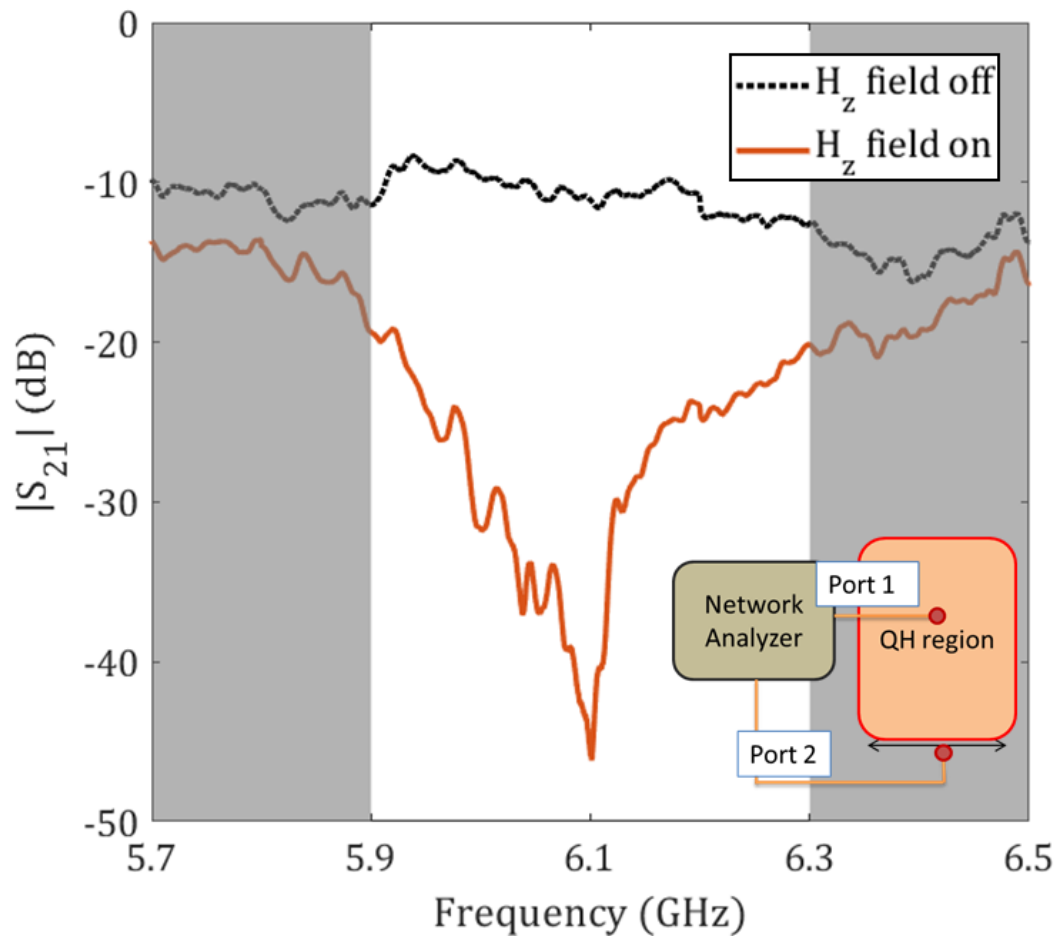


Figure 8.2:  $|S_{21}|$  transmission results through a bulk QH structure in the  $\Gamma - K(K')$  direction for both magnetized and un-magnetized ferrites. With  $H_z$  on (magnetized ferrites, red curve), we observe a decrease in transmission S-parameter at 5.9-6.3 GHz, which is caused by the absence of bulk modes inside the bandgap region. Inset: schematic of the experiment.

The composite QH-QSH PTI structure has  $39 \times 5$  BMW rods in both regions. We use the VNA to conduct 2-port measurements for edgemode transmission along the QH-QSH interface. In Fig. 8.3 (a)/(b), the left/right-going transmission  $S_{AB}/S_{BA}$  for the two possible magnetic field biasing orientations is 35 dB higher than the transmission in the other direction in the joint band gap frequency range. These experimental results show that a QH-QSH interface can only support an edgemode with one synthetic spin direction.

The backscattering-free property of an edgemode is also examined in Appendix G. The inversion of applied H-field in the  $z$ -direction will invert the sign of the normalized bandgap  $\Delta_T$  for QH-PTIs [200]. With the QSH-PTIs unchanged, the supported edgemode at the QH-QSH interface will flip its spin, and more importantly invert its spin-locked propagation direction. The topologically protected edgemodes ensure strong suppression of the reflected flow of waves in the un-desired direction. The QH-QSH structure serves as an effective 2-port PTI isolator which can be turned on/off by external H-field. The isolator's allowed propagating direction can be switched in real-time by the inversion of the H-field.

## 8.4 Topological Y-junction

With the experimental realizations of both QSH-QSH [3] and QH-QSH waveguides, we next propose a 'Y-junction' PTI structure which mixes three different topological phases (Fig. 8.4(a)). The 3-port Y-junction possesses unique functions compared to more traditional devices, such as a 3-port circulator. With its spin DOF and propagation direction locked together, the edgemode transmission behavior inside the Y-junction can

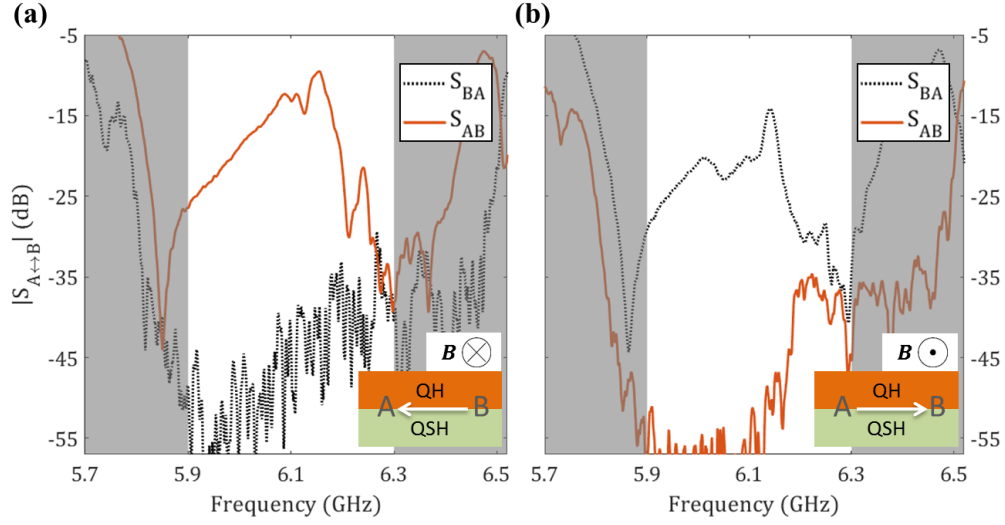


Figure 8.3: (a) and (b) are the measured edgemode transmission along the QH-QSH interface with opposite H-field directions applied to the QH region. The black-dot(red-line) curves represent the right(left)-going waves. The insets show the locations of port A and B along with the direction of the applied H-field. The white arrows mark the expected edgemode propagating directions. We find that the edgemode propagation direction is reversed when the biasing magnetic field direction is inverted.

be predicted theoretically. For instance, an edgemode with either spin up ( $\psi^\uparrow$ ) or down ( $\psi^\downarrow$ ) can exist at interface ‘ab’, with their propagating direction restricted to right and left-going, respectively. Governed by the direction of the external H-field in the QH-region, a  $-H_z$  field will dictate that the Y-junction’s port 3 (2) becomes a forbidden source (receiver). To illustrate a forbidden source (receiver) experimentally, note the decrease of both  $S_{23}$  and  $S_{13}$  ( $S_{23}$  and  $S_{21}$ ) from 5.9-6.3 GHz shown in Fig. 8.4(b) (Fig. 8.4(b) and (c)). Because the interface ‘bc’ can only support an up-spin mode  $\psi^\uparrow$ , the signal injected at port 3 can not travel left to port 1 or 2. In Fig. 8.4(c) the amplitude of  $S_{31}$  is 20 dB higher than  $S_{21}$ , indicating that a right-going wave transmitted from port 1 will travel to port 3 instead of port 2. This choice of path is dictated by the fact that such an up-spin TPSW can only propagate along interface ‘bc’ but not ‘bd’. For similar reasons, a down-spin wave

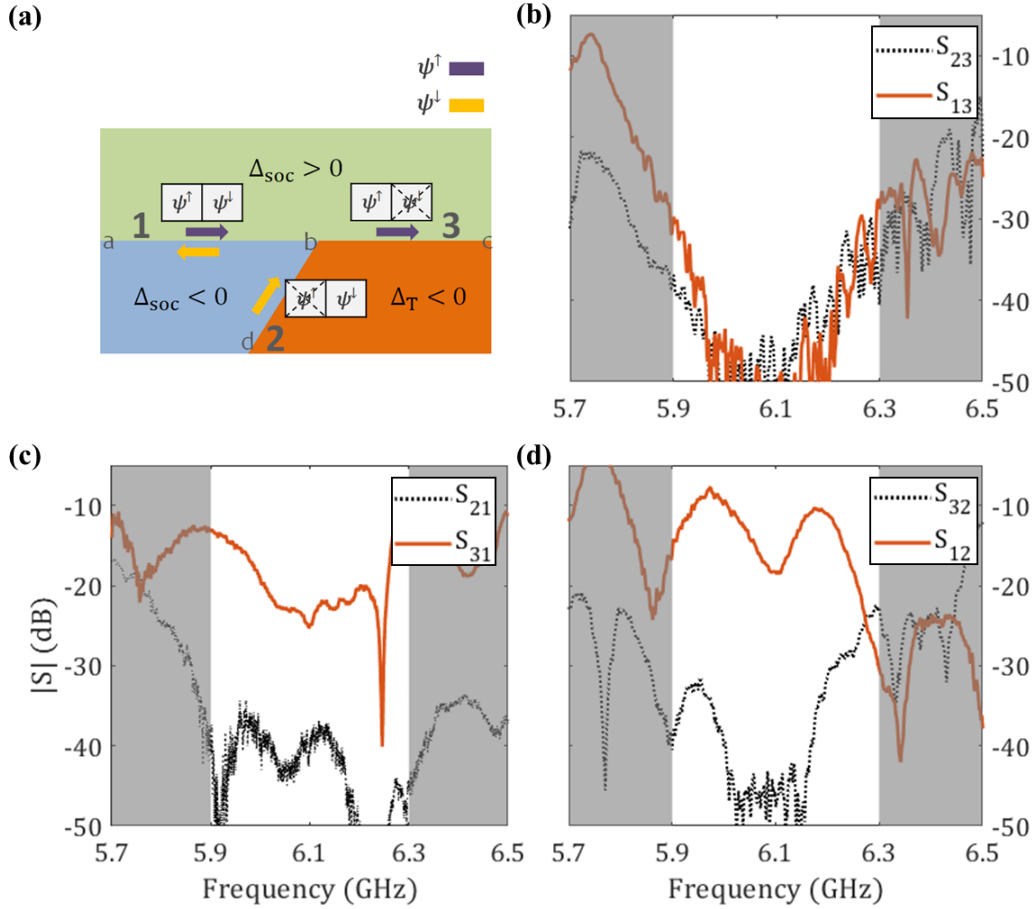


Figure 8.4: (a): The Y-junction design consist of three different topological domains: two QSH domains (green and blue) and a QH region (red), creating three interfaces: ab, bd and bc. The  $\psi^\uparrow/\downarrow$  represents an edgemode with spin up/down. Purple/yellow arrows: propagation directions of  $\psi^\uparrow/\downarrow$  modes. Plot (b-d) are the transmission measurements of the Y-junction with  $-H_z$  in the QH region. The edgemode will follow the  $2 \rightarrow 1$  and the  $1 \rightarrow 3$  paths strictly without backscattering. Port 3 becomes a forbidden source as shown in (b).

$\psi^\dagger$  transmitted by port 2 will only go to port 1 as shown in Fig. 8.4(d). The ideal S-matrix

of the topological Y-junction can be written as  $S_{Topo-Y} = \begin{bmatrix} 0 & 1 & 0 \\ 0 & 0 & 0 \\ 1 & 0 & 0 \end{bmatrix}$ , which differs from

a traditional 3-port circulator  $S_{Circ} = \begin{bmatrix} 0 & 1 & 0 \\ 0 & 0 & 1 \\ 1 & 0 & 0 \end{bmatrix}$  which creates a  $1 \rightarrow 3 \rightarrow 2 \rightarrow 1$

circulation. The functionality of a topological Y-junction is similar to the active quasi-circulator [208]. Inversion of the H-field direction will turn port 3 (2) into a forbidden receiver (source), due to the change in propagating edgemode spin polarization at the two QH-QSH interfaces (observed but not shown here) [200]. The topological Y-junction will act as a building block for more sophisticated structures, such as the 4-port circulator. The demonstrated Y-junction can serve as a versatile platform for many novel photonic applications based on various combinations of topological domains. For example, one can construct a backscattering-free photonic combiner with a QSH region and two QH regions with opposite H-field directions that leads edgemodes from two paths to merge onto the same third path with no backscattering. Furthermore, an inversion of biasing H-fields in the QH domains will turn the photonic combiner into a spin filter that divides photons with different synthetic spins into different paths, effectively creating a Stern-Gerlach device for the spin DOF of light. Such junctions may find application in quantum communication, Boolean networks models, and photonic devices based on manipulating photons with different polarization states.

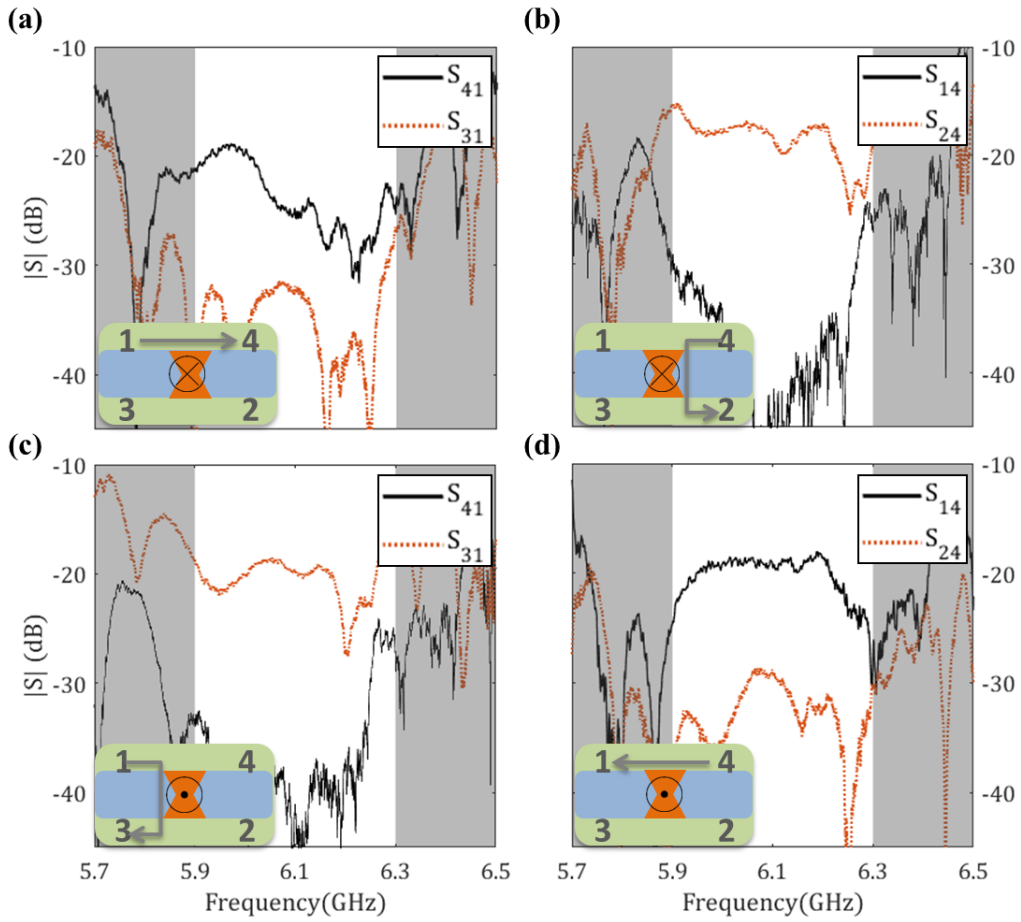


Figure 8.5: Experimental results of edge waves propagating in a topologically protected 4-port circulator. The QH (QSH with  $\Delta_{SOC} > 0$  and  $\Delta_{SOC} < 0$ ) domains are color-coded as red (green and blue) for all insets. The applied H-field direction is inverted between plots (a-b) and (c-d), creating a clockwise and counter-clockwise circulation around the center QH island, respectively.

## 8.5 Topological 4-port Circulator

Novel non-reciprocal structure designs, like isolators and circulators, have been proposed recently due to their important roles in photonic and microwave circuits [75, 209, 210, 211, 212, 213, 214, 215]. After the experimental demonstration of the Y-junction structure, we are in position to integrate different PTIs into another practical

structure, namely a 4-port circulator. The ideal S-matrix of a 4-port circulator  $S_{Circ} =$

$$\begin{bmatrix} 0 & 0 & 0 & 1 \\ 0 & 0 & 1 & 0 \\ 1 & 0 & 0 & 0 \\ 0 & 1 & 0 & 0 \end{bmatrix}$$

which creates a  $1 \rightarrow 3 \rightarrow 2 \rightarrow 4 \rightarrow 1$  circulation.

In contrast to realizing optical circulators with only 2D gyromagnetic PTIs [201], here we report the experimental realization of the combined PTI system with different types of topological phases [172, 200]. Similar to the design in [200], the realized 4-port BMW circulator consists of a center QH island and four surrounding QSH regions with alternating  $\Delta_{SOC}$  signs (Fig. 8.5). The directions of both QSH-QSH and QH-QSH waveguides are chosen to be in the  $K(K')$  directions for optimized edgemode propagation.

The operation of the BMW circulator is as follows. To start with, consider the trajectory of the up-spin edgemode  $\psi^\uparrow$  which is launched from port 1 and propagating right along the QSH(green)-QSH(blue) waveguide (inset of Fig. 8.5(a)). When the edgemode arrives at the QSH-QH-QSH Y-junction, there exist two QH-QSH waveguides ('red-blue' and 'red-green') which support edgemodes with opposite spins. The topological nature of these modes will lead the wave to only one of the two QH-QSH waveguides, without backscattering [200]: at the first Y-junction, the spin up wave  $\psi^\uparrow$  will merge on to the horizontal QH-QSH interface; at the second Y-junction, it will choose the QSH-QSH interface over the vertical QH-QSH interface because that QH-QSH interface does not support spin up edgemodes. As shown in Fig. 8.5(a), the measured transmission from port 1 to 4 ( $S_{41}$ ) enjoys an averaged 15 dB boost compared to the competing vertical

path (port 1 to 3) in the bulk band gap from 5.9 to 6.3 GHz. Combined with the other three guided edgemode paths, a clear circulation pattern is observed around the center QH-island.

The inversion of the  $H_z$  direction will change the sign of  $\Delta_T$  of the QH region and further lead to the flip of spins of the propagating modes at all QH-QSH interfaces. Considering again the same up-spin TPSW launched from port 1: instead of choosing the horizontal QH-QSH interface, it will merge on to the vertical QH-QSH interface and finally flow to port 3. As shown in Fig. 8.5(c),  $S_{31}$  (the transmission from port 1 to port 3) is now higher than  $S_{41}$ . To conclude: we observed the change of circulation direction from counter-clockwise (Fig. 8.5 (a) and (b)) to clockwise (Fig. 8.5 (c) and (d)) controlled by the external H-field biasing direction on the QH BMW region. The isolation of the circulator design is 20 dB on average, the input power is +5 dBm limited only by the VNA, and the frequency range is 5.9-6.3 GHz which can be tuned by scaling the structural dimensions.

Note that the parallel QSH-QSH waveguides can have cross-coupling issues caused by the finite-size limitation of the structure. The devices also face energy dissipation due to the finite line-width of the ferrite, and enhanced insertion loss due to imperfect coupling between the antenna and guided modes in the structure. Implementation of a rotating dipole source will enhance the power delivery by directly and efficiently exciting uni-directional edgemodes on the QSH-QSH interfaces [3].

## Chapter 9: Chaotic Gaussian Symplectic Ensemble Structures with Photonic Topological Insulator Graphs

### 9.1 Overview

Unprecedented wave phenomena have been introduced with the creation of photonic topological insulator (PTI) technologies [145]. One of them is the emulation of spin in the photonic context, where a pair of topologically protected modes with opposite effective spins have emerged. Mesoscopic condensed matter physics concepts, including the quantum Hall, quantum spin Hall (QSH), and quantum valley Hall effects (QVH), have been demonstrated in a series of landmark papers [162, 163, 164, 165, 166, 167, 193]. The bi-anisotropic metawaveguide (BMW) is a versatile platform for realizing quantum Hall, quantum spin Hall, and quantum valley Hall effects for electromagnetic waves. The remarkable transmission properties of PTI have excited a wide range of real-life applications, for example, delay line devices, isolators, and circulators. However, the spin-1/2 like degree of freedom of the topological modes is not as widely exploited.

Random Matrix Theory has enjoyed great success in describing the energy level spacing statistics of large nuclei with various symmetries [10]. The statistics of complex systems that show time-reversal invariance (TRI) are described by the Gaussian orthogonal

ensemble (GOE), the statistics of systems showing broken time-reversal invariance are described by the Gaussian unitary ensemble (GUE), and the statistics of systems with TRI and antiunitary symmetry show Gaussian symplectic ensemble (GSE) statistics [16, 18, 31, 37]. Both GOE and GUE statistics were observed in a wide variety of chaotic microwave systems [18, 216]. Complex metric graphs made with standard coaxial cables have been shown to have statistical properties described by the GOE and GUE random matrix ensembles [126, 152]. However, due to the lack of a photonic analog of a spin-1/2 degree of freedom, the realization of a GSE system was not observed for a long time in classical wave systems [41].

Here we aim to create a microwave simulator of GSE statistics by utilizing the intrinsic physical properties of the QSH-BMW PTIs [3, 70, 206]. The bianisotropic effect introduces an artificial gauge field and Berry connection for the two spin modes and gives rise to a QSH-PTI. The system we consider here is a pyramidal graph with graph bonds realized by PTI waveguides. Edge modes with both spin-up and spin-down indices can travel through the entire graph so that there is an interference of waves at all of the nodes. In addition to the clear observation of double (Kramers) degeneracy from photonic band structure studies and edge mode transmission measurement, we will also prove that the BMW Hamiltonian falls into the symplectic group and define the associated antiunitary operator.

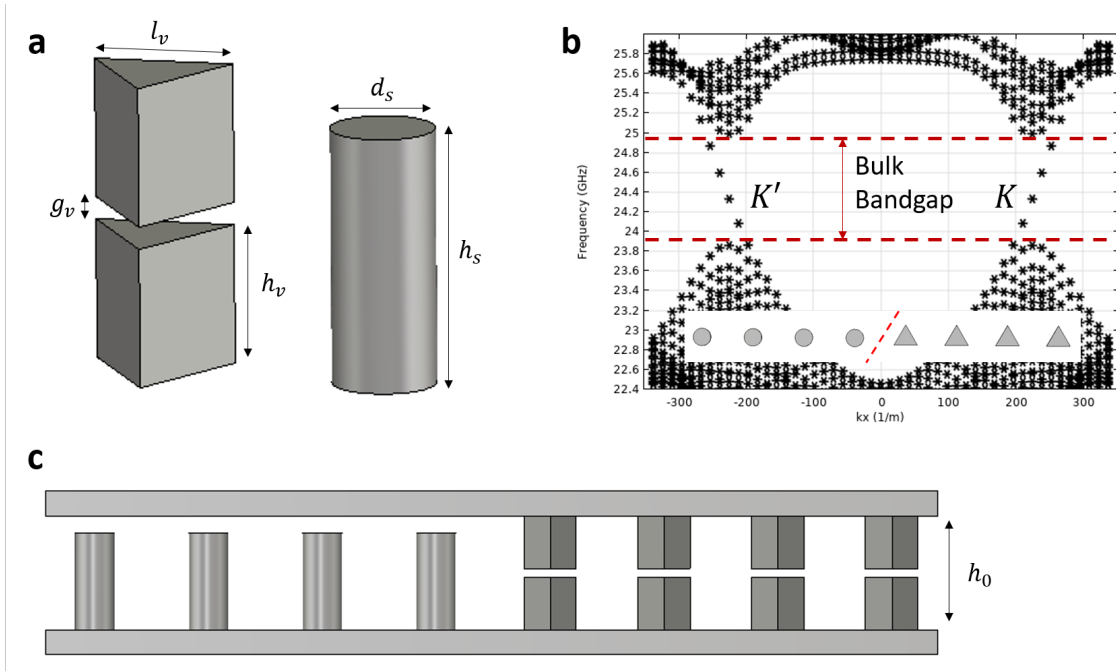


Figure 9.1: **a**. The schematic of the unit cell structure that define the QVH and QSH regions. The quantities  $l_v, g_v, h_v$  are the prism side length, the air gap distance, and the prism height of one QVH rod. The quantities  $d_s, h_s$  are the diameter and height of the QSH cylinder rod. **b**. The photonic band structure of the QSH-QVH interface waveguide. Inset shows a schematic of the supercell simulation model. The red-dashed line marks the interface between the QSH (left) and the QVH (right) region. **c**. The side-view of the QSH-QVH structure (same structure as the **b** inset). The top and bottom metallic plates are separated by  $h_0$ . All QSH rods are attached to one of the metallic plates, and the QVH rods are mounted on both plates, leaving an air gap.

## 9.2 Design of QVH-QSH Graphs

The BMW-PTI system can host domains with different topological orders inside one composite structure. The first principle of the design of a composite QVH-QSH structure is matching the bulk-bandgap of the single QVH and the QSH regions. There have been several designs of QVH-QSH BMW structures [193, 217]. In principle, we can adopt either QVH-QSH blueprint from Refs. [193, 217] to build the graph structure. However, the design in Ref. [193] requires the QVH region to have metallic inclusions that float between the top and bottom metal plates. Because we aim to build a graph structure with many QVH (and QSH) rods, the proper fixation and alignment of these ‘airborne’ QVH rods is too tricky. The design in Ref. [217] uses QSH rods which can change topological order through sliding the rod up and down mechanically. This is a convenient design indeed. However, our focus is not on flipping the QSH domain order but altering the shape of the QVH-QSH interface waveguide. This design goal requires a uniform and robust mounting method for the QVH and QSH domains. Thus we have designed a revised version of the QVH and QSH BMW region that operates near 24.5GHz. As shown in Fig. 9.1 (a), the QVH region consists of two identical metallic prisms with length  $l_v = 4.30mm$ , height  $h_v = 4.32mm$ , and the middle air gap  $g_v = 0.69mm$ . Each prism is firmly attached to one of the two metallic plates. The QSH region is a metallic cylinder with diameter  $d_s = 3.22mm$  and height  $h_s = 8.3mm$ , and it is attached to one of the two plates. Both regions are placed between two metallic surfaces with a spacing of  $h_0 = 9.33mm$  in the vertical direction. The lattice constant of the triangular BMW lattice is  $a_0 = h_0 = 9.33mm$ . Fig. 9.1 (c) illustrates how

the QSH and QVH rods are mounted between the two metallic covering plates. We examine the existence of edgemodes in the QVH-QSH waveguide through the so-called supercell simulation, as shown in Fig. 9.1 (b). The supercell structure consists of a slice of QSH and QVH rods (8 rods for each domain in our simulation), where the Floquet boundary condition is applied to the two long sides to simulate an infinitely long waveguide structure. It is clearly shown that the QVH-QSH waveguide can host two counter-propagating edgemodes between  $23.8 \sim 24.8\text{GHz}$ . The two modes have opposite spin and valley degrees of freedom (DOF).

The PTI graph can be thought of as the shape of a square pyramid realized in the 2D plane. Each bond of the graph is built with a QVH-QSH interface waveguide. The graph will be electrically large and have an asymmetric shape so that the scattering will be complex. The open-plate view of the QVH-QSH PTI-graph is shown in Fig. 9.2. All parts are made with Aluminum 1070 alloy due to the high purity of Al ( $> 99.7\%$ ), a relatively low percentage of iron ( $< 0.25\%$ ), and a reasonable cost. This choice of Aluminum alloy is to enable a superconducting transition in the entire graph structure below a temperature of 1.2K. Because of the relatively high operating frequency ( $\sim 24.5\text{GHz}$ ), we can create a graph structure with many lattice periods but moderate overall size. We note that further scaling up of the operating frequency is limited by the bandwidth of the VNA, and the further scale-up of the total graph size is limited by the room under the dilution refrigerator mixing chamber plate (50cm diameter). To prevent the bending and flexure of the covering plates, we have also installed several support rods (with diameter  $d_s$  and height  $h_0$ ) at the four corners and several spots in the horizontal plane. An ensemble of PTI graphs can be realized by changing each of the graph bonds' shape and/or length.

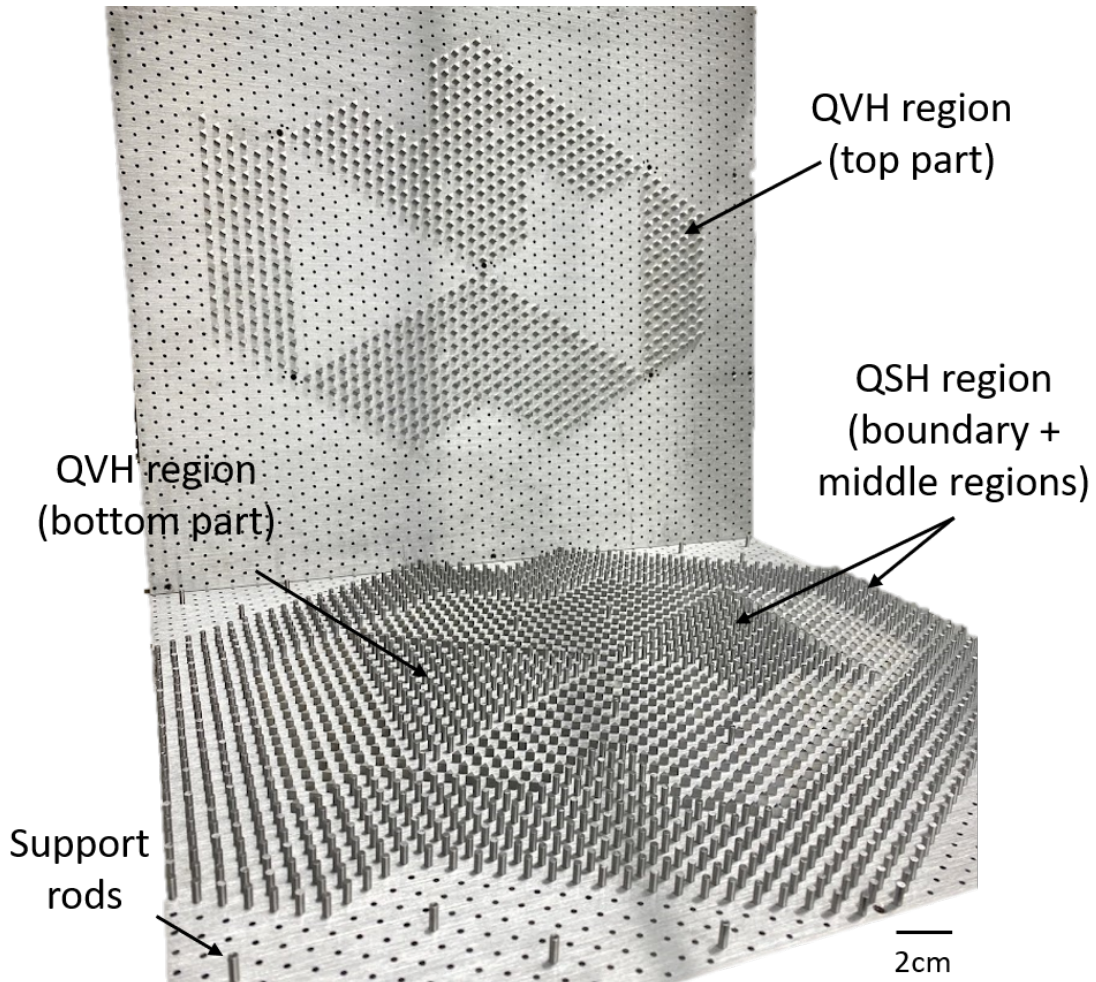


Figure 9.2: The open-plate view of the PTI-graph structure. Shown are the top and bottom metallic plates and the rods/prisms attached to each one of them. The top plate has the top part of the QVH rods. On the bottom plate, we have installed the QSH rods as well as the bottom part of the QVH rods. Several supporting rods are installed which will spread out the weight of the top-plate evenly, and provide a fixed and uniform separation between the plates,  $h_0$ .

The conductive loss of the structure can be lowered by cooling down the graph using the refrigerator.

### 9.3 Symplectic Group Analysis for BMW Systems

We are interested in using the QSH-QVH BMW system as a chaotic wave system whose statistical properties fall in the universality class of the Gaussian symplectic ensemble (GSE), which is appropriate for time-reversal invariant systems with a spin-1/2 degree of freedom. An essential feature of a spin-1/2 system is an anti-unitary T-operator ( $T^2 = -1$ ). For a time-reversal invariant system,  $T^2 = -1$  leads to  $|\psi\rangle$  and  $T|\psi\rangle$  being two different states with the same energy directly creates a Kramers degeneracy. An existing microwave experiment on simulating GSE systems uses many elegant tricks to create conditions that mimic a GSE graph [41]. As far as we know, no research group has built an artificial physical system that replicates the full spin-1/2 analog. In Ref. [41], the GSE statistics is emulated through a careful design graph which has two symmetry-related sub-graphs. This approach is not general. Other than a limited number of works [218, 219, 220], the derivation of the anti-unitary condition  $T^2 = -1$  is not widely discussed for PTI systems and not discussed at all for the BMW system.

We started by proposing a guessed T-operator of the BMW system,

$$T_b = a \cdot \tau_x s_y \sigma_0 K \tag{9.1}$$

where  $a$  is a complex number coefficient with  $|a|^2 = 1$ ,  $K$  is the complex conjugation operator ( $K^2 = 1$  and  $K i = -i K$ ).  $\tau$ ,  $s$  and  $\sigma$  are the Pauli matrices operating on

the space of the  $K$  and  $K'$  valley, the spin states, and the Dirac degeneracy, respectively. The reason for guessing  $T_b \propto \tau_x$  and  $s_y$  in Eqn. 9.1 comes from the valley and spin flip associated with a time-reversal (TR) operation. The Kronecker product ( $\tau_i \sigma_j \equiv \tau_i \otimes \sigma_j$ ) shorthand is used.

A time reversal invariant system has  $[H(r), T] = 0$ , or in the momentum representation  $TH(k)T^{-1} = H(-k)$  where  $T$  represents the TR operator of the system. Here we will examine  $TH(k)T^{-1} = H(-k)$ . The effective Hamiltonians of the BMW lattice at the  $K$  and  $K'$  valleys are written as [206]:

$$H_K^{\uparrow\downarrow}(\delta k_x, \delta k_y) = v_D s_0(\delta k_x \sigma_x + \delta k_y \sigma_y) + \omega_D \Delta_{em} s_z \sigma_z \quad (9.2)$$

$$H_{K'}^{\uparrow\downarrow}(\delta k_x, \delta k_y) = v_D s_0(-\delta k_x \sigma_x + \delta k_y \sigma_y) - \omega_D \Delta_{em} s_z \sigma_z \quad (9.3)$$

The quantities  $\delta k = k - K$  refers to the distance to the Dirac point  $K$ , and  $\delta k = (\delta k_x, \delta k_y)$ ,  $v_D$  is the group velocity for both the degenerate TE and TM modes near the Dirac point. The quantities  $s_0$  is identity matrix acting on the spin states,  $\omega_D$  is the Dirac point frequency, and  $\Delta_{em}$  is the bianisotropic terms which describes the coupling between field components inside the air gap region. Note that the reason behind TE and TM modes having the same group velocity is a process of carefully engineering the structure geometry. The detailed introduction of the BMW system Hamiltonian theory is not the goal here, and we kindly direct the readers to find more discussions in Refs. [200, 206].

With  $T_b = a \cdot \tau_x s_y \sigma_0 K$  and  $K \sigma_y K^{-1} = -\sigma_y$ , it is clear that

$$T_b H_K^{\uparrow\downarrow}(k) T_b^{-1} = T_b H_K^{\uparrow\downarrow}(\delta k_x, \delta k_y) T_b^{-1} = H_{K'}^{\uparrow\downarrow}(-\delta k_x, -\delta k_y) = H_{K'}^{\uparrow\downarrow}(-k) \quad (9.4)$$

This result also applies to the  $K'$ -Hamiltonian. One can also combine Eqns. 9.2 and 9.3 and write out the total Hamiltonian, which is [206]

$$H = v_D s_0 (\tau_z \delta k_x \sigma_x + \tau_0 \delta k_y \sigma_y) + \omega_D \Delta_{em} \tau_z s_z \sigma_z, \quad H \Psi = \Omega \Psi \quad (9.5)$$

where  $\Psi$  is an 8-component spinor  $\Psi = [\Psi_{\mathbf{K}}; \Psi_{\mathbf{K}'}]$ . Similarly we find that  $T_b H(k) T_b^{-1} = H(-k)$ . We next study the effect of the TR operation on the spinor  $\Psi$ .

$$T_b \Psi = a s_y \sigma_0 K \begin{bmatrix} 0 & 1 \\ 1 & 0 \end{bmatrix} \begin{bmatrix} \Psi_{\mathbf{K}} \\ \Psi_{\mathbf{K}'} \end{bmatrix} = a s_y \sigma_0 K \begin{bmatrix} \Psi_{\mathbf{K}'} \\ \Psi_{\mathbf{K}} \end{bmatrix} \quad (9.6)$$

As shown in Eqn. 9.6, the two valley indices switch under  $T_b$ . The  $s_y$  and  $\sigma_0$  will operate on both the  $K$  and  $K'$  valleys. For simplicity, we will only look at the  $K$  valley here.

The  $K$ -valley state  $\Psi_{\mathbf{K}} = [\psi_K^\uparrow; \psi_K^\downarrow]$  is a 4-component spinor with  $\psi_K^\uparrow = [\psi_K^{R,\uparrow}; \psi_K^{L,\uparrow}]$  and  $\psi_K^\downarrow = [\psi_K^{R,\downarrow}; \psi_K^{L,\downarrow}]$  [206].  $R(L)$  refers to the right (left) circular polarization. By choosing  $a = i$ , we have  $T_b = i\tau_x s_y \sigma_0 K$  and  $i s_y \sigma_0 K \Psi_{\mathbf{K}} =$

$$i s_y \otimes \sigma_0 K \begin{bmatrix} \psi_K^\uparrow \\ \psi_K^\downarrow \end{bmatrix} = \begin{bmatrix} 0 & 1 \\ -1 & 0 \end{bmatrix} \otimes \begin{bmatrix} 1 & 0 \\ 0 & 1 \end{bmatrix} K \begin{bmatrix} \psi_K^\uparrow \\ \psi_K^\downarrow \end{bmatrix} = K \begin{bmatrix} 0 & 0 & 1 & 0 \\ 0 & 0 & 0 & 1 \\ -1 & 0 & 0 & 0 \\ 0 & -1 & 0 & 0 \end{bmatrix} \begin{bmatrix} \psi_K^{R,\uparrow} \\ \psi_K^{L,\uparrow} \\ \psi_K^{R,\downarrow} \\ \psi_K^{L,\downarrow} \end{bmatrix} = K \begin{bmatrix} \psi_K^{R,\downarrow} \\ \psi_K^{L,\downarrow} \\ -\psi_K^{R,\uparrow} \\ -\psi_K^{L,\uparrow} \end{bmatrix} \quad (9.7)$$

Thus the effective TRS operator  $T_b = i\tau_x s_y \sigma_0 K$  meets its expectation: it results in flipping both momentum (valley) and spin, as well as introduce a negative sign. However,

our job is not finished since we have not discussed the effect of the complex conjugate operator  $K$  acting on the spinor  $\Psi$ . On the other hand, one might ask why the orbital degree of freedom, represented by the circular polarization, is not discussed. Presumably both spin and orbital angular momentum should flip sign under TR operation. It will be clear later that the effect of  $K$  is to flip the orbital DOF.

The physical meaning of the  $K$  operator may be better understood in the original TE and TM linear polarized basis  $\mathbf{A}_K$  [206], where  $\Psi_K^{R/L,\uparrow} = [1; \mp i; 1; \mp i]$ ,  $\Psi_K^{R/L,\downarrow} = [1; \pm i; -1; \pm i]$ , and the superscripts R/L represent RCP/LCP. Note that the valley DOF is linked to the circular polarity of the edgemode. Combining Eqns. 9.6 and 9.7, one may sum-up the effect of  $T_b$  as:

$$T_b \Psi_{K,K'}^{R/L,\uparrow} = \Psi_{K',K}^{L/R,\downarrow}, \quad T_b \Psi_{K,K'}^{R/L,\downarrow} = -\Psi_{K',K}^{L/R,\uparrow}. \quad (9.8)$$

To sum-up, we first examined that the BMW Hamiltonian is invariant under  $T_b = i\tau_x s_y \sigma_0 K$ . We then inspect the effect of  $T_b$  acting on the spinor  $\Psi$ . As shown in Eqn. 9.8, we see that operator  $T_b$  flips the valley, spin and orbital degrees of freedom of the BMW spin-mode. It is also clear that  $T_b^2 = (i\tau_x s_y \sigma_0 K)(i\tau_x s_y \sigma_0 K) = i\tau_x s_y \sigma_0 (-i)\tau_x (-s_y)\sigma_0 K^2 = -1$ . Aside from deriving the effective  $T_b$  operator for the BMW Hamiltonian, we present an alternative method of showing that the BMW belongs to the GSE group in Appendix H.

## 9.4 Numerical Results

We first conduct studies of the eigenmodes of closed graphs using the numerical simulation software CST (shown in Fig. 9.3). The eigenmode solver can obtain the modal spectrum for closed systems with reasonable accuracy. It is clearly shown that, inside the bulk bandgap frequencies ( $24 \sim 24.8GHz$  as shown in Fig. 9.1 (b)), we observe only doubly degenerated edgemodes. At the lower edge of the bulk bandgap ( $\sim 23.5GHz$ ), a co-existence of the degenerated edgemodes and the more continuous bulkmodes is observed.

We then conduct studies of the eigenmodes of closed graphs using the numerical simulation software HFSS. We used HFSS for this study because it is compatible with the UMD High Performance Computing (HPC) cluster DeepThought2. For us, the ability to run eigenmode simulations on an HPC is a must-have due to the PTI-graph models' large amount of RAM consumption. We note that if RAM is not a limiting factor, using COMSOL for eigenvalue simulations tends to be the best approach.

The simulated pyramidal graph has the area of  $\sim 35 \times 60$  photonic crystal lattice constants, where  $\sim 90$  levels are sampled in the topological edgemode bandwidth. We construct the graph structure with both QSH and QVH BMW-domains, and the two-fold degeneracy (Kramers degeneracy) of system eigenmodes are observed from eigenvalue simulations in HFSS. The normalized spacing statistics of the graph eigenfrequencies are computed and compared to the theoretical predictions of GOE, GUE, and GSE systems. The quantity  $s_i = e_{i+1} - e_i$ , where  $e_i$  is the normalized (unfolded with the mean-mode-spacing) graph eigenmode and the subscript  $i$  refers to the mode index. Details of the

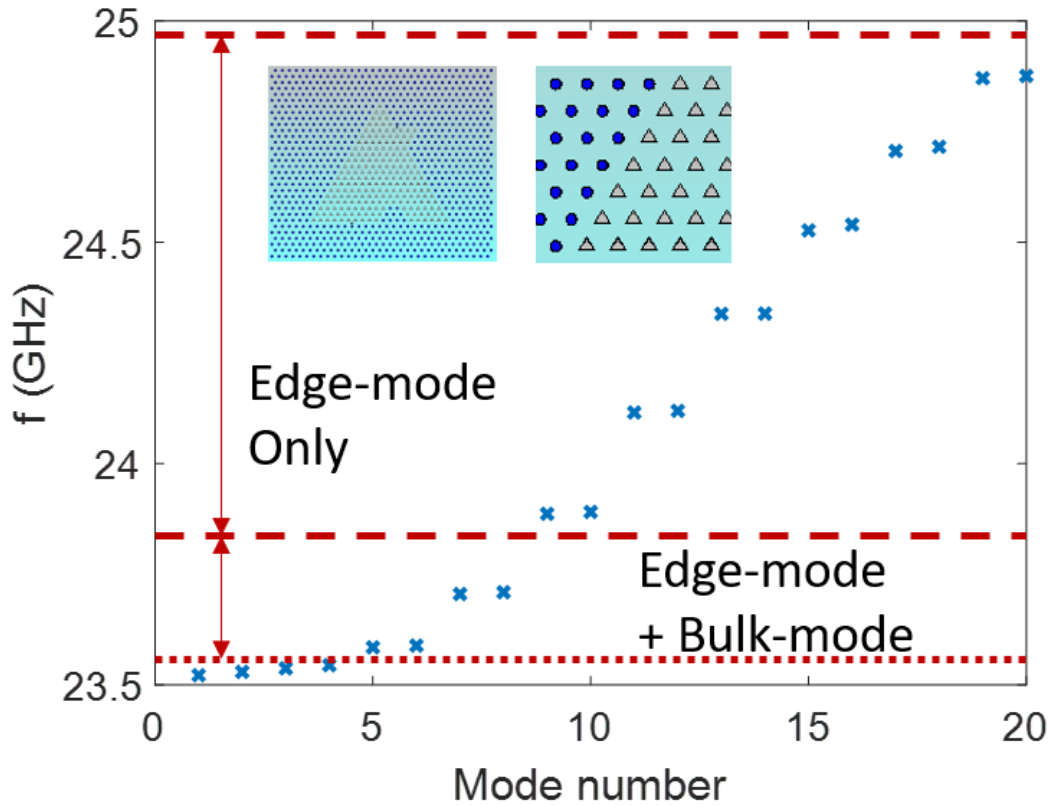


Figure 9.3: The simulated eigenmode results of a PTI-graph realization. It is clearly shown that the two-fold degeneracy is present at the bulk bandgap frequencies. At the edge of the bandgap ( $\sim 23.5GHz$ ), we observe a hybridization of the edgemode and bulk modes. Inset shows the graph structure used in this numerical study, consisting of a QSH region show by blue circles and a QVH region shown by grey triangles. The second inset shows an enlarged region of the QVH-QSH boundary.

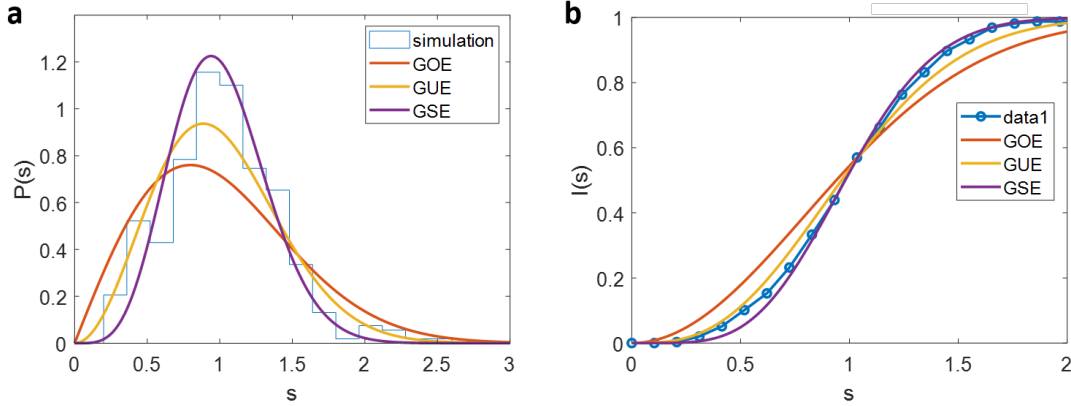


Figure 9.4: **a** The histogram approximation probability distribution of the PTI graph nearest-neighbor mode-spacing  $s$ . The prediction of the GOE, GUE, and GSE groups are plotted as solid lines for reference. **b**. The integrated probability function of  $s$  along with the theory predictions of the three groups.

mode-spacing normalization process can be found in Chapter 7 Section 3. As shown in Fig. 9.4 (a) and (b), the level spacing statistics of the pyramidal graph agree reasonably well with the GSE statistics and show a distinctly different shape as compared to the GOE and GUE systems. For small spacing values ( $s \sim 0.5$ ), we find that the graph system deviates from the GSE class prediction.

## 9.5 Room-temperature Experimental Results

With the QVH-QSH region designed and verified by simulation tests, we fabricated the QSH, QVH, supporting rods, and the top/bottom plates as shown in Fig. 9.2. Room temperature S-parameter measurements are conducted with dipole antennas installed at several of the graph nodes (shown as the black stars in Fig. 9.5). We use port 3 and port 4 of the VNA to conduct S-parameter measurements. The reflection S-parameters are shown in Fig. 9.6 (a), where several peaks can be spotted in the edgemode operating frequency range ( $23.7 \sim 24.8$  GHz). From only one round of measurement, we have

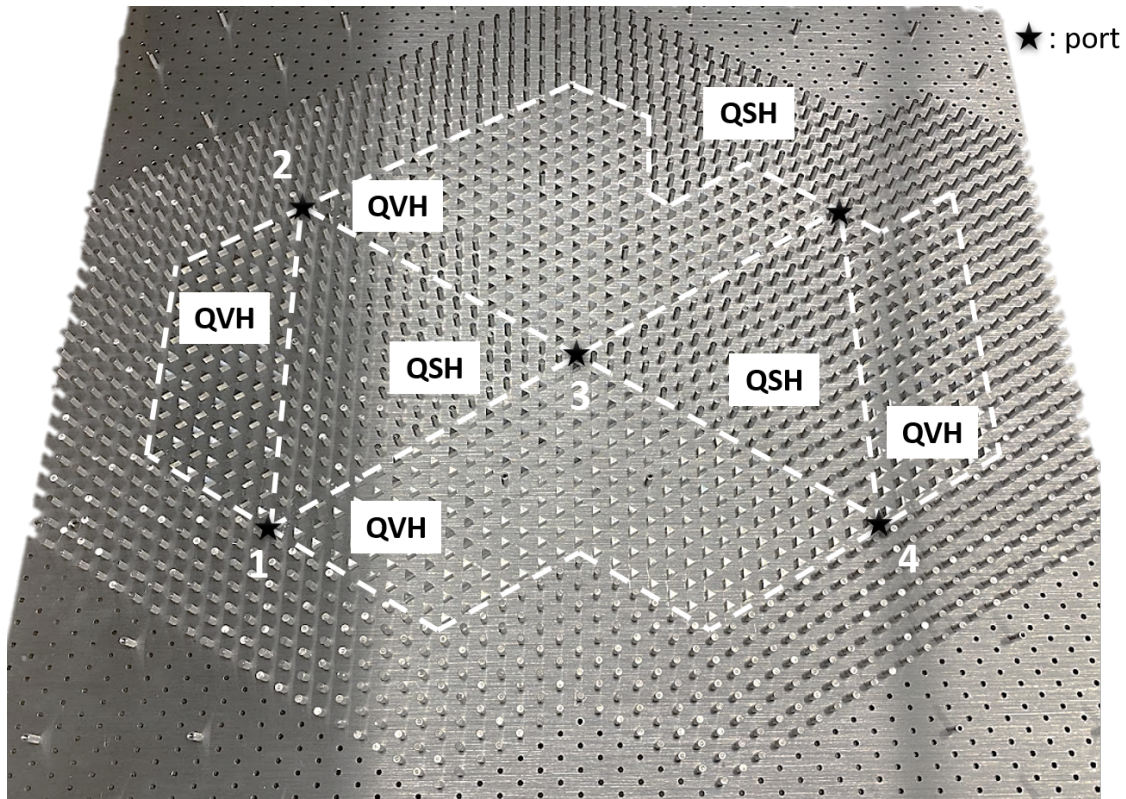


Figure 9.5: Top view of the graph bottom plate, showing all QSH rods, and showing the bottom half of the QVH rods. The white dashed lines are drawn to outline the interface between the QVH and QSH domains, which represents the graph that hosts the topologically-protected modes. The ports locations are marked by the black stars, along with their numbering.

obtained a mean-mode-spacing of the graph of  $\Delta f = 0.09GHz$ , which is close to the theoretical prediction  $\Delta f = \frac{c}{2L_{tot}} = 0.073GHz$ , where the quantity  $L_{tot} = 2.05m$  is the total length of all graph bonds.

Our first goal is to identify the Kramers degeneracy expected in the graph modes. To better examine the degenerate mode property of the data, we compute the Wigner time-delay  $\tau_W = -\frac{i}{M} \frac{d}{df} \ln[\det(S)]$  which helps us to identify scattering matrix poles and zeros. The quantity  $M$  is the number of measurement channels, and  $S$  refers to the full  $M \times M$  complex scattering matrix, measured as a function of frequency. The  $\tau_W$  around groups of modes, as a function of frequency, is fit by Eqn. (7, 8) in Ref. [221]. For convenience, we write down the  $\tau_W$  modeling equations here:

$$Re(\tau_W) = C - \frac{1}{M} \sum_{n=1}^N \left[ \frac{\Gamma_n - \eta}{(f - f_n)^2 + (\Gamma_n - \eta)^2} - \frac{\Gamma_n + \eta}{(f - f_n)^2 + (\Gamma_n + \eta)^2} \right] \quad (9.9)$$

$$Im(\tau_W) = -\frac{1}{M} \sum_{n=1}^N \left[ (f - f_n) \left( \frac{1}{(f - f_n)^2 + (\Gamma_n - \eta)^2} - \frac{1}{(f - f_n)^2 + (\Gamma_n + \eta)^2} \right) \right] \quad (9.10)$$

where the quantities  $\eta, f_n$  and  $C$  are the uniform loss factor, the  $n$ 'th system energy level in frequency, and a constant term for the use of fitting to the data and accounts for contributions to  $Re(\tau_W)$  from far-away resonances, respectively. The quantity  $N$  refers to the total number of modes used during the fitting process. Since we are looking at the Kramers degeneracy, we have  $N = 2$  throughout the Chapter. Here we simplified the fitting process by assuming the zeros and poles of the S-matrix, written as  $z_n$  and  $f_n + i\Gamma_n$  in Ref. [221], where  $n$  is the mode index, are just the complex conjugate of each other. The quantities  $f_n$  and  $\Gamma_n$  are the real and imaginary parts of the  $n$ 'th

pole. This assumption is good for the PTI-graph systems because there is no lumped loss element. We note that the quality of the computed  $\tau_W$  curves is closely related to the noise present in the S-parameter measurement. As advised by my colleague Lei Chen, we adopted an intermediate frequency bandwidth of 10kHz on the VNA for a balance between measurement speed and relatively low phase noise.

Based on Eqns. 9.9 and 9.10, we are able to fit the measured  $\tau_W(f)$  data. The fitted curves are shown as the red solid lines in Fig. 9.6 (b) and (c). Note that we have assumed that the two degenerate modes share the same uniform loss factor  $\eta$ . It is clear from the asymmetric  $\tau_W(f)$  curves in Fig. 9.6 (b) and (c) that the PTI-graph system does host nearly degenerate modes. Our fitting results also back up this observation, and high-quality fitting is achieved by assuming the existence of two nearly degenerate modes. The best-fit parameters are  $(f_1, f_2) = (24.18, 24.20)GHz$  and  $(\Gamma_1, \Gamma_2, \eta) = (0.007, 0.0073, 0.0146)GHz$  for the data in Fig. 9.6 (b), and  $(f_1, f_2) = (24.45, 24.46)GHz$  and  $(\Gamma_1, \Gamma_2, \eta) = (0.0019, 0.005, 0.0098)GHz$  for Fig. 9.6 (c). One may argue that the two nearby modes shown in Fig. 9.6 (b) and (c) might just be two closely located un-related modes. However, the spacing between these two modes is on the order of  $\sim 10MHz$ , which is much smaller than the  $\sim 70MHz$  mean-mode spacing. Thus we believe that we have identified some hints of 2-fold Kramers degeneracy in room-temperature S-parameter experiments.

Note that we did not find 2-fold degeneracy characteristics for all modes evident in the  $\tau_W(f)$  data. In fact, the two sets of curves shown in Fig. 9.6 (b) and (c) are the only examples where the two degenerate modes poles/zeros have a large enough real-part splitting. For other cases, the real part values of the degenerate mode pair might be almost

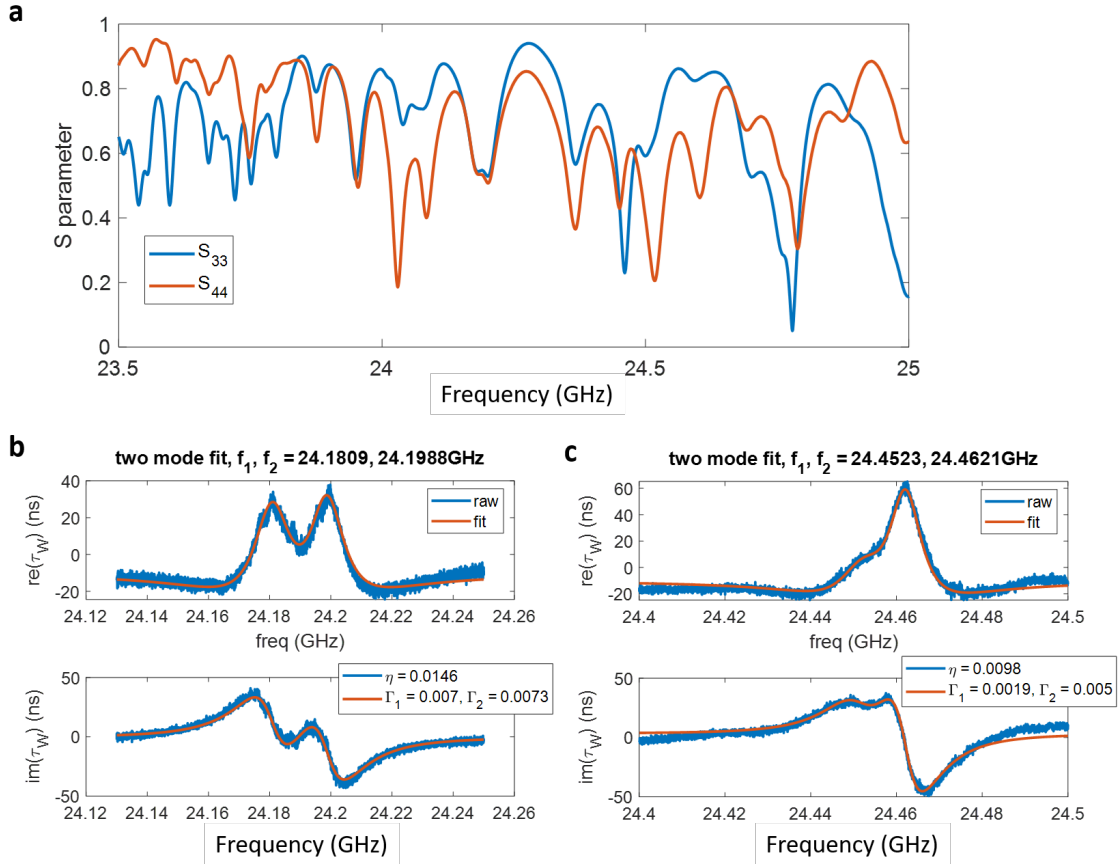


Figure 9.6: **a.** The measured reflection S-parameters as a function of frequency in the bulk bandgap at Ports 3 and 4 of the composite QSH-QVH shown in Fig. 9.5 at room temperature. The measured complex Wigner time delay curves near 24.20 and 24.46 GHz, shown in **b** and **c**, respectively. The fitting results are shown in solid red curves.

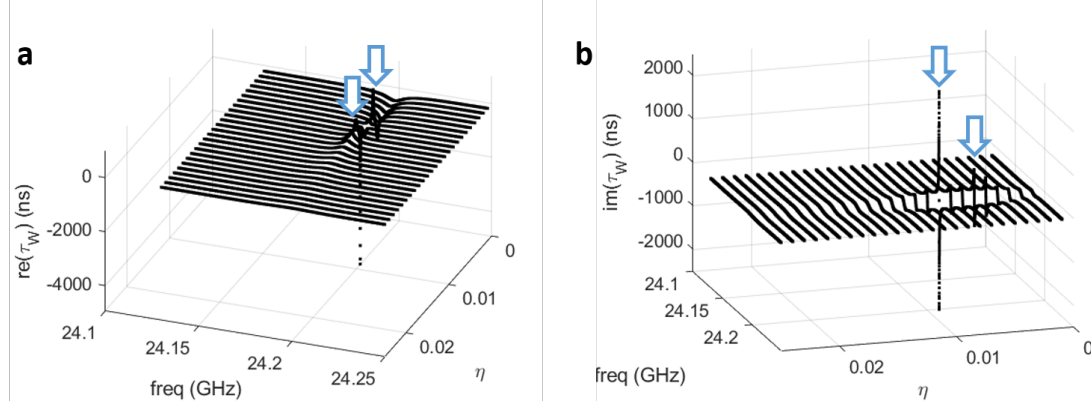


Figure 9.7: **a** and **b** show the real and imaginary parts of the  $\tau_W$  as a function of frequency computed using different values of  $\eta$ , respectively. The  $Re(\tau_W)$  and  $Im(\tau_W)$  show two divergences as  $\eta$  is varied (marked out by the blue arrows) and match the values of  $\Gamma_1$  and  $\Gamma_2$ .

identical so that the corresponding  $\tau_W$  curves do not have an asymmetric shape. However, we believe that one may utilize the difference in degenerate mode imaginary parts  $\Gamma_n$  to reveal the 2-fold degeneracy. This can be accomplished by smoothly decreasing the uniform loss  $\eta$  value from high to low. For example, one may strategically set the initial value of  $\eta$  to be greater than  $\max(\Gamma_1, \Gamma_2)$ , and then decreasing  $\eta$  until  $\eta < \min(\Gamma_1, \Gamma_2)$ . Note that this initial condition for  $\eta$  is satisfied for the modes shown in Figs. 9.6 (b) and (c). During this process, the value of  $\eta$  will become equal to the  $\Gamma_n$  value of one of the two degenerate modes. When this happens, we know from Eqns. 9.9 and 9.10 that the time delay curve will diverge as the denominator  $\rightarrow 0^2 + 0^2$ . And since we usually have  $\Gamma_1 \neq \Gamma_2$ , we can find that  $\tau_W$  curve ‘diverges’ twice during the process. One may call this process a Lazarus time-delay behavior, where  $\eta$  has made  $\tau_W$  ‘die’verge twice to demonstrate the power of degeneracy. We conducted a numerical exercise to illustrate this process in Fig. 9.7. The  $\tau_W$  real and imaginary parts are computed using Eqns. 9.9 and 9.10, where we have set  $f_1 = f_2 = 24.2GHz$  (degenerate modes),  $\Gamma_1 = 0.007GHz$ ,  $\Gamma_2 =$

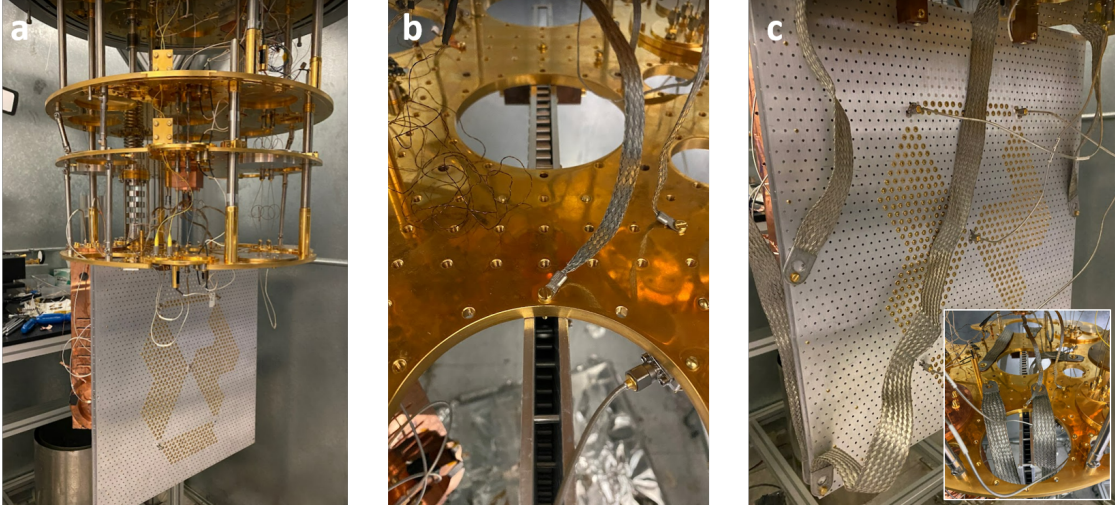


Figure 9.8: **a** and **b** show the front and top views of the PTI-graph structure mounted below the mixing chamber plate, respectively. **c**. The thermal connection (copper connectors and heat straps) and cable connection on the PTI-graph structure. The inset shows the heat-strap fixations on the mixing chamber plate.

$0.0073GHz(\Gamma_1 \neq \Gamma_2)$ , and the uniform loss  $\eta$  is swept from low to high through these values of  $\Gamma$ . It is shown that when the value of uniform loss  $\eta$  equals either  $\Gamma_1$  or  $\Gamma_2$ , the time-delay curve diverges (the real-part flips sign, and the imaginary-part shows high absolute values). This double time-delay divergence can not take place if only one mode exists. We believe that a low-temperature experiment will allow us to gradually change the degree of uniform loss by controlling the conductivity loss of the entire PTI structure but keep the values of  $\Gamma_1$  and  $\Gamma_2$  approximately constant. In this way we can reveal the existence of nearly degenerate modes from the evolution of complex time delay as  $\eta$  is systematically varied with temperature.

## 9.6 Low-temperature Experimental Results

Our first objective is to identify Kramers degenerate pairs of modes in the experiment. We shall use the Lazarus method, created by cooling the graph to  $mK$  temperatures. To vary the degree of loss  $\eta$  in the PTI graph system, we have put the graph structure inside a dilution refrigerator (dil-fridge). The dil-fridge cools the graph structure and reaches a 30mK base temperature (measured by the mixing chamber plate thermometer). During the cooldown from room temperature, the conductivity loss of the PTI graph will decrease. Around the  $T_c$  of aluminum (1.2K), we should see a discontinuous change of transmission measurement due to the superconducting transition of all the metal making up the graph. The graph structure is mounted vertically to the mixing chamber plate (mxc plate) using 4 copper blocks. As shown in Fig. 9.8 (a), the graph structure takes up nearly the entire diameter of the mxc plate and can be considered as a large thermal load to the dil-fridge. Two of the copper connection blocks can be seen in Fig. 9.8 (b). Fig. 9.8 (c) and its inset show the thermal braid connection and cable connection of the graph structure. We used 5 braided heat straps to aid the thermal connection between the graph and the mxc plate to ensure that the temperature of the graph is uniform and close to that of the mxc plate.

In the first cooldown, we encountered several measurement issues that interrupted the temperature sweep. Before discussing these practical issues, we first present the analysis of measured  $\tau_W(f)$  curves during the cooldown. As discussed in the previous section, we expect to find a double divergence of the  $\tau_W(f)$  as  $\eta$  is swept through  $\Gamma_1$  and  $\Gamma_2$ . We have found clear signs of the double divergence for the energy level near

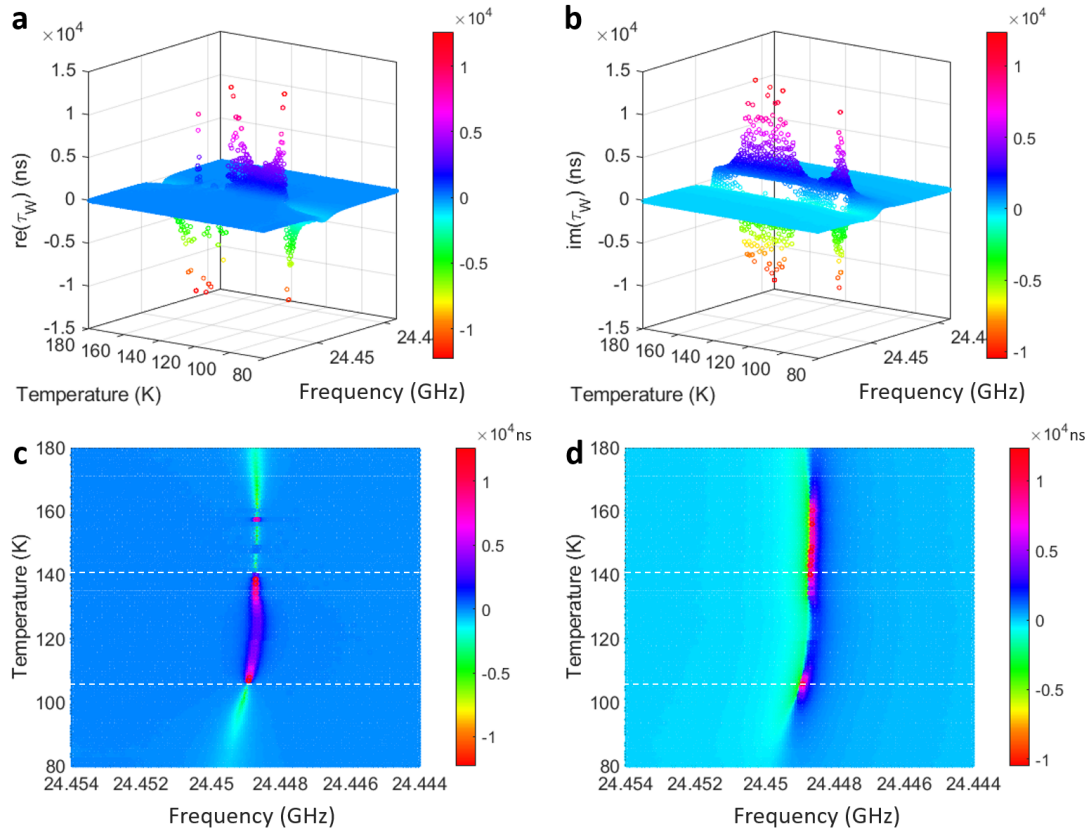


Figure 9.9: **a** and **b** show the real and imaginary part of the measured PTI-graph  $\tau_W$  versus temperature and frequency, respectively. **c** and **d** are the top view of **a** and **b**. To guide the eye, white dashed lines are added to mark the temperatures at which  $\text{Re}(\tau_W)$  changes sign and  $\text{Im}(\tau_W)$  diverges.

24.45GHz. As shown in Fig. 9.9 (a) and (b), the  $\tau_W$  curves diverge twice when temperature changes from 180K to 80K. To guide the eye, we use white dashed lines in 9.9 (c) and (d) to mark out the locations of the  $\tau_W$  divergences ( $Re(\tau_W)$  changes sign and  $Im(\tau_W)$  shows high values). In the real part of  $\tau_W$  curves, we find a double sign flip, and in the imaginary part of  $\tau_W$  curves, we find double high values. In Fig. 9.9 (c) and (d) we plot the top view of the figures in Fig. 9.9 (a) and (b). It is clear that in Fig. 9.9 (c) and (d) only one ridge region of  $\tau_W(f)$  exists during the measurement. This phenomenon means that the frequencies of the two degenerate modes are almost identical. Fig. 9.9 (a) to (d) shows exactly the case where the 2-fold degeneracy can not be identified in the different real part of S-matrix poles/zeros ( $f_i$ ) but can be spotted from the difference in imaginary parts ( $\Gamma_i$ ) during uniform loss ( $\eta$ ) changes. We note that there exists an outlier event near 160K. It can be clearly spotted in 9.9 (a) and (c).

Here we discuss the issues discovered during the first cooldown. Firstly, it became clear that we needed to install a thermometer onto the graph structure so that the PTI-graph temperature could be better monitored. The rods and triangles in Fig. 9.5 are attached to the aluminum plate using a mixture of non-magnetic brass and nylon screws. We plan to change all of the screws from nylon to brass to achieve a better thermal connection and less thermal contraction during the cooldown. Lastly, an odd calibration issue was discovered. We have conducted a 4-port calibration at the end of the long cables, which are connected at the top of the dil-fridge (Fig. 9.10 (a)). The resulting graph measurements are shown in Fig. 9.10 (b) and (c). The S-parameter results (Fig. 9.10 (b)) are acceptable because we did see some differences between the measurements taken at different temperatures. However, the computed  $\tau_W$  results (Fig. 9.10 (c)) show

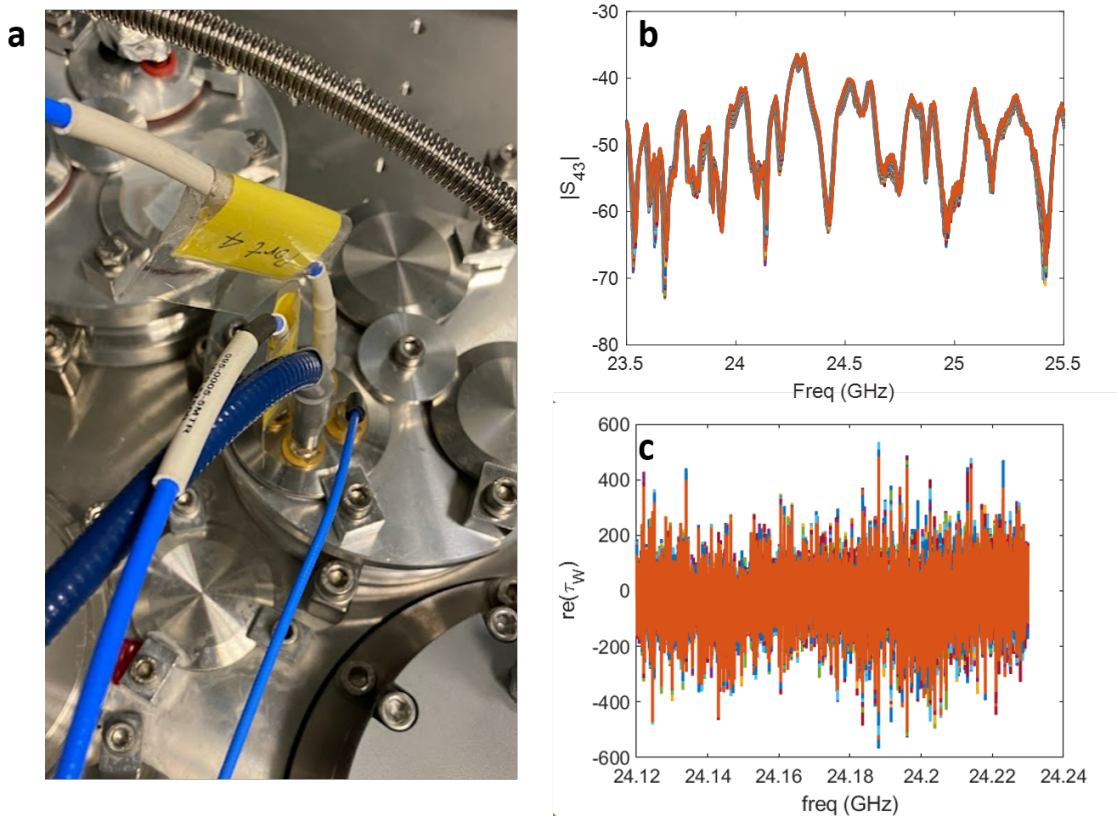


Figure 9.10: **a** shows the 4 cable connections at the top of the fridge. These cables connect to the VNA in room temperature, and go to the PTI-graphs in low temperature environment. **b** and **c** show the measured S-parameter and the real part of  $\tau_W$ , respectively. Different colors represent data measured at 130 different temperatures (from 80K to 4K).

rather noisy results. We hope to resolve these problems in the next cooldown.

## 9.7 Discussion

To sum up, we have proposed a PTI-graph system as a new platform for realizing GSE statistics. An effective T-operator  $T_b$  for the BMW system is presented, and we showed that the operator shows anti-unitary behavior ( $T_b^2 = -1$ ). A QVH-QSH composite BMW structure is designed and fabricated. We first conducted a series of numerical simulations for an ensemble of PTI-graph structures and conducted nearest neighbor level spacing statistics. A relatively good agreement between the GSE theory prediction and the simulated graph system data is found. We have identified the Kramers degeneracy in experimental tests through the asymmetric shape of  $\tau_W(f)$  in room-temperature tests. With the help of low-temperature measurements, we can systematically alter the system uniform loss and find clear double divergence in the measured  $\tau_W$ . Thus, theoretical, numerical, and experimental studies have presented clear evidence for Kramers degeneracy. Our next objective will be conducting the nearest neighbor level spacing statistical test with room-temperature experiments.

## Chapter 10: Conclusions

In this chapter, I hope to summarize the thesis and discuss future directions for the projects. Fig. 10.1 shows a Venn diagram which includes the projects in Chapters 2-9. The general theme of the thesis is wave chaos. In Fig. 10.1, the wave chaos project shows up as the biggest area circle. Under the theme of wave chaos, my projects focus on studying the EM wave propagation in multiple connected chaotic cavities. From the theoretical end, the Random Coupling Model (RCM) is successfully extended from single enclosure systems to multiple coupled systems. I considered both few-mode coupling as well as multi-mode coupling through different sizes of the aperture. Based on the experimental structure designed by Bo Xiao, I conducted the experimental verification of the multi-enclosure RCM theory. Building beyond this, we worked with our colleagues at the University of Nottingham and applied the Power Balance Model to simplify the multi-enclosure RCM model.

In addition to the frequency domain work, I have started to work on a time-domain RCM (TD-RCM). Because the TD-RCM program is a finite difference method that operates in the time-domain, we can include a variety of port-loads, including nonlinear elements. We have also tested the agreement between TD-RCM and the experiment at late times compared to the arrival of short orbits. For future work, the testing of early-time receiver

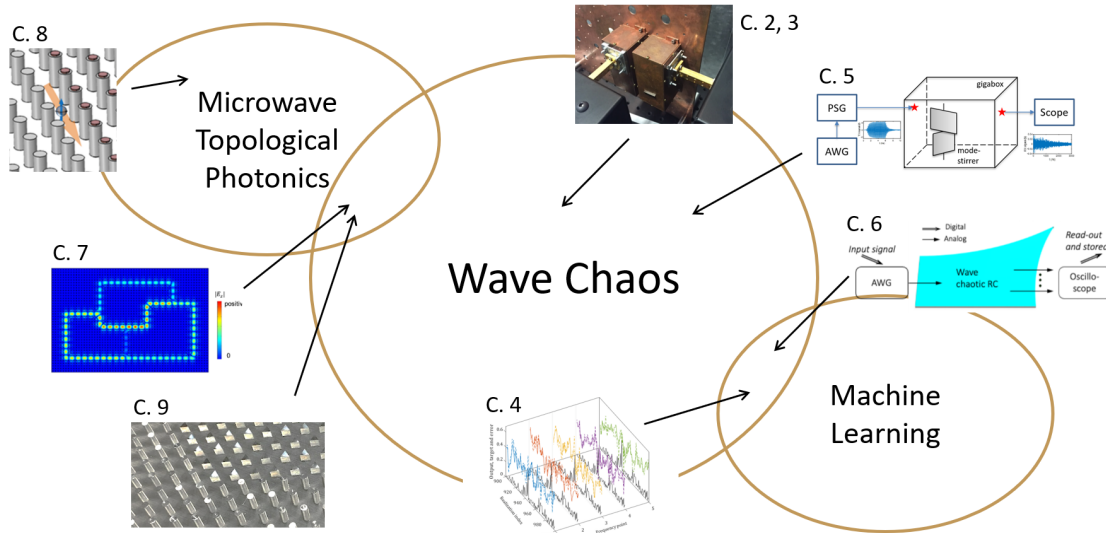


Figure 10.1: Summary of the projects. There are three themes in the thesis: wave chaos, microwave topological photonics, and machine learning. The corresponding chapter indices for the projects are also shown in this diagram. Wave chaos takes the center stage. The topological photonics and the machine learning projects also intersects with the wave chaos themes.

port signal and the experimental study of transmitting port reflected signal can be conducted.

We will also work on developing new types of statistical analysis that can also be simulated with TD-RCM programs. An experimental study of the nonlinear port load cases is also of interest. Another future direction can be packaging the TD-RCM codes into a graphical software (through Matlab GUI).

As side projects, I have studied the photonic topological insulator (PTI) structures and realized a composite PTI structure with both quantum Hall and quantum spin Hall domains. I have also applied machine learning techniques to understand wave chaotic system data details. These two fields of study are represented by two smaller circles in Fig. 10.1. With the knowledge gained from these two projects centered around the theme of wave chaos, I later started three projects: photonic crystal-graphs, PTI-graphs, and wave-based reservoir computing. Because these projects are mixes of wave chaos and a

different field, they are pointed to the area where two circles intersected in Fig. 10.1. For the wave-based reservoir computing project, I use the chaotic EM waves to operate as a physical realization of reservoir computers. Future directions include the scaling down of the resonator to 2D silicon photonics systems. One may also increase the mode-density by changing the experimental structure from 2D to 3D. An increase of mode-density will, in principle, enhance the degree of complexity of the wave-based reservoir. For the PTI-graph project, I use a unique PTI waveguide to build a chaotic graph structure that falls into the GSE (Gaussian Symplectic Ensemble) universality group. Future directions include the low-temperature measurement of the PTI-graph system. By varying the bond length of the PTI-graph, one can create an ensemble of graphs and study the system's eigenmode-spacing statistics, as well as scattering matrix statistics.

## Appendix A: Multi-cavity RCM Modeling

Here we give a brief derivation of expressions for the input and trans-impedances of a coupled multi-enclosure system through extension of the RCM. This material supplements chapter 2.

### A.1 Single Cavity Treatment

We write the radiation admittance matrix  $\underline{\underline{Y_{rad}}}$  of a single cavity, as:

$$\underline{\underline{Y_{rad}}} = \begin{bmatrix} \underline{\underline{Y_{rad,a}}} & 0 \\ 0 & \underline{\underline{Y_{rad,b}}} \end{bmatrix} \quad (\text{A.1})$$

Here  $\underline{\underline{Y_{rad}}}$  is a block diagonal matrix, where the diagonal elements  $\underline{\underline{Y_{rad,a}}}$  or  $\underline{\underline{Y_{rad,b}}}$  are either the radiation admittance of the port  $Y_{rad,port}$ , or the radiation admittance matrix of the aperture modes  $\underline{\underline{Y_{rad,aper}}}$ , depending solely on whether a port or an aperture is connected to that side of the cavity. The off-diagonal components are set to zero under the assumption that there is no direct coupling between ports and apertures. We next incorporate the RCM fluctuating quantities into the description of the fluctuating cavity admittance. The cavity admittance matrix  $\underline{\underline{Y_{cav}}}$  is:

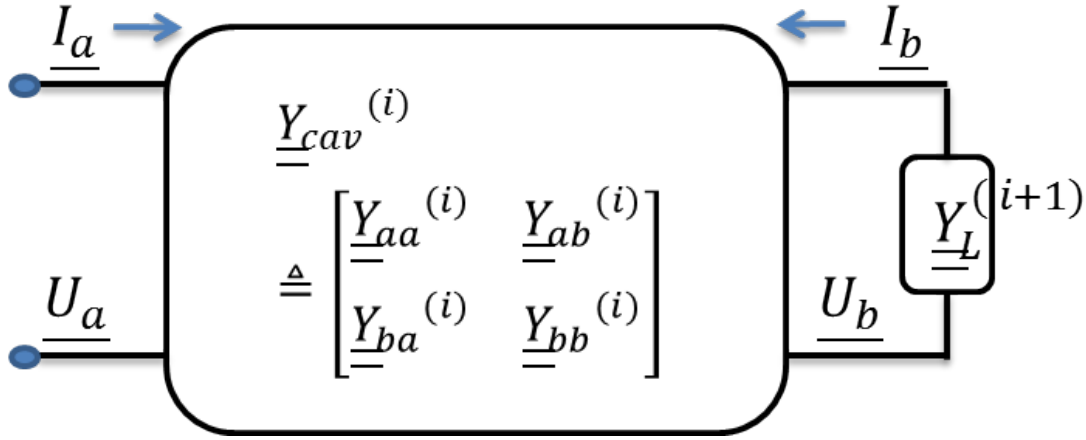


Figure A.1: Schematic diagram of the  $i^{\text{th}}$  cavity in a cascade with port  $a$  on the left and port  $b$  on the right. Here  $U$  and  $I$  refer to the voltage and current at each port (a vector quantity in general).

$$\underline{\underline{Y_{cav}}} = i \cdot \text{Im}(\underline{\underline{Y_{rad}}}) + \text{Re}(\underline{\underline{Y_{rad}}})^{0.5} \cdot \underline{\underline{\xi}} \cdot \text{Re}(\underline{\underline{Y_{rad}}})^{0.5} \quad (\text{A.2})$$

We represent the cavity admittance matrix  $\underline{\underline{Y_{cav}}}$  (as shown in Fig. A.1) as

$$\underline{\underline{Y_{cav}}} = \begin{bmatrix} \underline{\underline{Y_{aa}}} & \underline{\underline{Y_{ab}}} \\ \underline{\underline{Y_{ba}}} & \underline{\underline{Y_{bb}}} \end{bmatrix} \quad (\text{A.3})$$

We then have:

$$\begin{bmatrix} \underline{\underline{I_a}} \\ \underline{\underline{I_b}} \end{bmatrix} = \underline{\underline{Y_{cav}}} \begin{bmatrix} \underline{\underline{U_a}} \\ \underline{\underline{U_b}} \end{bmatrix} = \begin{bmatrix} \underline{\underline{Y_{aa}}} & \underline{\underline{Y_{ab}}} \\ \underline{\underline{Y_{ba}}} & \underline{\underline{Y_{bb}}} \end{bmatrix} \begin{bmatrix} \underline{\underline{U_a}} \\ \underline{\underline{U_b}} \end{bmatrix} \quad (\text{A.4})$$

where the matrix  $\underline{\underline{\xi}}$  is the normalized impedance which has the universal statistical properties predicted by Random Matrix Theory (whose statistics depend only on the loss parameter  $\alpha$ ). The dimension of the matrix  $\underline{\underline{\xi}}$  is equal to the dimension of  $\underline{\underline{Y_{rad}}}$ , which is  $N_a + N_b$ , where  $N_a$  or  $N_b$  is the dimension of the radiation admittance matrices on the two sides of

this cavity.

## A.2 Total Admittance of an N-Cavity Chain

After we construct the  $\underline{\underline{Y}}_{cav}$  matrices for all cavities in the cascade, we are in position to develop the cascade quantities for the enclosure chain. For the  $i^{th}$  cavity in the cavity cascade chain, with the information of how the  $i^{th}$  cavity is connected to its left (previous) and right (next) neighboring cavities, and knowledge of the load admittance presented by the  $(i + 1)^{st}$  cavity  $\underline{\underline{Y}}_L^{(i+1)}$  and everything beyond it, we will have an iterative approach to calculating the total chain admittance matrix:

$$\left\{ \begin{array}{l} \begin{bmatrix} \underline{I}_a \\ \underline{I}_b \end{bmatrix} = \underline{\underline{Y}}_{cav}^{(i)} \cdot \begin{bmatrix} \underline{U}_a \\ \underline{U}_b \end{bmatrix} \\ -\underline{I}_b = \underline{\underline{Y}}_L^{(i+1)} \cdot \underline{U}_b \end{array} \right. \quad (\text{A.5})$$

Eqn. A.5 (same as Eqn. 2.3) expresses the continuity of voltage and current in all modes of the aperture. By solving Eqn. A.5 in matrix form, we have:

$$\underline{\underline{Y}}_L^{(i)} = \underline{\underline{Y}}_{aa}^{(i)} - \underline{\underline{Y}}_{ab}^{(i)} \left( \underline{\underline{Y}}_{bb}^{(i)} + \underline{\underline{Y}}_L^{(i+1)} \right)^{-1} \underline{\underline{Y}}_{ba}^{(i)} \quad (\text{A.6})$$

$$\underline{U}_b = - \left( \underline{\underline{Y}}_{bb}^{(i)} + \underline{\underline{Y}}_L^{(i+1)} \right)^{-1} \underline{\underline{Y}}_{ba}^{(i)} \underline{U}_a \quad (\text{A.7})$$

Eqn. A.6 and Eqn. A.7 are in the exact forms of Eqn. 2.5 and Eqn. 2.4 in the main text. Eqn. A.6 gives the  $\underline{\underline{Y}}_L$  recursion relationship which calculates the load admittance  $\underline{\underline{Y}}_L^{(i)}$  of the  $i^{th}$  cavity given the  $\underline{\underline{Y}}_L^{(i+1)}$  of the  $(i + 1)^{st}$  cavity and everything beyond it. At the end of the cavity chain, the load impedance is the VNA measurement port

load impedance  $Z_0 = 50\Omega$ . We can now calculate the total load admittance of the entire structure from the end load all the way back towards the input port at the first cavity.

### A.3 Input and Trans-Impedances

We will investigate the trans-impedance  $Z_t$  and the input impedance  $Z_{in}$  of the cascaded system from the voltage and  $Y_L$  recursion relationships (Eqn. A.6 and Eqn. A.7). For the scalar  $Z_{in}$ , we have

$$Z_{in} = \frac{U_a^{(1)}}{I_a^{(1)}} = \frac{1}{Y_L^{(1)}} \quad (\text{A.8})$$

where the  $U_a^{(1)}$  and  $I_a^{(1)}$  refers to the scalar voltage and current at the input side of the first cavity.

From Eqn. A.6 and A.7, we have:

$$\begin{aligned} Z_t &= \frac{U_b^{(N)}}{I_a^{(1)}} = \frac{-\left(Y_{bb}^{(N)} + Y_L^{(N+1)}\right)^{-1} \underline{Y}_{ba}^{(N)} \cdot \underline{U}_a^{(N)}}{I_a^{(1)}} \\ &= \frac{-\left(Y_{bb}^{(N)} + Y_L^{(N+1)}\right)^{-1} \underline{Y}_{ba}^{(N)} \cdot \underline{U}_b^{(N-1)}}{I_a^{(1)}} \\ &= \prod_{i=1}^N \left[ -\left(\underline{Y}_{bb}^{(i)} + \underline{Y}_L^{(i+1)}\right)^{-1} \underline{Y}_{ba}^{(i)} \right] \cdot \frac{U_a^{(1)}}{I_a^{(1)}} \\ &= \underline{\Gamma}^{(1)} \left( \prod_{i=2}^{N-1} \underline{\Gamma}^{(i)} \right) \underline{\Gamma}^{(N)} \cdot Z_{in} \end{aligned} \quad (\text{A.9})$$

The quantities  $U_b^{(N)}, I_b^{(N)}, U_a^{(1)}, I_a^{(1)}$  are the scalar voltages and currents at the load connected to the output side of the  $N^{th}$  cavity (subscript  $b$ ), and the input port at the first cavity (subscript  $a$ ). The multiplier  $\underline{\Gamma}^{(i)}$  of the  $i^{th}$  cavity is defined as

$\underline{\underline{\Gamma}}^{(i)} = - \left( \underline{\underline{Y}}_{bb}^{(i)} + \underline{\underline{Y}}_L^{(i+1)} \right)^{-1} \underline{\underline{Y}}_{ba}^{(i)}$ . As discussed in the main text, the elements of  $\underline{\underline{\Gamma}}^{(i)}$  are small because the matrix elements of  $\underline{\underline{Y}}_{bb}$  are larger than  $\underline{\underline{Y}}_{ba}$ . The dimension of  $\underline{\underline{\Gamma}}^{(i)}$  is  $(N_a, N_b)$  where  $N_{a,b}$  refers to the number of propagating modes of the aperture at either the a side or the b side of the cavity. Thus  $\underline{\underline{\Gamma}}^{(i)}$  can be either a matrix or a vector depending on the specific location of the  $i^{th}$  cavity in the entire cascade chain. For example,  $\Gamma^{(i)}$  is in vector form at the first/last cavity ( $i = 1 \text{ or } N$ ) since the input/output of such cavity is a single-mode port.  $\Gamma^{(i)}$  is a matrix at the intermediate cavities ( $i \in [2, N - 1]$ ) due to the fact that these cavities are equipped with multi-mode apertures at both ends. With Eqn. [A.8](#) and [A.9](#), we present the full theoretical formulas of  $Z_{in}$  and  $Z_t$  based on the RCM.

## Appendix B: Multi-cavity RCM Experimental Details

### B.1 Aperture and port radiation admittance studies

The radiation admittance  $Y_{rad}$  and impedance  $Z_{rad}$  refer to the cases where apertures or ports radiate into free space [30, 37, 42]. Numerical simulations and experimental methods are adopted in order to characterize the radiation information of the apertures and ports employed in the experimental set-ups.

We use CST [222] to calculate the frequency dependent radiation admittance matrix of both the scaled and full scale apertures. As shown in Fig. B.1, the aperture is carved out of the surface of a Perfect Electrical Conductor (PEC) plate. The thickness of the PEC plate equals to the thickness of the aperture of interest. The carved plate is attached to a large vacuum box whose boundaries are assigned as radiating. The simulation is run in the time domain solver mode. The waveguide port is assigned at the aperture surface (blue circle in Fig. B.1). Given the operating frequency and the total number of port (which is the aperture) modes, the simulation directly calculates the frequency dependent complex radiation admittance matrix of the aperture. Similar techniques are employed in the aperture cross section numerical study of Ref. [223].

The radiation impedance of the ports are obtained from experimental methods. For the WR10 waveguide port used in the scaled set-up, the  $1 \times 1$  radiation S-parameter ( $S_{rad}$ )

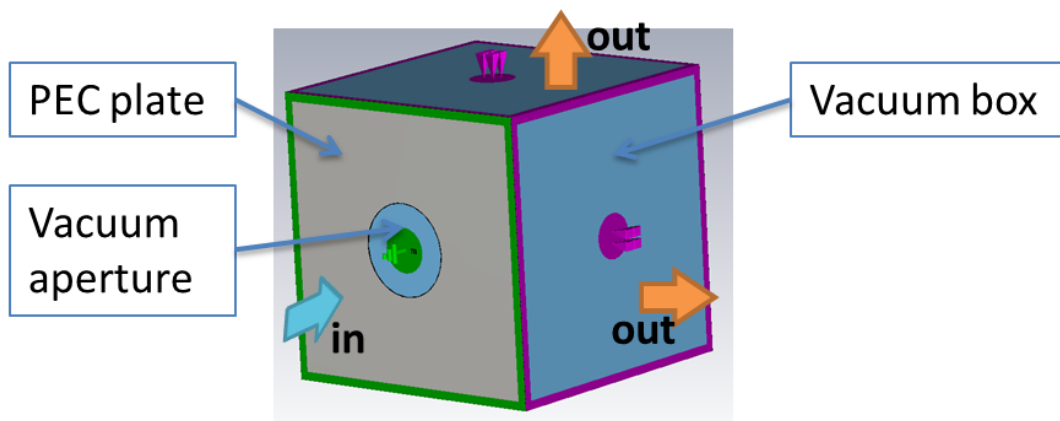


Figure B.1: The model set-up for aperture admittance matrix calculations in the CST simulations. A PEC plate is carved with the dimension of the aperture, and attached to a vacuum box. The port is assigned at the 2D surface of the aperture. The wave enters the aperture (blue arrow) and flows into the vacuum space before absorbed by the surrounding radiation boundaries (orange arrows).

is measured by exposing the bare waveguide flange to a large radiating environment.

The  $Z_{rad}$  is then transformed from the measured  $S_{rad}$ . For the WR178 waveguide ports used in the full scale measurements, time-gating techniques are adopted to calculate the corresponding  $Z_{rad}$  [224].

## B.2 Convergence of the RCM formalism with inclusion of aperture modes

As introduced in the main text, the aperture radiation admittance  $Y_{rad}$  is a  $(n, n)$  matrix where  $n$  is the total number of considered aperture modes. Though the total number of propagating modes can be calculated for given aperture dimensions and operating frequency, the choice of the total number of non-propagating modes which are taken into account is unclear. Here we demonstrate that the RCM cavity cascade formalism can find convergence with an increasing number of considered non-propagating modes. As shown

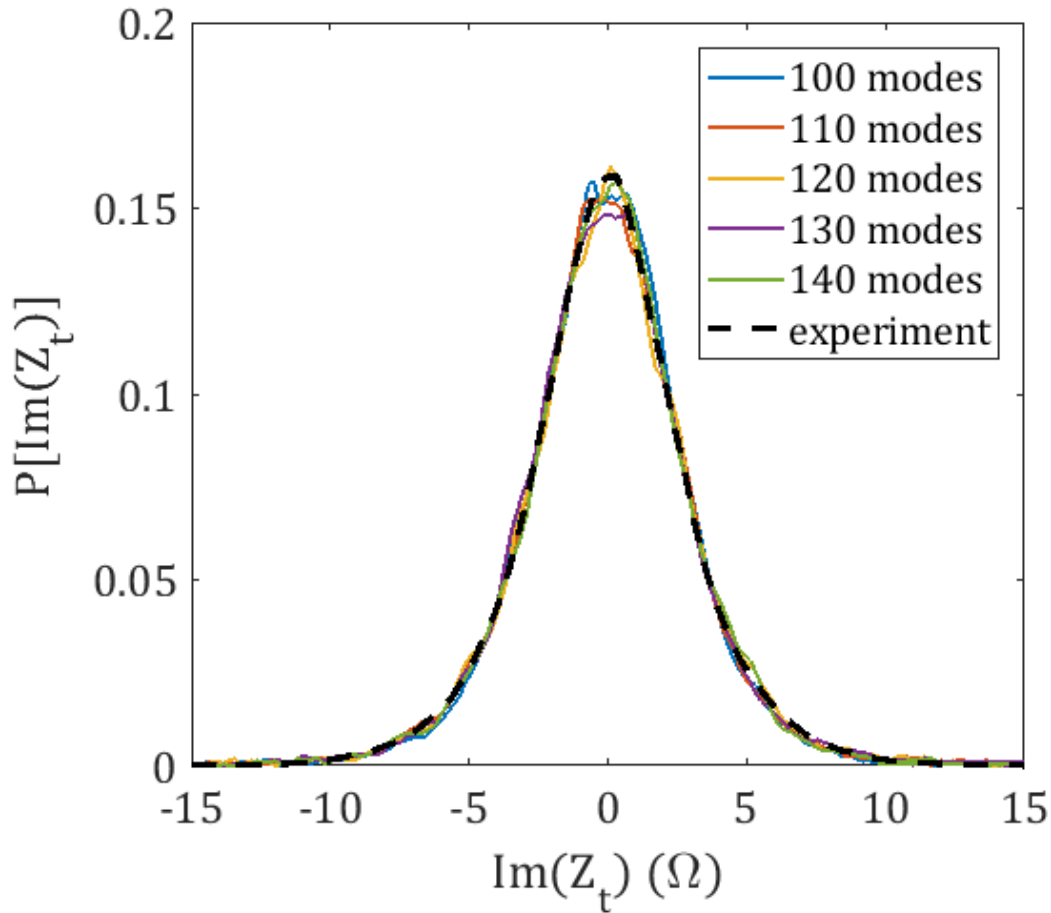


Figure B.2: Statistics of the imaginary part of the trans-impedance for a scaled 3-cavity cascade with circular aperture connections, illustrating the convergence of the theoretical model with increasing mode number included in the aperture admittance matrix. The circular aperture allows 100 propagating modes. The model PDFs curves are nearly unchanged when the non-propagating modes are included.

in Fig. B.2, the convergence of the model is tested by adding circular aperture modes from 100 to 140 in the 3-cavity connection case. The statistics obtained from the theoretical model with different aperture mode numbers remains unchanged beyond 100 modes, and agrees well with the experimental results in that limit.

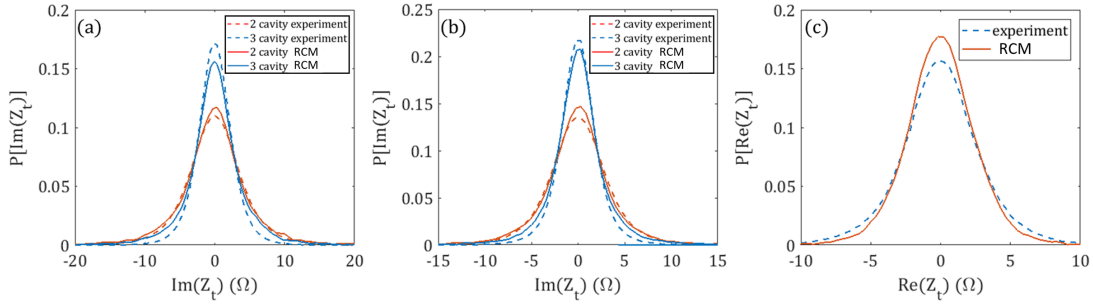


Figure B.3: (a) and (b): Statistics of the imaginary part of the trans-impedance of 2- and 3-cavity cascades when the loss of the system changes. (c): Comparison of the  $Re(Z_t)$  statistics experimental and model results for the scaled 2 cavity set-up, with circular aperture connection. In (a), (b) and (c), the single cavity loss parameter  $\alpha$  is measured to be  $\alpha = 5.7, 7.5$  and  $9.1$ , respectively.

### B.3 Additional cavity cascade experimental studies

The 2- and 3-cavity cascade systems are studied experimentally with various single cavity loss parameter values. As shown in Fig. B.3 (a) and (b), the statistics of 2- and 3-cavity model and experiment  $Im(Z_t)$ s are shown with single cavity loss parameter  $\alpha = 5.7$  and  $7.5$ , respectively. The cascaded cavity structure studied in Fig. B.3 (a) and (b) are full scale structures with circular shaped aperture connections. By placing 2 and 4 RF absorber cones in each individual cavity, single cavity loss parameters are measured as  $\alpha = 5.7$  and  $7.5$ , respectively. We observed reasonably good agreement between the model-generated  $Im(Z_t)$  PDFs (solid lines) and the measured results (dashed lines). In Fig. B.3 (c), the statistics of the  $Re(Z_t)$  of the scaled-down 2-cavity cascade with circular aperture connection are studied. We observed good agreement between the measured data and model-generated results.

## Appendix C: Multi-channel analysis for the cavity cascade system

Within the RCM description, the  $n^{\text{th}}$  cavity in the cavity cascade chain can be modeled by the following equation:

$$\begin{bmatrix} \underline{V}_n^i \\ \underline{V}_n^o \end{bmatrix} = \begin{bmatrix} \underline{Z}_n^{ii} & \underline{Z}_n^{io} \\ \underline{Z}_n^{oi} & \underline{Z}_n^{oo} \end{bmatrix} \begin{bmatrix} \underline{I}_n^i \\ \underline{I}_n^o \end{bmatrix}. \quad (\text{C.1})$$

The superscripts  $i$  and  $o$  refer to the input and output side of the  $n^{\text{th}}$  cavity where we adopt the convention that “input” is on the side closest to the input TX port of the cavity chain and “output” is on the side with the RX port. The voltage vectors  $\underline{V}$  and current vectors  $\underline{I}$  at the input and output sides of a cavity are connected through the cavity impedance matrix as shown in Eq. ((C.1)). The Z-matrix of the  $n^{\text{th}}$  cavity is written as a  $2 \times 2$  block matrix. Assuming the  $n^{\text{th}}$  cavity has  $m_1$  and  $m_2$  coupling channels at its input and output

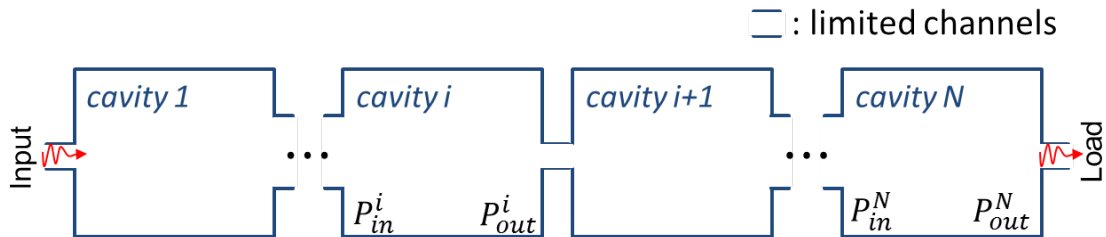


Figure C.1: Schematic of a cavity cascade array with many-channel connecting apertures between all cavities except that between cavity  $i$  and cavity  $i + 1$ . Note the definition of input and output powers at each cavity aperture.

sides, the input vectors  $(\underline{V}_n^i, \underline{I}_n^i)$  are  $m_1 \times 1$ , and the output vectors  $(\underline{V}_n^o, \underline{I}_n^o)$  are  $m_2 \times 1$ . Correspondingly, the dimension of the  $\underline{Z}$ -matrix elements are  $m_1 \times m_1$ ,  $m_2 \times m_2$ ,  $m_1 \times m_2$  and  $m_2 \times m_1$  for  $\underline{Z}_n^{ii}$ ,  $\underline{Z}_n^{oo}$ ,  $\underline{Z}_n^{io}$  and  $\underline{Z}_n^{oi}$ , respectively. For simplicity, we assume the RCM description of the off-diagonal impedance matrices as

$$\underline{Z}_n^{oi} = (\underline{R}_n^o)^{1/2} \underline{\xi}_n (\underline{R}_n^i)^{1/2}, \quad (\text{C.2})$$

and the matrices  $\underline{Z}_n^{oo,ii}$  are diagonal. The  $\underline{R}_n^{i,o}$  are the input and output radiation resistance matrices, and  $\underline{\xi}_n$  is the RCM normalized impedance matrix. Since the output side of the  $n^{\text{th}}$  cavity is connected to the input side of the  $(n+1)^{\text{st}}$  cavity, the continuity relationships of voltages and currents between the two cavities are:

$$\underline{V}_n^o = \underline{V}_{n+1}^i, \quad \underline{I}_n^o = -\underline{I}_{n+1}^i. \quad (\text{C.3})$$

In the high-loss limit, the output current at the  $(n+1)^{\text{st}}$  cavity  $\underline{I}_{n+1}^o$  is much smaller than the input current at the  $n^{\text{th}}$  cavity  $\underline{I}_n^i$ . By solving Eqs. (C.1) and (C.3) and neglecting terms  $\underline{Z}_{n+1}^{io} \underline{I}_{n+1}^o$  (small compared to the  $\underline{Z}_n^{ii}$  terms), the relationship between the input currents at the  $n^{\text{th}}$  and  $(n+1)^{\text{st}}$  cavity in the high-loss limit is written as

$$(\underline{Z}_{n+1}^{ii} + \underline{Z}_n^{oo})^{-1} \underline{Z}_n^{oi} \underline{I}_n^i = \underline{I}_{n+1}^i.$$

We then rewrite this equation as:

$$\begin{aligned}\underline{\psi}_{n+1} &= \underline{\tau}_{n \rightarrow n+1} \underline{\xi}_{\underline{n}} \underline{\psi}_{\underline{n}} \quad \text{with} \\ \underline{\tau}_{n \rightarrow n+1} &= (\underline{R}_{n+1}^i)^{1/2} (\underline{Z}_{n+1}^{ii} + \underline{Z}_{\underline{n}}^{oo})^{-1} (\underline{R}_{\underline{n}}^o)^{1/2},\end{aligned}\tag{C.4}$$

a transition matrix which describes the coupling from the  $n^{\text{th}}$  cavity to the  $(n+1)^{\text{st}}$  with  $\underline{R}_{\underline{n}}^{i,o}$  as in (C.2), and the  $\underline{\psi}_{\underline{n}} = (\underline{R}_{\underline{n}}^i)^{1/2} \underline{I}_{\underline{n}}^i$  is a current-like vector that describes the input signal of the cavity  $n$ . The power entering the  $n^{\text{th}}$  cavity is given by,

$$P_n = \frac{1}{2} \text{Re} \left[ \underline{I}_{\underline{n}}^{\dagger} \underline{Z}_{\underline{n}}^{ii} \underline{I}_{\underline{n}} \right] = \frac{1}{2} \underline{\psi}_{\underline{n}}^{\dagger} \underline{\psi}_{\underline{n}}\tag{C.5}$$

We first assume the transition matrix  $\underline{\tau}$  to be diagonal. The input power at the  $(n+1)^{\text{st}}$  cavity is written as:

$$\begin{aligned}P_{n+1} &= \frac{1}{2} \underline{\psi}_{n+1}^{\dagger} \underline{\psi}_{n+1} \\ &= \frac{1}{2} \left( \underline{\tau}_{n \rightarrow n+1} \underline{\xi}_{\underline{n}} \underline{\psi}_{\underline{n}} \right)^{\dagger} \left( \underline{\tau}_{n \rightarrow n+1} \underline{\xi}_{\underline{n}} \underline{\psi}_{\underline{n}} \right) \\ &= \frac{1}{2} \sum_{i,j,k} (\psi_{n,i}^* \xi_{ji}^* |\tau_j|^2 \xi_{jk} \psi_{n,k})\end{aligned}\tag{C.6}$$

The more general cases, where the constraint of  $\underline{\tau}$  being diagonal is lifted, will be discussed later in this section. With  $\langle P_n \rangle = \frac{1}{2} \langle \underline{\psi}_{\underline{n}}^{\dagger} \underline{\psi}_{\underline{n}} \rangle$  being the average input power at the  $n^{\text{th}}$  cavity, and the fact that  $\langle \xi_{ji}^* \xi_{j'i'} \rangle = \langle \xi_{ji}^* \xi_{ji} \rangle \delta_{ii'} \delta_{jj'}$ , we can further simplify Eq. (C.6) as:

$$\langle P_{n+1} \rangle = \langle P_n \rangle \cdot \langle |\xi|^2 \rangle \cdot \sum_j |\tau_j|^2 = \langle P_n \rangle \langle |\xi|^2 \rangle \sum_j T_j\tag{C.7}$$

where  $T_j = |\tau_j|^2$  and the sum on  $j$  runs from all transmitting channels. Based on the relationship in Eq. (C.7), we next analyze the fluctuation level of the power delivered to the load ( $P_L$ ) by studying the ratio  $\kappa = \langle P_L^2 \rangle / \langle P_L \rangle^2$ . To simplify the following expression,  $X_j = \psi_{n,j}^* \psi_{n,j}$  and  $Y_j = \psi_{n+1,j}^* \psi_{n+1,j}$  are employed in the following calculations.

Equation (C.6) is now rewritten as  $Y_j = T_j \sum_{i,i'} \psi_{n,i}^* \psi_{n,i'} \xi_{ji}^* \xi_{ji'}$ , and further we have  $\langle Y_j \rangle = T_j \langle |\xi|^2 \rangle \sum_i \langle X_i \rangle$ . Utilizing  $\langle |\xi|^4 \rangle = 2 \langle |\xi|^2 \rangle^2$  and  $\langle \xi_{ji}^* \xi_{ji'} \xi_{ji}^* \xi_{ji'} \rangle = \langle \xi_{ji}^* \xi_{ji}^* \rangle \langle \xi_{ji'} \xi_{ji'} \rangle = 0$  when  $i \neq i'$ , we have:

$$\sum_{jj'} \langle Y_j Y_{j'} \rangle = \langle |\xi|^2 \rangle^2 \sum_{i,i''} \langle X_i X_{i''} \rangle \left[ \sum_{jj'} T_j T_{j'} + \sum_j T_j^2 \right] \quad (\text{C.8})$$

We then introduce a mean power transmission coefficient for the  $n^{\text{th}}$  cavity  $\bar{T}_n$  and an effective total number of channels  $M_n$ , defined as:

$$\bar{T}_n = \langle |\xi|^2 \rangle \sum_j T_j, \quad M_n^{-1} = \sum_j T_j^2 / \left( \sum_j T_j \right)^2, \quad (\text{C.9})$$

respectively. Thus we have the power transmitted into the  $(n+1)^{\text{st}}$  cavity (Eq. (C.7)) written as:

$$\langle P_{n+1} \rangle = \bar{T}_n \langle P_n \rangle, \quad (\text{C.10})$$

and

$$\langle P_{n+1}^2 \rangle = \bar{T}_n^2 (1 + M_n^{-1}) \langle P_n^2 \rangle. \quad (\text{C.11})$$

The fluctuation level of the power after  $N$  cavities is:

$$\kappa = \frac{\langle P_L^2 \rangle}{\langle P_L \rangle^2} = \frac{\langle P_1^2 \rangle}{\langle P_1 \rangle^2} \prod_{n=1}^N (1 + M_n^{-1}) = \prod_{n=1}^N (1 + M_n^{-1}). \quad (\text{C.12})$$

Here we utilized the fact that the power injected into the first cavity ( $P_1$ ) is a fixed scalar in the case of a steady input. Since the last cavity is connected to the load with a single-mode port in experiments, we have  $(1 + M_N^{-1}) = 2$  at the last cavity. The overall fluctuating level of load power is

$$\kappa = \frac{\langle P_L^2 \rangle}{\langle P_L \rangle^2} = 2 \times \left[ \prod_{n=1}^{N-1} (1 + M_n^{-1}) \right]. \quad (\text{C.13})$$

For a system with a large number of connecting channels ( $M_n \gg 1$ ) between the neighbouring cavities, such as the circular aperture connection which allows  $\sim 100$  propagating modes, the factor  $(1 + M_n^{-1}) \rightarrow 1$ . In this limit, the mean field methods are sufficient to describe the power flow for cavities with strong coupling. On the contrary, the hybrid model is not expected to work for system with few coupling channels inside a cavity cascade. The study explains the experimental observations that hybrid models are successfully applied to systems with multi-mode apertures connections, while fail to generate predictions for systems with “bottlenecks”.

We also note that the proposed hybrid model assumes each input current throughout the chain is Gaussian distributed while the RCM predicts non-Gaussian statistics [33]. In the presence of a “bottleneck” connection, a deviation from Gaussian statistics of the input current distribution will be present caused by the fluctuating nature of the narrow

aperture coupling.

We next expand the analysis to the more general cases where the transition matrix  $\underline{\tau}$  is no longer a diagonal matrix. With Eqs. (C.6) and (C.8), the expression for  $Y_j$  becomes:

$$Y_j = \sum_{j'j''} \tau_{jj'}^* \tau_{jj''} \sum_{i',i''} \psi_{n,i'}^* \psi_{n,i''} \xi_{j'i'}^* \xi_{j''i''}. \quad (\text{C.14})$$

And correspondingly the average of  $Y_j$  is  $\langle Y_j \rangle = \sum_{j'} \tau_{jj'}^* \tau_{jj'} \langle |\xi|^2 \rangle \sum_i \langle X_i \rangle$ . With the updated  $\bar{T}_n = \langle |\xi|^2 \rangle \sum_{jj'} \tau_{jj'}^* \tau_{jj'}$ , we sum on  $j$  and have

$$\sum_j \langle Y_j \rangle = \langle |\xi|^2 \rangle \sum_{jj'} \tau_{jj'}^* \tau_{jj'} \sum_i \langle X_i \rangle = \bar{T}_n \sum_i \langle X_i \rangle, \quad (\text{C.15})$$

and the average of the product of  $Y$ 's is

$$\begin{aligned} \langle Y_k Y_{k'} \rangle &= \sum_{j,j',j'',j'''} \tau_{kj}^* \tau_{kj'} \tau_{k'j''}^* \tau_{k'j'''} \cdot \\ &\sum_{i,i',i'',i'''} \langle \psi_{n,i}^* \psi_{n,i'} \psi_{n,i''}^* \psi_{n,i'''} \rangle \langle \xi_{ji}^* \xi_{j'i'} \xi_{j''i''}^* \xi_{j'''i'''} \rangle. \end{aligned} \quad (\text{C.16})$$

With careful calculation, the double summation of Eq. (C.16) over  $k$  and  $k'$  gives:

$$\begin{aligned} \sum_{k,k'} \langle Y_k Y_{k'} \rangle / \langle |\xi|^2 \rangle^2 &= \sum_{ii'} \langle X_i X_{i'} \rangle \left[ \sum_{jk} \tau_{kj}^* \tau_{kj} \right]^2 + \\ &\sum_{ii'} \langle X_i X_{i'} \rangle \sum_{jj'} \left[ \sum_k \tau_{kj}^* \tau_{kj'} \right]^2. \end{aligned} \quad (\text{C.17})$$

With the updated  $\bar{T}_n$ , we reach a similar expression of the power flow as in Eq. (C.11)

with the new  $M_n^{-1}$  written as

$$M_n^{-1} = \sum_{jj'} \left[ \sum_k \tau_{kj}^* \tau_{kj'} \right]^2 / \left[ \sum_{jj'} \tau_{jj'}^* \tau_{jj'} \right]^2. \quad (\text{C.18})$$

Thus the conclusions of the multi-channel analysis can be applied to the more general cases with the refined  $\underline{\tau}$ ,  $\bar{T}_n$  and  $M_n^{-1}$ .

## Appendix D: Applying the Hybrid Model to Generic Cavity Systems

Here we propose a scheme of applying the hybrid model to more general cases, where there exists several limited-channel connections between the intermediate cavities. Due to the large power flow fluctuations induced by these “bottlenecks”, we apply RCM to better characterize these connections. A general case is shown in Fig. C.1. We study the treatment of limited channel connections between the  $i^{th}$  and  $(i + 1)^{st}$  cavities in a N-cavity cascade chain. The treatment involves four steps:

1. Use the PWB N-cavity model to calculate the input, output power of the  $i^{th}$  cavity

$$P_{in}^i|_{PWB}, P_{out}^i|_{PWB}, \text{ and the input power at the last } (N^{th}) \text{ cavity } P_{in}^N|_{PWB}.$$

2. For the case of a bottleneck between cavity  $i$  and cavity  $i + 1$  (Fig. C.1), use the calculated  $P_{in}^i|_{PWB}$  and RCM treatment to calculate an ensemble of the output power of the  $i^{th}$  cavity  $P_{out}^i|_{RCM}$ .

3. Update the input power at the last cavity by

$$P_{in}^N|_{RCM} = P_{out}^i|_{RCM} \cdot \frac{P_{in}^N}{P_{out}^i}|_{PWB}.$$

Note that we therefore obtain an ensemble of the input power to the last cavity

$$P_{in}^N|_{RCM}.$$

4. Use RCM to calculate an ensemble of the output power of the  $N^{th}$  cavity  $P_{out}^N|_{RCM}$  with the ensemble of  $P_{in}^N|_{RCM}$  obtained from (3).

For cases where there exist multiple “bottlenecks” inside the chain (beyond cavity  $i$ ), one may repeat the procedure (2)-(4) by actively changing the cavity index  $N$  to the next cavity connected through a bottleneck.

## Appendix E: Simplified PWB-RCM Hybrid Method

Here we present a simplified treatment of the PWB-RCM hybrid model where the full-wave simulated aperture radiation admittance matrix is no longer required. We assume that all inter-cavity apertures are large on the scale of a wavelength, ie. the original PWB-RCM treatment is applicable. We also will assume that all cavities are in the high-loss ( $\alpha > 1$ ) limit. This  $Y_{aper}$ -free treatment will further decrease the computational cost of the hybrid model. We utilize Eqs. (C.4-C.6) from Appendix C to introduce the new treatment.

Consider an N-cavity cascade chain, one may treat the load connected to the output port of the  $N^{th}$  cavity as the  $(N + 1)^{st}$  effective cavity. The induced power is equal to the input power of the  $(N + 1)^{st}$  cavity:

$$\begin{aligned} P_{load} = P_{N+1} &= \frac{1}{2} \psi_{N+1}^\dagger \psi_{N+1} \\ &= \frac{1}{2} \left( \tau_{N \rightarrow N+1} \underline{\xi}_N \underline{\psi}_n \right)^\dagger \left( \tau_{N \rightarrow N+1} \underline{\xi}_N \underline{\psi}_n \right) \end{aligned} \quad (\text{E.1})$$

where  $\tau_{N \rightarrow N+1} = (R_{N+1}^i)^{1/2} (Z_{N+1}^{ii} + Z_N^{oo})^{-1} (R_N^o)^{1/2}$  is a scalar transition factor due to the fact that a single-mode port acts as a single-mode ‘aperture’ connecting the  $N^{th}$  and  $(N + 1)^{st}$  cavity (the load). As introduced in the main text, the radiation impedance of the port, which is used to calculate  $\tau_{N \rightarrow N+1}$ , is obtained from the scattering matrix

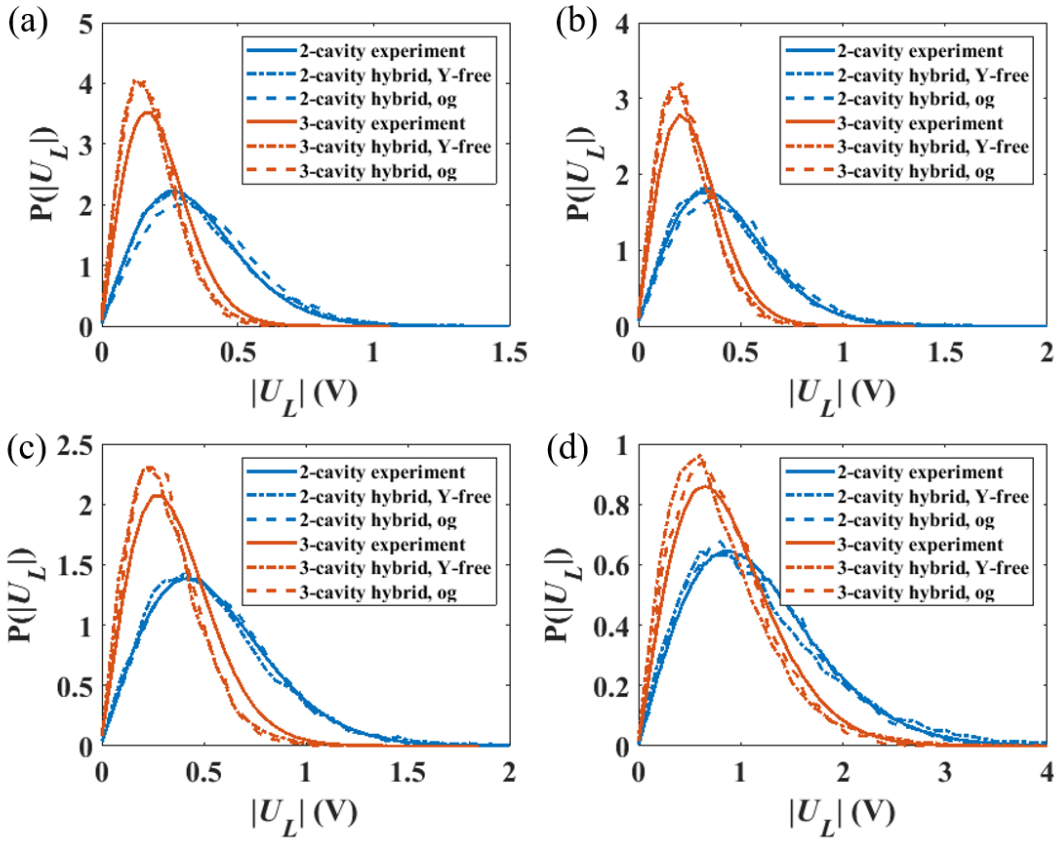


Figure E.1: The PDFs of load induced voltage  $|U_L|$  of 2- and 3-cavity experiments (solid), hybrid model (dashed), and the simplified hybrid model (dash-dotted). The single cavity loss parameter is varied from 9.7, 7.5, 5.7 and 1.7 from (a-d), respectively.

measurements of the waveguide ports.

Equation (E.1) is further generalized as:

$$P_{load} = \frac{1}{2} \psi_{N+1}^\dagger \psi_{N+1} = \frac{1}{2} |\tau_{N \rightarrow N+1}|^2 \underline{\psi}_n^\dagger \underline{\xi}_N^\dagger \underline{\xi}_N \underline{\psi}_n. \quad (\text{E.2})$$

The ensemble average of  $P_{load}$  is

$$\begin{aligned} \langle P_{load} \rangle &= \frac{1}{2} |\tau_{N \rightarrow N+1}|^2 \left\langle \underline{\psi}_n^\dagger \underline{\xi}_N^\dagger \underline{\xi}_N \underline{\psi}_n \right\rangle \\ &= \frac{1}{2} |\tau_{N \rightarrow N+1}|^2 \underline{\psi}_n^\dagger \underline{\psi}_n \left\langle \underline{\xi}_N^\dagger \underline{\xi}_N \right\rangle. \end{aligned} \quad (\text{E.3})$$

In the above equation, the quantity  $\underline{\psi}_n$  is moved out of the ensemble averaging because only  $\underline{\xi}_N$  is varying under ensemble average while  $\underline{\psi}_n$  and  $\tau_{N \rightarrow N+1}$  are not. As defined in Appendix C, we write  $\underline{\psi}_n = \underline{R}_N^{ii 1/2} \cdot \underline{I}_n^i$  under the high-loss assumption. Here  $\underline{R}_N^{ii}$  is set as the radiation impedance of the aperture which does not change value under ensemble averaging. The input current vector  $\underline{I}_n^i$  is also considered to be not changing since the cavity off-diagonal impedance element  $\underline{Z}_n^{io}$  (Eq. (C.1)) is small at high-loss limit, and the input power of the  $N^{th}$  cavity is fixed from the prior PWB calculation. Since the input power of the  $N^{th}$  cavity  $P_N = \frac{1}{2} \underline{\psi}_N^\dagger \underline{\psi}_N$  is given by the PWB calculation, we may further simplify Eq. (E.3) as  $\langle P_{load} \rangle = \frac{1}{2} |\tau_{N \rightarrow N+1}|^2 \underline{\psi}_n^\dagger \underline{\psi}_n \left\langle \underline{\xi}_N^\dagger \underline{\xi}_N \right\rangle = P_N |\tau_{N \rightarrow N+1}|^2 \cdot \left\langle \underline{\xi}_N^\dagger \underline{\xi}_N \right\rangle$ . The vector element of  $\underline{\xi}_N$ ,  $\xi_i$ , is generated using the same method as in Section III. The vector product  $\underline{\xi}_N^\dagger \underline{\xi}_N$  is the summation of a large number of  $\xi_i^* \xi_i$ s. Thus  $\underline{\xi}_N^\dagger \underline{\xi}_N$  and  $\xi_i^* \xi_i$  have the same expected value according to the law of large numbers. We finally write  $\langle P_{load} \rangle = P_N |\tau_{N \rightarrow N+1}|^2 \langle \xi_i^* \xi_i \rangle$  and Eq. (E.2) is reduced to scalar components  $P_{load} = P_N |\tau_{N \rightarrow N+1}|^2 \xi_i^* \xi_i$ .

The comparison of the original hybrid model and the  $Y_{aper}$ -free hybrid model is presented in Fig. E.1. Good agreement between the simplified hybrid model predictions and the experimental cases for the PDF of load induced voltages are found. The original hybrid model slightly outperforms its simplified version for the 3-cavity cases (red curves in Fig. E.1 (a-d)), and it is expected that the accuracy of predictions will decrease for longer chains. Such an effect may be caused by the absence of an aperture admittance matrix in the simplified hybrid model. The  $Y_{aper}$ -free treatment would broaden the applicable range of the PWB-RCM hybrid model to situations where the exact shape of the aperture is unknown and the numerical simulation of the aperture is unavailable. However, this shortcut shares the same high-loss ( $\alpha > 1$ ) assumption since it is built on the multi-channel analysis (Appendix C). We also note that for situations discussed in Appendix D, the admittance matrix of the narrow aperture (bottleneck) is required to compute the transition matrix  $\underline{\underline{\tau}}$ .

## Appendix F: Wave-based Reservoir Computing Details

### F.1 Simulation setup

We have conducted numerical simulations of the wave chaotic RC with the software package CST Studio. The RC tasks are simulated with the time-domain solver, where the bowtie-billiard is realized with the exact geometry and the same input waveforms used in the experiment. The system parameters are matched to the experimental cases, including the loss of the enclosure, the parameters of the microwave diodes, the amplitude and the center frequency of the input signal. The high-dimensional combined RC is realized with the RETs, where the boundary condition perturbation is realized using the cylindrical metallic perturber with the same dimension as the experimental one. The simulated RCs go through the same off-line training process using the simulated induced voltage signal at the diode-loaded ports.

### F.2 Observer tasks for dynamical systems

For the observer tasks, the input is a subset of a complex multi-variable dynamical system and the output is the full set of variables of the system. We have applied the observer task for two common chaotic attractors. The chaotic Rössler system is governed

by

$$\begin{aligned}
 \dot{x} &= -y - z, \\
 \dot{y} &= x + ay, \\
 \dot{z} &= b + z(x - c),
 \end{aligned} \tag{F.1}$$

where  $a = 0.5, b = 2.1, c = 3.5$ . The Hénon-map is governed by

$$\begin{aligned}
 x_{n+1} &= 1 - ax_n^2 + y_n, \\
 y_{n+1} &= bx_n,
 \end{aligned} \tag{F.2}$$

where  $a = 1.4, b = 0.3$ . The Rössler  $x$  component is transformed into a continuously waveform with a center frequency around  $4GHz$ , and the RC is expected to produce continuous predictions of both the  $y$  and  $z$  components without knowing the governing equations. In the training period, the input is the Rössler  $x$  component with  $\sim 250$  oscillation periods  $T_{osc}$ , and the testing period includes  $\sim 50$  periods. The input of the discrete Hénon-map is the  $x$  series where each bit is sampled for  $T_{bit} \sim 60ps$ . Similarly, the processing speed of the task can be further improved using equipment with higher sampling rates. The training waveform of the Hénon-map has a length of 4000 bits, and the testing waveform is set to 1000 bits. The Hénon-map observer task aims to infer the  $y$  series solely with the knowledge of the  $x$  series. For both attractor observer tasks, the input series are scaled to have a zero mean and unit standard deviation in order to balance the positive and negative amplitudes. Depending on the nature of the chaotic attractors, the optimal observer task performance is achieved under different RC parameters as shown in Fig. 6.3. With a well-trained system, the wave chaotic RC is able to infer

the full set of chaotic attractors accurately as long as the observation of the system subset is provided consistently.

### F.3 Benchmark tests

For the NARMA10 task, the input is a random bit series  $u(n)$  drawn from a uniform distribution over the interval  $[0, 0.5]$ . The target output is computed from the following 10th-order nonlinear relationship:  $y(n + 1) = 0.3y(n) + 0.05y(n) [\sum_{i=0}^9 y(n - i)] + 1.5u(n - 9) \cdot u(n) + 0.1$ . Its complex behaviour and a 10-state memory requirement make the NARMA10 task one of the most popular benchmark tests for both software and hardware RC. In the experiment, the input is a time-domain waveform where each bit is sampled for  $T_{bit} \sim 60ps$ . We note that such choices of input waveform speeds are limited by the sampling speed of both the AWG and the oscilloscope. The training waveform has a length of 4000 random bits, and the testing waveform is set to 1000 bits.

For the function simulator task, the wave chaotic RC is expected to reproduce the dynamics of the function  $s(t) = \frac{3}{4}u(t)^3$ , where  $u(t)$  is a continuous sine-wave input. In the experiment, we employ a  $4GHz$  sine wave input with a duration of  $\sim 300$  oscillation periods. The length of the training and testing sets are set to a 80-20 ratio. We note that the wave chaotic RC is also able to simulate other types of input functions, including two-tone and three-tone signals.

For the nonlinear channel equalizer (NCE) task, the goal is to recover the random 4-level symbol sequence from a noisy series which simulates the received signal sent through a nonlinear multi-path RF channel. The random input  $d(n)$  is chosen between

four levels  $\{-3, -1, 1, 3\}$ , and the channel output is defined as  $q(n) = 0.08d(n + 2) - 0.12d(n + 1) + d(n) + 0.18d(n - 1) - 0.1d(n - 2) + 0.091d(n - 3) - 0.05d(n - 4) + 0.04d(n - 5) + 0.03d(n - 6) + 0.01d(n - 7)$ . The input for NCE is the channel signal  $q(n)$ , and the task aims to retrieve the original four-level random  $d(n)$  series. In the experiment, a similar input speed ( $T_{bit} \sim 60ps$ ) is adopted, and the training/testing set includes 4000/1000 bits, respectively. The winner-takes-all method is applied where the direct RC output is regularized to the nearest level.

#### F.4 RC operation speed analysis

Here we evaluate the effective operation speed of the wave chaotic reservoir computer. The computation cost an RC task is estimated with a software RC problem [122]. Considering a software RC with an  $N$ -dimensional reservoir layer, the execution of each input consumes at least a  $\sim N^2$  times digital operations (from a  $N \times N$  matrix multiplication). Thus the total number of commands required for a  $M$ -point input signal is  $M \cdot N^2$ . We note that only the computation efficiency of the reservoir evolution is considered here, as the same training procedure is adopted in both software and hardware RCs. We next consider the same problem executed on a wave chaotic RC. For this  $M$ -point task, the RC operation time is determined by the duration of the input series  $\tau_0 = M/f_{sam}$ , where  $f_{sam}$  is the sampling rate of the AWG. A system with  $N_0$  output channels will reach a combined  $N$ -dimensional reservoir with  $N/N_0$  times RET applications. Thus, the wave chaotic RC completes the same problem with  $\tau_{tot} = \tau_0 N/N_0$ , and the effective operation speed is  $M \cdot N^2 / \tau_{tot} = N \cdot N_0 \cdot f_{sam}$  OPS. It is clear that the speed of the wave chaotic RC will

scale up linearly with larger  $N$ ,  $N_0$ , and  $f_{sam}$  parameters.

## Appendix G: Heterogeneous BMW Structure Details

### G.1 Experimental Methods

The experimental set-up for the 4-port circulator is shown in an open-plate fashion in Fig. G.1. The left (right) component are the top (bottom) plates with BMW rods mounted. The QH island and QSH regions adopt the same color coding as the inset in Fig. 5. The locations of the four ports are shown as \* signs in Fig. G.1. We used Coilcraft 1812SMS-68NGLB loop inductor coils to excite the kink modes at the ports. The magnetic coil antennas are adopted in all measurements shown from Fig. 2 to 5. We can further use rotating magnetic dipole antennas to better excite the modes, which are circularly polarized [29]. The S-parameter measurement is conducted with a Keysight E8364C PNA Network Analyzer (2-port QH bulk region transmission measurement in Fig. 2), and Keysight N5242A PNA-X Network Analyzer (2-port measurements in Fig. 3, 3-port measurements in Fig. 4 and 4-port measurement in Fig. 5). We mount the antenna connected to port 2 (in Fig. 2) on the M-415.DG moving stage from Physik Instrumente to measure the bulk transmission at various locations along the edge of the structure. The QH region consists of Aluminum rods, YG-14 Yttrium-Garnet ferrites from HTD-RF Technology and further magnetized by D150E Nd-Fe-B permanent magnets from Amazing Magnets. The transmission results are first calibrated by an S-parameter measurement

of an empty BMW structure where the rods are removed (i.e., just parallel plates with antennas) and then normalized by the maximum value. Such a calibration method (see SM of [14]) is meant to remove the impedance mismatch between antenna and the experimental structure.

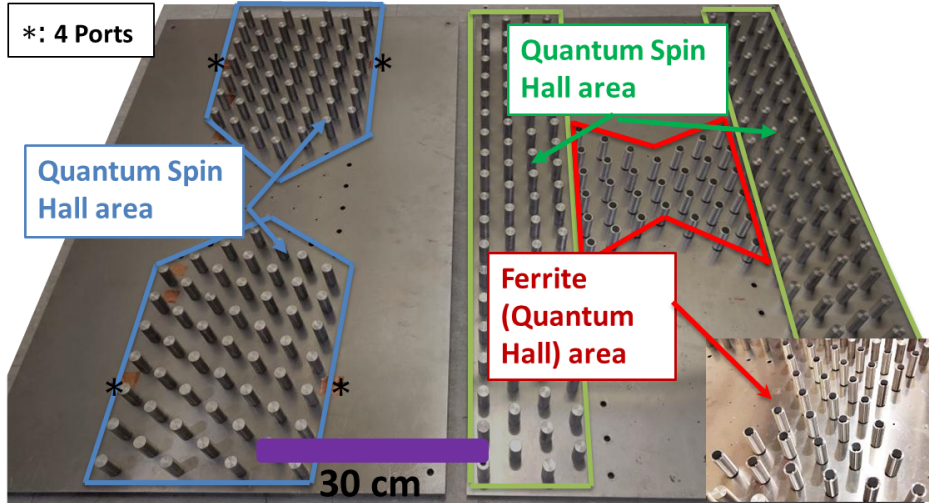


Figure G.1: An open-plate view of the experimental set-up of the 4-port BMW circulator structure. Each region is color coded to match the insets in Fig. 5.

## G.2 Ferrite Material

The YG-14 Yttrium-Garnet ferrites have saturation magnetization  $M_s = 1400Oe$  and resonance line-width  $\Delta H = 25Oe$ . The permeability tensor [47] adopted in the simulation models is:

$$\mu(\omega) = \begin{bmatrix} \mu_1(\omega) & \mu_2(\omega) & 0 \\ -\mu_2(\omega) & \mu_1(\omega) & 0 \\ 0 & 0 & 1 \end{bmatrix} \quad (\text{G.1})$$

where  $\mu_1(\omega) = \mu_\infty + \frac{\omega_m(\omega_l + i\omega\alpha)}{(\omega_l + i\omega\alpha)^2 - \omega^2}$  and  $\mu_2(\omega) = \frac{i\omega\omega_m}{(\omega_l + i\omega\alpha)^2 - \omega^2}$ . The Lamor frequency  $\omega_l = \gamma\mu_0 H_0$  where  $\gamma$  is the gyromagnetic ratio and  $H_0$  is the applied H-field. The gyrotropic frequency is  $\omega_m = \gamma 4\pi M_s$  where  $M_s$  is the saturation magnetization. The damping factor  $\alpha$  is defined here as  $\alpha = \frac{\mu_0 \gamma \Delta H}{2\omega_m}$  where  $\Delta H$  is the ferrite resonance line-width as a function of magnetic field at a certain reference frequency  $\omega_m$ . The BMW bandgap frequency range is near the ferromagnetic anti-resonance regime for the biasing conditions used in this experiment. The Polder tensor values used in the COMSOL simulations are assumed to be independent of frequency and evaluated at the Dirac point (6.08 GHz).

### G.3 Kink mode Back-scattering Studies

We first conduct band structure simulations in COMSOL for a QH-QSH composite PTI structure. The simulation model shown in Fig. G.2 is a supercell structure: a strip of BMW rods with 15 periods in both the QH and QSH regions, and an interface in the middle. We will invert the applied H-field direction in the QH region and study the kink mode properties at the QH-QSH interface. The band structures show that the propagating direction of kink modes is the same in both the  $K$  and  $-K$  direction. This kink mode propagating direction is inverted when the H-field direction is inverted (compare Fig.

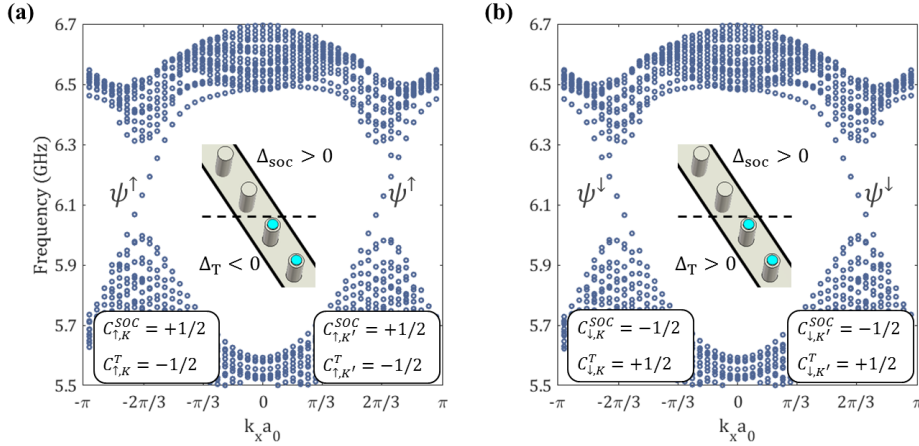


Figure G.2: The photonic band structure of a 15+15 period QH-QSH Supercell structure from COMSOL simulations. The insets are the supercell structures near the QH-QSH interface. The dashed lines represent the location of the QH-QSH interface. Under applied magnetic field in opposite directions ( $-H_z/ +H_z$  in (a)/(b)), the supported kink mode will have opposite synthetic spin (up/down-spin shown as  $\psi^{\uparrow/\downarrow}$ ) and group velocity. Dirac points are at  $k_x a_0 = \pm 2\pi/3$ . Boxed tags: the Chern numbers of the bulk modes below the bandgap for QSH and QH domains.

G.2(a) and (b)).

Transmission measurements at the QH-QSH interface are shown in Fig. G.4. We excite the kink mode at one end of the interface and measure the kink mode transmission at various pick-up locations along the interface. As shown in Fig. G.4(a), the kink mode transmission will not be damped significantly when the measurement location moves further from the source along the propagating direction. On the other end, the signal amplitude on the non-propagating direction will remain 25 dB lower than the propagating direction at various pick-up locations as shown in Fig. G.4(b).



Figure G.3: An open-plate view of the QH-QSH interface 2-port isolator experimental set-up. Note that the biasing magnets on the QH region are not shown.

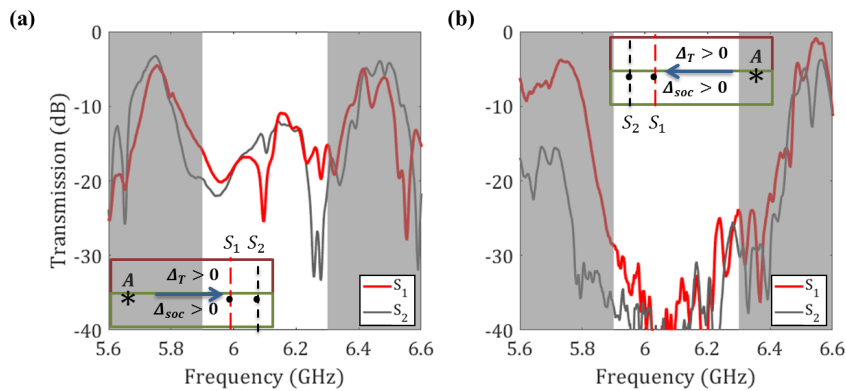


Figure G.4: Plots of kink mode transmission measurement in (a) propagating and (b) non-propagating directions along a QH-QSH interface. In both plots, the S-parameters represent the transmission between two ports:  $S_2$  is measured at a port further from the source (port A) than  $S_1$ . The plots show that the amplitude of the kink mode along the propagating direction does not attenuate significantly, while the amplitude of kink mode in the backward direction is always low.

## G.4 Coupled waveguide issue

In transmission measurements of the 4-port circulator structure, we observed unexpected increase of transmission between two parallel QSH-QSH waveguides near 6.1 GHz as shown in Fig. 5 (a) and (d). This phenomenon is caused by the finite-size problem. As shown in the Fig. G.1, the middle QSH area (highlighted by blue boundaries) is only 7 lattice periods in size. The close proximity between two parallel QSH-QSH waveguides will induce coupling between them. In order to decrease the coupling effect between two parallel QSH-QSH waveguides, we employed DD-13490 absorber from ARC Technologies in the middle QSH (blue) area but away from the QH-QSH interfaces (red boundaries in Fig. G.1). The absorber will decrease the transmission between two coupled QSH-QSH waveguides, while not disturbing the QH-QSH waveguides around the center QH island.

It is well known that two waveguides can couple to each other via their fringing fields and lead to power transfer from one waveguide to another. This can be verified from the PBS (photonic band structure) of a supercell consisting of three QSH region with alternating  $\Delta_{SOC}$ , where the central region contains 7 unit cells. Fig. G.5 shows the PBS near the K' valley. There are 4 modes in the figure, originated from 2 TPSWs (one forward, one backward propagating) at each waveguide (QSH-QSH interface). It is evident from the figure that coupling between co-propagating modes and counter-propagating modes both takes place. Most importantly, the coupling between counter-propagating modes creates a secondary bandgap around 6.06-6.09 GHz. If one launches a TPSW at one interface, it will exponentially decay as it propagates and gets reflected

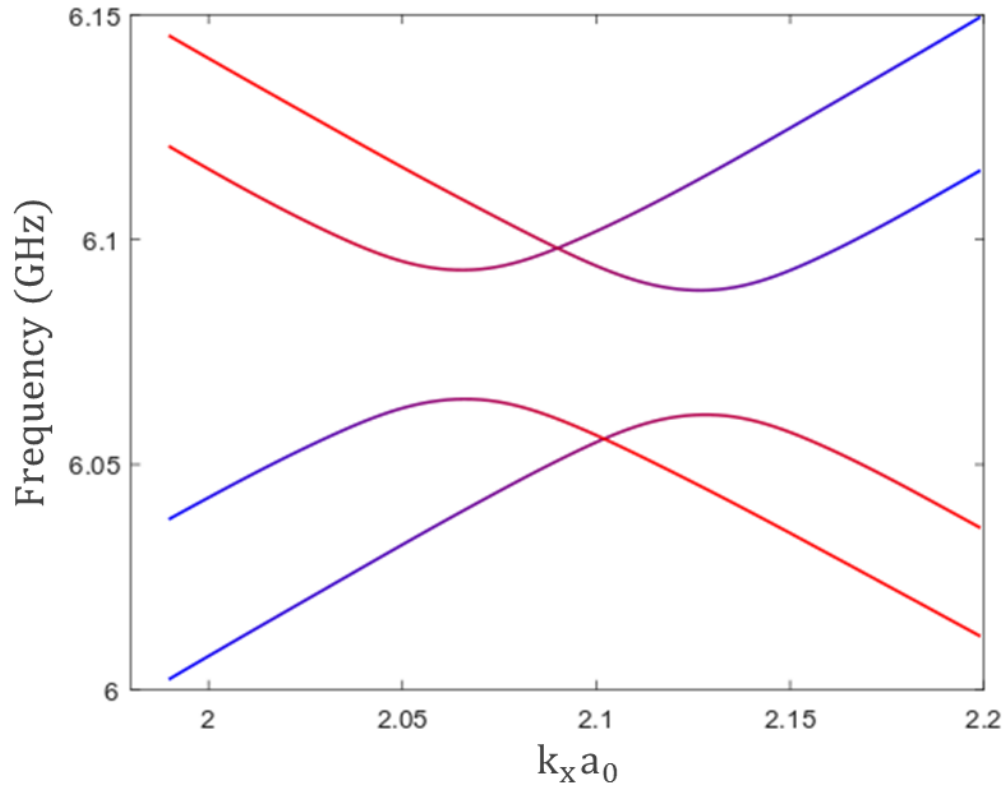


Figure G.5: The 3-QSH supercell PBS near the Dirac point. The positive/negative group velocity parts (blue/red) are mixture of the up/down-spin mode localized at the top interface and down/up-spin mode at the bottom interface. Near the secondary bandgap at about 6.06-6.09 GHz, there is a four-mode mixing.

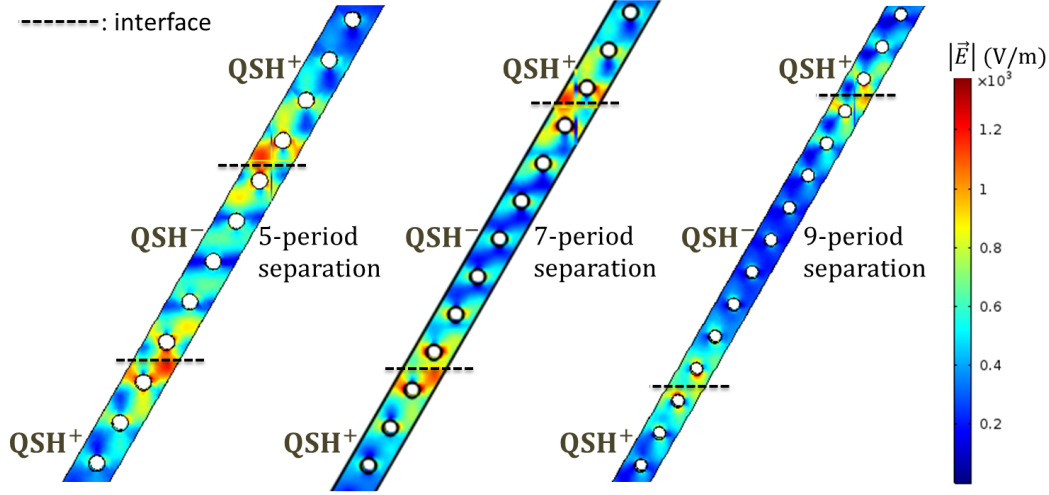


Figure G.6: Supercell simulations results of the kink mode at the Dirac point. Color:  $|\mathbf{E}|$  of the eigenmodes near 6.1 GHz. The 5 and 7 periods of unit cell separation cases cause E-field spreading in the entire middle QSH region, while the 9-period separation case makes the kink modes better localized at the interfaces.

through the other interface. This is exactly what is happening in Fig. 5 near 6.08 GHz, causing high transmission  $S_{31}$  and  $S_{42}$ , in (a) and (d), respectively.

To illustrate the coupled waveguide effect, we conducted supercell parallel waveguide simulations in COMSOL as shown in Fig. G.6. The supercell consists of three QSH bulk regions with alternating  $\Delta_{SOC}$  signs. We examine the E-field profile of the eigenmodes while increasing the size of the middle QSH region. To overcome the finite-size problem, we find that at least a 9-period lattice in the middle region is required to establish clear isolation between two parallel waveguides.

## G.5 QH-QSH structure with no external magnetic field

In contrast to the QH-QSH interface transmission experiments under external H-field shown in Fig. 3, we conducted a zero H-field test using the same experimental

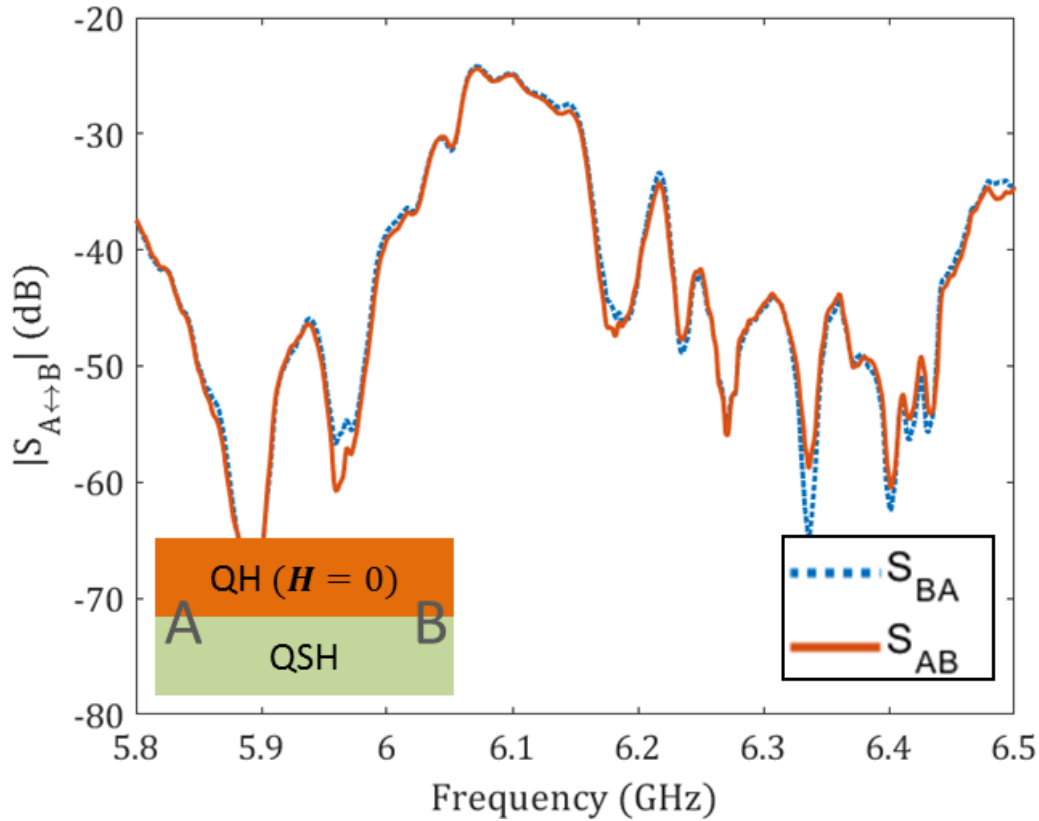


Figure G.7: Zero magnetic field transmission measurement between port A and B. Two ports are in the same locations as in the measurement shown in Fig. 3, located on the QH-QSH interface. We find that the transmission profile between two ports are very similar, indicating the time-reversal symmetry is not broken in the un-magnetized ferrite case.

structure shown in Fig. G.7. The QH bulk region will no longer have a band gap in the absence of an applied magnetic field (see QH bulk transmission in Fig. 2). Though the QSH region is insensitive to the magnetic field, an interface between QSH and a unbiased QH region is not able to host uni-directional TPSWs. Compared to the 35dB contrast between left/right going waves in Fig. 3, the transmission between port A and B are nearly the same in both directions.

## G.6 Topological Y-junction

Figure G.8 shows an open-plate view of the topological Y-junction.

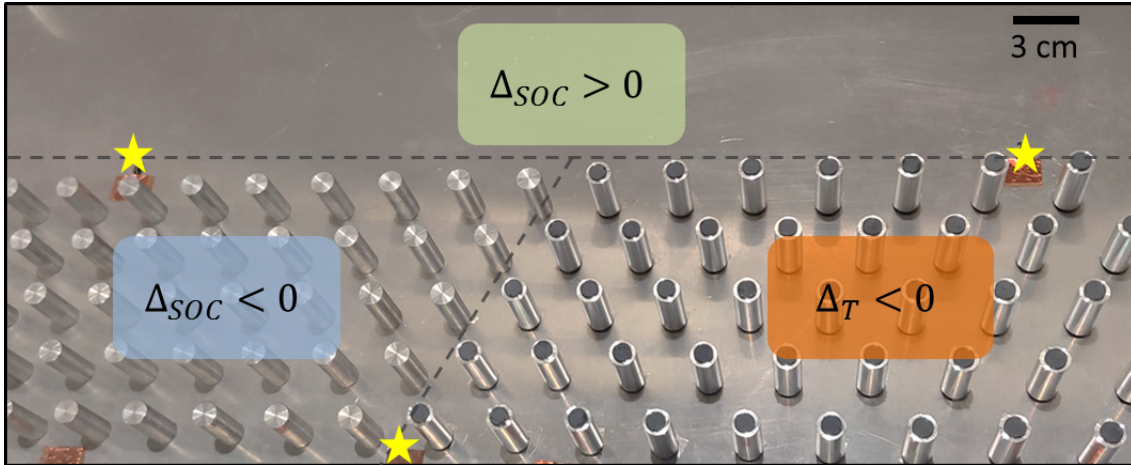


Figure G.8: The open-plate view of the topological Y-junction. The magnets for QH region and the upper QSH rods and are not shown in this view. The three topological regions are color-coded as in Fig. 4(a). The dashed lines mark the interface between different topological phases. The stars are the locations of the ports.

## Appendix H: Extended Symplectic Group Analysis of BMW Hamiltonian

Here we present a quick proof to show that the BMW Hamiltonian falls into the symplectic group. The effective Hamiltonian of the BMW lattice can be written as  $H(\delta k) = H_0 + H_{SOC/P}$ , where  $\delta k = (\delta k_x, \delta k_y)$  is the wavenumber measured from the Dirac points  $K$  and  $K'$ .  $H_0$  and  $H_{SOC/P}$  are the unperturbed Hamiltonian and the perturbation term, respectively. The subscripts represents the type of perturbations that are introduced inside the BMW unit cell and which give rise to different topological phases, namely the spin-orbit coupling (for QSH-PTI) and parity breaking (for QVH-PTI). Here we note that both QSH and QVH-BMW systems are suitable as platforms to realize GSE statistics. For simplicity, we focus on the QSH-BMW analysis in this paper, while a similar analysis also applies to the QVH-BMW system. The effective Hamiltonian of the QSH-BMW lattice at the  $K$  and  $K'$  valleys are written as [206]:

$$H_K^{\uparrow\downarrow}(\delta k_x, \delta k_y) = v_D s_0(\delta k_x \sigma_x + \delta k_y \sigma_y) + \omega_D \Delta_{em} s_z \sigma_z \quad (\text{H.1})$$

$$H_{K'}^{\uparrow\downarrow}(\delta k_x, \delta k_y) = v_D s_0(-\delta k_x \sigma_x + \delta k_y \sigma_y) - \omega_D \Delta_{em} s_z \sigma_z \quad (\text{H.2})$$

where  $s$  and  $\sigma$  are the Pauli matrices acting on the spin and the Dirac degeneracy, respectively.

The arrow  $\uparrow$  ( $\downarrow$ ) refers to the up (down) spin index. The quantities  $\omega_D$  and  $v_D$  are the

frequency and the group velocity at the Dirac points. Note that the Kronecker product ( $s\sigma \equiv s \otimes \sigma$ ) shorthand is used. The BMW Hamiltonian is Hermitian with real eigenvalues. It is shown by Mehta and Dyson that a quaternion-real matrix  $\mathbf{H}$  can be diagonalized by a symplectic matrix [9, 10]. Our goal is to show that the BMW Hamiltonian is quaternion-real (see the definition in Ref. [9]). For simplicity, we look at the BMW Hamiltonian at the  $K$ -valley (Eqn. H.1). In matrix form, we have  $H_K^{\uparrow\downarrow} = \begin{bmatrix} q_{11} & 0 \\ 0 & q_{22} \end{bmatrix}$ , where  $q_{11}, q_{22}$  are quaternion numbers written as  $q_{11} = 0 + \sigma \cdot \mathbf{q}_{\uparrow}$  and  $q_{22} = 0 + \sigma \cdot \mathbf{q}_{\downarrow}$ . The quantities  $\mathbf{q}_{\uparrow} = (v_D \delta k_x, v_D \delta k_y, \omega_D \Delta_{em})$  and  $\mathbf{q}_{\downarrow} = (v_D \delta k_x, v_D \delta k_y, -\omega_D \Delta_{em})$  are real. Thus it is clear that the matrix  $H_K = \begin{bmatrix} q_{11} & 0 \\ 0 & q_{22} \end{bmatrix}$  is quaternion-real and fits into the symplectic group.

As discussed above, we have shown that the BMW Hamiltonian falls into the GSE universality group, and further written out the anti-unitary T-operator for the BMW system that leaves the Hamiltonian invariant.

## Bibliography

- [1] Y. Y. Atas, E. Bogomolny, O. Giraud, and G. Roux, *Physical Review Letters* **110**, 084101 (2013).
- [2] A. Gokirmak, D.-H. Wu, J. S. A. Bridgewater, and S. M. Anlage, *Review of Scientific Instruments* **69**, 3410 (1998).
- [3] B. Xiao, T. M. Antonsen, E. Ott, and S. M. Anlage, *Physical Review E* **93**, 052205 (2016).
- [4] E. Ott, *Chaos in Dynamical Systems* (Cambridge University Press, Cambridge, 2002).
- [5] E. N. Lorenz, (1972).
- [6] O. E. Rossler, *Physics Letters A* **71**, 155 (1979).
- [7] E. N. Lorenz, *Journal of the Atmospheric Sciences* **20**, 130 (1963).
- [8] E. P. Wigner, *The Annals of Mathematics* **62**, 548 (1955).
- [9] F. J. Dyson, *Journal of Mathematical Physics* **3**, 140 (1962).
- [10] M. L. Mehta, *Academic Press* (2004) p. 706, arXiv:0509286 [hep-ph] .
- [11] O. Bohigas, M. J. Giannoni, and C. Schmit, *Physical Review Letters* **52**, 1 (1984).
- [12] R. U. Haq, A. Pandey, and O. Bohigas, *Physical Review Letters* **48**, 1086 (1982).
- [13] Y. Alhassid, *Reviews of Modern Physics* **72**, 895 (2000).
- [14] D. H. Wu, J. S. A. Bridgewater, A. Gokirmak, and S. M. Anlage, *Physical Review Letters* **81**, 2890 (1998).
- [15] B. Dietz and A. Richter, *Chaos: An Interdisciplinary Journal of Nonlinear Science* **25**, 097601 (2015).
- [16] S. Ma, B. Xiao, Z. Drikas, B. Addissie, R. Hong, T. M. Antonsen, E. Ott, and S. M. Anlage, *Physical Review E* **101**, 022201 (2020).

- [17] E. Doron, U. Smilansky, and A. Frenkel, *Physical Review Letters* **65**, 3072 (1990).
- [18] P. So, S. M. Anlage, E. Ott, and R. N. Oerter, *Physical Review Letters* **74**, 2662 (1995).
- [19] U. Kuhl, M. Martínez-Mares, R. A. Méndez-Sánchez, and H.-J. Stöckmann, *Physical Review Letters* **94**, 144101 (2005).
- [20] M. Hoijer and L. Kroon, *IEEE Transactions on Electromagnetic Compatibility* **55**, 1328 (2013).
- [21] A. Gifuni, I. D. Flintoft, S. J. Bale, G. C. R. Melia, and A. C. Marvin, *IEEE Transactions on Electromagnetic Compatibility* **58**, 678 (2016).
- [22] B. Dietz, T. Klaus, M. Miski-Oglu, A. Richter, M. Wunderle, and C. Bouazza, *Physical Review Letters* **116**, 023901 (2016).
- [23] M. Dupré, P. Del Hougne, M. Fink, F. Lemoult, and G. Lerosey, *Physical Review Letters* **115**, 017701 (2015).
- [24] N. Kaina, M. Dupré, G. Lerosey, and M. Fink, *Scientific Reports* **4**, 6693 (2015).
- [25] P. del Hougne, M. F. Imani, T. Sleasman, J. N. Gollub, M. Fink, G. Lerosey, and D. R. Smith, *Scientific Reports* **8**, 6536 (2018).
- [26] J. P. Parmantier, *IEEE Transactions on Electromagnetic Compatibility* **46**, 359 (2004).
- [27] X. Zheng, T. M. Antonsen, and E. Ott, *Electromagnetics* **26**, 37 (2006).
- [28] X. Zheng, T. M. Antonsen, and E. Ott, *Electromagnetics* **26**, 3 (2006).
- [29] J. A. Hart, T. M. Antonsen, and E. Ott, *Physical Review E* **80**, 041109 (2009).
- [30] J.-H. Yeh, J. A. Hart, E. Bradshaw, T. M. Antonsen, E. Ott, and S. M. Anlage, *Physical Review E* **82**, 041114 (2010).
- [31] G. Gradoni, J.-H. Yeh, B. Xiao, T. M. Antonsen, S. M. Anlage, and E. Ott, *Wave Motion* **51**, 606 (2014).
- [32] X. Zheng, S. Hemmady, T. M. Antonsen, S. M. Anlage, and E. Ott, *Physical Review E* **73**, 046208 (2006).
- [33] G. Gradoni, T. M. Antonsen, and E. Ott, *Physical Review E* **86**, 046204 (2012).
- [34] X. Li, C. Meng, Y. Liu, E. Schamiloglu, and S. D. Hemmady, *IEEE Transactions on Electromagnetic Compatibility* **57**, 448 (2015).
- [35] J. Q. Fan, Y. Pan, J. H. Hao, and H. Y. Zhang, *Progress in Electromagnetics Research Letters* **65**, 81 (2017).

- [36] L. Luyao, M. Hongge, and W. Ming, in *2017 IEEE 2nd Advanced Information Technology, Electronic and Automation Control Conference (IAEAC)* (IEEE, 2017) pp. 1526–1529.
- [37] S. Hemmady, X. Zheng, E. Ott, T. M. Antonsen, and S. M. Anlage, *Physical Review Letters* **94**, 014102 (2005).
- [38] S. Hemmady, X. Zheng, J. Hart, T. M. Antonsen, E. Ott, and S. M. Anlage, *Physical Review E* **74**, 036213 (2006).
- [39] M. V. Berry, *European Journal of Physics* **2**, 91 (1981).
- [40] Y. V. Fyodorov and D. V. Savin, *Journal of Experimental and Theoretical Physics Letters* **80**, 725 (2004).
- [41] A. Rehemangiang, M. Allgaier, C. H. Joyner, S. Müller, M. Sieber, U. Kuhl, and H.-J. Stöckmann, *Physical Review Letters* **117**, 064101 (2016).
- [42] G. Gradoni, T. M. Antonsen, S. M. Anlage, and E. Ott, *IEEE Transactions on Electromagnetic Compatibility* **57**, 1049 (2015).
- [43] M. Notomi, E. Kuramochi, and T. Tanabe, *Nature Photonics* **2**, 741 (2008).
- [44] A. Wallraff, D. I. Schuster, A. Blais, L. Frunzio, R.-S. Huang, J. Majer, S. Kumar, S. M. Girvin, and R. J. Schoelkopf, *Nature* **431**, 162 (2004).
- [45] H. Alt, C. I. Barbosa, H.-D. Gräf, T. Guhr, H. L. Harney, R. Hofferbert, H. Rehfeld, and A. Richter, *Physical Review Letters* **81**, 4847 (1998).
- [46] A. Ö. Kaya, L. J. Greenstein, and W. Trappe, *IEEE Transactions on Wireless Communications* **8**, 4165 (2009).
- [47] W. Porod, Z.-A. Shao, and C. S. Lent, *Applied Physics Letters* **61**, 1350 (1992).
- [48] F. R. Waugh, M. J. Berry, D. J. Mar, R. M. Westervelt, K. L. Campman, and A. C. Gossard, *Physical Review Letters* **75**, 705 (1995).
- [49] R. Brunner, R. Akis, D. K. Ferry, F. Kuchar, and R. Meisels, *Physical Review Letters* **101**, 024102 (2008).
- [50] J. T. Chalker and P. D. Coddington, *Journal of Physics C: Solid State Physics* **21**, 2665 (1988).
- [51] J. D. Sau and S. D. Sarma, *Nature Communications* **3**, 964 (2012).
- [52] C. W. J. Beenakker, *Reviews of Modern Physics* **87**, 1037 (2015).
- [53] P. Zhang and F. Nori, *New Journal of Physics* **18**, 043033 (2016).
- [54] B. Dietz, T. Guhr, H. L. Harney, and A. Richter, *Physical Review Letters* **96**, 254101 (2006).

- [55] G. B. Tait, R. E. Richardson, M. B. Slocum, and M. O. Hatfield, *IEEE Transactions on Electromagnetic Compatibility* **53**, 846 (2011).
- [56] G. B. Tait, R. E. Richardson, M. B. Slocum, M. O. Hatfield, and M. J. Rodriguez, *IEEE Transactions on Electromagnetic Compatibility* **53**, 229 (2011).
- [57] I. Junqua, J.-P. Parmantier, and F. Issac, *Electromagnetics* **25**, 603 (2005).
- [58] S. Hemmady, T. M. Antonsen, E. Ott, and S. M. Anlage, *IEEE Transactions on Electromagnetic Compatibility* **54**, 758 (2012).
- [59] L. Gagliardi, D. Micheli, G. Gradoni, F. Moglie, and V. M. Primiani, *IEEE Antennas and Wireless Propagation Letters* **14**, 1463 (2015).
- [60] B. Xiao, T. M. Antonsen, E. Ott, Z. B. Drikas, J. G. Gil, and S. M. Anlage, *Physical Review E* **97**, 062220 (2018).
- [61] D. A. Hill, *Electromagnetic Fields in Cavities* (IEEE, 2009) p. 280.
- [62] J. Gil Gil, Z. B. Drikas, T. D. Andreadis, and S. M. Anlage, *IEEE Transactions on Electromagnetic Compatibility* **58**, 1535 (2016).
- [63] M. Zhou, E. Ott, T. M. Antonsen, and S. M. Anlage, *Chaos* **27**, 103114 (2017).
- [64] J.-H. Yeh, Z. Drikas, J. Gil Gil, S. Hong, B. Taddese, E. Ott, T. Antonsen, T. Andreadis, and S. Anlage, *Acta Physica Polonica A* **124**, 1045 (2013).
- [65] J.-H. Yeh and S. M. Anlage, *Review of Scientific Instruments* **84**, 034706 (2013).
- [66] S. Ma, S. Phang, Z. Drikas, B. Addissie, R. Hong, V. Blakaj, G. Gradoni, G. Tanner, T. M. Antonsen, E. Ott, and S. M. Anlage, *Physical Review Applied* **14**, 14022 (2020).
- [67] D. Hill, M. Ma, A. Ondrejka, B. Riddle, M. Crawford, and R. Johnk, *IEEE Transactions on Electromagnetic Compatibility* **36**, 169 (1994).
- [68] D. Hill, *IEEE Transactions on Electromagnetic Compatibility* **40**, 209 (1998).
- [69] D. Coppersmith and S. Winograd, *Journal of Symbolic Computation* **9**, 251 (1990).
- [70] S. Ma, B. Xiao, R. Hong, B. Addissie, Z. Drikas, T. Antonsen, E. Ott, and S. Anlage, *Acta Physica Polonica A* **136**, 757 (2019).
- [71] P. Mehta, C.-H. Wang, A. G. R. Day, C. Richardson, M. Bukov, C. K. Fisher, and D. J. Schwab, *A high-bias, low-variance introduction to Machine Learning for physicists*, Tech. Rep. (2018) arXiv:1803.08823v1 .
- [72] S. Das Sarma, D.-L. Deng, and L.-M. Duan, *Physics Today* **72**, 48 (2019).
- [73] J. Carrasquilla and R. G. Melko, *Nature Physics* **13**, 431 (2017).

- [74] J. Venderley, V. Khemani, and E.-A. Kim, *Physical Review Letters* **120**, 257204 (2018).
- [75] A. Seif, K. A. Landsman, N. M. Linke, C. Figgatt, C. Monroe, and M. Hafezi, *Journal of Physics B: Atomic, Molecular and Optical Physics* **51**, 174006 (2018).
- [76] C. J. van Diepen, P. T. Eendebak, B. T. Buijtdorp, U. Mukhopadhyay, T. Fujita, C. Reichl, W. Wegscheider, and L. M. K. Vandersypen, *Applied Physics Letters* **113**, 033101 (2018).
- [77] S. S. Kalantre, J. P. Zwolak, S. Ragole, X. Wu, N. M. Zimmerman, M. D. Stewart, and J. M. Taylor, *npj Quantum Information* **5**, 6 (2019).
- [78] Z. Lu, J. Pathak, B. Hunt, M. Girvan, R. Brockett, and E. Ott, *Chaos: An Interdisciplinary Journal of Nonlinear Science* **27**, 041102 (2017).
- [79] J. Pathak, B. Hunt, M. Girvan, Z. Lu, and E. Ott, *Physical Review Letters* **120**, 024102 (2018).
- [80] G. Neofotistos, M. Mattheakis, G. D. Barmparis, J. Hizanidis, G. P. Tsironis, and E. Kaxiras, *Frontiers in Physics* **7**, 1 (2019).
- [81] M. Frazier, B. Taddese, T. Antonsen, and S. M. Anlage, *Physical Review Letters* **110**, 063902 (2013).
- [82] M. Frazier, B. Taddese, B. Xiao, T. Antonsen, E. Ott, and S. M. Anlage, *Physical Review E* **88**, 062910 (2013).
- [83] Z. B. Drikas, J. Gil Gil, S. K. Hong, T. D. Andreadis, J.-H. Yeh, B. T. Taddese, and S. M. Anlage, *IEEE Transactions on Electromagnetic Compatibility* **56**, 1480 (2014).
- [84] Y. Lecun, Y. Bengio, and G. Hinton, “Deep learning,” (2015), arXiv:arXiv:1312.6184v5 .
- [85] S. Ma, T. Antonsen, S. Anlage, and E. Ott, (2021), 10.21203/rs.3.rs-783820/v1.
- [86] Y. Zhang, A. Mesaros, K. Fujita, S. D. Edkins, M. H. Hamidian, K. Ch’ng, H. Eisaki, S. Uchida, J. C. S. Davis, E. Khatami, and E.-A. Kim, *Nature* **570**, 484 (2019).
- [87] Y. K. Chembo, *Chaos: An Interdisciplinary Journal of Nonlinear Science* **30**, 013111 (2020).
- [88] B. J. Shastri, A. N. Tait, T. Ferreira de Lima, W. H. P. Pernice, H. Bhaskaran, C. D. Wright, and P. R. Prucnal, *Nature Photonics* **15**, 102 (2021).
- [89] H. Esmaeilzadeh, E. Blem, R. St. Amant, K. Sankaralingam, and D. Burger, *IEEE Micro* **32**, 122 (2012).

- [90] K. Roy, A. Jaiswal, and P. Panda, *Nature* **575**, 607 (2019).
- [91] P. A. Merolla, J. V. Arthur, R. Alvarez-Icaza, A. S. Cassidy, J. Sawada, F. Akopyan, B. L. Jackson, N. Imam, C. Guo, Y. Nakamura, B. Brezzo, I. Vo, S. K. Esser, R. Appuswamy, B. Taba, A. Amir, M. D. Flickner, W. P. Risk, R. Manohar, and D. S. Modha, *Science* **345**, 668 (2014).
- [92] J. Feldmann, N. Youngblood, C. D. Wright, H. Bhaskaran, and W. H. P. Pernice, *Nature* **569**, 208 (2019).
- [93] Y. Shen, N. C. Harris, S. Skirlo, M. Prabhu, T. Baehr-Jones, M. Hochberg, X. Sun, S. Zhao, H. Larochelle, D. Englund, and M. Soljačić, *Nature Photonics* **11**, 441 (2017).
- [94] P. Yao, H. Wu, B. Gao, J. Tang, Q. Zhang, W. Zhang, J. J. Yang, and H. Qian, *Nature* **577**, 641 (2020).
- [95] J. Torrejon, M. Riou, F. A. Araujo, S. Tsunegi, G. Khalsa, D. Querlioz, P. Bortolotti, V. Cros, K. Yakushiji, A. Fukushima, H. Kubota, S. Yuasa, M. D. Stiles, and J. Grollier, *Nature* **547**, 428 (2017).
- [96] D. Canaday, A. Griffith, and D. J. Gauthier, *Chaos: An Interdisciplinary Journal of Nonlinear Science* **28**, 123119 (2018).
- [97] K. Nakajima, K. Fujii, M. Negoro, K. Mitarai, and M. Kitagawa, *Physical Review Applied* **11**, 034021 (2019).
- [98] F. Laporte, *Novel architectures for brain-inspired photonic computers*, Ph.D. thesis, Universiteit Gent (2020).
- [99] Y. Zhong, J. Tang, X. Li, B. Gao, H. Qian, and H. Wu, *Nature Communications* **12**, 408 (2021).
- [100] A. Sirunyan, A. Tumasyan, W. Adam, F. Ambrogio, and A. et al., *Journal of Instrumentation* **15**, P10017 (2020).
- [101] G. Tanaka, T. Yamane, J. B. Héroux, R. Nakane, N. Kanazawa, S. Takeda, H. Numata, D. Nakano, and A. Hirose, *Neural Networks* **115**, 100 (2019).
- [102] N. Mohammadi Estakhri, B. Edwards, and N. Engheta, *Science* **363**, 1333 (2019).
- [103] T. W. Hughes, I. A. D. Williamson, M. Minkov, and S. Fan, *Science Advances* **5**, eaay6946 (2019).
- [104] G. Wetzstein, A. Ozcan, S. Gigan, S. Fan, D. Englund, M. Soljačić, C. Denz, D. A. B. Miller, and D. Psaltis, *Nature* **588**, 39 (2020).
- [105] J. Feldmann, N. Youngblood, M. Karpov, H. Gehring, X. Li, M. Stappers, M. Le Gallo, X. Fu, A. Lukashchuk, A. S. Raja, J. Liu, C. D. Wright, A. Sebastian, T. J. Kippenberg, W. H. P. Pernice, and H. Bhaskaran, *Nature* **589**, 52 (2021).

- [106] L. Appeltant, M. Soriano, G. Van der Sande, J. Danckaert, S. Massar, J. Dambre, B. Schrauwen, C. Mirasso, and I. Fischer, *Nature Communications* **2**, 468 (2011).
- [107] Q. Vinckier, F. Duport, A. Smerieri, K. Vandoorne, P. Bienstman, M. Haelterman, and S. Massar, *Optica* **2**, 438 (2015).
- [108] G. Van Der Sande, D. Brunner, and M. C. Soriano, *Nanophotonics* **6**, 561 (2017).
- [109] L. Grigoryeva and J.-P. Ortega, *Neural Networks* **108**, 495 (2018).
- [110] P. Vlachas, J. Pathak, B. Hunt, T. Sapsis, M. Girvan, E. Ott, and P. Koumoutsakos, *Neural Networks* **126**, 191 (2020).
- [111] X. Lin, Y. Rivenson, N. T. Yardimci, M. Veli, Y. Luo, M. Jarrahi, and A. Ozcan, *Science* **361**, 1004 (2018).
- [112] K. Vandoorne, P. Mechet, T. Van Vaerenbergh, M. Fiers, G. Morthier, D. Verstraeten, B. Schrauwen, J. Dambre, and P. Bienstman, *Nature Communications* **5**, 3541 (2014).
- [113] P. O'Connor, J. Gehlen, and E. J. Heller, *Physical Review Letters* **58**, 1296 (1987).
- [114] C. Liu, R. E. C. van der Wel, N. Rotenberg, L. Kuipers, T. F. Krauss, A. Di Falco, and A. Fratilocchi, *Nature Physics* **11**, 358 (2015).
- [115] K. Pichler, M. Kühmayer, J. Böhm, A. Brandstötter, P. Ambichl, U. Kuhl, and S. Rotter, *Nature* **567**, 351 (2019).
- [116] B. W. Frazier, T. M. Antonsen, S. M. Anlage, and E. Ott, *Physical Review Research* **2**, 043422 (2020).
- [117] L. Chen, T. Kottos, and S. M. Anlage, *Nature Communications* **11**, 5826 (2020).
- [118] K. Kim, S. Bittner, Y. Zeng, S. Guazzotti, O. Hess, Q. J. Wang, and H. Cao, *Science* **371**, 948 (2021).
- [119] C. Fernando and S. Sojakka, in *Lecture Notes in Artificial Intelligence (Subseries of Lecture Notes in Computer Science)*, Vol. 2801 (Springer Verlag, 2003) pp. 588–597.
- [120] F. Laporte, A. Katumba, J. Dambre, and P. Bienstman, *Optics Express* **26**, 7955 (2018).
- [121] G. Marcucci, D. Pierangeli, and C. Conti, *Physical Review Letters* **125**, 093901 (2020).
- [122] M. Rafayelyan, J. Dong, Y. Tan, F. Krzakala, and S. Gigan, *Physical Review X* **10**, 041037 (2020).
- [123] M. Zhou, E. Ott, T. M. Antonsen, and S. M. Anlage, *Chaos: An Interdisciplinary Journal of Nonlinear Science* **29**, 033113 (2019).

- [124] S. Hemmady, X. Zheng, J. Hart, T. M. Antonsen, E. Ott, and S. M. Anlage, *Physical Review E* **74**, 036213 (2006).
- [125] S. Ma, T. M. Antonsen, E. Ott, and S. M. Anlage, (2021), 10.48550/arxiv.2112.05306, arXiv:2112.05306 .
- [126] O. Hul, S. Bauch, P. Pakoński, N. Savytsky, K. Życzkowski, and L. Sirko, *Physical Review E* **69**, 056205 (2004).
- [127] A. M. Martínez-Argüello, A. Rehemangiang, M. Martínez-Mares, J. A. Méndez-Bermúdez, H.-J. Stöckmann, and U. Kuhl, *Physical Review B* **98**, 075311 (2018).
- [128] A. Rehemangiang, M. Richter, U. Kuhl, and H.-J. Stöckmann, *Physical Review Letters* **124**, 116801 (2020).
- [129] J. Lu, J. Che, X. Zhang, and B. Dietz, *Physical Review E* **102**, 022309 (2020).
- [130] C. Dembowski, B. Dietz, H.-D. Gräf, A. Heine, F. Leyvraz, M. Miski-Oglu, A. Richter, and T. H. Seligman, *Physical Review Letters* **90**, 014102 (2003).
- [131] C. Dembowski, B. Dietz, T. Friedrich, H.-D. Gräf, H. L. Harney, A. Heine, M. Miski-Oglu, and A. Richter, *Physical Review E* **71**, 046202 (2005).
- [132] U. Kuhl, R. Höhmann, J. Main, and H.-J. Stöckmann, *Physical Review Letters* **100**, 254101 (2008).
- [133] S. Shinohara, T. Harayama, T. Fukushima, M. Hentschel, T. Sasaki, and E. E. Narimanov, *Physical Review Letters* **104**, 163902 (2010).
- [134] B. Dietz and A. Richter, *Physica Scripta* **94**, 014002 (2019).
- [135] B. Dietz, A. Heusler, K. H. Maier, A. Richter, and B. A. Brown, *Physical Review Letters* **118**, 012501 (2017).
- [136] Y. Aurégan and V. Pagneux, *Acta Acustica united with Acustica* **102**, 869 (2016).
- [137] M. Białous, V. Yunko, S. Bauch, M. Ławniczak, B. Dietz, and L. Sirko, *Physical Review Letters* **117**, 144101 (2016).
- [138] B. Dietz, V. Yunko, M. Białous, S. Bauch, M. Ławniczak, and L. Sirko, *Physical Review E* **95**, 052202 (2017).
- [139] J. Che, J. Lu, X. Zhang, B. Dietz, and G. Chai, *Physical Review E* **103**, 042212 (2021).
- [140] S. Johnson, A. Mekis, S. Fan, and J. Joannopoulos, *Computing in Science Engineering* **3**, 38 (2001).
- [141] J. D. Joannopoulos, P. R. Villeneuve, and S. Fan, *Nature* **386**, 143 (1997).

- [142] J. D. Joannopoulos, S. G. Johnson, J. N. Winn, and R. D. Meade, *Photonic Crystals* (Princeton University Press, 2008).
- [143] K. Lai, T. Ma, X. Bo, S. Anlage, and G. Shvets, *Scientific Reports* **6**, 28453 (2016), 1601.01311 .
- [144] S. Ma, B. Xiao, Y. Yu, K. Lai, G. Shvets, and S. M. Anlage, *Physical Review B* **100**, 085118 (2019).
- [145] S. Ma and S. M. Anlage, *Applied Physics Letters* **116**, 250502 (2020).
- [146] Y. G. N. Liu, P. S. Jung, M. Parto, D. N. Christodoulides, and M. Khajavikhan, *Nature Physics* **17**, 704 (2021).
- [147] W. Maimaiti, B. Dietz, and A. Andreanov, *Physical Review B* **102**, 214301 (2020).
- [148] W. Zhang and B. Dietz, *Physical Review B* **104**, 064310 (2021).
- [149] M. Reisner, M. Bellec, U. Kuhl, and F. Mortessagne, *Optical Materials Express* **11**, 629 (2021).
- [150] S. Bittner, B. Dietz, M. Miski-Oglu, A. Richter, C. Ripp, E. Sadurní, and W. P. Schleich, *Physical Review E* **87**, 042912 (2013).
- [151] A. Mekis, J. C. Chen, I. Kurland, S. Fan, P. R. Villeneuve, and J. D. Joannopoulos, *Physical Review Letters* **77**, 3787 (1996).
- [152] T. Kottos and U. Smilansky, *Physical Review Letters* **79**, 4794 (1997).
- [153] T. Kottos and U. Smilansky, *Annals of Physics* **274**, 76 (1999).
- [154] G. Casati, F. Valz-Gris, and I. Guarneri, *Lettere al Nuovo Cimento* **28**, 279 (1980).
- [155] A. Kudrolli, V. Kidambi, and S. Sridhar, *Physical Review Letters* **75**, 822 (1995).
- [156] S.-H. Chung, A. Gokirmak, D.-H. Wu, J. S. A. Bridgewater, E. Ott, T. M. Antonsen, and S. M. Anlage, *Physical Review Letters* **85**, 2482 (2000).
- [157] U. Kuhl, E. Persson, M. Barth, and H.-J. Stöckmann, *The European Physical Journal B* **17**, 253 (2000).
- [158] Y. Hlushchuk, L. Sirko, U. Kuhl, M. Barth, and H.-J. Stöckmann, *Physical Review E* **63**, 046208 (2001).
- [159] L. Kaplan, *Physical Review E* **64**, 036225 (2001).
- [160] H. Alt, H. D. Gräf, H. L. Harney, R. Hofferbert, H. Lengeler, A. Richter, P. Schardt, and H. A. Weidenmüller, *Physical Review Letters* **74**, 62 (1995).
- [161] O. Hul, P. Šeba, and L. Sirko, *Physical Review E* **79**, 066204 (2009).

- [162] F. D. M. Haldane and S. Raghu, *Physical Review Letters* **100**, 013904 (2008).
- [163] M. Z. Hasan and C. L. Kane, *Reviews of Modern Physics* **82**, 3045 (2010).
- [164] Y. E. Kraus, Y. Lahini, Z. Ringel, M. Verbin, and O. Zilberberg, *Physical Review Letters* **109**, 106402 (2012).
- [165] S. Raghu and F. D. M. Haldane, *Physical Review A* **78**, 033834 (2008).
- [166] B.-y. Xie, H.-F. Wang, X.-y. Zhu, M.-H. Lu, Z. D. Wang, and Y.-f. Chen, *Optics Express* **26**, 24531 (2018).
- [167] F. Zhang, *Science* **358**, 1075 (2017).
- [168] J. Hou, Z. Li, X.-W. Luo, Q. Gu, and C. Zhang, (2018), arXiv:1808.06972 .
- [169] C. L. Kane and E. J. Mele, *Physical Review Letters* **95**, 226801 (2005).
- [170] B. A. Bernevig and S.-C. Zhang, *Physical Review Letters* **96**, 106802 (2006).
- [171] X.-L. Qi and S.-C. Zhang, *Reviews of Modern Physics* **83**, 1057 (2011).
- [172] A. B. Khanikaev and G. Shvets, *Nature Photonics* **11**, 763 (2017).
- [173] Z. Wang, Y. D. Chong, J. D. Joannopoulos, and M. Soljačić, *Physical Review Letters* **100**, 013905 (2008).
- [174] Z. Wang, Y. Chong, J. D. Joannopoulos, and M. Soljačić, *Nature* **461**, 772 (2009).
- [175] S. A. Skirlo, L. Lu, Y. Igarashi, Q. Yan, J. Joannopoulos, and M. Soljačić, *Physical Review Letters* **115**, 253901 (2015).
- [176] S. Longhi, D. Gatti, and G. D. Valle, *Scientific Reports* **5**, 13376 (2015).
- [177] L. Lu, J. D. Joannopoulos, and M. Soljačić, *Nature Physics* **12**, 626 (2016).
- [178] Z.-G. Chen, J. Mei, X.-C. Sun, X. Zhang, J. Zhao, and Y. Wu, *Physical Review A* **95**, 043827 (2017).
- [179] B. Yang, H. Zhang, T. Wu, R. Dong, X. Yan, and X. Zhang, *Physical Review B* **99**, 045307 (2019).
- [180] M. Hafezi, E. A. Demler, M. D. Lukin, and J. M. Taylor, *Nature Physics* **7**, 907 (2011).
- [181] M. Hafezi, S. Mittal, J. Fan, A. Migdall, and J. M. Taylor, *Nature Photonics* **7**, 1001 (2013).
- [182] W. Gao, M. Lawrence, B. Yang, F. Liu, F. Fang, B. Béri, J. Li, and S. Zhang, *Physical Review Letters* **114**, 037402 (2015).

- [183] S. Mittal, J. Fan, S. Faez, A. Migdall, J. M. Taylor, and M. Hafezi, *Physical Review Letters* **113**, 087403 (2014).
- [184] D. Leykam, S. Mittal, M. Hafezi, and Y. D. Chong, *Physical Review Letters* **121**, 023901 (2018).
- [185] A. B. Khanikaev, S. Hossein Mousavi, W.-K. Tse, M. Kargarian, A. H. MacDonald, and G. Shvets, *Nature Materials* **12**, 233 (2013).
- [186] W.-J. Chen, S.-J. Jiang, X.-D. Chen, B. Zhu, L. Zhou, J.-W. Dong, and C. T. Chan, *Nature Communications* **5**, 5782 (2014).
- [187] X. Cheng, C. Jouvaud, X. Ni, S. Hossein Mousavi, A. Z. Genack, A. B. Khanikaev, S. H. Mousavi, A. Z. Genack, and A. B. Khanikaev, *Nature Materials* **15** (2016).
- [188] A. P. Slobozhanyuk, A. B. Khanikaev, D. S. Filonov, D. A. Smirnova, A. E. Miroschnichenko, and Y. S. Kivshar, *Scientific Reports* **6**, 22270 (2016).
- [189] B. Xiao, K. Lai, Y. Yu, T. Ma, G. Shvets, and S. M. Anlage, *Physical Review B* **94**, 195427 (2016).
- [190] Y. Yang, Y. F. Xu, T. Xu, H.-X. Wang, J.-H. Jiang, X. Hu, and Z. H. Hang, *Physical Review Letters* **120**, 217401 (2018).
- [191] X. D. Chen, W. M. Deng, J. C. Lu, and J. W. Dong, *Physical Review B* **97**, 184201 (2018).
- [192] J. Noh, S. Huang, K. P. Chen, and M. C. Rechtsman, *Physical Review Letters* **120**, 063902 (2018).
- [193] F. Gao, H. Xue, Z. Yang, K. Lai, Y. Yu, X. Lin, Y. Chong, G. Shvets, and B. Zhang, *Nature Physics* **14**, 140 (2017).
- [194] R. G. Gladstone, M. Jung, and G. Shvets, (2018), arXiv:1809.02819 .
- [195] X.-D. Chen, F.-L. Shi, H. Liu, J.-C. Lu, W.-M. Deng, J.-Y. Dai, Q. Cheng, and J.-W. Dong, *Physical Review Applied* **10**, 044002 (2018).
- [196] K. Fang, Z. Yu, and S. Fan, *Physical Review Letters* **108**, 153901 (2012).
- [197] K. Fang, Z. Yu, and S. Fan, *Nature Photonics* **6**, 782 (2012).
- [198] M. C. Rechtsman, J. M. Zeuner, A. Tünnermann, S. Nolte, M. Segev, and A. Szameit, *Nature Photonics* **7**, 153 (2013).
- [199] M. C. Rechtsman, J. M. Zeuner, Y. Plotnik, Y. Lumer, D. Podolsky, F. Dreisow, S. Nolte, M. Segev, and A. Szameit, *Nature* **496**, 196 (2013).
- [200] T. Ma and G. Shvets, *Physical Review B* **95**, 165102 (2017).
- [201] Z. Wang and S. Fan, *Optics Letters* **30**, 1989 (2005).

- [202] W. Qiu, Z. Wang, and M. Soljačić, *Optics Express* **19**, 22248 (2011).
- [203] S. R. Zandbergen and M. J. A. de Dood, *Physical Review Letters* **104**, 043903 (2010).
- [204] S. Bittner, B. Dietz, M. Miski-Oglu, P. Oria Iriarte, A. Richter, and F. Schäfer, *Physical Review B* **82**, 014301 (2010).
- [205] U. Kuhl, S. Barkhofen, T. Tudorovskiy, H.-J. Stöckmann, T. Hossain, L. de Forges de Parny, and F. Mortessagne, *Physical Review B* **82**, 094308 (2010).
- [206] T. Ma, A. B. Khanikaev, S. H. Mousavi, and G. Shvets, *Physical Review Letters* **114**, 127401 (2015).
- [207] D. Polder, *Phys. Rev.* **73**, 155 (1948).
- [208] S. W. Mung and W. S. Chan, *IEEE Microwave Magazine* **20**, 55 (2019).
- [209] K. Fang, J. Luo, A. Metelmann, M. H. Matheny, F. Marquardt, A. A. Clerk, and O. Painter, *Nature Physics* **13**, 465 (2017).
- [210] Z. Shen, Y.-L. Zhang, Y. Chen, F.-W. Sun, X.-B. Zou, G.-C. Guo, C.-L. Zou, and C.-H. Dong, *Nature Communications* **9**, 1797 (2018).
- [211] X. Ni, M. Weiner, A. Alù, and A. B. Khanikaev, *Nature Materials* **18** (2018), 10.1038/s41563-018-0252-9.
- [212] H. Jia, R. Zhang, W. Gao, Q. Guo, B. Yang, J. Hu, Y. Bi, Y. Xiang, C. Liu, and S. Zhang, *Science* **363**, 148 (2019).
- [213] R. Fleury, D. L. Sounas, C. F. Sieck, M. R. Haberman, and A. Alù, *Science* **343**, 516 (2014).
- [214] S. Maayani, R. Dahan, Y. Kligerman, E. Moses, A. U. Hassan, H. Jing, F. Nori, D. N. Christodoulides, and T. Carmon, *Nature* **558**, 569 (2018).
- [215] A. B. Khanikaev, R. Fleury, S. H. Mousavi, and A. Alù, *Nature Communications* **6** (2015), 10.1038/ncomms9260.
- [216] U. Stoffregen, J. Stein, H.-J. Stöckmann, M. Kuś, and F. Haake, *Physical Review Letters* **74**, 2666 (1995).
- [217] Y. Kang, X. Ni, X. Cheng, A. B. Khanikaev, and A. Z. Genack, *Nature Communications* **9**, 3029 (2018), arXiv:1804.08707 .
- [218] L.-H. Wu and X. Hu, *Physical Review Letters* **114**, 223901 (2015).
- [219] C. He, X.-C. Sun, X.-P. Liu, M.-H. Lu, Y. Chen, L. Feng, and Y.-F. Chen, *Proceedings of the National Academy of Sciences* **113**, 4924 (2016).

- [220] X.-C. Sun, C. He, X.-P. Liu, Y. Zou, M.-H. Lu, X. Hu, and Y.-F. Chen, *Crystals* **9**, 137 (2019).
- [221] L. Chen, S. M. Anlage, and Y. V. Fyodorov, *Physical Review E* **103**, L050203 (2021), 2101.08335 .
- [222] Computer Simulation Technology, “Weblink,” .
- [223] R. Gunnarsson and M. Backstrom, in *2014 International Symposium on Electromagnetic Compatibility* (IEEE, 2014) pp. 169–174.
- [224] B. D. Addissie, J. C. Rodgers, and T. M. Antonsen, in *2015 IEEE Metrology for Aerospace (MetroAeroSpace)* (IEEE, 2015) pp. 214–219.